Generalized Locally Exact Homogenization Theory for Unidirectionally-Reinforced Composites

---

A Dissertation

Presented to

the Faculty of the School of Engineering and Applied Science

University of Virginia

In Partial Fulfillment of the Requirements for the Degree of

Doctoral of Philosophy

(Civil and Environmental Engineering/Applied Mechanics)

by

Guannan Wang

August 2016

Approval Sheet

This dissertation is submitted in partial fulfillment of the requirements

for the degree of

Doctoral of Philosophy

(Civil and Environmental Engineering/Applied Mechanics)

This dissertation has been read and approved by the examining committee:

Thomas T. Baber (Chairman), CEE/
Jonathan L. Goodall, CEE

Marek-Jerzy Pindera (Advisor), CEE

Houston G. Wood, MAE

Osman E. Ozbulut, CEE

Baoxing Xu, MAE

Accepted for the School of Engineering and Applied Science

Dean, School of Engineering and Applied Science

August 2016

Abstract

This dissertation describes the construction, validation and applications of a stable and quickly converging elasticity-based locally exact homogenization theory for unidirectionally-reinforced composites. Elasticity-based homogenization approaches offer a number of advantages relative to finite-element, finite-difference or finite-volume homogenization schemes, including extremely fast input data construction, ability to investigate composites with very thin coatings or interphases without experiencing convergence issues common to finite-element analyses, and ability to efficiently accommodate phases with cylindrically orthotropic constituents without much effort. The constructed homogenization theory enables efficient analysis of the elastic and viscoelastic response of unidirectional composite materials with rectangular, square, hexagonal and tetragonal periodic microstructures comprised of isotropic, transversely isotropic, and (cylindrically or circumferentially) orthotropic phase constituents, and third phases such as coatings or interphases.

The success of this homogenization theory is rooted in the balanced variational principle which plays a key role in the implementation of non-separable periodic boundary conditions, leading to quickly-converging homogenized moduli and stable local stress distributions. This variational principle, originally proposed by Drago and Pindera (2008) for rectangular unit cell architectures, was extended herein to hexagonal and tetragonal unit cells and demonstrated to produce quickly converging homogenized moduli and local stress fields regardless of phase modulus contrast, orthotropy type or viscoelasticity effects.

The constructed homogenization theory has been validated upon comparison with known elasticity solutions and micromechanics models. These include the solution to the Eshelby problem which was used as a benchmark to demonstrate the robustness and stability of the developed unit cell solution approach, and the finite volume direct averaging micromechanics (FVDAM) theory which produces high-fidelity results comparable to the finite-element method. Comparison with the classical composite cylinder assemblage (CCA) and Mori-Tanaka micromechanics models establishes applicability and limitations of these approaches based on simplified geometric representation of composite material microstructures. Selected numerical results are generated to provide insight into the efficiency and robustness of the theory. To

demonstrate its advantage, the key component of the theory, namely the balanced variational principle, is compared with recently adopted approaches based on a derivative variational principle proposed originally in the context of locally-exact finite-element solutions. Finally, the elastic problem has been extended to viscoelastic domain via the elastic-viscoelastic correspondence principle, validated at the homogenized and local field levels at different times, and employed to investigate thus-far undocumented features of time-dependent response of polymeric matrix composites. The significant findings include the effect of array type on the creep response which increases dramatically with increasing time for certain loading directions. The theory's utility in support of constructing homogenized response functions of polymeric matrix composites from experimental data was also demonstrated.

Because of its analytical nature, the constructed theory may easily be incorporated into larger structural analysis algorithms in a multi-scale computational setting. This capability is illustrated herein in the context of laminated plate and functionally graded tube analyses, wherein local homogenized elastic moduli of the investigated structural components are generated on the fly for use in the governing equations at the structural level.

The theory's efficiency and stability in generating homogenized moduli and stress fields with very simple input data construction make it readily accessible to professionals and non-professionals alike. Hence it is expected that this approach will quickly gain popularity and become not only a design and research tool used by diverse communities involved in materials characterization, design and development, but also a comparison standard for bench mark purposes.

Acknowledgments

First of all, I would like to express my sincere gratitude to my advisor, Professor Marek-Jerzy Pindera for his inspiring guidance and dedicated instructions for both academic and personal experience. From my work experience with him side by side, I learnt that research was fun, but definitely not a joke. His working attitude toward his research really impressed me. We have been working like 7-eleven, especially in the past half-year.

Beside my advisor, I would also like to thank my committee members for their generous support and patience, as well as a bunch of "A"s they give me in my courses. They are Dr. Tom T. Baber, Dr. Houston Wood, Dr. Jim Simmonds, Dr. Osman Ozbulut, Dr. Baoxing Xu.

In addition, I am also thankful to Professor Goodall and Dr. Anne Ingram for letting me participate into the "TTSP" program. They totally opened a new window for me so I could learn a lot of new things besides my Ph.D. dissertation. The funding coming from the program and Civil Department of University of Virginia also helped me to accomplish my Ph.D. degree.

During my Ph.D. study at UVa, I have benefited a lot from my friends, who came from different countries with different backgrounds. They taught me many exciting new things that I didn't have a chance to understand from elsewhere.

My special thanks should go to my girlfriend, Ms. Jiayin Zhao, who still lets me to be her husband candidate even if I spent more time on my work than with her.

It would be unfair to not mention my dearest parents, who always give their full support either when I ran out cash in my wallet or could not find the way forward. They have been playing a critical part in this achievement. Cheers, Dad and Mom!

A new journey will start right after the Ph.D. stage, may my dream and passion still exist along with my hair.

Contents

Chapter 1

Introduction

1.1 Motivation

All solid materials can be treated as composite materials if the scale is small enough. A composite material is a material made from two or more constituent phases with significantly different physical or chemical properties that, when combined, produce a material with characteristics different from the individual components. The definition cited from Wikipedia suggests the reason why composite materials experience ever increasing applications: they may be lighter or cheaper than the individual constituents, but the combination might be stronger or more durable.

The history of man-made composite materials may be traced to biblical times when straw was added to clay to make more durable bricks. In the 12th century ancient Mongols developed more advanced weapons, which were smaller and more powerful archery bows in their days, by combining cattle tendons, horns, bamboo and silk bonded with natural pine resin. The most common applications of composite materials in recent human history were also in the military arena. During World War I (WWI), military aircraft benefited greatly from composite wing skins made of laminated wood, which made the wing frames lighter and stronger. Metal matrix composites (MMCs) based on boron fibers were developed for modern military aircraft in the 1960's and 1970's for use in control surfaces such as the vertical stabilizer on the F-15 Eagle jet fighter. Introduction of new fibers developed in research labs, such as carbon, graphite and Kevlar, and subsequent rapid growth of the fiber-reinforced plastics industry, stimulated new demand from markets across diverse areas, including commercial aircraft, civil infrastructure, automotive and electrical engineering industries, as well as biomedical engineering. Composite materials, in the long run, are playing and will play increasingly greater and more significant roles. Taking Boeing 787 as an example, fifty percent of the airplane body is comprised of

composite materials, whereas the dominant material used in Boeing 747 and 777 airplanes is aluminum. Different forms of composite materials such as particle-reinforced composites, fiber-reinforced composites and their laminates, woven composites, etc., are usually tailored to different applications based on structural requirements.

Two basic mechanical properties are needed in the analysis and design of structural components that utilize combinations of diverse material systems, namely: (1) thermo-elastic properties and strength; and (2) time-dependent response. There are two approaches in characterizing these properties, one of which is experimental characterization aimed at specific composites. The other approach, which is broadly called micromechanics or homogenization, plays the role of a virtual laboratory which is used to identify potential material systems for given applications through a validated analysis procedure. This approach eliminates the trial-and-error procedure often used in developing new materials, and the associated laborious and expensive preparation and manufacturing steps. Micromechanics involves analysis of composite or heterogeneous media with the aim of predicting average or macroscopic behavior on the basis of geometric arrangement and mechanical properties of individual phases. For materials with periodic (repeating) microstructures, it is also called homogenization. Micromechanics or homogenization techniques aid in the rapid identification of material systems for specific structural application, as well as in the development of new materials.

A variety of micromechanical models have been developed by researchers and scientists during the past fifty years. This development continues and is motivated by advances in the computational technology. In the next section, three conceptual categories of micromechanics and homogenization techniques are reviewed and discussed with the aim of providing motivation for the developments and contributions described in this dissertation.

1.2 Literature Review

Micromechanics theories of heterogeneous materials can be separated into three categories: 1) microstructural detail-free strategies; 2) theories for statistically homogeneous composites based on the representative volume element (RVE) concept; and 3) theories developed for periodic composites based on the repeating unit cell (RUC) concept, see Fig. 1.1, in which (b) and (c) are referred to Pindera et al. (2009).

The key step in a micromechanical or homogenization procedure is to determine Hill's

strain (or stress) concentration tensors – $\mathbf{A}^{(k)}$, which relate the average strains (or stresses) in each individual phase to the average or macroscopic strain imposed on the heterogeneous medium, Hill (1963), through so-called localization relations, which can be expressed as

$$\bar{\varepsilon}^{(k)} = \mathbf{A}^{(k)}\bar{\varepsilon} \tag{1.1}$$

in which *k* represents the *k*th phase, e.g. fiber, coating, matrix.

These local concentration tensor are employed in the definition of the average stress given in terms of the phases averages, expressed in terms of the phase average strains through Hooke's law, to obtain the homogenized stiffness matrix for the composite shown as follows

$$\mathbf{C}^{*} = \sum_{k=1}^{N} v_k \mathbf{C}^{(k)}\mathbf{A}^{(k)} \tag{1.2}$$

in terms of the elastic moduli $\mathbf{C}^{(k)}$ and phase volume fractions v_k, respectively. This concept will percolate through this entire dissertation.

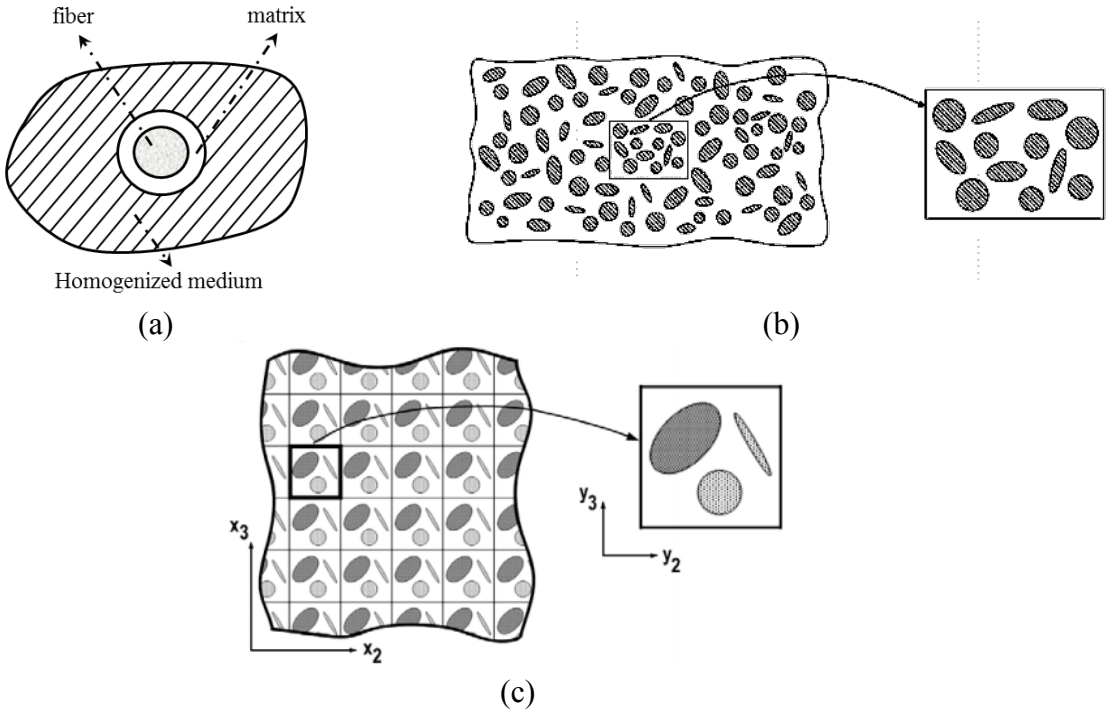

Figure 1.1 Three geometric representations of a material microstructure: (a) detailed-free microstructure (Three-phase model); (b) statistically homogeneous microstructure characterized by an RVE; (c) periodic microstructure characterized by an RUC.

1.2.1 Microstructure Detail-Free Estimates

The early micromechanics calculations of average moduli of composite materials are based on Voigt (Voigt, 1889) and Reuss (Reuss, 1929) estimates which were established for uniform dispersions of isotropic constituents or phases. For the Voigt estimate, the strain concentration tensors for the matrix and inclusion phases are taken as unity; whereas for the Reuss estimate the stress concentration tensors for the matrix and inclusion phases are taken as unity. These estimates originally were used for the predictions of homogenized moduli of polycrystalline metals wherein the modulus contrast between individual grains was small. Hence poor results are obtained for composite materials for which the phase moduli differ by more than a factor of two.

The Reuss and Voigt estimates provided the foundation for the rule-of-mixtures formula, which were applied preferentially to mimic the oriented microstructures of unidirectionally-reinforced composites. For instance, the average strain in the fiber and matrix phases was taken to be the same as that of the composite along the fiber direction, while transverse to the fiber direction the average stresses were equal. Hence an accurate estimate of the Young's modulus along the fiber direction may be obtained due to the correct kinematic constraint, but the remaining moduli associated with transverse normal and shear loading, as well as with axial shear loading, are typically inaccurate especially for large mismatch of fiber/matrix moduli.

In the 1950's, the self-consistent scheme (Hershey, 1954; Kröner, 1958) was proposed as an alternative to Voigt and Reuss estimates to calculate stress or strain concentration matrices in polycrystalline metals, with a single anisotropic grain playing the role of an inclusion phase embedded in a homogenized medium of sought properties. An orientational averaging over all grains of a polycrystal provided implicit self-consistent relations for the unknown homogenized moduli.

This scheme was subsequently adopted to the calculation of average properties of particulate and unidirectionally-reinforced composites by assuming that the concentration matrices calculated for a single fiber were the same as those of all fibers, (Hill, 1963). This scheme was shown to suffer from several shortcomings as it did not explicitly take into account the presence of the matrix phase around a fiber inclusion. This shortcoming was overcome by the method proposed by Mori and Tanaka (Mori and Tanaka, 1973), who provided a different

interpretation of the embedding approach based on the average stress in the matrix phase determined from the solution of an Eshelby-type problem for a two-phase composite with isotropic or transversely isotropic macroscopic moduli. Some problems with this approach remained, however, including: 1) the matrix phase was taken into account, but only in an average sense; 2) the loss of homogenized stiffness matrix symmetry would occur under certain circumstances. In order to overcome these shortcomings the three-phase model was proposed by Christensen and Lo (1979), wherein a composite fiber/matrix inclusion was embedded in an equivalent homogenized medium.

The above approaches do not take into account the actual microstructural details of heterogeneous materials, and may be viewed as vehicles for calculating Hill's stress or strain concentration matrices necessary for the determination of the homogenized moduli. More detailed information on the homogenized moduli and local stress fields that account explicitly for the microstructural details may be obtained using microstructural analysis of heterogeneous materials based on two different concepts of material microstructures: representative volume element (RVE) and repeating unit cell (RUC), as discussed by Drago and Pindera (2007). Representative volume element is the smallest subvolume of the statistically homogeneous microstructure that contains the same phase volume fractions and statistical distribution as the material-at-large, and also responds in a manner identical to that of the entire assemblage under either homogeneous displacement or homogeneous traction boundary conditions. Repeating unit cell is the smallest element of periodic microstructure that serves as the basic building block for the material through replication regardless of its content. Thus, the response of the entire array under macroscopically uniform loading is identical to that of an arbitrary RUC subjected to the same loading.

1.2.2 RVE-Based Approaches

Composite spherical assemblage (CSA) and Composite cylinder assemblage (CCA) (Hashin, 1962; Hashin and Rosen, 1964) were the earliest and most classic geometric RVE-based models that provided closed-form expressions for the average or effective moduli. The composite was viewed as an assemblage of inclusion/matrix spheres or fiber/matrix cylinders of varying sizes but fixed radii ratio of fiber/matrix. This allowed the entire space to be completely filled by such composite inclusions while maintaining a fixed inclusion volume content. Taking the CCA model as an example, for axisymmetric and longitudinal shear loading,

exact expressions for the moduli are obtained by applying continuity conditions and boundary conditions of displacements and stresses in cylindrical coordinates. However, the homogeneous boundary condition equivalence no longer holds under transverse normal and shear loading, only bounds on the moduli may be obtained by applying a variational principle because a single composite cylinder ceases to respond as an RVE. Similar situation occurs in the case of the three-dimensional counterpart, the CSA model. Furthermore, because an isolated composite sphere or cylinder was considered in the calculation of effective moduli, direct particle-particle interaction remained absent in this approach.

The CCA model was extended by Pindera and co-workers, (Pindera et al., 1993a,b), by developing solutions to a multiple concentric cylinder of arbitrarily layered geometry with elastic-plastic phases subjected to axisymmetric and axial shear loading by a combination of a uniform temperature change, axial deformation and externally applied transverse pressure. This model was employed to study the evolution of residual stresses in metal matrix composites, taking into account the complex microstructures of the titanium matrix in SiC/Ti composites, and engineered interfaces introduced to mitigate excessively high residual stresses.

The models mentioned above are easy-to-use and produce comparatively accurate predictions of the homogenized moduli (such as the CCA model), as discussed in more details in this dissertation (Chapter #6). Hence they continue to be employed by the composite mechanics and materials communities. However, because they are based in simple geometric representations of a composite material, they do not always capture local stress fields with high accuracy because of the absence of fiber-fiber interactions that occur in real microstructures. Moreover, the CCA model is limited to transversely isotropic composites due to its geometric representation of the composite microstructure. The above limitations have given rise to the development of techniques based on the concept of periodicity and the concomitant unit cell representation of the material microstructure. These techniques continue to develop and form a dominant part of the micromechanics field.

1.2.3 RUC-Based Approaches

Much research has been done in simulating the response of periodic composites in the elastic and inelastic regions based on the RUC concept. The semi-analytical approaches include the method of cells (MOC) and its generalization (GMC), (Aboudi, 1989; Paley and Aboudi, 1992), wherein the composite material's microstructure was discretized into rectangular rows

and columns with the resulting subcells assigned properties that mimic the microstructural details. Pindera and Bednarcyk (1997) showed that the intrinsic assumptions on the form of the displacement field in each subcell in these two models produced essentially spring models wherein each column and row behaved either like two-dimensional springs capable of supporting uniform normal stress components or one-dimensional springs independently supporting axial or transverse shear stress components. These shortcomings led to a more accurate model based on a two-level discretization of the unit cell into generic cells and subcells, with a higher-order displacement field representation in each subcell, called high-fidelity generalized method of cells – HFGMC, (Aboudi et al., 2003). The explicit solution for the strains and stress fields in the unit cell was obtained by satisfying 0^{th}, 1^{st} and 2^{nd} moments of equilibrium equations in each subcell, in addition to the interfacial traction and displacement continuity conditions within each, and between adjacent, generic cells and the periodic boundary conditions on the external faces of boundary generic cells. The two-level unit cell discretization complicated the theoretical framework and created a large system of equations that governed the unit cell response. Subsequently, this approach was substantially re-constructed and simplified by Bansal and Pindera (2005), and the re-construction revealed that the method was really a finite-volume technique.

At present, most homogenization techniques for periodic materials continue to rely on numerical solutions of the unit cell boundary-value problem using mainly finite-element and finite-volume techniques, and to a lesser extent techniques based on finite-difference and Fourier transform approaches (Michel et al., 1999; Pindera et al., 2009; Charalambakis, 2010; Cavalcante et al., 2012; Tu and Pindera, 2014). The finite-element technique is the dominant method mainly because of the easy-to-use character and wide availability of commercial packages. However, because commercial finite-element codes are general structural analysis codes, the implementation of periodic boundary conditions under general loading is not readily achievable, and the geometric representation of unidirectional composites under three-dimensional loading requires full three-dimensional models. Hence new techniques continue to be developed. The finite-volume method, first used to investigate fluid mechanics problems (Versteeg and Malalasekera, 2007), is one such technique that is rapidly developing.

Cavalcante et al. (2006a,b) incorporated parametric mapping into the finite-volume direct averaging micromechanics (FVDAM) theory developed by Bansal and Pindera (2003), which

resulted from the re-construction of HFGMC, that enabled modeling of complex microstructures using quadrilaterals rather than rectangular subvolumes. The use of quadrilateral subvolumes made possible by the mapping facilitated efficient modeling of microstructures with arbitrarily shaped heterogeneities, and eliminated artificial stress concentrations produced by the rectangular subvolumes employed in the standard version. Closed-form expressions were constructed for the elements of a local stiffness matrix for each subvolume that related the surface-averaged fluctuating displacements to the surface-averaged tractions on each face of the subvolume used in the assembly of the global system of equations.

Interest in elasticity-based methods has revived within the past 15 years in light of advances in computational technology, as well as due to the potential advantages offered by these techniques (Crouch and Mogilevskaya, 2006; Wang et al., 2005). For instance, microstructural optimization will profit from analytical solutions of unit cell problems due to the significantly smaller design variable space, more efficient specification of objective functions and implementation of more efficient search procedures. Another application is the reconstruction of local fields from homogenized-based results within a multi-scale analysis of local failure modes (Lipton, 2003), and material development which relies on rapid answers to what/if questions. Theoretical issues concerning the use of approximations in homogenization schemes may also be addressed by elasticity solutions (Mogilevskaya et al., 2012).

Elasticity solutions for the homogenized moduli of periodic heterogeneous materials had been developed by a number of investigators with various degrees of success since the early development stage of composite materials. For unidirectional composites with circular fibers or porosities the main obstacle to an accurate solution is the inseparable nature of the problem due to the different coordinate systems required to solve the interior and exterior unit cell problems. The interior problem involves satisfaction of the elasticity field equations subject to the fiber/matrix continuity conditions most conveniently implemented in the cylindrical coordinate system, whereas the exterior problem involves enforcement of periodicity conditions on the boundary of the unit cell in the Cartesian coordinate system. The interior problem is readily handled using Fourier series representations of stress or displacement fields, (Chen and Cheng, 1967; Heaton, 1968; Leissa and Clausen, 1968; Pickett, 1968), or complex potential methods for plane problems, (Koiter, 1960; Fil'shinskii, 1964; Wilson and Hill, 1965; Grigolyuk and Fil'shinskii, 1966). The more difficult exterior problem had been tackled in an approximate

manner through the use of collocation or least-squares techniques in the implementation of periodic boundary conditions on the unit cell's bounding surfaces. While this approach has produced reasonable estimates of the homogenized moduli, convergence of stress fields with increasing number of terms in the series representation of the displacement field remains problematic.

To circumvent the problem with the implementation of periodic boundary conditions, series expansions of the displacement field have been employed that reflect the overall microstructural periodicity using the eigenstrain device to represent inclusion strains, thereby avoiding the problem of explicitly enforcing continuity conditions at the fiber/matrix interface while *a priori* ensuring displacement field periodicity (Nemat-Nasser et al., 1982; Luciano and Barbero, 1995). This approach has been applied to both square and hexagonal arrays of inclusions in the matrix phase by Guinovart-Diaz et al. (2010). An alternative approach to implement periodic boundary conditions into the exact elasticity solution of the interior unit cell problem for unidirectionally reinforced composites has been proposed by Drago and Pindera (2008) in the form of a balanced variational principle. This variational principle produces rapid convergence of the coefficients in the series representation of the displacement fields which satisfy both the Navier's equations and fiber/matrix continuity conditions in the interior of the unit cell representative of rectangular or square arrays of isotropic inclusions. As a result, converged homogenized moduli and local stress fields are obtained with relatively few terms in the displacement field representation.

1.3 Significance of Elasticity-Based Homogenization Techniques

Despite the widespread use of numerical techniques in the homogenization of composites due to their ability to model complex microstructures and accommodate inelastic behavior of constituent phases, there are number of instances where the elasticity approach has certain advantages. The construction of an input data file for an elasticity-based homogenization algorithm is at least an order-of-magnitude faster relative to numerical methods based on geometric discretization, and may be quickly automated for use in parametric or optimization studies. In the case of numerical analyses, model construction which defines the input data consumes a major part of the simulation effort. Moreover, studies aimed at the important effects of fiber/matrix interfaces on the homogenized moduli and local stress fields are much more

efficiently carried out using the elasticity approach due to both mesh construction and convergence issues. Similar comments apply to the modeling of cylindrically orthotropic fiber microstructures such as those found in graphite fibers. These two important areas in the mechanics of composite materials which continue to be explored with numerical techniques that account for the local fiber interactions absent in the simple geometric models are discussed in detail in the following subsections.

Lastly, an analytical solution to an elasticity problem of a unit cell subjected to macroscopic loading provides solution to the corresponding linearly viscoelastic problem in the Laplace-transform domain through replacement of the constituent phase moduli by their Carson transforms, and elastic variables by their Laplace transforms. This is known as the elastic-viscoelastic correspondence principle. Inversion of the Laplace-transformed solution to the time domain may be obtained numerically, enabling investigations into little explored time-dependent response of unidirectional polymeric matrix composites with different architectures. The success of the inversion procedure is very much dependent on the particular inversion scheme which must be chosen carefully.

1.3.1 Interfaces

Interfaces play a key role in stress transfer between fiber and matrix phases of a fiber-reinforced composite, which is at the core of reinforcement principles in the mechanics of composite materials. They take different forms that depend on the fiber/matrix system and hence different names have been used to describe them. Examples include regions with variable properties, or interphases, due to altered chemical bond structure of the matrix phase adjacent to the fiber's surface in polymeric matrix composites; fabrication-induced reaction zones with degraded properties in metal matrix composites reinforced by ceramic fibers; as well as coatings that promote fiber/matrix adhesion, control fracture toughness or reduce residual stresses. The effect of interfaces or interphases on the homogenized and local response of unidirectional composites has been investigated by many researchers using different modeling approaches within various micromechanics or homogenization theories, including distinct interfacial layers with properties different from those of the adjacent fiber or matrix, and spring and cohesive zone models. For very thin interface/interphase regions the latter two models offer an attractive alternative to finite-thickness interfacial layers especially when variational techniques requiring detailed geometric discretization are employed.

Review of the early approaches based on simple geometric models of unidirectional composites such as the CCA, Mori-Tanaka and GSC (generalized self-consistent) models was provided by Jasiuk and Kouider (1993). A more recent discussion of the various approaches may be found in Duan et al. (2005). The simple geometric models based on a single fiber embedded in the matrix phase, which may in turn be embedded in the homogenized medium of sought properties, yield estimates of homogenized moduli in the presence of interphases or coatings with uniform or variable (so-called graded) properties, but do not provide accurate estimates of stress fields that account for adjacent fiber interaction. To gauge the effect of coatings or interphases on the homogenized moduli without sacrificing local stress field accuracy critical in failure analysis, the finite-element approach has been, and continues to be, employed by a number of investigators, (Lagache et al., 1994; Veazie and Qu, 1995; Asp et al., 1996; Shen and Li, 2003; Maligno et al., 2010; Wang et al., 2011; Sideridis et al., 2015). In the presence of thin coatings, however, detailed mesh discretization is required for converged stress fields. Alternative approaches to the homogenization of unidirectional composites include elasticity-based solutions for periodic microstructures and finite-volume techniques. A recent focus on the incorporation of interphase and spring models into elasticity-based solutions has been highlighted by several researchers, (Mogilevskaya et al., 2010; Sevostianov et al., 2012; Guinovart-Díaz et al., 2013). Optimization of interfacial properties will profit from the use of analytical techniques in the solution of unit cell problems due to the significantly smaller design variable space, more efficient specification of objective functions and implementation of more efficient search procedures. Another benefit is the efficient reconstruction of local fields from homogenized-based results within a multi-scale analysis of local failure modes, and material development which relies on rapid answers to what/if questions.

1.3.2 Cylindrically Orthotropic Fiber Microstructures

Materials and structures with cylindrically orthotropic architectures are found in nature as well as in man-made constructs. Examples include tree trunks, biological tissues and bones, masonry structures and graphite/carbon fibers used as reinforcement in advanced composites. Leknitskii and Fern (1963) were perhaps the first to provide solutions to cylindrically orthotropic materials and structural components under certain geometric and loading constraints, including cylinders subjected to axisymmetric and bending loads. The problem with singular stress fields that occur at the origin of radially orthotropic fibers was sidestepped by focusing on structural

components that were hollow. To gauge the impact of cylindrical orthotropy in graphite fibers on the homogenized moduli and local stress fields in unidirectional graphite/epoxy composites, simplified models based on the concentric cylinder geometry had been employed by several investigators. For instance, Avery and Herakovich (1986) employed the composite cylinder geometry to investigate the impact of graphite fiber's cylindrically orthotropic microstructure on residual stresses that arise during the fabrication process and the potential failure modes in the graphite fiber induced by these stresses. In a follow-up investigation, Knott and Herakovich (1991) calculated four of the fiver transversely isotropic moduli of graphite/epoxy unidirectional composites and related stress fields using the CCA model. Similar investigation was carried out by Hashin (1990) and Christensen (1994) using the CCA and three-phase models wherein the cylindrically orthotropic moduli of graphite fibers were replaced by equivalent homogenized transversely isotropic moduli, thereby sidestepping the singular nature of stress fields in radially orthotropic fibers. The issue of stress singularity in cylindrically orthotropic solid cylinders has been discussed by Antman and Negrón-Marrero (1987), Tarn (2002), Cowin and Fraldi (2005).

The simple geometric models based on a single fiber embedded in the matrix phase such as the CCA model, which may in turn be embedded in the homogenized medium of sought properties, e.g., three-phase model, yield estimates of homogenized moduli but do not provide accurate estimates of stress fields that account for adjacent fiber interaction. Hence the finite-element approach continues to be employed in predicting both the homogenized moduli and local stress fields necessary for local failure analysis. Thus far, however, little work can be found dealing with finite-element analysis of unidirectional composites with cylindrically orthotropic fibers, although results on the homogenized moduli and local stress fields in unidirectional composites with nano-fibrils which effectively act as cylindrically orthotropic fiber coatings have recently become available, (Chatzigeorgiou et al., 2011, 2012). Hence the micromechanics community would benefit from a unified elasticity-based homogenization approach that accounts for cylindrically orthotropic fibers in both the homogenization process and local stress field calculations, while admitting local fiber interactions.

1.4 Objectives

The main objective, and achievement, of this dissertation is the construction of a comprehensive set of homogenization theories for unidirectional composite materials based on

the elasticity approach, with the following features and modeling capabilities:

- Transversely isotropic constituent phases, extending the previous work of Drago and Pindera (2008) with isotropic phases;
- Radially and circumferentially orthotropic fibers to study the effect of graphite fiber morphology on composite properties and local stress fields within a unified framework;
- Three-phase microstructures through inclusion of coatings or interphases (interfaces) between fiber and matrix;
- Three types of microstructural representations based on rectangular (square), hexagonal and parallelogram (tetragonal) arrays that mimic different arrangements of fibers in the matrix phases;
- Viscoelastic response of polymeric matrices to study the effect of unit cell architectures on the time-dependent homogenized response and the transmission of phase time-dependent characteristics to the macro-level.

1.5 Approach and Outcomes

The construction of the locally exact homogenization theory with the aforementioned features follows the framework of the original theory for rectangular arrays containing isotropic elastic phases developed by Drago and Pindera (2008). The solution to the unit cell problem is carried out in two steps. The displacement fields are represented using Fourier series expansions in cylindrical coordinates which satisfy equilibrium and continuity conditions in the fiber, interface and matrix phases. This is the interior unit cell problem which is separable. The inseparable periodic boundary conditions in the Cartesian coordinates are implemented using the variational principle proposed by Drago and Pindera (2008) which is demonstrated to work extremely well for hexagonal and tetragonal unit cell architectures incorporated in this dissertation.

The theory is validated against exact elasticity solutions in the limit as the fiber volume fraction becomes dilute and shown to reduce to the classical solution of Eshelby (1957) regardless of the number of harmonics employed in the displacement field approximation, demonstrating also its robustness and stability. In the non-dilute case, the homogenized moduli

and local stress fields are compared with those of the FVDAM theory previously demonstrated to be of the same fidelity as the finite-element method. Convergence studies indicate that homogenized moduli converge rapidly to their values with relatively small number of harmonics, whereas local stress fields require somewhat greater, but not large, number of harmonics for convergence. This rapid convergence is due to the balanced variational principle originally proposed by Drago and Pindera (2008) for rectangular periodic arrays, and extended herein to hexagonal and tetragonal arrays.

The capability and efficiency of the developed locally exact homogenization theory are illustrated throughout the dissertation with the aim of highlighting the following outcomes and features:

- Comparison of stress distributions and homogenized moduli predicted locally exact homogenization theory (LEHT) and FVDAM illustrates the robustness and accuracy of this method;
- The stability of the method and its quick convergence in predicting homogenized moduli and local stress fields in a wide range of volume fractions, phase moduli contrasts and fiber arrays sets this method apart from other elasticity-based homogenization theories;
- The total time required for problem definition and execution is an order of magnitude smaller relative to variational or finite-volume techniques because time-consuming mesh discretization is not required, while post-processing of output data is easily automated. This facilitates rapid visualization of stress distributions, and applications involving optimization and multiscale modeling, etc.;
- The input data construction requires a few geometric and material parameters, facilitating use by specialists and non-specialists alike;
- Rapid assessment of widely employed classical models such as the CCA and Mori-Tanaka models for both elastic and viscoelastic behavior;
- Assessment of recently proposed elasticity-based models that employ a related variational principle, and the related problem of the effect of boundary condition implementation on the resulting homogenized moduli and stress fields.

The advantages of the locally-exact homogenization theory relative to other numerical and

analytical techniques extend beyond those discussed above. Taking the cylindrically orthotropic fiber case as an example, hundreds if not thousands of elements or subvolumes need to be employed to accurately capture the local fiber stresses near the origin because of the very high stress gradients produced by singular nature of the stress field. Moreover, a small transversely isotropic core is needed to eliminate the difficulties of simulating the singularity. This problem does not appear in the locally-exact theory. The unknown coefficients that govern the displacement and stress distributions are easily obtained upon rapidly solving the unit-cell boundary value problem, thereby leading to explicit expressions for stress distributions and homogenized moduli.

Based on the theoretical framework and validation described and conducted in this dissertation, the constructed locally exact homogenization theory may be used as a standard against which other microstructural analytical and numerical models may be compared due to the ease-of-implementation, solution stability, quick convergence and accuracy.

1.6 Outline

This dissertation has the following organization. In Chapter 2, the basic theoretical framework is presented for both two-phase and three-phase composite materials with continuous reinforcement along one direction. The derivation is valid for transversely isotropic fiber and matrix phases, which may be easily degenerated to isotropic phases, as well as cylindrically orthotropic fibers. Three types of periodic microstructures (rectangular, hexagonal, tetragonal arrays) may be simulated by the developed theory which may be used to study microstructures with resultant transversely isotropic, orthotropic or monoclinic homogenized moduli.

In Chapter 3, several cases are used to validate the theory developed in Chapter 2. First, rapid convergence of the homogenized moduli and local stress fields is demonstrated with increasing number of harmonics employed in the displacement field representation in the fiber and matrix phases. For dilute fiber volume fractions, stress distributions are compared with Eshelby and Kirsch problems for stiff fibers and cylindrical porosities. Chapter 4 presents a number of numerical results and examples which demonstrate the advantages of the locally-exact homogenization theory in dealing with different applications. The homogenized moduli in a wide range of fiber and cylindrical porosity volume fractions are compared with Mori-Tanaka and CCA models, as well as with the FVDAM theory shown previously to be as accurate as the

finite-element calculations in both Chapter 3 and 4. The elastic unit cell solution for different array types is extended to viscoelastic domain using the correspondence principle in order to study the time-dependent behavior of polymeric matrix composites in Chapter 5. The method proposed by Zakian (1969), which is chosen for inverting Laplace-transformed homogenized moduli, is proven to be a stable and accurate inversion technique from Laplace domain to the time domain. Two types of assumptions on the time-dependent response of a polymeric matrix – constant Poisson's ratio and constant bulk modulus cases, are employed in simulating homogenized creep compliances of unidirectional graphite/epoxy composites and compared with experimental data. Chapter 6 compares LEHT with CCA and Mori-Tanaka models for both elastic and viscoelastic behavior. By comparing the homogenized moduli and stress distributions, it is concluded that even if the CCA model can just provide bounds on the transverse shear modulus which the Mori-Tanaka model can predict precisely, it is still an easy-to-use and efficient method which gives accurate homogenized moduli and stress distributions relative to LEHT. In Chapter 7, the balanced variational principle is compared with Jirousek's constrained variational approach in dealing with periodic boundary conditions for different types of microstructural arrays, showing its quickly convergent and more stable characteristics. At last, summary and conclusions are presented in Chapter 8, and future work is proposed with the aim of further enhancing the theory's computational and predictive capabilities.

Chapter 2

Theoretical Framework

2.1 Unit Cell Solution Overview

We consider a periodic material with continuous reinforcement along the x_1 axis, characterized by a repeating unit cell that defines the material's microstructure. Fig 2.1 shows three types of two-phase microstructures: rectangular, hexagonal, parallelogram arrays; while Fig 2.2 shows three-phase microstructures with additional coating or interphase between fiber and matrix (parallelogram array not shown). The unit cell, which contains an inclusion offset from the center to demonstrate the approach's robustness, is loaded by homogenized strain components $\bar{\varepsilon}_{ij}$. The solution for the displacement field is obtained subject to the periodic boundary conditions imposed on the external surface displacements and tractions

$$u_i(\mathbf{x_o}+\mathbf{d}) = u_i(\mathbf{x_o}) + \bar{\varepsilon}_{ij} d_j \quad \text{and} \quad t_i(\mathbf{x_o}+\mathbf{d}) = -t_i(\mathbf{x_o}) \tag{2.1}$$

where $(\mathbf{x_o}, \mathbf{x_o}+\mathbf{d}) \in S$, S is the unit cell boundary, $\mathbf{d}$ is a characteristic distance that defines the unit cell microstructure, and $t_i = \sigma_{ji} n_j$ from Cauchy's relations, with n_i denoting the ith component of the unit normal to S.

The boundary-value problem is first solved in the interior of the unit cell for the displacement fields in the fiber, coating and matrix phases such that local equilibrium equations and interfacial continuity conditions are satisfied exactly. The problem is separable in the cylindrical coordinate system, facilitating exact solution. The exterior problem involves satisfaction of the periodic boundary conditions in the Cartesian coordinate system and hence is inseparable using the interior solution in cylindrical coordinates. To solve the exterior problem, the balanced variational principle proposed by Drago and Pindera (2008) for rectangular unit cells comprised of isotropic phases is adapted herein for hexagonal or tetragonal (or

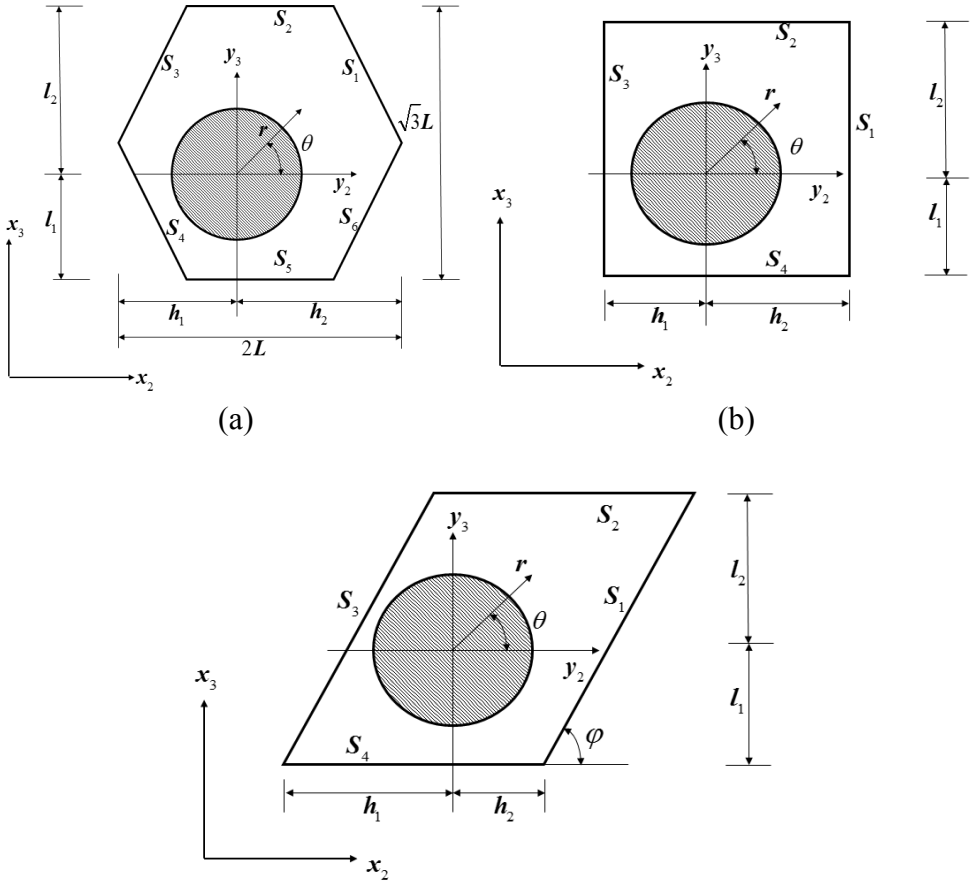

Figure 2.1 Repeating unit cells of hexagonal (a), rectangular (b) and parallelogram (c) arrays

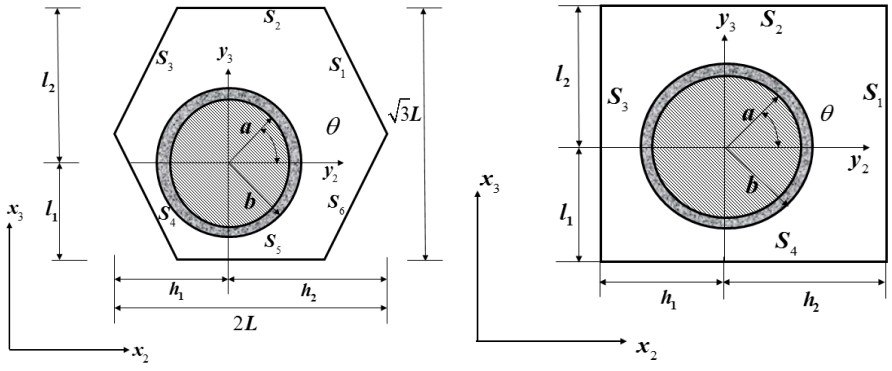

Figure 2.2 Repeating unit cells of hexagonal (a), rectangular (b) arrays with coated fibers

parallelogram) arrays comprised of transversely isotropic phases. Solution of exterior problem involves minimization of the functional

$$H_{D-P} = \frac{1}{2}\int_V \sigma_{ij}\varepsilon_{ij} dV - \int_{S_u} \mathbf{t}_i \mathbf{u}_i^0 dS - \int_{S_t} \mathbf{t}_i^0 \mathbf{u}_i dS = 0 \tag{2.2}$$

where $\mathbf{t}=\mathbf{t}^0$ and $\mathbf{u}=\mathbf{u}^0$ are periodic traction and displacement constraints imposed on S_t and S_u, respectively. Taking the first variation of H_{D-P}, and using the fact that the interior elasticity solution satisfies the stress equilibrium equations *a priori*, so that

$$\frac{1}{2}\int_V \sigma_{ij}\varepsilon_{ij} dV = \frac{1}{2}\int_S t_i u_i dS \tag{2.3}$$

The variational principle is obtained in the final form

$$\int_{S_t} \delta\mathbf{u}_i (\mathbf{t}_i - \mathbf{t}_i^0) dS + \int_{S_u} \delta\mathbf{t}_i (\mathbf{u}_i - \mathbf{u}_i^0) dS = 0 \tag{2.4}$$

The displacement and traction components on the six surfaces of the hexagonal unit cell, Figs. 2.1-2.2, are obtained from the periodicity conditions, Eq. (2.1), in the form,

$$\begin{gathered} u_i(S_1) = u_i(S_4) + \bar{\varepsilon}_{i2} d, \quad u_i(S_2) = u_i(S_5) + \bar{\varepsilon}_{i3} d, \quad u_i(S_3) = u_i(S_6) + \bar{\varepsilon}_{i3} d \\ T_i(S_1) = -T_i(S_4), \qquad T_i(S_2) = -T_i(S_5), \qquad T_i(S_3) = -T_i(S_6) \end{gathered} \tag{2.5}$$

where $d = \sqrt{3}L$.

In the case of rectangular (Drago and Pindera, 2008) or parallelogram unit cell with length d_2 and height d_3, these components are

$$\begin{gathered} u_i(S_1) = u_i(S_3) + \bar{\varepsilon}_{i2} d_2, \quad u_i(S_2) = u_i(S_4) + \bar{\varepsilon}_{i3} d_3 \\ T_i(S_1) = -T_i(S_3), \qquad T_i(S_2) = -T_i(S_4) \end{gathered} \tag{2.6}$$

The solution for the displacement and stress fields in the fiber, coating and matrix phases is carried out within the homogenization theory's framework wherein the global coordinates $\mathbf{x} = (x_1, x_2, x_3)$ describe the average response of the entire periodic array, and the local coordinates $\mathbf{y} = (y_1, y_2, y_3)$ describe the interior unit cell response (Suquet, 1985; Bensoussan et al., 2011). Accordingly, a two-scale displacement field expansion is employed within the unit cell,

$$u_i^{(k)}(\mathbf{x}, \mathbf{y}) = \bar{\varepsilon}_{ij} x_j + u_i'^{(k)}(\mathbf{y}) \tag{2.7}$$

where the fluctuating displacement components u' induced by the medium's heterogeneity are functions of local coordinates (y_2, y_3), in light of the constraint along the x_1 direction by the continuous reinforcement, and the superscripts $k = f, c, m$ denote fiber, coating (interphase)

and matrix phases, respectively. The above displacement field generates the local strains,

$$\varepsilon_{ij}^{(k)}(\mathbf{y}) = \bar{\varepsilon}_{ij} + \varepsilon_{ij}'^{(k)}(\mathbf{y}) \tag{2.8}$$

Once the solution for the unknown fluctuating displacement components $u_z'(r,\theta)$, $u_r'(r,\theta)$, $u_\theta'(r,\theta)$ is obtained in each phase in the cylindrical coordinate system, the corresponding strains are determined from the strain-displacement relations. To implement periodicity conditions in the variational principle, the fluctuating displacements in the cylindrical coordinate system are transformed to the Cartesian system using the standard transformation equations

$$u_1' = u_z',\ u_2' = u_r'\cos\theta - u_\theta'\sin\theta,\ u_3' = u_r'\sin\theta + u_\theta'\cos\theta \tag{2.9}$$

Similarly the fluctuating Cartesian strains are obtained from the transformations,

Out of plane:

$$\begin{aligned} \varepsilon_{12}' &= \varepsilon_{zr}'\cos\theta - \varepsilon_{z\theta}'\sin\theta \\ \varepsilon_{13}' &= \varepsilon_{zr}'\sin\theta + \varepsilon_{z\theta}'\cos\theta \end{aligned} \tag{2.10}$$

Inplane:

$$\begin{aligned} \varepsilon_{22}' &= \frac{1}{2}(\varepsilon_{rr}' + \varepsilon_{\theta\theta}') + \frac{1}{2}(\varepsilon_{rr}' - \varepsilon_{\theta\theta}')\cos 2\theta - \varepsilon_{r\theta}'\sin 2\theta \\ \varepsilon_{33}' &= \frac{1}{2}(\varepsilon_{rr}' + \varepsilon_{\theta\theta}') - \frac{1}{2}(\varepsilon_{rr}' - \varepsilon_{\theta\theta}')\cos 2\theta + \varepsilon_{r\theta}'\sin 2\theta \\ \varepsilon_{23}' &= \frac{1}{2}(\varepsilon_{rr}' - \varepsilon_{\theta\theta}')\sin 2\theta + \varepsilon_{r\theta}'\cos 2\theta \end{aligned} \tag{2.11}$$

which are subsequently used in the calculation of stresses and then tractions in the Cartesian coordinate system through Hooke's law and Cauchy's relations.

2.2 The Interior Problem

2.2.1 Transversely Isotropic Phases

The solution of the interior problem for unit cells with transversely isotropic phases follows the solution procedure by Drago and Pindera (2008). Hence only the main results are stated here with appropriate modifications accounting for transversely isotropic phases possessing plane of isotropy perpendicular to the reinforcement direction x_1. The generalized Hooke's law for such materials takes the uncoupled form

$$\begin{bmatrix}\sigma_{zz}\\ \sigma_{rr}\\ \sigma_{\theta\theta}\\ \sigma_{r\theta}\\ \sigma_{zr}\\ \sigma_{z\theta}\end{bmatrix}=\begin{bmatrix}C_{11} & C_{12} & C_{12} & 0 & 0 & 0\\ C_{12} & C_{22} & C_{23} & 0 & 0 & 0\\ C_{12} & C_{23} & C_{23} & 0 & 0 & 0\\ 0 & 0 & 0 & \frac{1}{2}(C_{22}-C_{23}) & 0 & 0\\ 0 & 0 & 0 & 0 & C_{66} & 0\\ 0 & 0 & 0 & 0 & 0 & C_{66}\end{bmatrix}\begin{bmatrix}\varepsilon_{zz}\\ \varepsilon_{rr}\\ \varepsilon_{\theta\theta}\\ 2\varepsilon_{r\theta}\\ 2\varepsilon_{zr}\\ 2\varepsilon_{z\theta}\end{bmatrix} \tag{2.12}$$

where the stiffness elements are given in terms of the axial Young's and shear moduli E_A, μ_A and Poisson's ratio ν_A, and the transverse plane strain bulk and shear moduli k_T, μ_T: $C_{11}=E_A+4k_T\nu_A^2, C_{12}=2k_T\nu_A,\ C_{22}=k_T+\mu_T,\ C_{23}=k_T-\mu_T,\ C_{66}=\mu_A.$ The use of the generalized Hooke's law and strain-displacement relations

$$\begin{aligned}
\varepsilon_{zz}&=\bar{\varepsilon}_{zz}+\frac{\partial u_z'}{\partial z}=\bar{\varepsilon}_{zz}\\
\varepsilon_{rr}&=\bar{\varepsilon}_{rr}+\frac{\partial u_r'}{\partial r}=\bar{\varepsilon}_{rr}+\varepsilon_{rr}'\\
\varepsilon_{\theta\theta}&=\bar{\varepsilon}_{\theta\theta}+\frac{u_r'}{r}+\frac{1}{r}\frac{\partial u_\theta'}{\partial\theta}=\bar{\varepsilon}_{\theta\theta}+\varepsilon_{\theta\theta}'\\
\varepsilon_{r\theta}&=\bar{\varepsilon}_{r\theta}+\frac{1}{2}\left(\frac{1}{r}\frac{\partial u_r'}{\partial\theta}+\frac{\partial u_\theta'}{\partial r}-\frac{u_\theta'}{r}\right)=\bar{\varepsilon}_{r\theta}+\varepsilon_{r\theta}'\\
\varepsilon_{rz}&=\bar{\varepsilon}_{rz}+\frac{1}{2}\frac{\partial u_z'}{\partial r}=\bar{\varepsilon}_{rz}+\varepsilon_{rz}'\\
\varepsilon_{\theta z}&=\bar{\varepsilon}_{\theta z}+\frac{1}{2r}\frac{\partial u_z'}{\partial\theta}=\bar{\varepsilon}_{\theta z}+\varepsilon_{\theta z}'
\end{aligned} \tag{2.13}$$

in the equilibrium equations in the cylindrical coordinate system yields the Navier's equations for the three unknown fluctuating displacements in each phase

$$\frac{\partial^2 u_z'}{\partial r^2}+\frac{1}{r}\frac{\partial u_z'}{\partial r}+\frac{1}{r^2}\frac{\partial^2 u_z'}{\partial\theta^2}=0$$

$$(k_T+\mu_T)\left(\frac{\partial^2 u_r'}{\partial r^2}+\frac{1}{r}\frac{\partial u_r'}{\partial r}-\frac{u_r'}{r^2}\right)+\frac{\mu_T}{r^2}\frac{\partial^2 u_r'}{\partial\theta^2}+\frac{k_T}{r}\frac{\partial^2 u_\theta'}{\partial r\partial\theta}-\frac{2(k_T+2\mu_T)}{r^2}\frac{\partial u_\theta'}{\partial\theta}=0 \tag{2.14}$$

$$\mu_T\left(\frac{\partial^2 u_\theta'}{\partial r^2}+\frac{1}{r}\frac{\partial u_\theta'}{\partial r}-\frac{u_\theta'}{r^2}\right)+\frac{(k_T+\mu_T)}{r^2}\frac{\partial^2 u_\theta'}{\partial\theta^2}+\frac{k_T}{r}\frac{\partial^2 u_r'}{\partial r\partial\theta}+\frac{2(k_T+2\mu_T)}{r^2}\frac{\partial u_r'}{\partial\theta}=0 \tag{2.16}$$

Since the out-of-plane and in-plane displacements u_z' and u_r', u_θ', respectively, are uncoupled in the differential equations above, the two problems are solved independently for the displacement field that generates homogenized moduli associated with respective loading.

2.2.1.1 Axial shear loading

The displacement field $u_z'(r,\theta)$ for the fiber, coating and matrix phases has the same form as that for isotropic phases

$$u_z' = H_{01} + \sum_{n=1}^{\infty} a\left[\left(\xi^n H_{n1} + \xi^{-n} H_{n3}\right)\cos n\theta + \left(\xi^n H_{n2} + \xi^{-n} H_{n4}\right)\sin n\theta\right] \tag{2.17}$$

where $\xi = r/a$ is the nondimensionalized radial coordinate with respect to the fiber radius *a*, and $H_{nj}^{(f,c,m)}\left(j = 1,2,3,4\right)$ are unknown coefficients. Setting $H_{n3}^{(f)} = H_{n4}^{(f)} = 0$ to ensure that the out-of-plane displacement remains bounded in the fiber.

(a) For two-phase (fiber/matrix) material system, the coefficients $H_{n1}^{(m)}, H_{n2}^{(m)}, H_{n3}^{(m)}, H_{n4}^{(m)}$ are obtained in terms of $H_{n1}^{(f)}$ and $H_{n2}^{(f)}$ from the fiber/matrix interfacial displacement and traction continuity conditions

$$u_z'^{(f)}(a,\theta) = u_z'^{(m)}(a,\theta),\ \ \sigma_{zr}^{(f)}(a,\theta) = \sigma_{zr}^{(m)}(a,\theta) \tag{2.18}$$

(b) For three-phase (fiber/coating/matrix) material system, the matrix coefficients $H_{n1}^{(m)}, H_{n2}^{(m)}, H_{n3}^{(m)}, H_{n4}^{(m)}$ and coating coefficients $H_{n1}^{(c)}, H_{n2}^{(c)}, H_{n3}^{(c)}, H_{n4}^{(c)}$ are obtained in terms of $H_{n1}^{(f)}$ and $H_{n2}^{(f)}$ from the fiber/coating/matrix interfacial displacement and traction continuity conditions

fiber/coating interface: $u_z'^{(f)}(a,\theta) = u_z'^{(c)}(a,\theta),\ \ \sigma_{zr}^{(f)}(a,\theta) = \sigma_{zr}^{(c)}(a,\theta)$

coating/matrix interface: $u_z'^{(c)}(b,\theta) = u_z'^{(m)}(b,\theta),\ \ \sigma_{zr}^{(c)}(b,\theta) = \sigma_{zr}^{(m)}(b,\theta)$

(2.19)

The shear stress components σ_{zr} in the fiber, coating and matrix regions are obtained from Hooke's law, Eq. (2.12), and the strain-displacement relations, Eq. (2.13),

$$\sigma_{zr} = 2G_A\bar{\varepsilon}_{zr} + G_A\sum_{n=1}^{\infty} n\left[\left(\xi^{n-1}H_{n1} - \xi^{-n-1}H_{n3}\right)\cos n\theta + \left(\xi^{n-1}H_{n2} + \xi^{-n-1}H_{n4}\right)\sin n\theta\right] \tag{2.20}$$

where $\bar{\varepsilon}_{zr} = \bar{\varepsilon}_{12}\cos\theta + \bar{\varepsilon}_{13}\sin\theta$, since the periodic boundary conditions imposed on a hexagonal unit cell are given in terms of the macroscopic axial strain $\bar{\varepsilon}_{12}$ and $\bar{\varepsilon}_{13}$ in Cartesian coordinates.

Applying the interfacial continuity conditions and using the orthogonality of $\cos n\theta$ and $\sin n\theta$ terms, we obtain the following expressions for the matrix coefficients (two-phase model)

or coating coefficients (three-phase model): $H_{n1}^{(k)}, H_{n2}^{(k)}, H_{n3}^{(k)}, H_{n4}^{(k)}$:

$$\begin{bmatrix} H_{n1} \\ H_{n2} \\ H_{n3} \\ H_{n4} \end{bmatrix}^{(k)} = \begin{bmatrix} c_1 & 0 \\ 0 & c_1 \\ c_2 & 0 \\ 0 & c_2 \end{bmatrix}^{(r=a)} \begin{bmatrix} H_{n1} \\ H_{n2} \end{bmatrix}^{(f)} + \delta_{n1} c_2^{(r=a)} \begin{bmatrix} -1 & 0 \\ 0 & -1 \\ 1 & 0 \\ 0 & 1 \end{bmatrix} \begin{bmatrix} 2\bar{\varepsilon}_{12} \\ 2\bar{\varepsilon}_{13} \end{bmatrix} \tag{2.21}$$

where $c_1^{(r=a)} = (\mu_A^{(k)} + \mu_A^{(f)})/2\mu_A^{(k)}$ and $c_2^{(r=a)} = 1 - c_1^{(r=a)}$. Here $k = m$ for two-phase model, $k = c$ for three-phase model.

For the three-phase composite materials, another set of interfacial continuity conditions are employed to set up relationship of coefficients between coating and matrix at $r = b$:

$$\begin{bmatrix} H_{n1} \\ H_{n2} \\ H_{n3} \\ H_{n4} \end{bmatrix}^{(m)} = \begin{bmatrix} c_1 & 0 & (a/b)^{2n} c_2 & 0 \\ 0 & c_1 & 0 & (a/b)^{2n} c_2 \\ (b/a)^{2n} c_2 & 0 & c_1 & 0 \\ 0 & (b/a)^{2n} c_2 & 0 & c_1 \end{bmatrix}^{(r=b)} \begin{bmatrix} H_{n1} \\ H_{n2} \\ H_{n3} \\ H_{n4} \end{bmatrix}^{(c)} + \delta_{n1} c_2^{(r=b)} \begin{bmatrix} -1 & 0 \\ 0 & -1 \\ (b/a)^2 & 0 \\ 0 & (b/a)^2 \end{bmatrix} \begin{bmatrix} 2\bar{\varepsilon}_{12} \\ 2\bar{\varepsilon}_{13} \end{bmatrix} \tag{2.22}$$

where $c_1^{(r=b)} = (\mu_A^{(m)} + \mu_A^{(c)})/2\mu_A^{(m)}$ and $c_2^{(r=b)} = 1 - c_1^{(r=b)}$.

2.2.1.2 Axial normal and transverse loading

Similarly, the fully coupled displacement field $u_r'(r,\theta)$, $u_\theta'(r,\theta)$ that accommodates unit cells without planes of material symmetry in the $r-\theta$ plane and specified loading is obtained in the form,

$$\begin{aligned} u_r' &= F_{01} a\xi + F_{02} a\xi^{-1} + F_{12}\cos\theta + G_{12}\sin\theta + \sum_{n=2}^{\infty}\sum_{j=1}^{4} a\xi^{p_{nj}} \left[F_{nj}\cos n\theta + G_{nj}\sin n\theta \right] \\ u_\theta' &= -F_{12}\sin\theta + G_{12}\cos\theta + \sum_{n=2}^{\infty}\sum_{j=1}^{4} a\beta_{nj}\xi^{p_{nj}} \left[F_{nj}\sin n\theta - G_{nj}\cos n\theta \right] \end{aligned} \tag{2.23}$$

and $p_{n1} = n+1,\ p_{n2} = n-1,\ p_{n3} = -(n+1),\ p_{n4} = -(n-1)$ are the four eigenvalues with the corresponding eigenvectors β_{nj}

$$\beta_{nj} = \frac{(k_T + G_T)(1 - p_{nj}^2) + G_T n^2}{n(k_T p_{nj} - k_T - 2G_T)} \tag{2.24}$$

and $F_{nj}^{(f,c,m)}, G_{nj}^{(f,c,m)}\ (j = 1,2,3,4)$ are unknown coefficients. Setting $F_{02}^{(f)} = 0$ and $F_{n3}^{(f)} = F_{n4}^{(f)} = 0$, $G_{n3}^{(f)} = G_{n4}^{(f)} = 0$ to ensure that the fiber displacement field remains bounded,

(a) For two-phase composite materials, the remaining matrix coefficients $F_{nj}^{(m)}$ and $G_{nj}^{(m)}$ are

obtained in terms of the fiber coefficients $F_{nj}^{(f)}$ and $G_{nj}^{(f)}$ from the fiber/matrix interfacial displacement and traction continuity conditions

$$\begin{aligned} u_r'^{(f)}(a,\theta) &= u_r'^{(m)}(a,\theta),\ u_\theta'^{(f)}(a,\theta) = u_\theta'^{(m)}(a,\theta) \\ \sigma_{rr}^{(f)}(a,\theta) &= \sigma_{rr}^{(m)}(a,\theta),\ \sigma_{r\theta}^{(f)}(a,\theta) = \sigma_{r\theta}^{(m)}(a,\theta) \end{aligned} \tag{2.25}$$

(b) For three-phase composite materials, the matrix coefficients $F_{nj}^{(m)}$ and $G_{nj}^{(m)}$, as well as the coating coefficients $F_{nj}^{(c)}$ and $G_{nj}^{(c)}$ are obtained in terms of the fiber coefficients $F_{nj}^{(f)}$ and $G_{nj}^{(f)}$ from the displacement and traction continuity conditions between fiber/coating and coating/matrix interfaces.

fiber/coating:
$$\begin{aligned} u_r'^{(f)}(a,\theta) &= u_r'^{(c)}(a,\theta),\ u_\theta'^{(f)}(a,\theta) = u_\theta'^{(c)}(a,\theta) \\ \sigma_{rr}^{(f)}(a,\theta) &= \sigma_{rr}^{(c)}(a,\theta),\ \sigma_{r\theta}^{(f)}(a,\theta) = \sigma_{r\theta}^{(c)}(a,\theta) \end{aligned} \tag{2.26}$$

coating/matrix:
$$\begin{aligned} u_r'^{(c)}(a,\theta) &= u_r'^{(m)}(a,\theta),\ u_\theta'^{(c)}(a,\theta) = u_\theta'^{(m)}(a,\theta) \\ \sigma_{rr}^{(c)}(a,\theta) &= \sigma_{rr}^{(m)}(a,\theta),\ \sigma_{r\theta}^{(c)}(a,\theta) = \sigma_{r\theta}^{(m)}(a,\theta) \end{aligned} \tag{2.27}$$

The radial and shear stress components σ_{rr} and $\sigma_{r\theta}$ in the fiber, coating, and matrix regions are obtained from the Hooke's law, Eq. (2.12), and the strain-displacement relations, Eq. (2.13),

$$\begin{aligned} \sigma_{rr} &= 2k_T\nu_A\bar{\varepsilon}_{zz} + (k_T+\mu_T)(\bar{\varepsilon}_{rr}+\varepsilon_{rr}') + (k_T-\mu_T)(\bar{\varepsilon}_{\theta\theta}+\varepsilon_{\theta\theta}') \\ &= 2k_T\nu_A\bar{\varepsilon}_{zz} + (k_T+\mu_T)\bar{\varepsilon}_{rr} + (k_T-\mu_T)\bar{\varepsilon}_{\theta\theta} \\ &\qquad + 2k_T F_{01} - 2\mu_T F_{02}\xi^{-2} + \sum_{n=2}^{\infty}\sum_{j=1}^{4} P_{nj}\xi^{p_{nj}-1}\left(F_{nj}\cos n\theta + G_{nj}\sin n\theta\right) \\ \sigma_{r\theta} &= 2\mu_T(\bar{\varepsilon}_{r\theta}+\varepsilon_{r\theta}') = 2\mu_T\bar{\varepsilon}_{r\theta} + \sum_{n=2}^{\infty}\sum_{j=1}^{4} R_{nj}\xi^{p_{nj}-1}\left(F_{nj}\sin n\theta - G_{nj}\cos n\theta\right) \end{aligned} \tag{2.28}$$

where $P_{nj} = (k_T+\mu_T)p_{nj} + (k_T-\mu_T)(1+n\beta_{nj})$, and $R_{nj} = \mu_T\left[(p_{nj}-1)\beta_{nj} - n\right]$.

Interfacial continuity at $r = a$:

Applying the four interfacial continuity conditions at $r = a$, and using orthogonality of $\cos n\theta$ and $\sin n\theta$ terms, we obtain systems of equations for the coefficients $F_{nj}^{(m)}$ and $G_{nj}^{(m)}$ (or coating coefficients $F_{nj}^{(c)}$ and $G_{nj}^{(c)}$ for three-phase composites) in terms of the corresponding fiber coefficients. From the $n = 0$ contributions, we have

$$\begin{bmatrix} F_{01} \\ F_{02} \end{bmatrix}^{(k)} = \begin{bmatrix} b_{01} \\ b_{02} \end{bmatrix}^{(r=a)} F_{01}^{(f)} + \begin{bmatrix} c_{01} \\ c_{02} \end{bmatrix}^{(r=a)} \bar{\varepsilon}_{11} + \begin{bmatrix} d_{01} \\ d_{02} \end{bmatrix}^{(r=a)} (\bar{\varepsilon}_{22} + \bar{\varepsilon}_{33}) \tag{2.29}$$

where

$$\begin{aligned} b_{01}^{(r=a)} &= \frac{k_T^{(f)} + \mu_T^{(k)}}{k_T^{(k)} + \mu_T^{(k)}}, \quad c_{01}^{(r=a)} = \frac{k_T^{(f)} \nu_A^{(f)} - k_T^{(k)} \nu_A^{(k)}}{k_T^{(k)} + \mu_T^{(k)}}, \quad d_{01}^{(r=a)} = -\frac{1}{2} b_{02}^{(r=a)} \\ b_{02}^{(r=a)} &= \frac{k_T^{(k)} - k_T^{(f)}}{k_T^{(k)} + \mu_T^{(k)}}, \quad c_{02}^{(r=a)} = -c_{01}^{(r=a)}, \qquad\qquad d_{02}^{(r=a)} = -d_{01}^{(r=a)} \end{aligned} \tag{2.30}$$

From the $\boldsymbol{n \geq 2}$ contributions:

$$\begin{aligned} \mathrm{A}_n^{(k)} \mathrm{F}_n^{(k)} &= \mathrm{A}_n^{(f)} \mathrm{F}_n^{(f)} + \delta_{n2} \mathrm{A}_0 (\bar{\varepsilon}_{22} - \bar{\varepsilon}_{33}) \\ \mathrm{A}_n^{(k)} \mathrm{G}_n^{(k)} &= \mathrm{A}_n^{(f)} \mathrm{G}_n^{(f)} + \delta_{n2} \mathrm{A}_0 2\bar{\varepsilon}_{23} \end{aligned} \tag{2.31}$$

where

$$A_n^{(k)} = \begin{bmatrix} 1 & 1 & 1 & 1 \\ \beta_{n1} & \beta_{n2} & \beta_{n3} & \beta_{n4} \\ P_{n1} & P_{n2} & P_{n3} & P_{n4} \\ R_{n1} & R_{n2} & R_{n3} & R_{n4} \end{bmatrix}^{(k)}, \; A_n^{(f)} = \begin{bmatrix} 1 & 1 \\ \beta_{n1} & \beta_{n2} \\ P_{n1} & P_{n2} \\ R_{n1} & R_{n2} \end{bmatrix}^{(f)}, \; A_0^{(r=a)} = \begin{bmatrix} 0 \\ 0 \\ (\mu_T^{(f)} - \mu_T^{(c)}) \\ -(\mu_T^{(f)} - \mu_T^{(c)}) \end{bmatrix} \tag{2.32}$$

in which $k = m$ for two-phase model, and $k = c$ for three-phase model.

Interfacial continuity at $r = b$:

For fiber/coating/matrix three-phase composite materials, the additional interfacial continuity at $r = b$ can be applied to obtain the relationship between coating coefficients $\mathbf{F}_n^{(c)}, \mathbf{G}_n^{(c)}$ and matrix coefficients $\mathbf{F}_n^{(m)}, \mathbf{G}_n^{(m)}$.

For $n = 0$ contributions:

$$\begin{bmatrix} F_{01} \\ F_{02} \end{bmatrix}^{(m)} = \begin{bmatrix} b_{01} \\ b_{02} \end{bmatrix}^{(r=b)} F_{01}^{(c)} + \begin{bmatrix} b'_{01} \\ b'_{02} \end{bmatrix}^{(r=b)} F_{02}^{(c)} + \begin{bmatrix} c_{01} \\ c_{02} \end{bmatrix}^{(r=b)} \bar{\varepsilon}_{11} + \begin{bmatrix} d_{01} \\ d_{02} \end{bmatrix}^{(r=b)} (\bar{\varepsilon}_{22} + \bar{\varepsilon}_{33}) \tag{2.33}$$

where

$$\begin{aligned} b_{01}^{(r=b)} &= \frac{k_T^{(c)} + \mu_T^{(m)}}{k_T^{(m)} + \mu_T^{(m)}}, \qquad c_{01}^{(r=b)} = \frac{k_T^{(c)} \nu_A^{(c)} - k_T^{(m)} \nu_A^{(m)}}{k_T^{(m)} + \mu_T^{(m)}}, \quad d_{01}^{(r=b)} = \frac{k_T^{(c)} - k_T^{(m)}}{2(k_T^{(m)} + \mu_T^{(m)})} \\ b_{02}^{(r=b)} &= \frac{k_T^{(m)} - k_T^{(c)}}{k_T^{(m)} + \mu_T^{(m)}} (\frac{b}{a})^2, \quad c_{02}^{(r=b)} = -c_{01}^{(r=b)} (\frac{b}{a})^2, \qquad d_{02}^{(r=b)} = -d_{01}^{(r=b)} (\frac{b}{a})^2 \end{aligned}$$

$$b_{01}'^{(r=b)} = -\frac{\mu_T^{(c)} - \mu_T^{(m)}}{k_T^{(m)} + \mu_T^{(m)}}\left(\frac{a}{b}\right)^2,\ b_{02}'^{(r=b)} = \frac{\mu_T^{(c)} + k_T^{(m)}}{k_T^{(m)} + \mu_T^{(m)}} \tag{2.34}$$

For $n \geq 2$ contributions:

$$\begin{aligned} \mathrm{A}_n^{(m)}\mathrm{F}_n^{(m)} &= \mathrm{A}_n^{(c)}\mathrm{F}_n^{(c)} + \delta_{n2}\mathrm{A}_0(\bar{\varepsilon}_{22} - \bar{\varepsilon}_{33}) \\ \mathrm{A}_n^{(m)}\mathrm{G}_n^{(m)} &= \mathrm{A}_n^{(c)}\mathrm{G}_n^{(c)} + \delta_{n2}\mathrm{A}_0 2\bar{\varepsilon}_{23} \end{aligned} \tag{2.35}$$

where

$$A_n^{(k)} = \begin{bmatrix} (b/a)^{p_{n1}} & (b/a)^{p_{n2}} & (b/a)^{p_{n3}} & (b/a)^{p_{n4}} \\ \beta_{n1}(b/a)^{p_{n1}} & \beta_{n2}(b/a)^{p_{n2}} & \beta_{n3}(b/a)^{p_{n3}} & \beta_{n4}(b/a)^{p_{n4}} \\ P_{n1}(b/a)^{p_{n1}-1} & P_{n2}(b/a)^{p_{n2}-1} & P_{n3}(b/a)^{p_{n3}-1} & P_{n4}(b/a)^{p_{n4}-1} \\ R_{n1}(b/a)^{p_{n1}-1} & R_{n2}(b/a)^{p_{n2}-1} & R_{n3}(b/a)^{p_{n3}-1} & R_{n4}(b/a)^{p_{n4}-1} \end{bmatrix}^{(k)},\ A_0^{(r=b)} = \begin{bmatrix} 0 \\ 0 \\ (\mu_T^{(c)} - \mu_T^{(m)}) \\ -(\mu_T^{(c)} - \mu_T^{(m)}) \end{bmatrix} \tag{2.36}$$

in which $k = c, m$.

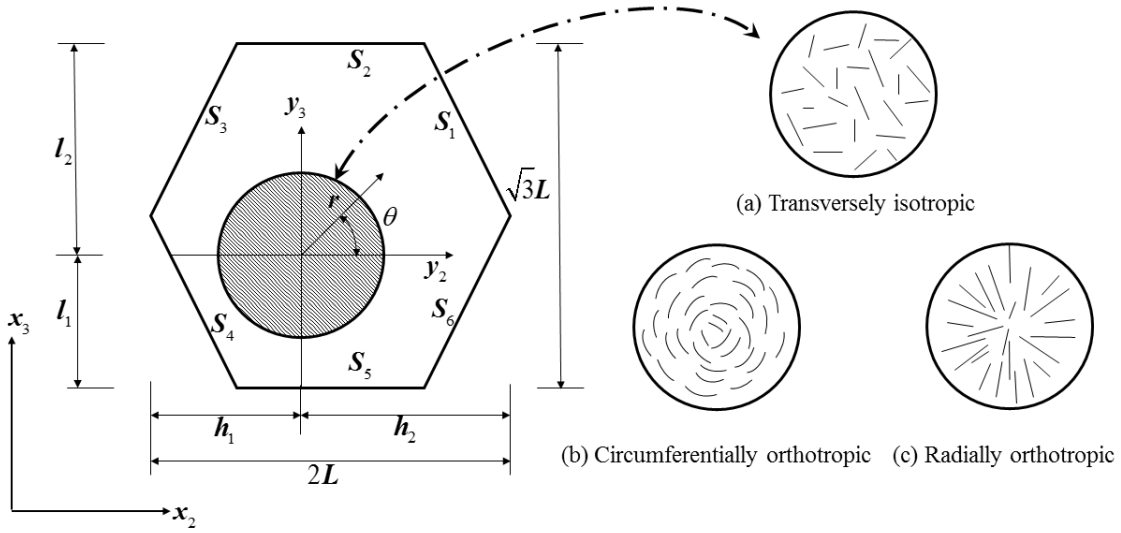

Figure 2.3 Repeating unit cell of a hexagonal array of fibers with cylindrically orthotropic microstructures.

2.2.2 The Interior Problem with Cylindrically Orthotropic Fibers

The Hooke's law for such materials naturally expressed in the cylindrical coordinates takes the form,

$$\begin{bmatrix}\sigma_{zz}\\ \sigma_{rr}\\ \sigma_{\theta\theta}\end{bmatrix}=\begin{bmatrix}C_{zz} & C_{zr} & C_{z\theta}\\ C_{zr} & C_{rr} & C_{r\theta}\\ C_{z\theta} & C_{r\theta} & C_{\theta\theta}\end{bmatrix}\begin{bmatrix}\varepsilon_{zz}\\ \varepsilon_{rr}\\ \varepsilon_{\theta\theta}\end{bmatrix},\qquad \begin{bmatrix}\sigma_{r\theta}\\ \sigma_{zr}\\ \sigma_{z\theta}\end{bmatrix}=\begin{bmatrix}\mu_{r\theta} & 0 & 0\\ 0 & \mu_{zr} & 0\\ 0 & 0 & \mu_{z\theta}\end{bmatrix}\begin{bmatrix}2\varepsilon_{r\theta}\\ 2\varepsilon_{zr}\\ 2\varepsilon_{z\theta}\end{bmatrix} \tag{2.37}$$

Two distinct types of cylindrically orthotropic microstructures can be identified which give rise to different stress fields. For radially orthotropic materials, the ratio $C_{rr}/C_{\theta\theta}>1$ with the concomitant microstructure resembles a bicycle wheel, whereas $C_{rr}/C_{\theta\theta}<1$ for circumferentially orthotropic materials whose microstructure resembles an onion. Fig 2.3 illustrates different types of microstructures found in graphite fibers characterized by differently oriented basal planes aligned with the fiber's axis which produce radially and circumferentially orthotropic effective behavior (Huang, 2009). A random dispersion of these planes perpendicular to the fiber axis produces transversely singular stress fields at the origin while those with circumferentially orthotropic moduli do not. The different graphite fiber microstructures have different impacts on the homogenized moduli, stress fields and fracture characteristics at both the single ply and laminated plate levels (Herakovich, 1989).

The solution of interior problem for unit cells with cylindrically orthotropic fibers whose elastic response is governed by Eq. (2.37), and (transversely) isotropic matrices follows the solution procedure described in Section 2.2.1. Hence only results which focus on the displacement field in cylindrically orthotropic fibers that require special treatment will be highlighted. The equilibrium equations in the cylindrical coordinate system yields the Navier's equations for the three unknown fiber displacements u_z, u_r and u_θ,

$$\begin{gathered}\frac{\partial^2 u_z}{\partial r^2}+\frac{1}{r}\frac{\partial u_z}{\partial r}+\frac{\mu_{z\theta}}{\mu_{zr}}\frac{1}{r^2}\frac{\partial^2 u_z}{\partial\theta^2}=0\\ C_{rr}\left(\frac{\partial^2 u_r}{\partial r^2}+\frac{1}{r}\frac{\partial u_r}{\partial r}\right)-C_{\theta\theta}\frac{u_r}{r^2}+\frac{\mu_{r\theta}}{r^2}\frac{\partial^2 u_r}{\partial\theta^2}+\frac{C_{r\theta}+\mu_{r\theta}}{r}\frac{\partial^2 u_\theta}{\partial r\partial\theta}-\frac{C_{\theta\theta}+\mu_{r\theta}}{r^2}\frac{\partial u_\theta}{\partial\theta}=\frac{C_{z\theta}-C_{zr}}{r}\bar{\varepsilon}_{zz}\\ \mu_{r\theta}\left(\frac{\partial^2 u_\theta}{\partial r^2}+\frac{1}{r}\frac{\partial u_\theta}{\partial r}-\frac{u_\theta}{r^2}\right)+\frac{C_{\theta\theta}}{r^2}\frac{\partial^2 u_\theta}{\partial\theta^2}+\frac{C_{r\theta}+\mu_{r\theta}}{r}\frac{\partial^2 u_r}{\partial r\partial\theta}+\frac{C_{\theta\theta}+\mu_{r\theta}}{r^2}\frac{\partial u_r}{\partial\theta}=0\end{gathered} \tag{2.38}$$

2.2.2.1 Displacement and stress fields

Assuming solutions for the fiber out-of-plane and in-plane displacements u_z and u_r, u_θ, respectively, in the separable form:

$$u_z^{(f)}(r,\theta)-\bar{\varepsilon}_{zz}z=\sum_{n=0}^{\infty}[h_n(r)\cos n\theta+h_n^*(r)\sin n\theta]$$

$$u_r^{(f)}(r,\theta)=\sum_{n=0}^{\infty}[f_n(r)\cos n\theta+g_n(r)\sin n\theta] \text{ and } u_\theta^{(f)}(r,\theta)=\sum_{n=0}^{\infty}[g_n^*(r)\cos n\theta+f_n^*(r)\sin n\theta],$$

substituting into Eq. (2.38), and using orthogonality for each harmonic contribution we obtain the fiber displacement field in the final form,

$$\begin{aligned}
u_z^{(f)}(r,\theta)&=\sum_{n=1}^{\infty}a\left[\left(\xi^{\bar{\lambda}_n}H_{n1}^{(f)}+\xi^{-\bar{\lambda}_n}H_{n3}^{(f)}\right)\cos n\theta+\left(\xi^{\bar{\lambda}_n}H_{n2}^{(f)}+\xi^{-\bar{\lambda}_n}H_{n4}^{(f)}\right)\sin n\theta\right]\\
u_r^{(f)}(r,\theta)&=F_{01}^{(f)}a\xi^{\lambda_0}+F_{02}^{(f)}a\xi^{-\lambda_0}+\sum_{n=2}^{\infty}\sum_{j=1}^{4}a\xi^{\lambda_{nj}}\left[F_{nj}^{(f)}\cos n\theta+G_{nj}^{(f)}\sin n\theta\right]+\bar{H}r\bar{\varepsilon}_{zz}\\
u_\theta^{(f)}(r,\theta)&=\sum_{n=2}^{\infty}\sum_{j=1}^{4}a\beta_{nj}\xi^{\lambda_{nj}}\left[F_{nj}^{(f)}\cos n\theta-G_{nj}^{(f)}\sin n\theta\right]
\end{aligned} \tag{2.39}$$

where $\bar{H}=(C_{z\theta}-C_{zr})/(C_{rr}-C_{\theta\theta})$. We note that rigid body terms associated with $n=0$ term in the expression for $u_z^{(f)}$, and $n=1$ terms in the expressions for $u_r^{(f)},u_\theta^{(f)}$ have been excluded by fixing the fiber at the origin. For the out-of-plane displacement $u_z^{(f)}$, the two eigenvalues are obtained in closed form $(\bar{\lambda}_n)_{1,2}=\pm(n\sqrt{\mu_{z\theta}/\mu_{zr}})$. For the in-plane displacements $u_r^{(f)},u_\theta^{(f)}$, when $n=0$ the two eigenvalues that characterize the axisymmetric displacement field are $(\lambda_0)_{1,2}=\pm\lambda_0=\pm(n\sqrt{C_{\theta\theta}/C_{rr}})$. When $n\geq 2$, the four eigenvalues $\lambda_{n1},...\lambda_{n4}$ are obtained from the characteristic equations,

$$C_{rr}\mu_{r\theta}\lambda_n^4-[n^2(C_{rr}C_{\theta\theta}-C_{r\theta}^2-2C_{r\theta}\mu_{r\theta})+(C_{rr}+C_{\theta\theta})\mu_{r\theta}]\lambda_n^2+(n^2-1)^2C_{\theta\theta}\mu_{r\theta}=0 \tag{2.40}$$

with the corresponding eigenvectors $\beta_{nj}^{(k)}$ given by

$$\beta_{nj}=\frac{C_{\theta\theta}-\lambda_{nj}^2C_{rr}+n^2\mu_{r\theta}}{n[(C_{r\theta}+\mu_{r\theta})\lambda_{nj}-(C_{\theta\theta}+\mu_{r\theta})]} \tag{2.41}$$

Figure 2.4 presents the four eigenvalues as a function of the harmonic number in a wide range of cylindrical orthotropy ratios that define radially $(C_{rr}/C_{\theta\theta}>1)$ and circumferentially $(C_{rr}/C_{\theta\theta}<1)$ orthotropic microstructures, illustrating that they are real for the graphite fiber considered herein.

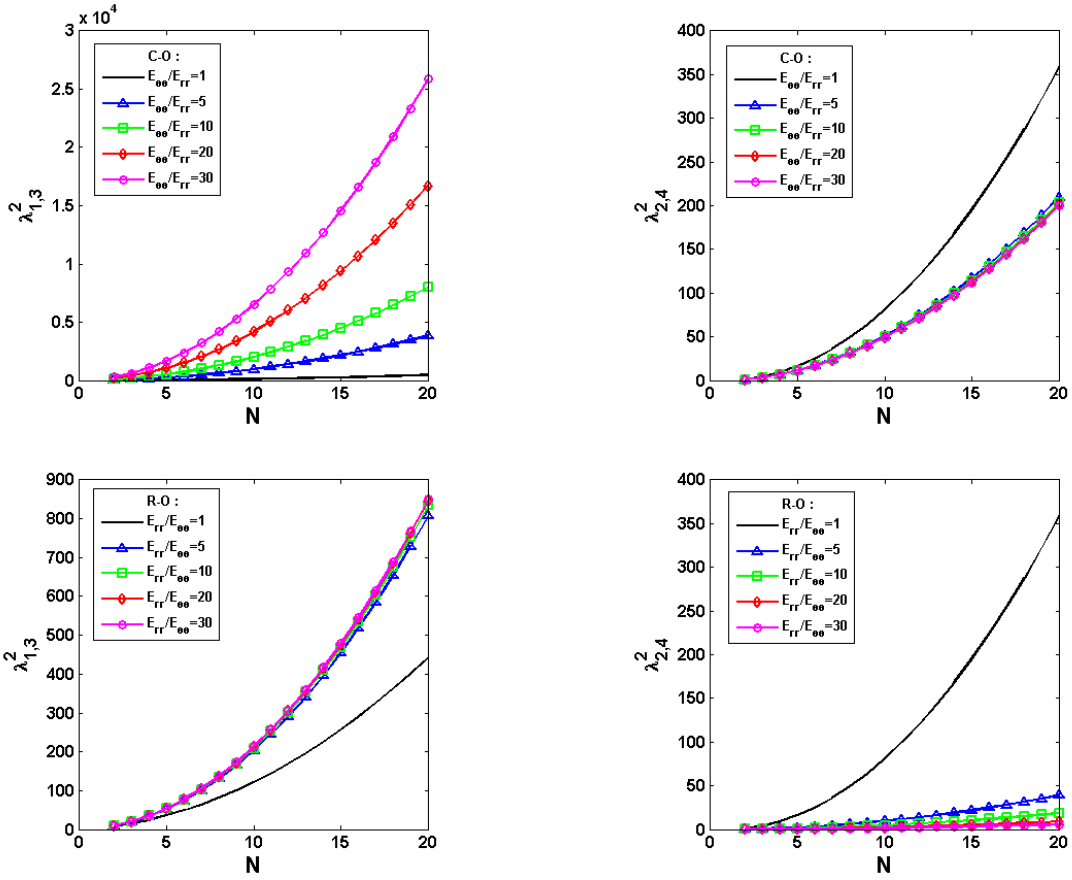

Figure 2.4 Eigenvalues for the inplane displacement field representation in fibers with different cylindrical orthotropy ratios as a function of harmonic number.

The unknown coefficient $H_{nj}^{(f)}, F_{nj}^{(f)}, G_{nj}^{(f)} (j = 1,2,3,4)$ are the fundamental unknowns in terms of which the corresponding matrix coefficients will be expressed using the continuity conditions, and $\xi = r/a$ is the nondimensionalized radial coordinate with respect to the fiber radius a. To ensure that the displacements remain bounded in the fiber, we still set $H_{n3}^{(f)} = H_{n4}^{(f)} = 0$ for $n \geq 1$ in the case of the out-of-plane displacement, and $F_{02}^{(f)} = 0$ and $F_{n3}^{(f)} = F_{n4}^{(f)} = 0,\ G_{n3}^{(f)} = G_{n4}^{(f)} = 0$ for $n \geq 2$ in the case of the in-plane displacements.

The stress components derived from the above displacement field employed in satisfying the continuity conditions at the fiber/matrix interface for cylindrically orthotropic fibers are

$$\sigma_{zr}^{(f)}(r,\theta) = \mu_{zr}^{(f)} \sum_{n=1}^{\infty} \bar{\lambda}_n \left[\xi^{\bar{\lambda}_n - 1} H_{n1}^{(f)} \cos n\theta + \xi^{\bar{\lambda}_n - 1} H_{n2}^{(f)} \sin n\theta \right]$$

$$\sigma_{rr}^{(f)}(r,\theta) = L_{rz}^{(f)}\bar{\varepsilon}_{zz} + (\sqrt{C_{rr}C_{\theta\theta}} + C_{r\theta})F_{01}^{(f)}\xi^{\lambda_0-1} + \sum_{n=2}^{\infty}\sum_{j=1}^{2} P_{nj}\xi^{\lambda_{nj}-1}\left[F_{nj}^{(f)}\cos n\theta + G_{nj}^{(f)}\sin n\theta\right]$$

$$\sigma_{r\theta}^{(f)}(r,\theta) = \sum_{n=2}^{\infty}\sum_{j=1}^{4} R_{nj}\xi^{\lambda_{nj}-1}\left[F_{nj}^{(f)}\sin n\theta - G_{nj}^{(f)}\cos n\theta\right] \tag{2.42}$$

where $L_{rz} = C_{zr} + \bar{H}(C_{rr} + C_{r\theta})$, $P_{nj} = C_{rr}\lambda_{nj} + C_{r\theta}(1+\beta_{nj})$, and $R_{nj} = \mu_{r\theta}[(\lambda_{nj}-1)\beta_{nj} - n]$.

2.2.2.2 Interfacial displacement and traction continuity

The coefficients $H_{nj}^{(m)}, F_{nj}^{(m)}$ and $G_{nj}^{(m)}$ that characterize the displacement field in the matrix phase given in the below are subsequently obtained in terms of the fiber coefficients $H_{nj}^{(f)}, F_{nj}^{(f)}$ and $G_{nj}^{(f)}$ from the interfacial displacement and traction continuity conditions at the fiber/matrix interface $r = a$,

$$\begin{aligned} &u_z^{(f)}(a,\theta) = u_z^{(m)}(a,\theta),\ u_r^{(f)}(a,\theta) = u_r^{(m)}(a,\theta),\ u_\theta^{(f)}(a,\theta) = u_\theta^{(m)}(a,\theta) \\ &\sigma_{zr}^{(f)}(a,\theta) = \sigma_{zr}^{(m)}(a,\theta),\ \sigma_{rr}^{(f)}(a,\theta) = \sigma_{rr}^{(m)}(a,\theta),\ \sigma_{r\theta}^{(f)}(a,\theta) = \sigma_{r\theta}^{(m)}(a,\theta) \end{aligned} \tag{2.43}$$

where the traction components at the common interface on the cylindrically orthotropic fiber side are given in the preceding section and the corresponding tractions on the (transverse) isotropic matrix side are given in Eqs. (2.20) and (2.28) in Section 2.2.1.

The axial shear problem is decoupled from the transverse normal and shear problems. Hence applying the two interfacial continuity conditions on the axial displacement $u_z(r,\theta)$ and axial shear stress $\sigma_{zr}(r,\theta)$ at $r = a$ and using the orthogonality of $\cos n\theta$ and $\sin n\theta$ terms, we obtain the following relations between fiber and matrix coefficients associated with different-order harmonic terms for $n \geq 1$,

$$\mathbf{H}_n^{(m)} = \mathbf{c}\cdot\mathbf{H}_n^{(f)} + \delta_{n1}\mathbf{d}\cdot[2\bar{\varepsilon}_{12}\ \ 2\bar{\varepsilon}_{13}] \tag{2.44}$$

where $\mathbf{H}_n^{(f)} = [H_{n1}^{(f)}, H_{n2}^{(f)}]^T$, $\mathbf{H}_n^{(m)} = [H_{n1}^{(m)}, H_{n2}^{(m)}, H_{n3}^{(m)}, H_{n4}^{(m)}]^T$, and the matrices $\mathbf{c}, \mathbf{d}$ are given below. The Kronecker delta term δ_{n1} is present because the average strains are introduced only through the $n = 1$ terms $\cos\theta$ and $\sin\theta$. Eq. (2.44) can be re-expressed as follows:

$$\begin{bmatrix} H_{n1} \\ H_{n2} \\ H_{n3} \\ H_{n4} \end{bmatrix}^{(m)} = \begin{bmatrix} c_1 & 0 \\ 0 & c_1 \\ c_2 & 0 \\ 0 & c_2 \end{bmatrix} \begin{bmatrix} H_{n1} \\ H_{n2} \end{bmatrix}^{(f)} + \delta_{n1} \begin{bmatrix} d_1 & 0 \\ 0 & d_1 \\ d_2 & 0 \\ 0 & d_2 \end{bmatrix} \begin{bmatrix} 2\bar{\varepsilon}_{12} \\ 2\bar{\varepsilon}_{13} \end{bmatrix} \tag{2.45}$$

in which $c_1 = (C_{zr}^{(f)}\bar{\lambda}_n^{(f)} + \mu_A^{(m)} n)/2\mu_A^{(m)} n$, $c_2 = 1 - c_1$, $d_1 = -1$, $d_2 = 0$.

The transverse normal and shear problems in the $r-\theta$ plane are coupled. Hence applying the four interfacial continuity conditions, and using orthogonality of $\cos n\theta$ and $\sin n\theta$ terms, we obtain the following relations between matrix and fiber coefficients, for $n = 0$

$$\begin{bmatrix} F_{01} \\ F_{02} \end{bmatrix}^{(m)} = \begin{bmatrix} b_{01} \\ b_{02} \end{bmatrix} F_{01}^{(f)} + \begin{bmatrix} c_{01} \\ c_{02} \end{bmatrix} \bar{\varepsilon}_{11} + \begin{bmatrix} d_{01} \\ d_{02} \end{bmatrix} (\bar{\varepsilon}_{22} + \bar{\varepsilon}_{33}) \tag{2.46}$$

where

$$\begin{aligned} b_{01} &= \frac{(C_{rr}^{(f)}\lambda_0^{(f)} + C_{r\theta}^{(f)}) - 2\mu_T^{(m)}}{2(k_T^{(m)} + \mu_T^{(m)})}, c_{01} = \frac{L_{rz}^{(f)} + 2\mu_T^{(m)}\bar{H} - \mu_A^{(m)}}{2(k_T^{(m)} + \mu_T^{(m)})}, \quad d_{01} = -\frac{1}{2}, \\ b_{02} &= \frac{2k_T^{(m)} - (C_{rr}^{(f)}\lambda_0^{(f)} + C_{r\theta}^{(f)})}{2(k_T^{(m)} + \mu_T^{(m)})}, c_{02} = \frac{-L_{rz}^{(f)} + 2k_T^{(m)}\bar{H} + \mu_A^{(m)}}{2(k_T^{(m)} + \mu_T^{(m)})}, d_{02} = 0 \end{aligned} \tag{2.47}$$

For $n \geq 2$

$$\begin{aligned} \mathrm{A}_n^{(m)}\mathrm{F}_n^{(m)} &= \mathrm{A}_n^{(f)}\mathrm{F}_n^{(f)} + \delta_{n2}\mathrm{A}_0(\bar{\varepsilon}_{22} - \bar{\varepsilon}_{33}) \\ \mathrm{A}_n^{(m)}\mathrm{G}_n^{(m)} &= \mathrm{A}_n^{(f)}\mathrm{G}_n^{(f)} + \delta_{n2}\mathrm{A}_0 2\bar{\varepsilon}_{23} \end{aligned} \tag{2.48}$$

in which

$$A_n^{(m)} = \begin{bmatrix} 1 & 1 & 1 & 1 \\ \beta_{n1} & \beta_{n2} & \beta_{n3} & \beta_{n4} \\ P_{n1} & P_{n2} & P_{n3} & P_{n4} \\ R_{n1} & R_{n2} & R_{n3} & R_{n4} \end{bmatrix}^{(m)}, \; A_n^{(f)} = \begin{bmatrix} 1 & 1 \\ \beta_{n1} & \beta_{n2} \\ P_{n1} & P_{n2} \\ R_{n1} & R_{n2} \end{bmatrix}^{(f)}, \; A_0 = \begin{bmatrix} 0 \\ 0 \\ -\mu_T^{(m)} \\ \mu_T^{(m)} \end{bmatrix} \tag{2.49}$$

The Kronecker delta term δ_{n2} is present because the average strains are introduced only through the $n = 2$ terms $\cos 2\theta$ and $\sin 2\theta$.

2.3 The Exterior Problem

To complete the solution to the unit cell problem, the unknown coefficient comprising $F_{nj}^{(f)}, G_{nj}^{(f)}, H_{nj}^{(f)}$ are determined by applying the variational principle, Eq. (2.2), with the surface displacements and tractions on the opposite faces of the unit cell related through the periodic boundary conditions. Use of the two-scale displacement representation given by Eq. (2.7) in the periodic displacement boundary conditions, Eq. (2.1), reduces these periodicity conditions to constraints on the fluctuating displacement components. For different geometrical arrays, we have,

(a) Rectangular or parallelogram arrays: $u_i'(S_1) = u_i'(S_3), \; u_i'(S_2) = u_i'(S_4)$

(b) Hexagonal array: $$u_i'(S_1)=u_i'(S_4),\;\; u_i'(S_2)=u_i'(S_5),\;\; u_i'(S_3)=u_i'(S_6) \tag{2.50}$$

Since the out-of-plane and in-plane problems are uncoupled, the coefficients comprising $F_{nj}^{(f)}, G_{nj}^{(f)}$ and $H_{nj}^{(f)}$ are found independently upon utilizing the reduced periodicity conditions in the variational principle. Implementing these conditions for the inplane problem in the first variation of the functional, Eq. (2.4), we obtain

(a) Rectangular or parallelogram arrays

$$\begin{aligned}&\sum_{i=1}^{2}\int_{S_i}\left\{\delta T_2(S_i)\left[u_2'(S_i)-u_2'(S_{i+2})\right]+\delta T_3(S_i)\left[u_3'(S_i)-u_3'(S_{i+2})\right]\right\}dS\\&\quad+\sum_{i=3}^{4}\int_{S_i}\left\{\delta u_2'(S_i)\left[T_2(S_i)+T_2(S_{i-2})\right]+\delta u_3'(S_i)\left[T_3(S_i)+T_3(S_{i-2})\right]\right\}dS=0\end{aligned} \tag{2.51}$$

(b) Hexagonal array

$$\begin{aligned}&\sum_{i=1}^{3}\int_{S_i}\left\{\delta T_2(S_i)\left[u_2'(S_i)-u_2'(S_{i+3})\right]+\delta T_3(S_i)\left[u_3'(S_i)-u_3'(S_{i+3})\right]\right\}dS\\&\quad+\sum_{i=4}^{6}\int_{S_i}\left\{\delta u_2'(S_i)\left[T_2(S_i)+T_2(S_{i-3})\right]+\delta u_3'(S_i)\left[T_3(S_i)+T_3(S_{i-3})\right]\right\}dS=0\end{aligned} \tag{2.52}$$

from which the system of equations for the unknown coefficients in $F_{nj}^{(f)}, G_{nj}^{(f)}$ are obtained in the form

$$\hat{\mathbf{A}}\left[\mathbf{F}^{(f)}\mathbf{G}^{(f)}\right]^T=\hat{\mathbf{B}}\bar{\varepsilon}_{in} \tag{2.53}$$

where $\bar{\varepsilon}_{in}=\left[\bar{\varepsilon}_{11},\bar{\varepsilon}_{22},\bar{\varepsilon}_{33},2\bar{\varepsilon}_{23}\right]^T$ and $\mathbf{F}^{(f)},\mathbf{G}^{(f)}$ are comprised of the individual vectors $\mathbf{F}_n^{(f)},\mathbf{G}_n^{(f)}$. Similarly, for the out-of-plane loading, the first variation of the functional becomes

(a) Rectangular or parallelogram arrays

$$\sum_{i=1}^{2}\int_{S_i}\delta T_1(S_i)\left[u_1'(S_i)-u_1'(S_{i+2})\right]dS+\sum_{i=3}^{4}\int_{S_i}\delta u_1'(S_i)\left[T_1(S_i)+T_1(S_{i-2})\right]dS=0 \tag{2.54}$$

(b) Hexagonal array

$$\sum_{i=1}^{3}\int_{S_i}\delta T_1(S_i)\left[u_1'(S_i)-u_1'(S_{i+3})\right]dS+\sum_{i=4}^{6}\int_{S_i}\delta u_1'(S_i)\left[T_1(S_i)+T_1(S_{i-3})\right]dS=0 \tag{2.55}$$

from which the system of equations for the unknown coefficients in $\mathbf{H}_n^{(f)}$ are obtained in the form

$$\tilde{\mathbf{A}}\mathbf{H}^{(f)}=\tilde{\mathbf{B}}\bar{\varepsilon}_{out} \tag{2.56}$$

where $\bar{\varepsilon}_{out} = [2\bar{\varepsilon}_{12}, 2\bar{\varepsilon}_{13}]^T$ and $\mathbf{H}^{(f)}$ contains the individual $\mathbf{H}_n^{(f)}$s. The elements of $\hat{\mathbf{A}}$, $\tilde{\mathbf{A}}$ and $\hat{\mathbf{B}}$, $\tilde{\mathbf{B}}$ are obtained in terms of surface integrals along the four or six sides $S_1, ...S_6$ of the unit cell.

To implement periodicity conditions in the variational principle, the fluctuating displacements in the cylindrical coordinate system are transformed to the Cartesian system using the displacement transformation equations. Similarly the fluctuating Cartesian strains, used in the calculation of stresses and tractions through Hooke's law and Cauchy's relations, respectively, are obtained from the strain transformation equations, with the cylindrical fluctuating strains determined from the corresponding fluctuating displacement components $u_z'(r,\theta)$, $u_r'(r,\theta)$, $u_\theta'(r,\theta)$ using strain-displacement relations (Wang and Pindera, 2015). The expressions for the axial shear stresses and transverse normal and shear stresses in the Cartesian coordinate system along the unit cell's boundary obtained from Hooke's law are

$$\begin{aligned}
\sigma_{12}^{(m)} &= 2\mu_A^m(\bar{\varepsilon}_{12} + \varepsilon_{12}'^{(m)}) \\
\sigma_{13}^{(m)} &= 2\mu_A^m(\bar{\varepsilon}_{13} + \varepsilon_{13}'^{(m)}) \\
\sigma_{22}^{(m)} &= 2k_T^m\nu_A^m\bar{\varepsilon}_{11} + (k_T^m + \mu_T^m)(\bar{\varepsilon}_{22} + \varepsilon_{22}'^{(m)}) + (k_T^m - \mu_T^m)(\bar{\varepsilon}_{33} + \varepsilon_{33}'^{(m)}) \\
\sigma_{33}^{(m)} &= 2k_T^m\nu_A^m\bar{\varepsilon}_{11} + (k_T^m - \mu_T^m)(\bar{\varepsilon}_{22} + \varepsilon_{22}'^{(m)}) + (k_T^m + \mu_T^m)(\bar{\varepsilon}_{33} + \varepsilon_{33}'^{(m)}) \\
\sigma_{23}^{(m)} &= 2\mu_T^m(\bar{\varepsilon}_{23} + \varepsilon_{23}'^{(m)})
\end{aligned} \tag{2.57}$$

where the fluctuating strain components are related to their counterparts in the cylindrical coordinates.

2.4 Homogenized Constitutive Equations

2.4.1 Transversely Isotropic Phases

The homogenized Hooke's law is obtained by averaging local constitutive equations in each phase

$$\bar{\boldsymbol{\sigma}} = \frac{1}{V}\sum_k \int \mathbf{C}^{(k)}\boldsymbol{\varepsilon}^{(k)} dV_k = \sum_k v_{(k)}\mathbf{C}^{(k)}\bar{\boldsymbol{\varepsilon}}^{(k)} \tag{2.58}$$

where the phase volume fractions obey the relationship $\sum_k v_{(k)} = 1$.

With the knowledge of the coefficients in $\mathbf{F}_n^{(f)}, \mathbf{G}_n^{(f)}$ and $\mathbf{H}_n^{(f)}$, the remaining coating and matrix phase coefficients may be calculated using Eqs. (2.21)-(2.22), and (2.29)-(2.36). Hence

the average strains $\bar{\varepsilon}^{(k)}(k=f,c,m)$ in the individual phases may be related to average macroscopic strains through the localization relations

$$\bar{\varepsilon}^{(k)} = \mathbf{A}^{(k)}\bar{\varepsilon} \tag{2.59}$$

where $\mathbf{A}^{(k)}$ are Hill's elastic strain concentration matrix for the each individual phase (Hill, 1963). The homogenized relationship between stress and strain averages then becomes

$$\bar{\sigma} = \sum\nolimits_k v_{(k)}\mathbf{C}^{(k)}\mathbf{A}^{(k)}\bar{\varepsilon} = \mathbf{C}^{*}\bar{\varepsilon} \tag{2.60}$$

where $\mathbf{C}^{*} = \sum\limits_k v_{(k)}\mathbf{C}^{(k)}\mathbf{A}^{(k)}$. In light of the phase volume fraction relationship, the homogenized stiffness matrix for the unit cell may be written as

(a) Fiber/matrix two-phase material system:

$$\mathbf{C}^{*} = \mathbf{C}^{(m)} + v_{(f)}\left(\mathbf{C}^{(f)} - \mathbf{C}^{(m)}\right)\mathbf{A}^{(f)} \tag{2.61}$$

(b) Fiber/coating/matrix three-phase material system:

$$\mathbf{C}^{*} = \mathbf{C}^{(m)} + v_{(f)}\left(\mathbf{C}^{(f)} - \mathbf{C}^{(m)}\right)\mathbf{A}^{(f)} + v_{(c)}\left(\mathbf{C}^{(c)} - \mathbf{C}^{(m)}\right)\mathbf{A}^{(c)} \tag{2.62}$$

The average fiber strains are obtained in closed form upon integrating the local expressions over the fiber strains contain only the applied average strains and the displacement coefficients associated with the $n=0,2$ harmonics in the case of transverse normal and shear strains, and the $n=1$ harmonic in the case of axial shear strains

$$\begin{aligned}
\bar{\varepsilon}_{22}^{(k)} &= \bar{\varepsilon}_{22} + F_{01}^{(k)} + \gamma^{(k)}\frac{3k_T^{(k)}}{2\left(k_T^{(k)} - \mu_T^{(k)}\right)}F_{21}^{(k)} + F_{22}^{(k)} & \bar{\varepsilon}_{11}^{(k)} &= \bar{\varepsilon}_{11} \\
\bar{\varepsilon}_{33}^{(k)} &= \bar{\varepsilon}_{33} + F_{01}^{(k)} - \gamma^{(k)}\frac{3k_T^{(k)}}{2\left(k_T^{(k)} - \mu_T^{(k)}\right)}F_{21}^{(k)} - F_{22}^{(k)} & \bar{\varepsilon}_{12}^{(k)} &= \bar{\varepsilon}_{12} + \frac{1}{2}H_{11}^{(k)} \\
\bar{\varepsilon}_{23}^{(k)} &= \bar{\varepsilon}_{23} + \gamma^{(k)}\frac{3k_T^{(k)}}{2\left(k_T^{(k)} - \mu_T^{(k)}\right)}G_{21}^{(k)} + G_{22}^{(k)} & \bar{\varepsilon}_{13}^{(k)} &= \bar{\varepsilon}_{13} + \frac{1}{2}H_{12}^{(k)}
\end{aligned} \tag{2.63}$$

where $k=f,c$, and $\gamma^{(f)}=1,\ \gamma^{(f)}=1+\left(b/a\right)^2$.

These relations reduce to the expressions reported by Drago and Pindera (2008) for isotropic phases. The columns of the matrices $\mathbf{A}^{(f)}$ and $\mathbf{A}^{(c)}$ are generated by solving the unit cell problem for one non-zero average strain of a known magnitude applied at a time, with the remaining average strains kept zero. The solution produces the unknown coefficients in $\mathbf{F}_n^{(k)}, \mathbf{G}_n^{(k)}$ and $\mathbf{H}_n^{(k)}$ for the applied loading, and thus the average fiber and coating strains. The

elements of the strain concentration matrix occupying the column that corresponds to the applied non-zero average strain are then obtained by taking the ratio of the averaged strain in the fiber phase and the average applied strain.

2.4.2 Orthotropic-Fiber Composites

Based on the special characteristics of orthotropic fiber constitutive equations, when transformed from polar coordinate to Cartesian coordinate, the stiffness matrix in Cartesian coordinate would have "θ" effects. So the homogenized Hooke's law for the unit cell is obtained directly by averaging the local stresses

$$\bar{\sigma} = \frac{1}{V}\sum_k \int \sigma^{(k)}(\mathbf{x}) dV_k = \sum_k v_{(k)} \bar{\sigma}^{(k)} = \mathbf{C}^* \bar{\varepsilon} \tag{2.64}$$

This is in contrast with the approach based on averaging local constitutive equations in each phase and then finding the relation between phase and composite strain averages through Hill's concentration factors. The present approach is preferable as it does not require a fourth order stiffness tensor transformation from cylindrical to Cartesian coordinates.

To generate the elements of homogenized stiffness matrix $\mathbf{C}^*$, one non-zero homogenized strain component is applied to the unit cell at a time, and the fiber phase coefficients $\mathbf{F}_n^{(f)}, \mathbf{G}_n^{(f)}$ and $\mathbf{H}_n^{(f)}$, are obtained for the particular loading upon solving the corresponding boundary-value problem, with the matrix phase coefficients obtained from Eqs. (2.44)-(2.49). Hence the local stresses in the individual phases are obtained in cylindrical coordinates, transformed to Cartesian coordinates using the standard 2nd-order transformation equations, and subsequently averaged throughout each phase domain. For the matrix phase, this is carried out numerically (and the explicit expressions of which are expressed in Section 2.2.1 and Appendix A), while for the fiber phase the following closed-form expressions are obtained analytically in the limit as the fiber core which excludes singular stresses tends to zero,

$$\bar{\sigma}_{11}^{(f)} = 2(C_{zr}^{(f)}\lambda_0 + C_{z\theta}^{(f)})\big/(\lambda_0 + 1)\cdot F_{01}^{(f)} + L_{zz}^{(f)} \cdot \bar{\varepsilon}_{11}$$

$$\bar{\sigma}_{22}^{(f)} = [(C_{rr}^{(f)} + C_{r\theta}^{(f)})\lambda_0 + C_{r\theta}^{(f)} + C_{\theta\theta}^{(f)}]\big/(\lambda_0 + 1)\cdot F_{01}^{(f)} + \sum_{j=1}^{2}(P_{2j}^{(f)} - S_{2j}^{(f)} - 2R_{2j}^{(f)})\big/2(\lambda_{2j}^{(f)} + 1)\cdot F_{2j}^{(f)} + (L_{rz}^{(f)} + L_{\theta z}^{(f)})\big/2 \cdot \bar{\varepsilon}_{11}$$

$$\bar{\sigma}_{33}^{(f)} = [(C_{rr}^{(f)} + C_{r\theta}^{(f)})\lambda_0 + C_{r\theta}^{(f)} + C_{\theta\theta}^{(f)}]\big/(\lambda_0 + 1)\cdot F_{01}^{(f)} + \sum_{j=1}^{2}(-P_{2j}^{(f)} + S_{2j}^{(f)} + 2R_{2j}^{(f)})\big/2(\lambda_{2j}^{(f)} + 1)\cdot F_{2j}^{(f)} + (L_{rz}^{(f)} + L_{\theta z}^{(f)})\big/2\cdot\bar{\varepsilon}_{11}$$

$$\bar{\sigma}_{23}^{(f)} = \sum_{j=1}^{2}(P_{2j}^{(f)} - S_{2j}^{(f)} - 2R_{2j}^{(f)})\big/2(\lambda_0 + 1)\cdot G_{2j}^{(f)}$$

$$\bar{\sigma}_{12}^{(f)} = (C_{zr}^{(f)}\bar{\lambda}_1 + C_{z\theta}^{(f)})\big/(\bar{\lambda}_1 + 1)\cdot H_{11}^{(f)}$$

$$\bar{\sigma}_{13}^{(f)} = (C_{zr}^{(f)}\bar{\lambda}_1 + C_{z\theta}^{(f)})\big/(\bar{\lambda}_1 + 1)\cdot H_{12}^{(f)} \tag{2.65}$$

where $L_{iz}^{(f)} = C_{iz}^{(f)} + \bar{H}(C_{i\theta}^{(f)} + C_{ir}^{(f)})$, $i = z, r, \theta$ and $S_{2j} = C_{r\theta}\lambda_{2j} + C_{\theta\theta}(1 + 2\beta_{2j})$.

Hence for the particular loading by one non-zero homogenized strain component, taking the ratio of the average stress to the applied average strain generates one column of the homogenized stiffness matrix $\mathbf{C}^*$. The accuracy of averaging the stress fields has been confirmed by employing both volume and surface integration using the average stress theorem,

$$\bar{\sigma}^{(k)} = \frac{1}{V_{(k)}}\int_{V_{(k)}}\sigma^{(k)}(\mathrm{x})\,dV_{(k)} = \frac{1}{V_{(k)}}\int_{S_{(k)}}\sigma^{(k)}(\mathrm{x})\circ\mathrm{n}^{(k)}\,dS_{(k)} \tag{2.66}$$

where $\mathrm{x}\in S_{(k)}$ in the surface integral. Moreover, we have also confirmed by direct numerical calculation that the stress and strain fields satisfy the Hill-Mandel energy equivalence between the homogenized and local quantities,

$$\frac{1}{V}\int_V \boldsymbol{\sigma}(\mathbf{x})\circ\boldsymbol{\varepsilon}(\mathbf{x})\,dV = \bar{\boldsymbol{\sigma}}\circ\bar{\boldsymbol{\varepsilon}} \tag{2.67}$$

which are discussed in details in next chapter. This provides additional confidence in the extended theory and the associated implemented numerical procedure.

2.5 Summary

This chapter establishes the theoretical framework of the locally exact homogenization theory. The displacement fields are expressed using Fourier series expansion representation with unknown coefficients after solving the Navier's equations. The relationship between the unknown coefficients of fiber, coating (for three-phase composites) and matrix is derived by applying the stress and displacement continuity conditions. Then two systems of equations, for the decoupled inplane and out-of-plane problem, are set up to solve the remaining unknowns by

employing the balanced variational principle proposed by Drago and Pindera (2008). Finally, the homogenized constitutive relationship is obtained by averaging local constitutive equations in each phase. Hill's concentration matrix (Hill, 1963) is used for (transversely) isotropic properties to simplify the process, but not preferred for orthotropic constituents that bring in "θ" effect during the fourth order stiffness tensor transformation from cylindrical to Cartesian coordinates.

The theory proposed can be treated as an efficient micromechanics tool to accommodate fiber/matrix or fiber/coating/matrix composites, and cover different geometrical properties – hexagonal, rectangular (square), parallelogram (tetragonal) arrays, as well as different material properties – (transversely) isotropic, orthotropic constituents. The easy input constructions, which are just geometrical and material properties of the composites, as well as the quick execution that is explained later in this dissertation, are the most significant contributions for the framework of LEHT. Compared with other models, this theory can be promoted among professionals and non-professionals alike because of the characteristics discussed above. Next chapter we will investigate the accuracy, stability and efficiency of the present theory against other classical theories, analytical and numerical techniques.

Chapter 3

Validation

3.1 Two-Phase Composite Materials

3.1.1 Convergence Study

We first demonstrate the extended theory's convergence behavior by calculating homogenized engineering moduli of graphite/epoxy and glass/epoxy unidirectional composites as a function of the number of eigenfunctions used in the displacement field representation. The elastic moduli of the fiber and matrix phases are listed in Table 3.1.

Material	E_A(GPa)	E_T(GPa)	μ_A(GPa)	μ_T(GPa)	ν_A
AS4 graphite fiber	225	15	15	7	0.20
E-glass fiber	69.0	69.0	28.28	28.28	0.22
Boron fiber	420	420	175	175	0.20
3501-6 epoxy	4.2	4.2	1.567	1.567	0.34
Aluminum	69.0	69.0	25.94	25.94	0.33

Table 3.1 Elastic fiber and matrix properties employed in the calculations. Note that the AS4 graphite fiber is transversely isotropic with $E_{22} = E_{33}$, $\nu_{12} = \nu_{13}$ and $G_{23} = E_{22}/2(1+\nu_{23})$ and the remaining constituents isotropic.

While the graphite fibers are transversely isotropic, glass fibers are isotropic with a greater in plane elastic modulus contrast relative to the epoxy matrix than in the case of graphite fibers.

Three fiber volume fractions are used in this convergence study to cover a wide range of reinforcement content, namely 0.05, 0.30 and 0.60. Unit cells with centered fibers were employed in the homogenized moduli calculations. The homogenized engineering moduli are evaluated by using the homogenized compliance matrix obtained from the inverse of the homogenized stiffness matrix established in Eq. (2.61) or (2.62), $\mathbf{S}^* = [\mathbf{C}^*]^{-1}$. Then the homogenized moduli for transversely isotropic materials are obtained from the following

relations,

$$E_A^* = E_{11}^* = \frac{1}{S_{11}^*},\ \ E_T^* = E_{22}^* = \frac{1}{S_{22}^*} = \frac{1}{S_{33}^*},\ \ \frac{\nu_A^*}{E_A^*} = \frac{\nu_{12}^*}{E_{11}^*} = -S_{12}^* = -S_{13}^*$$

$$\mu_A^* = G_A^* = \mu_{12}^* = \frac{1}{S_{55}^*} = \frac{1}{S_{66}^*},\ \ \mu_T^* = G_T^* = \mu_{23}^* = \frac{1}{S_{44}^*} \tag{3.1}$$

Figs. 3.1-3.3 demonstrate convergence behavior of the homogenized Young's and shear moduli E_T^* and G_A^* of hexagonal, square and tetragonal arrays, respectively, for both the graphite/epoxy and glass/epoxy composites. Similar behavior is observed for the homogenized Poisson's ratios ν_A^* and ν_T^*. The moduli of hexagonal and square arrays have been normalized by the corresponding moduli generated using the finite-volume direct averaging micromechanics (FVDAM) theory (Gattu et al., 2008; Khatam and Pindera, 2009), demonstrated to be comparable to that of the finite element method (Cavalcante et al., 2012); while the moduli of parallelogram array whose values have been normalized by moduli corresponding to harmonic number $N = 16$, which should be the converged values for their respective counterparts. Hence converged values correspond to moduli ratio of 1.0. As observed, generally greater number of eigenfunctions is required to obtain converged moduli with increasing fiber volume fraction for all different fiber types. Nonetheless, converged moduli are obtained with as few harmonics as 8, and at most 12 for both materials.

Figs. 3.4-3.6 compares the converged in-plane stress fields $\sigma_{22}(y_2, y_3)$, $\sigma_{33}(y_2, y_3)$, $\sigma_{23}(y_2, y_3)$ for hexagonal, square, and tetragonal arrays of unidirectional graphite/epoxy with fiber volume fraction of 0.25 generated using 12 harmonics under unidirectional loading by the homogenized stress $\bar{\sigma}_{22} \neq 0$. For these calculations offset fibers were employed placed at (0, −1, −1) relative to the unit cells' centroids. For the hexagonal array L = 6.204 while for the square array $L = H$ = 10, and for tetragonal array H = 10.746, L=9.306, and $\varphi = \pi/3$. For all of the three arrays the fiber radius was 2.8209. Examination of stress fields generated using 4, 8 and 12 harmonics indicates that rapid stress field convergence is achieved with just 8 harmonics, resulting in good estimates of stress field magnitudes and distributions. The higher transverse stress in the fiber embedded in the square unit cell produces higher transverse Young's modulus than the hexagonal array. This well-known result is demonstrated in the following section.

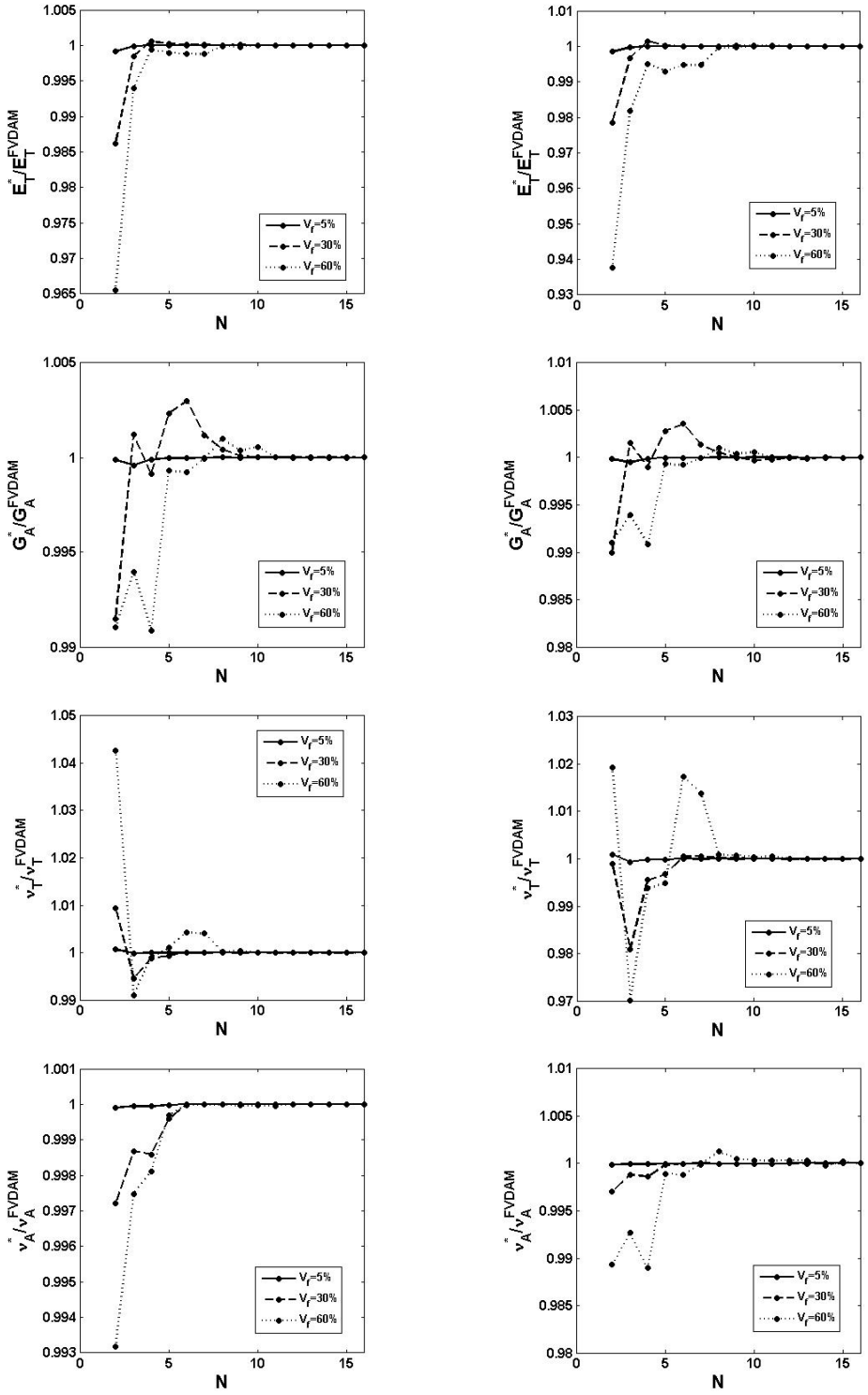

Graphite/epoxy Glass/epoxy

Figure 3.1 The convergence of homogenized moduli of hexagonal array with the number of harmonic eigenfunctions for graphite/epoxy and glass/epoxy with fiber volume fractions of 0.05, 0.30 and 0.60 relative to FVDAM predictions.

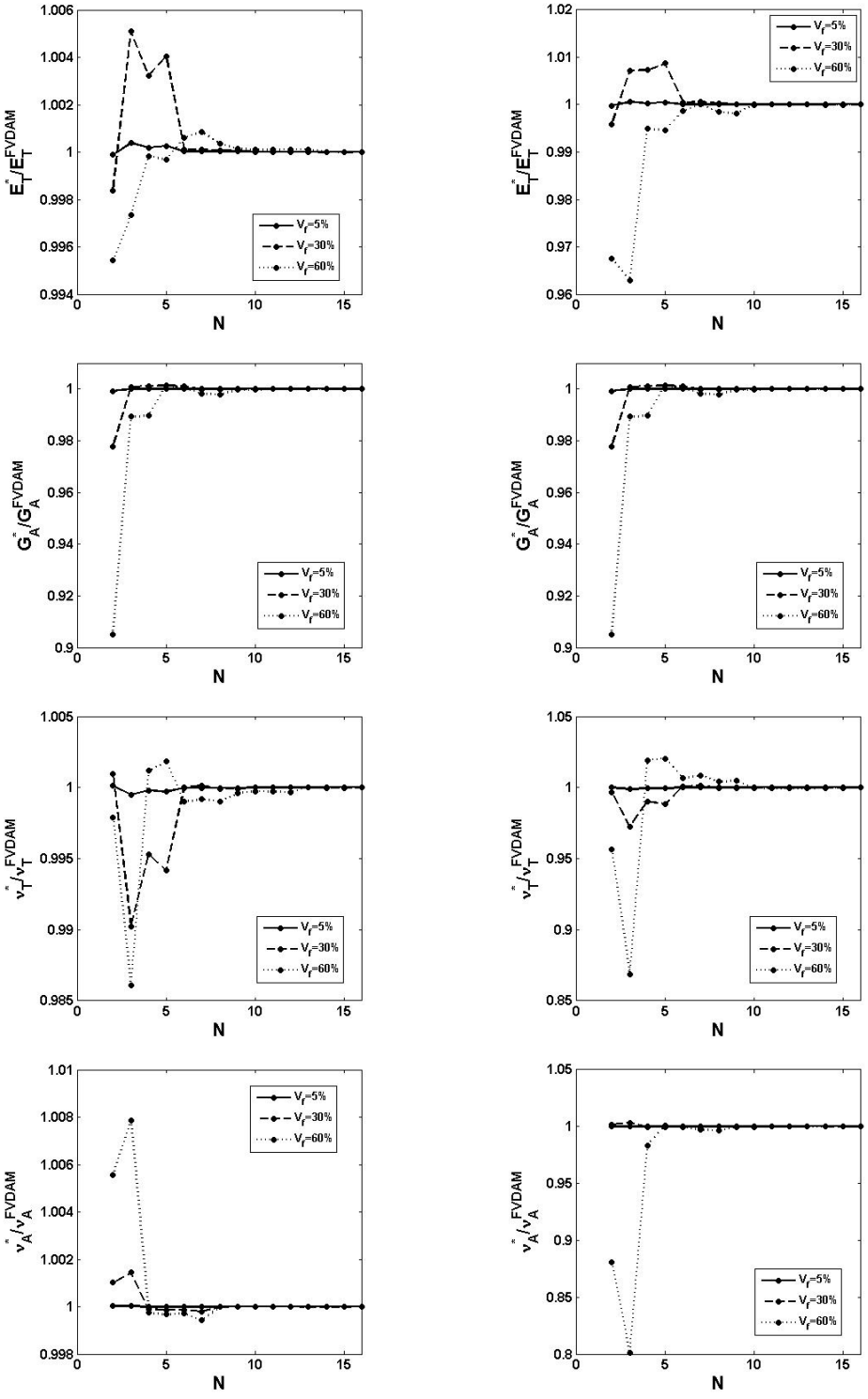

Graphite/epoxy Glass/epoxy

Figure 3.2 The convergence of homogenized moduli of hexagonal array with the number of harmonic eigenfunctions for graphite/epoxy and glass/epoxy with fiber volume fractions of 0.05, 0.30 and 0.60 relative to FVDAM predictions.

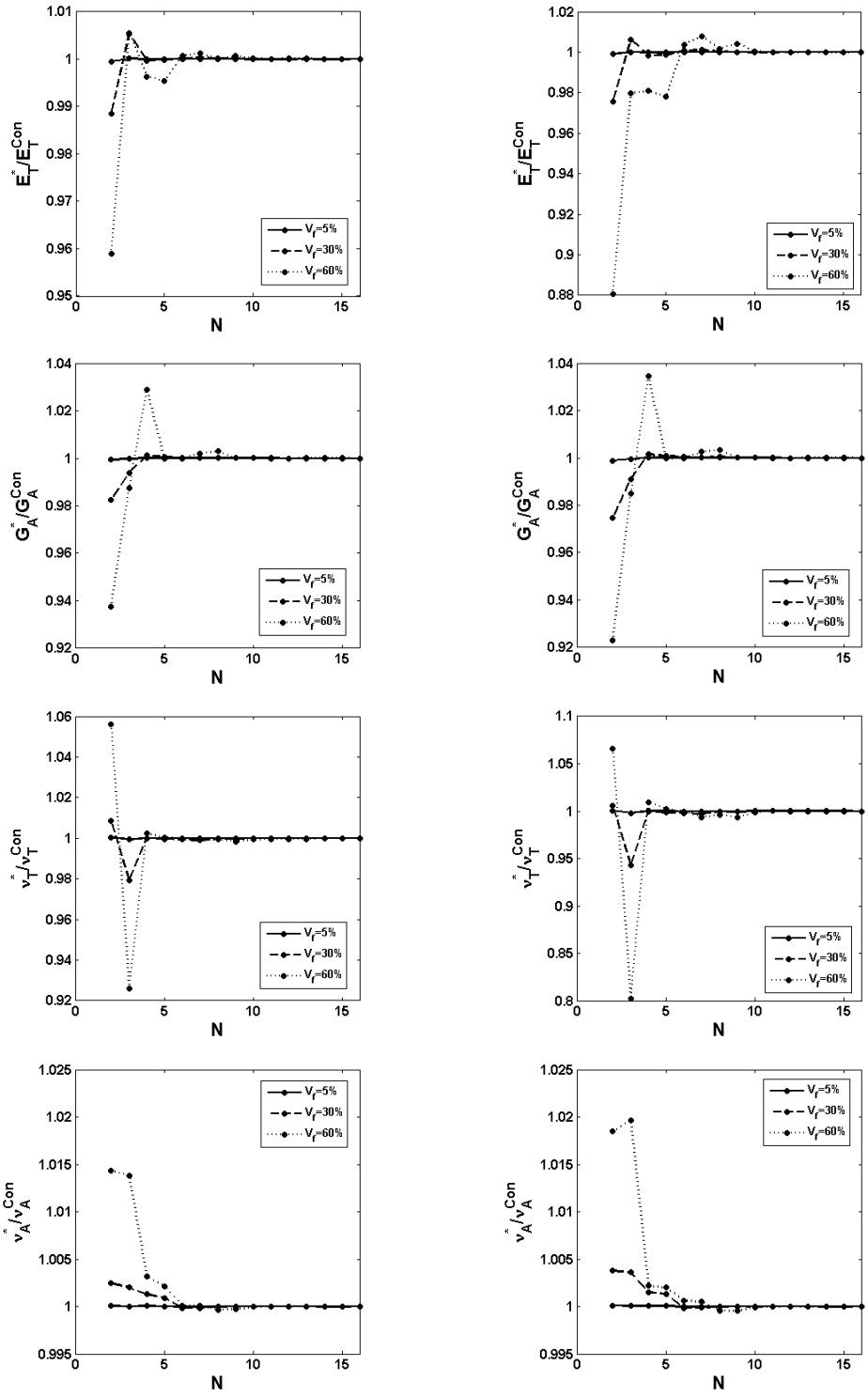

Graphite/epoxy Glass/epoxy

Figure 3.3 The convergence of homogenized moduli of parallelogram array with the number of harmonic eigenfunctions for graphite/epoxy and glass/epoxy with fiber volume fractions of 0.05, 0.30 and 0.60 relative to the converged value predictions.

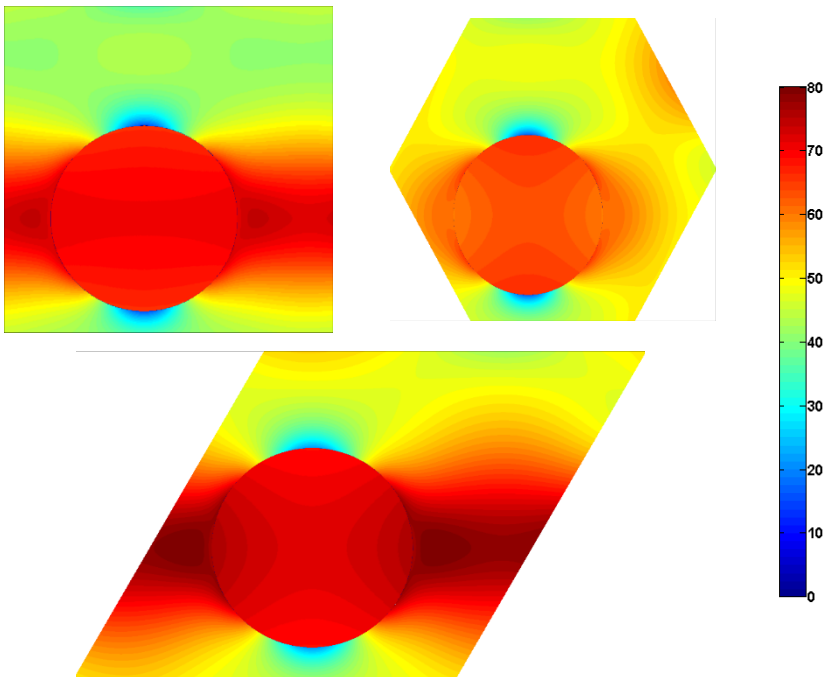

Figure 3.4 Converged stress distributions $\sigma_{22}(y_2, y_3)$ in hexagonal, square and parallelogram unit cells of a graphite/epoxy composite with the fiber volume fraction 0.25 subjected to the unidirectional loading $\bar{\sigma}_{22} \neq 0$ at the applied strain $\bar{\varepsilon}_{22} = 0.01$.

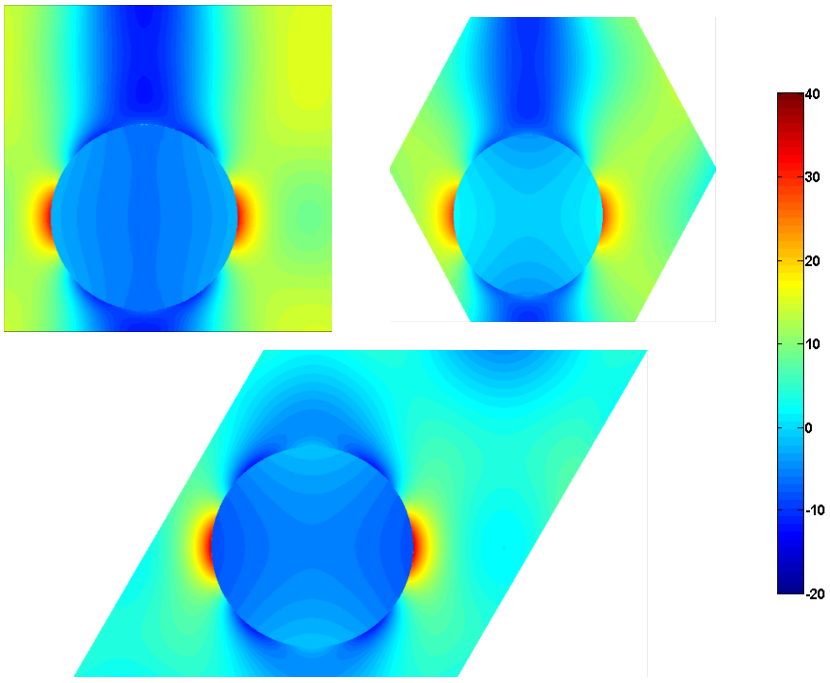

Figure 3.5 Converged stress distributions $\sigma_{33}(y_2, y_3)$ in hexagonal, square and parallelogram unit cells of a graphite/epoxy composite with the fiber volume fraction 0.25 subjected to the unidirectional loading $\bar{\sigma}_{22} \neq 0$ at the applied strain $\bar{\varepsilon}_{22} = 0.01$.

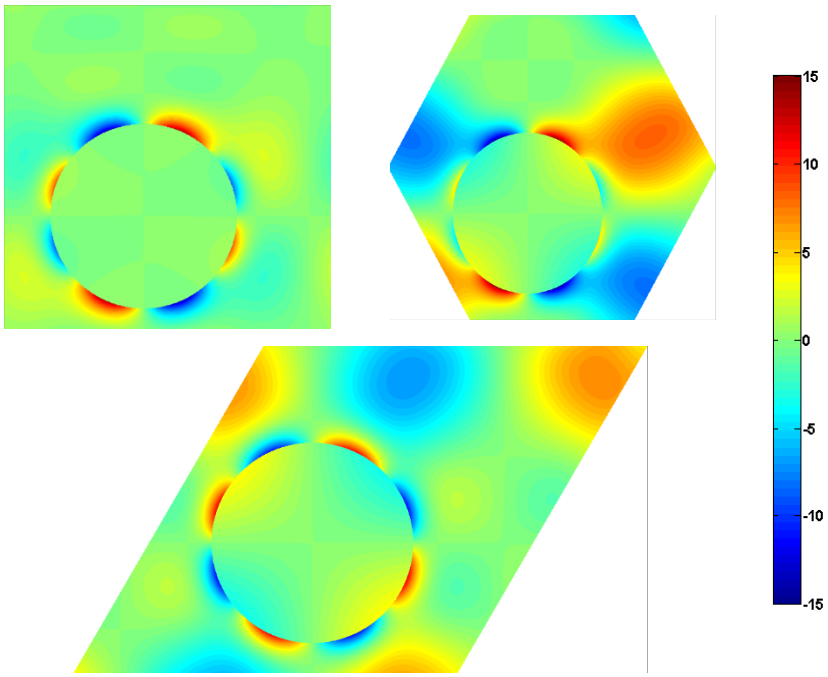

Figure 3.6 Converged stress distributions $\sigma_{23}(y_2, y_3)$ in hexagonal, square and parallelogram unit cells of a graphite/epoxy composite with the fiber volume fraction 0.25 subjected to the unidirectional loading $\bar{\sigma}_{22} \neq 0$ at the applied strain $\bar{\varepsilon}_{22} = 0.01$.

The utility of the analytical solution approach employed herein lies in its ability to ensure continuity of both tractions and displacements at the fiber/matrix interface. This will be important in our future investigations dealing with interfacial debonding as well as surface effects in nanotechnology applications. Fig. 3.7 demonstrates the rapid convergence of in-plane radial and circumferential tractions $\sigma_{rr}(r=a,\theta)$ and $\sigma_{r\theta}(r=a,\theta)$ with harmonic number calculated around the fiber/matrix interface. We note that traction continuity is maintained for all harmonics employed in the solution, with no visually discernible differences between traction components on either side of the fiber/matrix interface. This is due to the explicit enforcement of traction (and displacement) continuity in the unit cell solution. Similar results have been obtained for the in-plane interfacial displacement components $u_r(r=a,\theta)$, $u_\theta(r=a,\theta)$ and for the out-of plane interfacial displacement $u_z(r=a,\theta)$ and traction $\sigma_{rz}(r=a,\theta)$ under the corresponding loading.

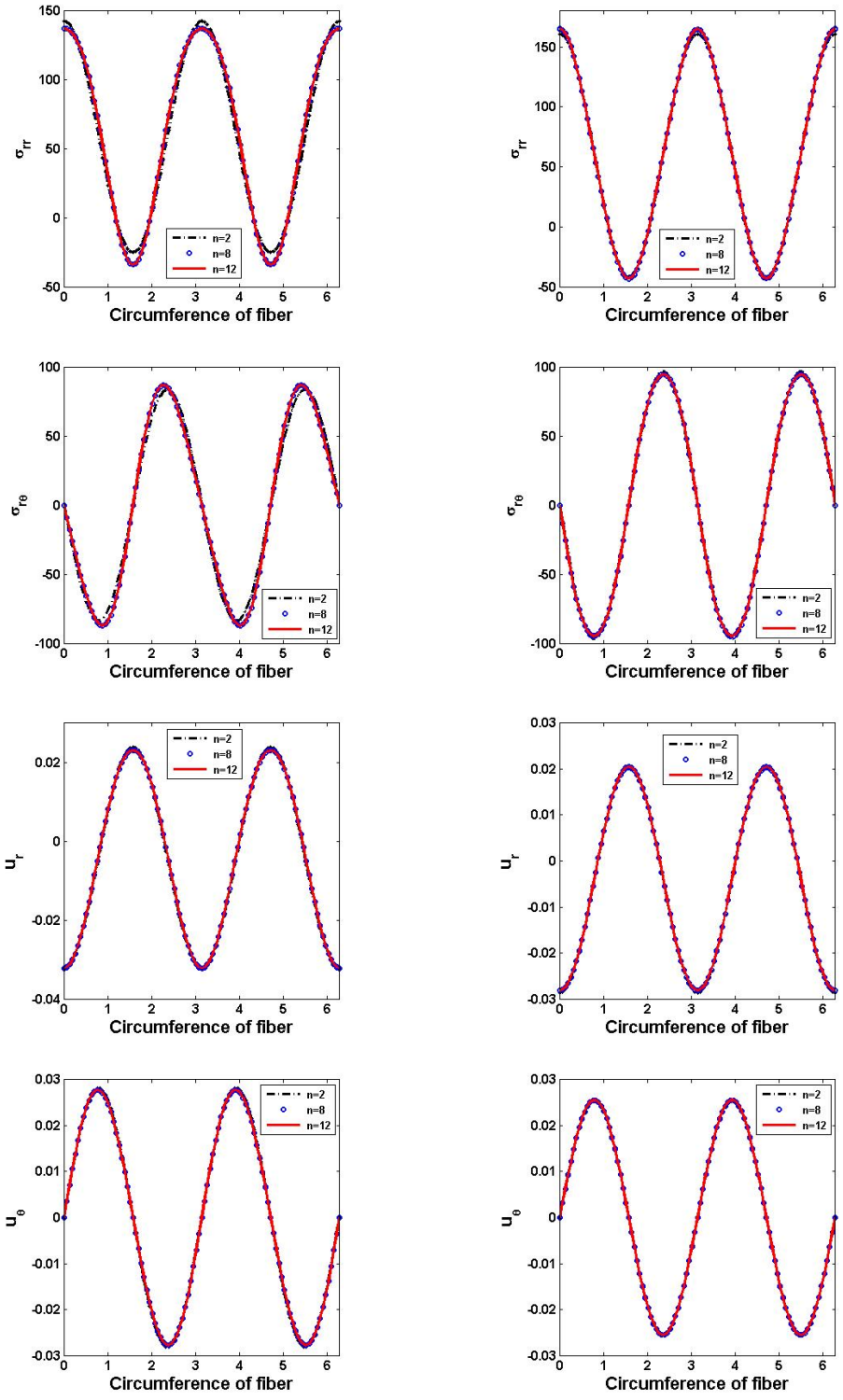

Hexagonal array Square array

Figure 3.7 Convergence of the radial and tangential tractions, as well as the displacement components at the fiber/matrix interface of a graphite/epoxy composite with 0.25 fiber volume fraction with increasing number of harmonics by applying uniaxial loading.

3.1.2 Stability of the Solution

Convergence of the homogenized moduli with the number of eigenfunctions demonstrated in the foregoing implies convergence of the unknown coefficients in the Fourier series representation of fluctuating displacements, Eqs. (2.17) and (2.23). This has been demonstrated by Drago and Pindera (2008) for square arrays of isotropic inclusion/matrix phases, and is also the case in the present study. A demanding test of the solution's stability is the demonstration that in the limit as the fiber volume fraction becomes very small, the solution reduces to the Eshelby solution (Eshelby, 1957) with just the first few terms remaining, and the higher-order coefficients becoming vanishingly small.

To demonstrate this, we subject a hexagonal unit cell with 0.05% fiber content to uniaxial loading by $\bar{\sigma}_{22} = 100\text{MPa}$. The material system is graphite/epoxy, Table 3.1. The solutions are then generated using an increasing number of harmonics from $n = 2$, which corresponds to the Eshelby solution as the fiber volume fraction tends to zero, to $n = 16$. The inplane stresses $\sigma_{22}(y_2, y_3)$, $\sigma_{33}(y_2, y_3)$, $\sigma_{23}(y_2, y_3)$ are illustrated in Fig. 3.8 for $n = 2$ and 16 harmonics and compared with the exact Eshelby solution. The stress distributions have been plotted in the square region in the vicinity of the fiber with the hexagonal boundaries outside of this region. The locally-exact homogenization theory solution is seen to remain very stable regardless of the number of harmonics employed (at least up to sixteen). Similar results are obtained for the in-plane shear stress $\sigma_{23}(y_2, y_3)$ distributions. Qualitative comparison with the Eshelby solution is very favorable. Quantitative comparison shown in Fig. 3.9 in terms of the absolute differences $\Delta\sigma_{ij}(y_2, y_3) = \sigma_{ij}(y_2, y_3) - \sigma_{ij}^{Eshelby}(y_2, y_3)$ for the inplane stress components is also favorable. The differences are seen to be very small fractions of the maximum stresses observed in each distribution. Examination of the leading coefficients $F_{01}^{(f)}, F_{22}^{(f)}$ as a function of harmonics vis-à-vis those of the Eshelby solution indicates insignificant differences, with the higher-order coefficients practically zero.

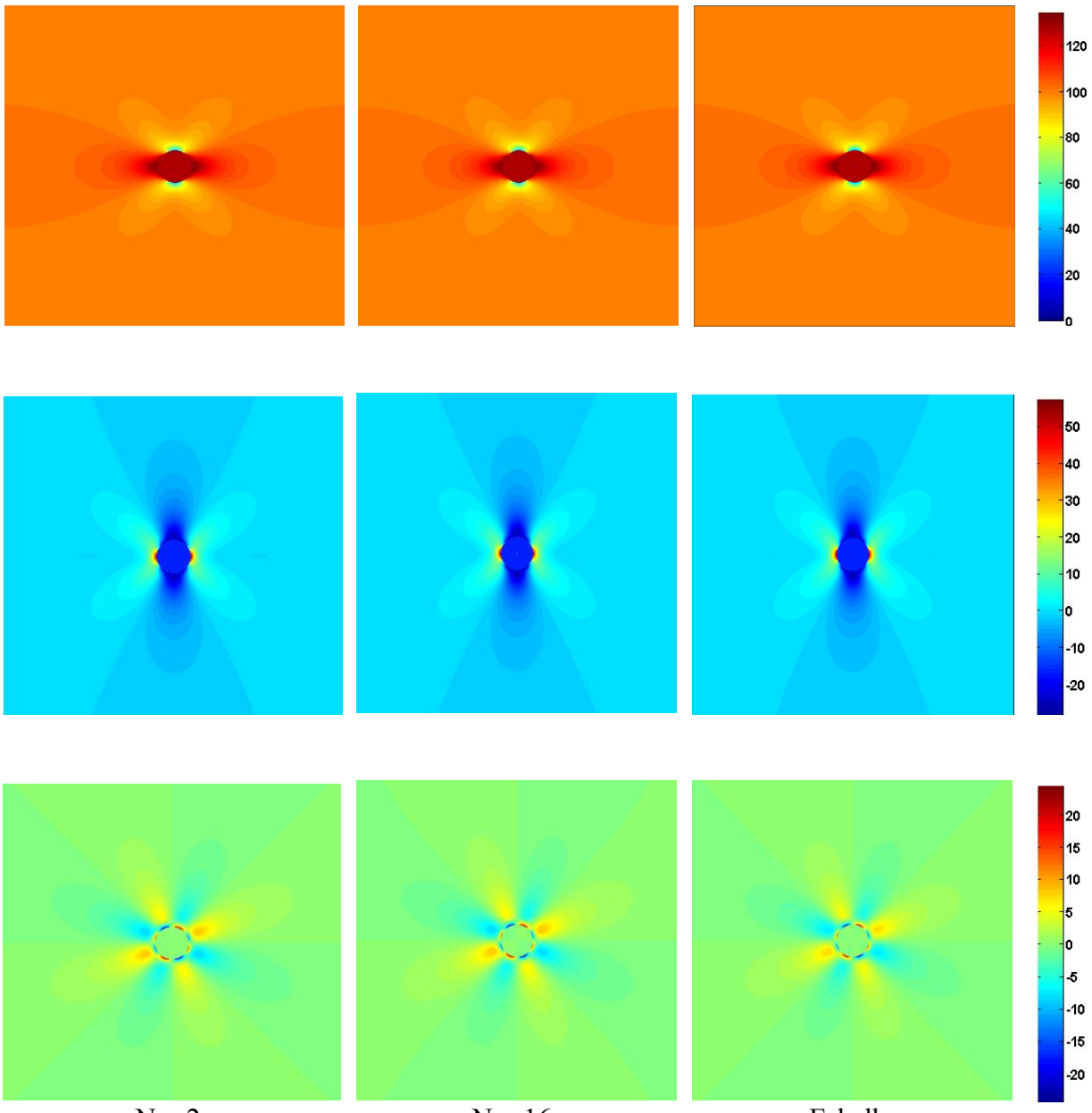

Figure 3.8 Stress distributions in a hexagonal unit cell with a dilute fiber volume fraction solution as a function of the number of harmonics, mimicking the Eshelby and demonstrating the locally-exact solution's stability with increasing harmonic number.

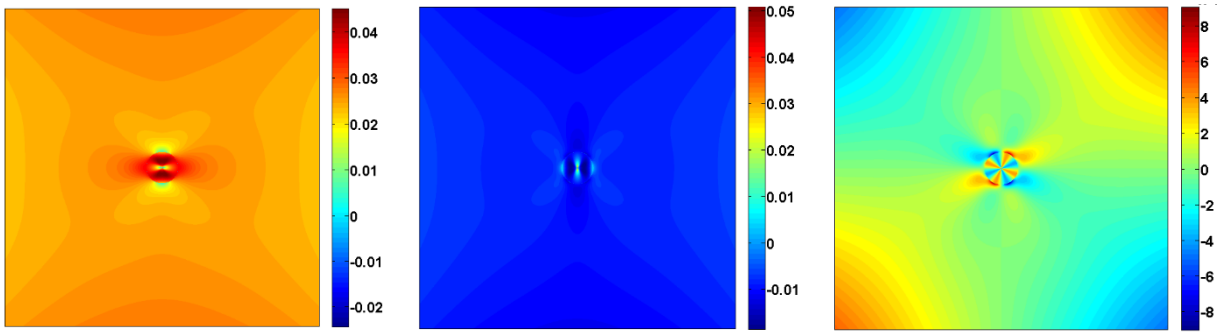

(a) $\Delta\sigma_{22}(y_2, y_3)$ (b) $\Delta\sigma_{33}(y_2, y_3)$ (c) $\Delta\sigma_{23}(y_2, y_3)$

Figure 3.9 Distributions of stress differences in a hexagonal unit cell with a dilute fiber volume fraction between the locally-exact homogenization theory results generated with 16 harmonics and the Eshelby solution based on results in Fig. 3.8.

3.1.3 Comparison with Published Results

Results for the homogenized moduli of hexagonal (as well as square) periodic arrays are available in the literature for quantitative comparison with present results. In particular, Eischen and Torquato (1993) have calculated inplane moduli of hexagonal arrays comprised of phases with a wide range of moduli contrast using the boundary-element method which have been used as benchmark results by several investigators. Helsing (1995) has demonstrated that these results may be obtained much more efficiently and with greater numerical resolution using an integral equation approach. Most recently, Mogilevskaya et al. (2012, 2014) provided comparison between the above results and the results generated using previously developed equivalent inhomogeneity and multi-pole expansion techniques for hexagonal and square arrays, respectively. These results are employed for quantitative comparison with our locally-exact homogenization theory.

Tables 3.2-3.3 shows comparison of the normalized homogenized plane bulk modulus $k_T^*/k^{(m)}$ and transverse shear modulus $\mu_T^*/\mu^{(m)}$ of an hexagonal array of stiff inclusions embedded in a much softer matrix generated by the locally-exact homogenization theory (LEHT) with the results reported in Refs. (Helsing, 1995; Mogilevskaya et al., 2012). This is case 2 with $\mu^{(m)}=1, \nu^{(m)}=0.35, \mu^{(f)}=135, \nu^{(f)}=0.20$ considered by Eischen and Torquato (1993) who reported data with just two significant digits (not included in Table 3.2). We report our results with five significant digits for direct comparison with those of Helsing (1995). In addition, we

also verify the accuracy of our calculations by leveraging the relationship that must be satisfied by transversely isotropic materials,

$$\mu_T^* = \frac{E_T^*}{2(1+\nu_T^*)} \tag{3.2}$$

As observed, the results of Ref. (Helsing, 1995) and LEHT agree to five, four, three and two significant digits in the low, medium, high and very high fiber volume fraction ranges, respectively. Moreover, the LEHT transverse shear moduli generated by the unit cell analysis coincide with those of Eq. (3.2) to five significant digits for all fiber volume fractions but one. Similar results have been obtained for the homogenized plane strain bulk modulus $k_T^*/k_T^{(m)}$. The results reported in Ref. (Mogilevskaya et al., 2012) to three significant digits agree with the LEHT and Ref. (Helsing, 1995) predictions in the low fiber volume fraction, but lose their significant digit accuracy with increasing fiber volume fraction. The accuracy deteriorates significantly at the highest fraction of 0.85. The above comparison provides additional evidence of the accuracy of the locally-exact homogenization theory with the newly extended capability to hexagonal periodicity.

$k_T^*/k^{(m)}$	Helsing	Mogilevskaya N=7	Mogilevskaya N=37	LEHT
0.1	1.14137	1.141	1.141	1.14137
0.2	1.31725	1.317	1.317	1.31725
0.3	1.54202	1.543	1.543	1.54202
0.4	1.83948	1.843	1.842	1.83948
0.5	2.25228	2.262	2.260	2.25227
0.6	2.86670	2.895	2.888	2.86667
0.7	3.89641	3.978	3.959	3.89632
0.8	6.12145	6.372	6.337	6.12090
0.85	8.87779	9.347	9.370	8.87498

Table 3.2 Quantitative comparison of the normalized homogenized transverse shear modulus $k_T^*/k_T^{(m)}$ of a hexagonal array of stiff inclusions with the results of Mogilevskaya et al. (2012) (both N=7 &37 cases) and Helsing (1995).

For completeness, we also compare our predictions with those reported by Mogilevskaya et al. (2014) for a square array of inclusions. In this case, we focus on the homogenized transverse Young's and shear moduli, as well as axial shear modulus of a porous solid whose comparison is presented in Table 3.4-3.5. Both sets of results are accurate to three significant digits upon

round-off of the LEHT predictions with the exceptions of the transverse shear modulus at very high porosity fractions. The result $C_{44}^{*}/\mu_T^{(m)}$ of Ref. (Mogilevskaya et al., 2014) at the porosity fraction of 0.75 appears to be erroneous as it increases relative to that at 0.70.

$\mu_T^{*}/\mu_T^{(m)}$	Helsing	Mogilevskaya N=7	Mogilevskaya N=37	LEHT	$G_T^{*}=E_T^{*}/[2(1+\nu_T^{*})]$
0.1	1.17821	1.178	1.178	1.17821	1.17821
0.2	1.40186	1.402	1.403	1.40186	1.40186
0.3	1.69713	1.696	1.699	1.69715	1.69715
0.4	2.11487	2.106	2.118	2.11489	2.11489
0.5	2.75227	2.718	2.688	2.75232	2.75232
0.6	3.80628	3.721	3.823	3.80637	3.80636
0.7	5.74678	5.611	5.841	5.74688	5.74688
0.8	**10.17840**	**10.463**	**11.213**	**10.17821**	**10.17821**
0.85	**15.64461**	**18.012**	**19.715**	**15.64173**	**15.64173**

Table 3.3 Quantitative comparison of the normalized homogenized transverse shear modulus $\mu_T^{*}/\mu_T^{(m)}$ of a hexagonal array of stiff inclusions with the results of Mogilevskaya et al. (2012) (both N=7 &37 cases) and Helsing (1995).

	$(c_{22}^{*}+c_{23}^{*})/2k_T^{(m)}$		$(c_{22}^{*}+c_{23}^{*})/2\mu_T^{m}$	
V_f	Mogilevskaya	LEHT	Mogilevskaya	LEHT
0.05	0.774	0.77407	0.894	0.89364
0.10	0.619	0.61873	0.810	0.81003
0.15	0.505	0.50532	0.741	0.74083
0.20	0.419	0.41877	0.681	0.68105
0.25	0.350	0.35040	0.628	0.62755
0.30	0.295	0.29488	0.578	0.57813
0.35	0.249	0.24873	0.531	0.53124
0.40	0.210	0.20959	0.486	0.48569
0.45	0.176	0.17581	0.441	0.44056
0.50	0.146	0.14619	0.395	0.39508
0.55	0.120	0.11979	0.348	0.34850
0.60	0.096	0.09583	0.300	0.29990
0.65	0.074	0.07357	0.248	0.24782
0.70	0.052	0.05212	0.190	0.18913
0.75	0.029	0.03065	0.117	0.11012

Table 3.4 Quantitative comparison of the normalized homogenized transverse moduli of a square array of porosities with the results of Mogilevskaya et al. (2014), with $\mu_T^{(m)}=\mu_A^{(m)}=1\text{GPa}$, $\nu_T^{(m)}=\nu_A^{(m)}=0.39$; $\mu_T^{(f)}=\mu_A^{(f)}=1\text{e}-6\text{GPa}$, $\nu_T^{(f)}=\nu_A^{(f)}=0.20$.

	c_{44}^{*}/μ_T^m		c_{55}^{*}/μ_A^m	
V_f	Mogilevskaya	LEHT	Mogilevskaya	LEHT
0.05	0.878	0.87763	0.905	0.90476
0.10	0.757	0.75685	0.818	0.81818
0.15	0.641	0.64099	0.739	0.73910
0.20	0.533	0.53289	0.667	0.66653
0.25	0.435	0.43468	0.600	0.59962
0.30	0.348	0.34761	0.538	0.53758
0.35	0.272	0.27214	0.480	0.47971
0.40	0.208	0.20809	0.425	0.42535
0.45	0.155	0.15476	0.374	0.37387
0.50	0.111	0.11121	0.325	0.32466
0.55	0.076	0.07635	0.277	0.27705
0.60	0.049	0.04910	0.230	0.23032
0.65	0.028	0.02861	0.183	0.18343
0.70	0.013	0.01480	0.135	0.13456
0.75	**0.034**	**0.00981**	0.078	0.07885

Table 3.5 Quantitative comparison of the normalized homogenized transverse and axial shear moduli of a square array of porosities with the results of (Mogilevskaya et al., 2014).

Material	E_A(GPa)	E_T(GPa)	μ_A(GPa)	μ_T(GPa)	ν_A
Graphite fiber	214	14	7	5.83	0.25
3501-6 epoxy	3.5	3.5	1.3	1.3	0.35
Interface	5.25	5.25	2.059	2.059	0.275

Table 3.6 Elastic fiber and matrix properties employed in the calculations. Note that the AS4 graphite fiber is transversely isotropic with $E_{22}=E_{33}$, $\nu_{12}=\nu_{13}$ and $G_{23}=E_{22}/2(1+\nu_{23})$ and the remaining constituents isotropic.

3.2 Three-Phase Composite Materials

We validate the developed solution by first showing that in the limit as the fiber volume fraction becomes very small, the results of Eshelby (1957); Kirsch (1898) are recovered regardless of the number of terms employed in the displacement field representation in the fiber, coating and matrix phases. This also demonstrates the solution's stability with increasing number of harmonics. In the first case, we take the coating Young's modulus to be thousand times stiffer than that of the matrix, while in the second case we take it thousand times softer. In both cases the ratio of the coating to fiber outer radii is $b/a=1.1$. Then we study the convergence of the

homogenized moduli and local stress fields as a function of the number of harmonic terms of non-dilute fiber volume fractions with different coating thicknesses. Finally, we compare our solution's predictions with those reported in the literature based on finite-element and elasticity-based calculations.

3.2.1 Stability of the Solution

To demonstrate the solution's stability and reduction to known solutions, we subject a hexagonal unit cell with the fiber volume fraction of 0.2% to uniaxial loading $\bar{\sigma}_{22} = 100\text{MPa}$ with the remaining stresses zero. The material system is graphite/epoxy considered by Jasiuk and Kouider (1993) with the fiber and matrix elastic moduli given in Table 3.6. The solutions are then generated using an increasing number of harmoncis from $n = 2$, which corresponds to the Eshelby solution as the fiber volume fraction tends to zeros, to $n = 16$. The inplane stresses $\sigma_{22}(y_2, y_3)$, $\sigma_{33}(y_2, y_3)$ and $\sigma_{23}(y_2, y_3)$ are illustrated in Fig. 3.10 for $n = 2$ and 16 harmonics and compared with the exact Eshelby solution for the coating that is thousand times stiffer than the matrix. The stress distributions have been plotted in the square region in the vicinity of the fiber with the hexagonal boundaries far outside this region. The locally-exact homogenization theory solution is seen to remain very stable regardless of the number of harmonics employed (at least up to sixteen). Comparison with the Eshelby solution is very favorable. Moreover, examination of the leading coefficients $F_{01}^{(f)}$, and $F_{22}^{(f)}$ as a function of harmonics vis-à-vis those of the Eshelby solution indicates insignificant differences, with the higher-order coefficients practically zero.

The above results have been plotted using a color map that highlights the fiber and matrix stresses at the expense of very large coating stresses owing to the large coating stiffness. Hence these stresses are compared separately with the Eshelby solution along radial paths with the largest stress gradients in Fig. 3.11 for the $n = 16$ harmonic case, illustrating the locally-exact solution's ability to accurately capture stress fields in thin interfacial layers.

Setting the coating Young's modulus to a very small value prevents stress transfer into the fiber, thereby mimicking a dilute hexagonal array of non-interacting holes equivalent to an infinite plate with a hole (Fig 3.12). For this problem, the maximum $\sigma_{22}(y_2, y_3)$ stress occurs at the top and bottom of the hole whose magnitude is three time the far-field stress, or 300 MPa.

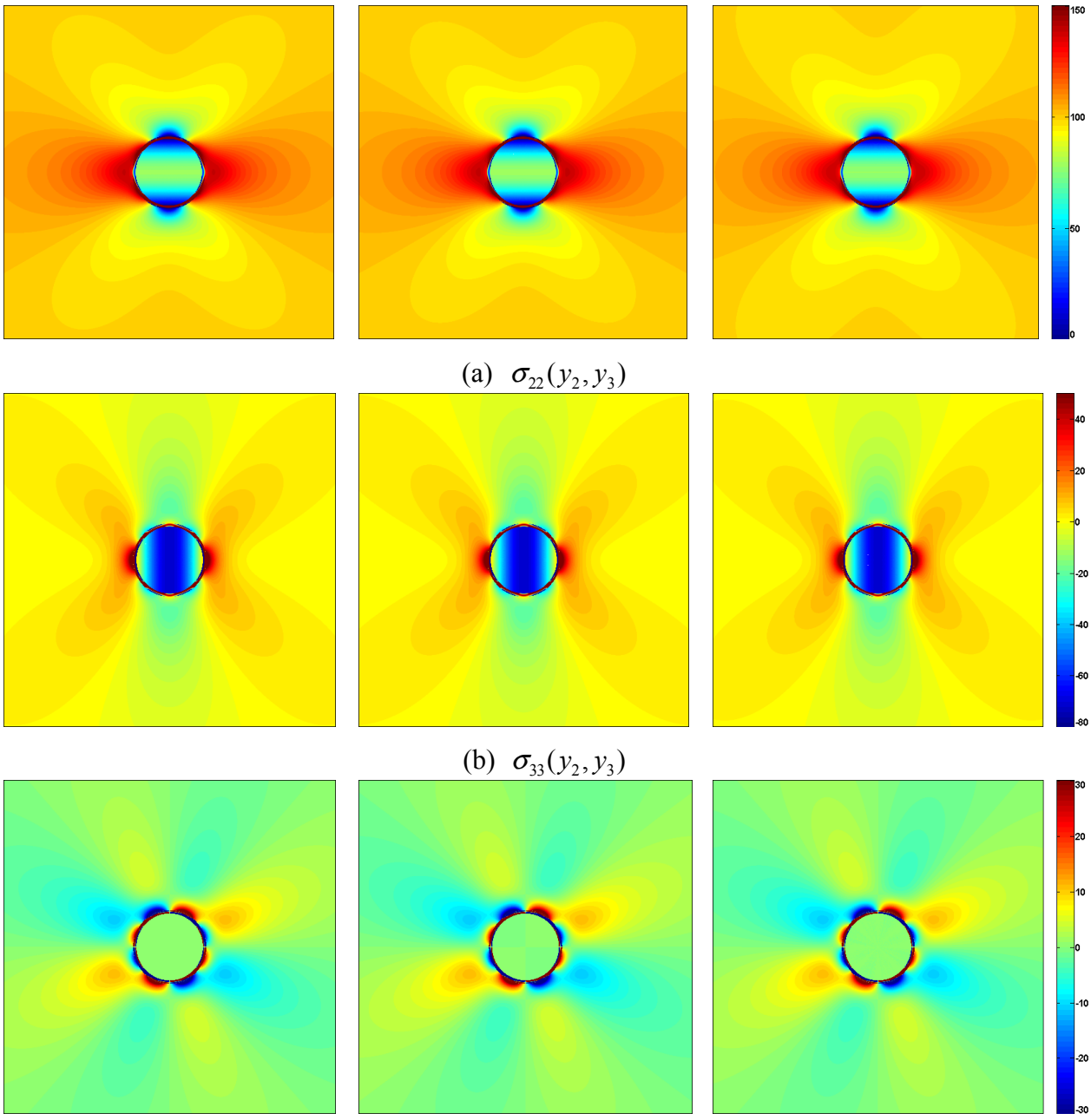

(a) $\sigma_{22}(y_2, y_3)$

(b) $\sigma_{33}(y_2, y_3)$

(c) $\sigma_{23}(y_2, y_3)$

N=2 N=16 Eshelby

Figure 3.10 Comparison of stress distributions in a hexagonal unit cell with a dilute fiber volume fraction as a function of the number of harmonics with the Eshelby solution, demonstrating the locally-exact solution's stability with increasing harmonic number for $E^{(c)} / E^{(m)} = 10^3$ and $b/a = 1.1$.

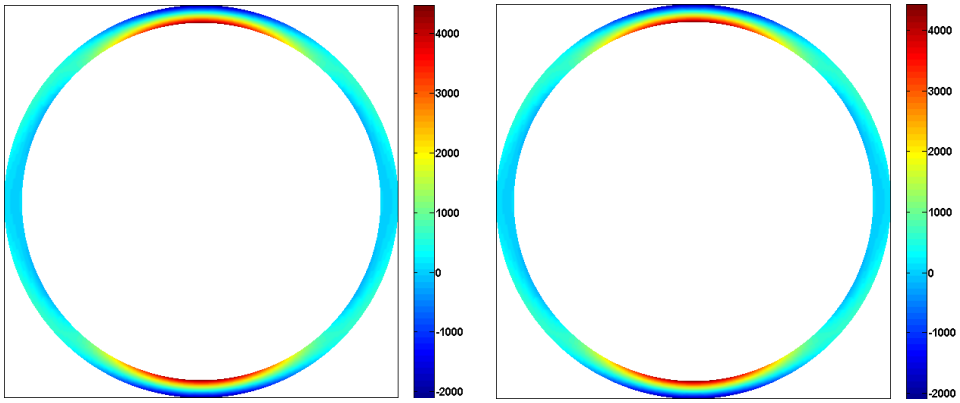

(a) $\sigma_{22}(y_2, y_3)$

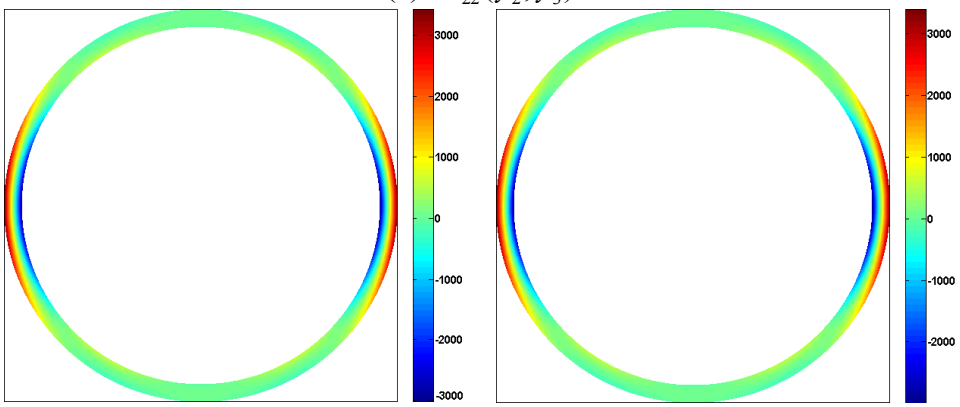

(b) $\sigma_{33}(y_2, y_3)$

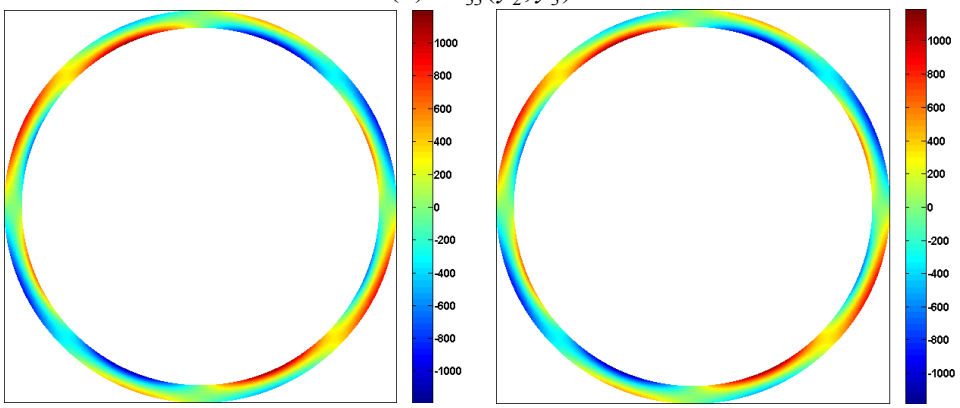

(c) $\sigma_{23}(y_2, y_3)$

N=16 Eshelby

Figure 3.11 Comparison of converged stress distributions in the stiff coating of a hexagonal unit cell with a dilute fiber volume fraction with the Eshelby solution for $E^{(c)}/E^{(m)} = 10^3$ and $b/a = 1.1$.

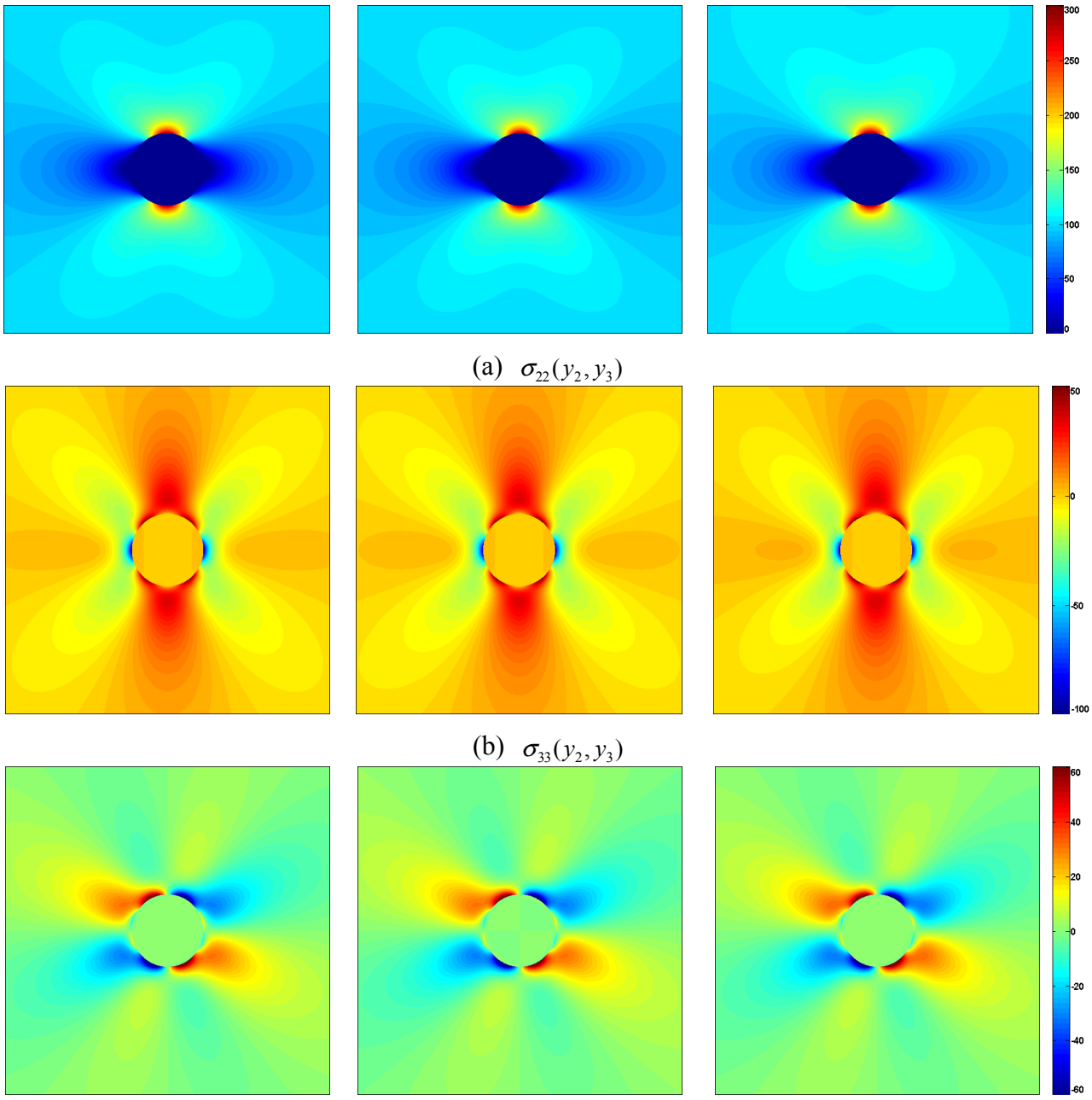

(a) $\sigma_{22}(y_2, y_3)$

(b) $\sigma_{33}(y_2, y_3)$

(c) $\sigma_{23}(y_2, y_3)$

N=2 N=16 Eshelby

Figure 3.12 Comparison of stress distributions in a hexagonal unit cell with a dilute fiber volume fraction as a function of the number of harmonics with the Kirsch solution, demonstrating the locally-exact solution's stability with increasing harmonic number for $E^{(c)} / E^{(m)} = 10^{-3}$ and $b/a = 1.1$.

Similarly, the minimum $\sigma_{33}(y_2, y_3)$ stress which is compressive occurs along the load axis at the hole boundary whose magnitude is equal to the far-field stress. These stresses are captured very well by the locally exact theory regardless of the number of harmonics used in the displacement fields.

3.2.2 Convergence Study

We consider hexagonal and square unit cells representative of graphite/epoxy composites with non-dilute reinforcement, and investigate convergence of the homogenized moduli and local stress fields with the number of harmonics in the displacement field representation for three interfacial layer thicknesses. The elastic moduli of the fiber and matrix phases are the same as in the preceding stability study listed in Table 3.6 which includes the coating Young's modulus 1.5 times that of the epoxy matrix. The non-dilute fiber volume fraction is 0.50 and the coating thicknesses yield coating/ fiber radius ratios b/a of 1.01, 1.05 and 1.10, with the thinnest coating providing a demanding test of the theory's computational capability.

The homogenized engineering moduli were calculated using the homogenized compliance matrix obtained from the inverse of the homogenized stiffness matrix established in Eq. (2.62), $\mathbf{S}^* = [\mathbf{C}^*]^{-1}$, as described in (Wang and Pindera, 2015). Fig. 3.13 illustrates convergence behavior of the homogenized transverse Young's and shear moduli E_T^* and G_T^*, respectively, and axial shear moduli G_A^* for hexagonal and square unit cell architectures. Similar behavior (not shown) is observed for the homogenized Poisson's radios ν_A^* and ν_T^*. The moduli have not been normalized to highlight the effect of the coating thickness whose increase yields stiffer response given its greater Young's modulus relative to that of the matrix. The result indicates that at the considered fiber volume fraction, generally quicker convergence of the homogenized moduli is observed for the hexagonal array, with as few as 5 harmonics yielding converged transverse and axial shear moduli, and 10 yielding converged transverse Young's modulus. Included in the figure are the corresponding results in the absence of coating ($b/a = 1.0$), illustrating that the convergence behavior is not altered by the coating presence in the considered thickness range.

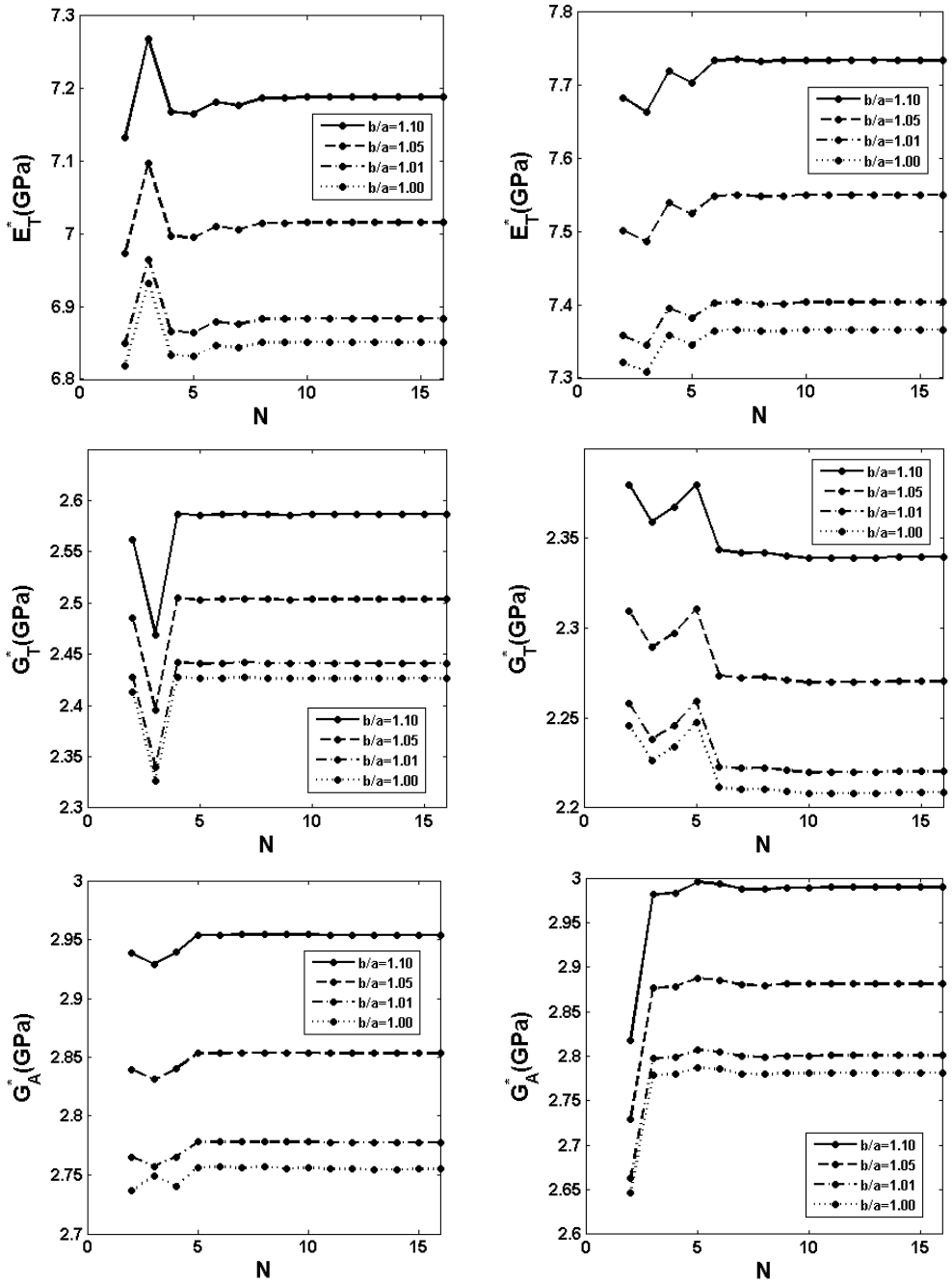

Hexagonal array Square array

Figure 3.13 Convergence of selected homogenized moduli with the number of harmonic eigenfunctions for a graphite/epoxy composite with fiber volume fraction of 0.50 and coating thickness as a parameter for $E^{(c)} / E^{(m)} = 1.5$.

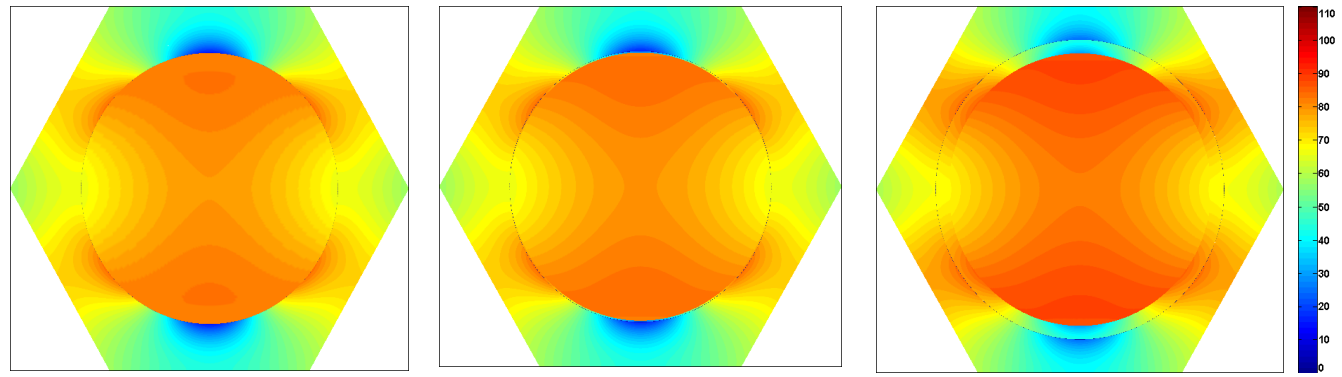

(a) $\sigma_{22}(y_2, y_3)$

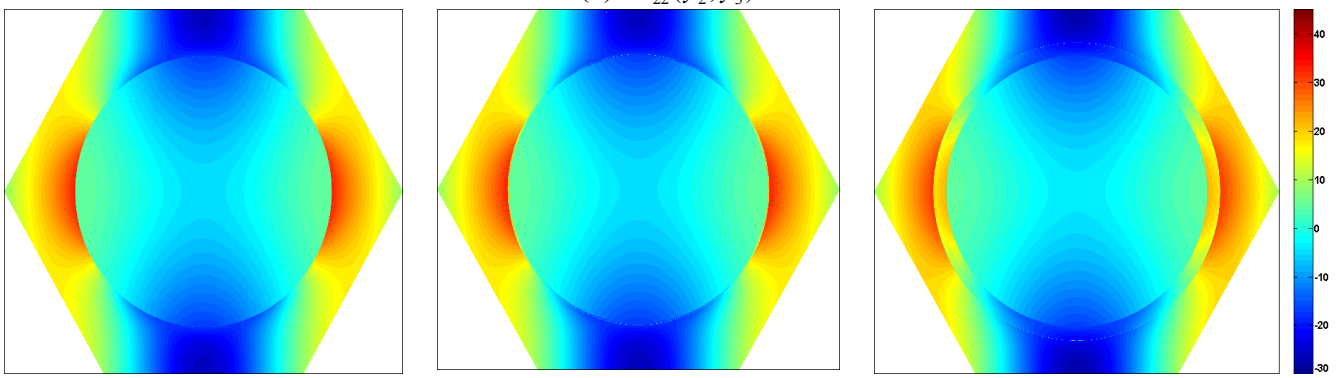

(b) $\sigma_{33}(y_2, y_3)$

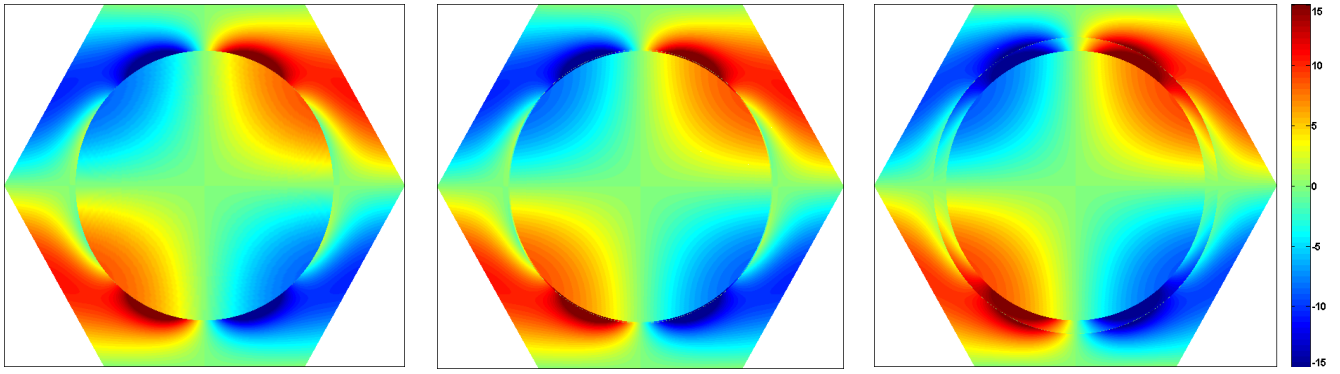

(c) $\sigma_{23}(y_2, y_3)$

Figure 3.14 Converged stress distributions generated with 12 harmonics in a hexagonal unit cell of a graphite/epoxy composite with the fiber volume fraction 0.50 and two coating thicknesses with modulus contrast $E^{(c)} / E^{(m)} = 1.5$ subjected to the unidirectional loading $\overline{\sigma}_{22} \neq 0$ at the applied strain $\overline{\varepsilon}_{22} = 0.01$: (left) $b/a = 1.0$, (middle) $b/a = 1.01$; (right) $b/a = 1.1$.

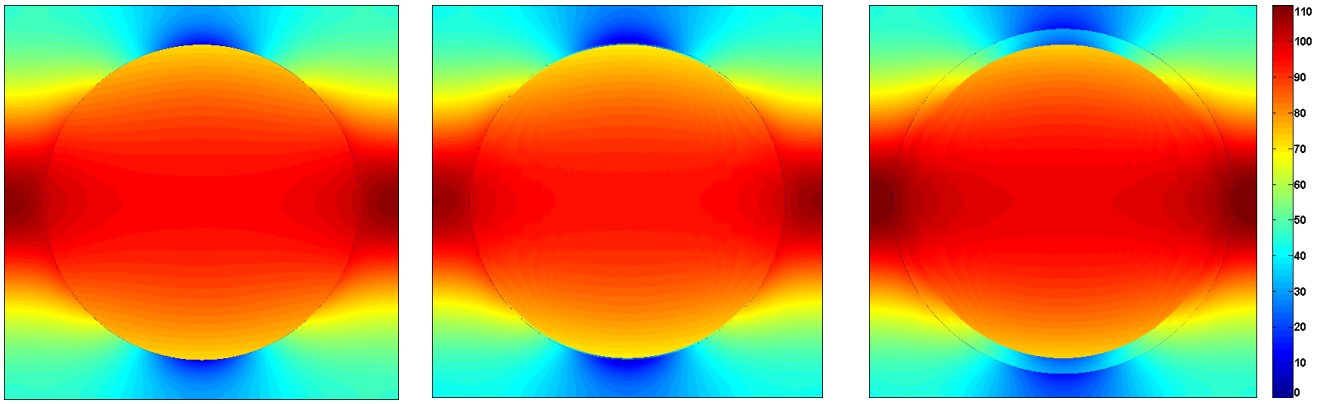

(a) $\sigma_{22}(y_2, y_3)$

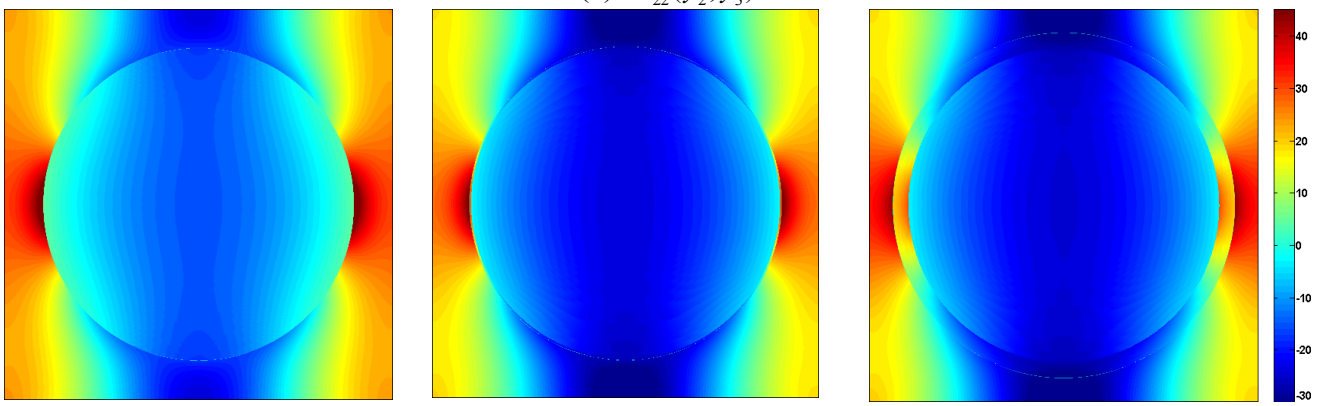

(b) $\sigma_{33}(y_2, y_3)$

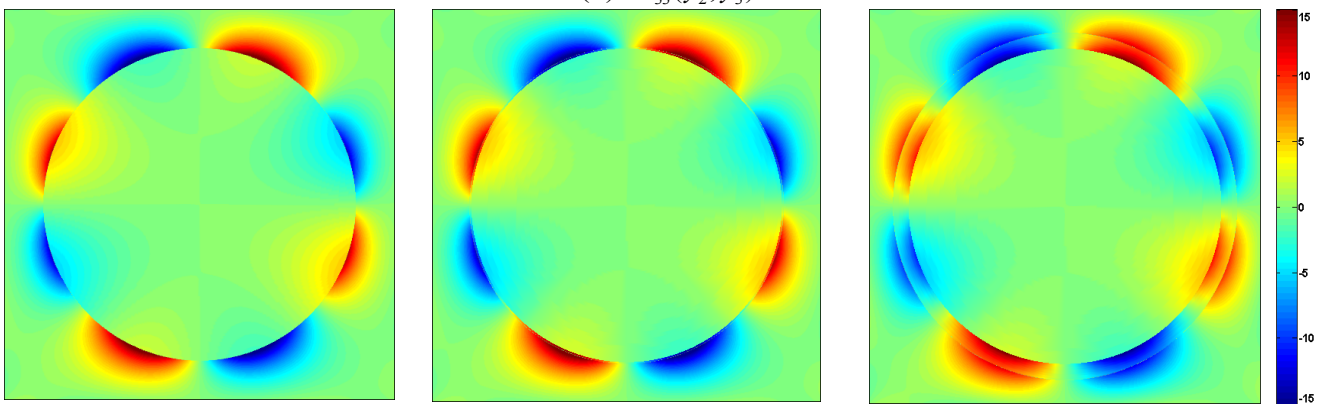

(c) $\sigma_{23}(y_2, y_3)$

Figure 3.15 Converged stress distributions generated with 12 harmonics in a square unit cell of a graphite/epoxy composite with the fiber volume fraction 0.50 and two coating thicknesses with modulus contrast contrast $E^{(c)} / E^{(m)} = 1.5$ subjected to the unidirectional loading $\overline{\sigma}_{22} \neq 0$ at the applied strain $\overline{\varepsilon}_{22} = 0.01$: (left) $b/a = 1.0$, (middle) $b/a = 1.01$; (right) $b/a = 1.1$.

Fig. 3.14 compares the converged stress fields $\sigma_{22}(y_2, y_3)$, $\sigma_{33}(y_2, y_3)$ and $\sigma_{23}(y_2, y_3)$ for hexagonal arrays of uncoated and coated fibers with the smallest and largest coating thickness. Similar stress fields are obtained for the square array (Fig. 3.15), with the higher transverse stress $\sigma_{22}(y_2, y_3)$ in the fiber yielding higher transverse Young's modulus than the hexagonal array for all coating thickness (see Fig. 3.13). These stress fields were generated using 12 harmonics under unidirectional loading by the homogenized stress $\bar{\sigma}_{22} \neq 0$ at the applied strain of $\bar{\varepsilon}_{22} = 0.01$. Unidirectional loading was achieved by adjusting the homogenized strains in Eq. (2.60) to obtain $\bar{\sigma}_{22}$ as the only nonzero homogenized stress. When the coating stiffness is higher than that of the matrix, increasing coating thickness produces greater stress transfer into the fiber for both hexagonal and square geometries for the loading, yielding increasingly greater moduli seen in the convergence study of Fig. 3.13. Comparison of the stress distributions in both arrays without and with the thinnest coating for the given coating/matrix modulus contrast indicates very little difference, suggesting little effect on the homogenized moduli as observed in Fig. 3.13 and further illustrated in next chapter. The locally-exact elasticity solution is sensitive enough to accurately capture the small differences in stress distributions in the presence of very think coatings, highlighting the method's ruggedness. The rapid convergence of both the homogenized moduli and local stress fields sets our method apart from other elasticity-based solutions such as the eigenstrain expansion approach, cf. Caporale et al. (2015), which require substantially greater number of harmonics for converged stress fields.

3.3.3 Comparison with Published Results

The results of an extensive investigation of the impact of interphases or coatings on homogenized moduli of unidirectionally-reinforced composites have been reported by Lagache et al. (1994). The authors employed the finite element method to generate the full set of homogenized moduli of transversely isotropic composites based on a hexagonal array of coated fibers with different coating moduli. The numerical solution was implemented following elements of the 0^{th}-order homogenization theory, including displacement decomposition into average and fluctuating components within generalized plane strain framework, and periodic boundary conditions applied on the faces of a hexagonal unit cell representative of the transversely isotropic composite. Hence the numerical results of Lagache et al. (1994) may be compared directly with the present results based on the same geometry and solution

methodology applied within elasticity, rather than variational, framework.

The results used in the comparison were generated for a unidirectional composite with the fiber volume fraction of 0.50 comprised of isotropic fibers embedded in an isotropic matrix with the elastic moduli: $E^{(f)} = 84\text{GPa}$, $\nu^{(f)} = 0.22$, and $E^{(m)} = 4\text{GPa}$, $\nu^{(m)} = 0.34$. These moduli are representative of a glass/epoxy composite. Four values of the interphase Young's modulus were used, namely 4, 6, 8 and 12 GPa with the Poisson's ratio fixed at $\nu^{(c)} = 0.34$. The fiber radius was 8.5 μm and the coating thickness 1.0 μm with the unit cell dimensions adjusted accordingly.

Homogenization Method	$E_T^*/E^{(m)}$	$E_A^*/E^{(m)}$	$G_T^*/G^{(m)}$	$G_A^*/G^{(m)}$	ν_T^*	ν_A^*	Coating $E^{(c)}$ (GPa)
LEHT	2.66358	11.00460	2.51952	2.69616	0.41647	0.27241	4
PMH	2.68875	11.00475	2.54948	2.71263	0.41321	0.27216	4
LEHT	2.92551	11.06774	2.78403	2.96176	0.40796	0.27216	6
PMH	2.91120	11.05735	2.77514	2.93674	0.40569	0.27191	6
LEHT	3.08409	11.13087	2.94736	3.11810	0.40203	0.27210	8
PMH	3.04255	11.10993	2.91075	3.06545	0.40067	0.27184	8
LEHT	3.26772	11.25710	3.13934	3.29485	0.39468	0.27217	12
PMH	3.19163	11.21508	3.06666	3.20829	0.39461	0.27187	12

Table 3.7 Comparison of selected homogenized moduli predicted by the locally-exact homogenization theory with the PMH model (Lagache et al., 1994) for coated fiber unidirectional composite with different coating moduli.

Table 3.7 presents comparison of the finite-element calculations and the present theory for the whole set of homogenized moduli normalized by the corresponding matrix moduli. However, three of them: $E_T^*/E^{(m)}$, $G_T^*/G^{(m)}$ and $G_A^*/G^{(m)}$ are more sensitive to changes in the coating's stiffness than the axial Young's modulus E_A^* and axial and transverse Poisson's ratios ν_A^* and ν_T^*. Overall, the results in Table 3.7 are seen to agree to one significant digit, whereas the axial and transverse Poisson's ratios differ only in the third decimal place. We note that when $E^{(c)} = 4\text{GPa}$, that is when the matrix and coating moduli are the same, we recover the results for the uncoated fiber composite. For this case, the moduli produced by the present method have been shown by Wang and Pindera (2015) to be accurate to 4 significant digits at the fiber volume fraction of 0.50 upon comparison with the results of Helsing (1995), often employed as a gold standard, which were generated using an integral equation method. In the present case, the

discrepancy is likely due to a relatively coarse discretization of both the matrix and the coating, with the coating discretized into a double-layer triangular element mesh as a compromise between efficiency and accuracy. The recent finite-element results of Sideridis et al. (2015) suggest that a larger number of elements is needed for fully converged results. Out results for the transverse Young's modulus E_T^* also compare favorably with those of Mogilevskaya et al. (2010) (reported in Table 1 of this reference in a different form) which were generated using the authors' elasticity-based equivalent inhomogeneity method under plain strain constraint.

We also compare our results with those of Sevostianov et al. (2012) based on the complex potential representation of displacement and stress fields in an infinite series form for a square array of isotropic fibers coated by a very thin interphase layer such that $b-a=0.001$. The fiber, coating and matrix moduli for this system are $E^{(f)}=24\text{GPa}$, $\nu^{(f)}=0.20$; $E^{(c)}=3.03\text{GPa}$, $\nu^{(c)}=0.50$ and $E^{(m)}=2.7\text{GPa}$, $\nu^{(m)}=0.35$. Table 3.8 presents comparison of the normalized homogenized transverse shear modulus $G_T^*/G^{(m)}$ in a wide fiber volume range predicted by the two analytical methods, showing very good agreement to within graphical resolution accuracy of the Sevostianov et al. data for this computationally demanding case.

v_f	0.10	0.20	0.30	0.40	0.50	0.60	0.70	0.75
LEHT	1.139	1.287	1.455	1.662	1.939	2.353	3.109	3.852
Sevostianov et al.	1.142	1.293	1.461	1.671	1.948	2.360	3.129	3.817

Table 3.8 Comparison of the normalized homogenized transverse shear modulus $G_T^*/G^{(m)}$ predicted by the locally exact homogenization theory with the three-phase square array calculations of Sevostianov et al. (2012) for unidirectional composite with a very thin fiber coating.

3.3 Validation for Composites with Cylindrically Orthotropic Fibers

We validate the developed solution by first showing that in the limit as the fiber volume fraction becomes very small, the results of Eshelby (1957) are recovered regardless of the number of terms employed in the displacement field representation in the fiber and matrix phases. This also demonstrates the solution's stability with increasing number of harmonics. First, we take the radial Young's modulus to be about twenty-eight times stiffer relative to the circumferential modulus, and then we reverse this ratio, see Table 3.9 for the remaining moduli.

These engineering moduli were calculated using the stiffness matrix coefficients of experimentally determined single crystal graphite arranged in radial and circumferential patterns considered by Christensen (1994).

Moduli	$C_{rr}/C_{\theta\theta}>1$	$C_{rr}/C_{\theta\theta}<1$
E_{zz}(MPa)	1,025,161	1,025,161
E_{rr}(MPa)	1,025,161	36,137
$E_{\theta\theta}$(MPa)	36,137	1,025,161
$\mu_{r\theta}$(MPa)	4,500	4,500
μ_{zr}(MPa)	440,000	4,500
$\mu_{z\theta}$(MPa)	4,500	440,000
$\nu_{r\theta}$	0.3432	0.0121
ν_{zr}	0.1649	0.3432
$\nu_{z\theta}$	0.3432	0.1649

Table 3.9 Elastic moduli of radially and circumferentially orthotropic graphite fibers based on single crystal graphite data reported in Christensen, (1994).

Moduli	$C_{rr}/C_{\theta\theta}>1$	$C_{rr}/C_{\theta\theta}<1$
E_A(MPa)	1,014,171	1,014,171
E_T(MPa)	79,611	42,400
μ_T(MPa)	24,600	11,800
μ_A(MPa)	44,497	44,497
ν_T	0.6181	0.7966
ν_A	0.1928	0.1928

Table 3.10 Effective transversely isotropic elastic moduli of graphite fibers based on data in Table 3.9 and equations provided by Christensen, (1994).

Subsequently, we study the convergence of the homogenized moduli as a function of the number of harmonic terms for a non-dilute fiber volume fraction with the two $E_{rr}/E_{\theta\theta}$ ratios. Included in the results are homogenized moduli based on equivalent transversely isotropic fiber moduli calculated using the formula developed by Christensen, (1994). The homogenized engineering moduli were calculated using the homogenized compliance matrix obtained from the inverse of the homogenized stiffness matrix established in Eq. (2.64), $\mathbf{S}^* = [\mathbf{C}^*]^{-1}$, as described

in Wang and Pindera (2015). We also show later that regardless of the $E_{rr}/E_{\theta\theta}$ ratio the homogenized stiffness matrix $\mathbf{C}^*$ for the graphite/epoxy composite with cylindrically orthotropic fibers is characteristic of a transversely isotropic composite with the plane of isotropy normal to the fiber direction that satisfies the relation $C_{44} = (C_{22} - C_{23})/2$.

3.3.1 Hill-Mandell Energy Equivalence

The Hill-Mandell energy equivalence can be expressed as

$$\frac{1}{V}\int_V \sigma_{ij}\varepsilon_{ij}dV = \bar{\sigma}_{ij}\bar{\varepsilon}_{ij} \tag{3.3}$$

in which local stress and strain distributions on the left side of the equation, for both fiber and matrix, can be obtained by applying macroscopic strain on the right side. Numerical results (Tables 3.11-3.12) are shown to prove the validity of the theory. Fiber volume fractions of 65% and 25% are employed to cover a wider range of fiber content, and the material properties are listed in Table 3.9.

C-O	$\bar{\varepsilon}_{11}$	$\bar{\varepsilon}_{22}$	$\bar{\varepsilon}_{33}$	$2\bar{\varepsilon}_{23}$	$2\bar{\varepsilon}_{12}$	$2\bar{\varepsilon}_{13}$	**Sum**/V
Left	324.4292	8.2994	8.2975	7.3273	10.5535	10.5501	76.4412
Right	324.4293	8.3015	8.2994	7.3287	10.5562	10.5572	76.4444

R-O	$\bar{\varepsilon}_{11}$	$\bar{\varepsilon}_{22}$	$\bar{\varepsilon}_{33}$	$2\bar{\varepsilon}_{23}$	$2\bar{\varepsilon}_{12}$	$2\bar{\varepsilon}_{13}$	**Sum**/V
Left	324.4296	8.7596	8.7582	9.1609	10.5535	10.5501	77.0112
Right	324.4296	8.7596	8.7582	9.1671	10.5516	10.5501	77.0121

Table 3.11 Numerical comparison of Hill-Mandel energy equivalence between left side and right side of the equation for both circumferentially and radially orthotropic fibers with the fiber volume fraction $V_f = 0.65$.

C-O	$\bar{\varepsilon}_{11}$	$\bar{\varepsilon}_{22}$	$\bar{\varepsilon}_{33}$	$2\bar{\varepsilon}_{23}$	$2\bar{\varepsilon}_{12}$	$2\bar{\varepsilon}_{13}$	**Sum**/V
Left	328.3878	9.9249	9.9253	9.2121	10.5358	10.5353	30.1218
Right	328.3878	9.9221	9.9240	9.2101	10.5337	10.5304	30.1207

R-O	$\bar{\varepsilon}_{11}$	$\bar{\varepsilon}_{22}$	$\bar{\varepsilon}_{33}$	$2\bar{\varepsilon}_{23}$	$2\bar{\varepsilon}_{12}$	$2\bar{\varepsilon}_{13}$	**Sum**/V
Left	328.3877	10.0075	10.0082	9.5431	10.5358	10.5352	30.1613
Right	328.3877	10.0057	10.0051	9.5448	10.5325	10.5346	30.1607

Table 3.12 Numerical comparison of Hill-Mandel energy equivalence between left side and right side of the equation for both circumferentially and radially orthotropic fibers with the fiber volume fraction $V_f = 0.25$.

As we can observe in the Tables 3.11 – 3.12, each column stands for the energy calculations for both left side and right side of the equation by apply the corresponding individual strain, while the last column means the average energy (total energy divided by volume) as shown in the Eq. (3.3). At least second decimal places are well matched for both individual and total energy calculations, which is sufficient to provide the proof and confidence.

3.3.2 Stability of the Solution for the Dilute Case

To demonstrate the solution's stability and reduction to known solutions, we subject a hexagonal unit cell with the fiber volume fraction of 0.2% to uniaxial loading by $\bar{\sigma}_{22} = 100\text{MPa}$ with the remaining stresses zero. The material system is graphite/epoxy with the fiber moduli given in the Table 3.9 and the epoxy matrix taken as isotropic with the Young's modulus $E = 3.5\text{GPa}$ and Poisson's ratio $\nu = 0.35$. The solutions were generated using an increasing number of harmonics from $n = 2$, which corresponds to the Eshelby solution as the fiber volume fraction tends to zeros, to $n = 16$. The inplane stresses $\sigma_{22}(y_2, y_3)$, $\sigma_{33}(y_2, y_3)$ and $\sigma_{23}(y_2, y_3)$ obtained from the locally-exact solution remain stable as the number of harmonics is increased to $n = 16$. Comparison with the Eshelby solution is very favorable. This is illustrated in Fig. 3.16 for the transverse normal stress field $\sigma_{22}(y_2, y_3)$ generated with the locally-exact theory using $n = 12$ where the stress distributions in the matrix and cylindrically orthotropic fibers with modulus ratios $E_{rr}/E_{\theta\theta} = 28.37$ and $1/28.37$ are illustrated separately. The stress distributions in the matrix have been plotted in the square region in the vicinity of the fiber with the hexagonal boundaries far outside this region. In the matrix region, the stress field is unaffected by the cylindrical orthotropy type, with the same distributions obtained for both the radially ($E_{rr}/E_{\theta\theta} = 28.37$) and circumferentially ($E_{rr}/E_{\theta\theta} = 1/28.37$) orthotropic fibers, Fig. 3.16a. In contrast, the cylindrically orthotropy type affects the fiber stress distributions dramatically, producing a singular value at the fiber's center for radially orthotropic fibers, Fig. 3.16b, and a finite value for circumferentially orthotropic fibers, Fig. 3.16c. No discernible differences are observed between the locally-exact and Eshelby solutions. Moreover, examination of the leading coefficients $F_{01}^{(f)}, F_{22}^{(f)}$ as a function of harmonics vis-à-vis those of the Eshelby solution indicates insignificant differences, with the higher-order coefficients practically zeros.

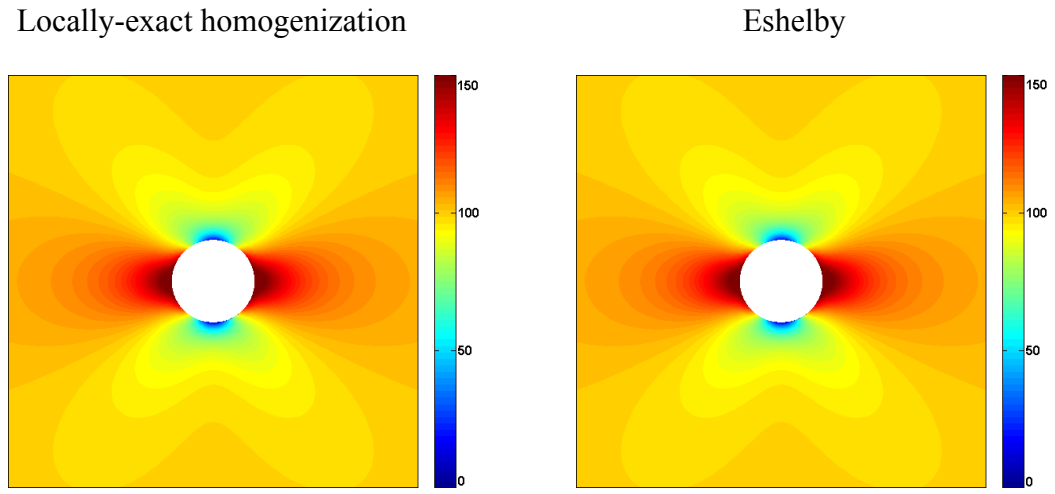

(a) matrix only

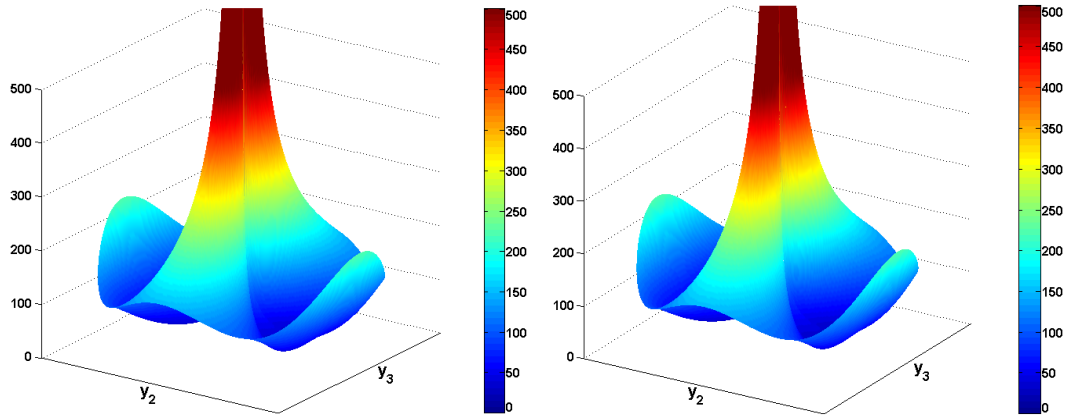

(b) radially orthotropic fiber only with $E_{rr}/E_{\theta\theta} \approx 28$

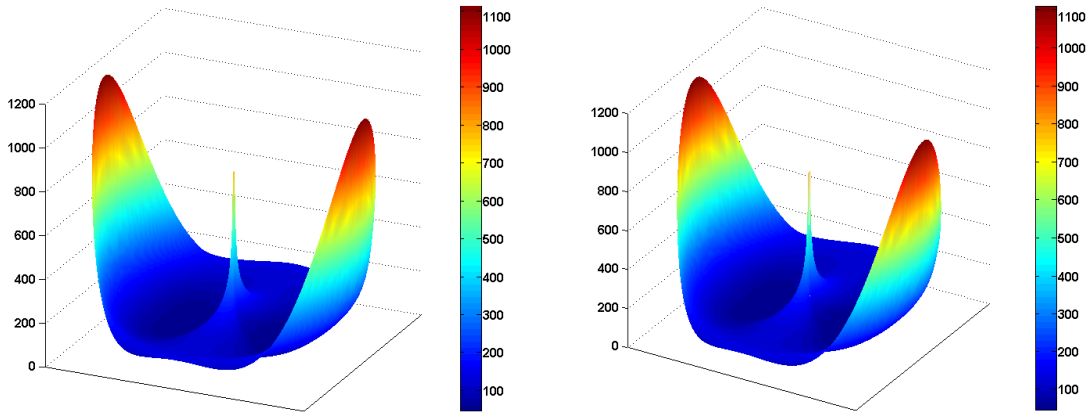

(c) circumferentialy orthotropic fiber only with $E_{rr}/E_{\theta\theta} \approx 1/28$

Figure 3.16 Comparison of converged stress distributions $\sigma_{22}(y_2, y_3)$ in a hexagonal unit cell with a dilute fiber volume fraction subjected to uniaxial loading by $\bar{\sigma}_{22} \neq 0$ only generated using 12 harmonics.

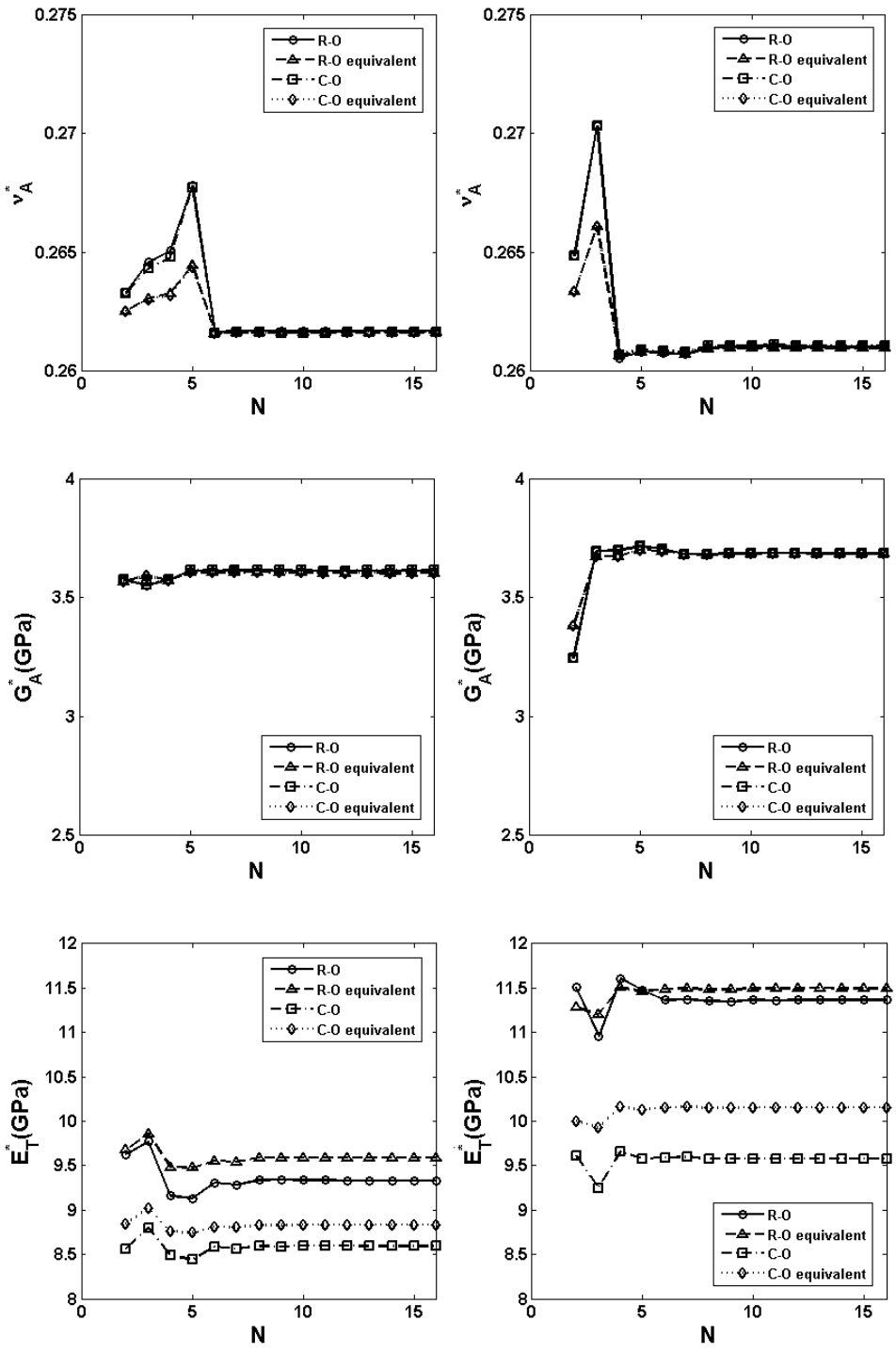

Hexagonal array Square array

Figure 3.17 Convergence of selected homogenized moduli with the number of harmonics for a graphite/epoxy composite with the fiber volume fraction 0.50 and modulus ratio $E_{rr}/E_{\theta\theta}$ as a parameter.

3.3.2 Convergence Study

Next, we consider a hexagonal unit cell representative of graphite/epoxy composites with the non-dilute fiber volume fraction $v_f = 0.50$, and investigate convergence of the homogenized moduli as a function of the harmonic number for the two fiber orthotropy ratios $E_{rr}/E_{\theta\theta}$, as well as the equivalent transversely isotropic properties. Figure 3.17 illustrates convergence behavior of the homogenized axial Poisson's ratio v_A^*, axial shear modulus G_A^* and transverse Young's modulus E_T^* for hexagonal and square unit cell architectures at the fiber volume fraction of 0.50. Convergence is rapid for the three moduli of both array types, attained with typically fewer than eight harmonics. While the axisymmetric (E_A^*, v_A^* and k_T^*) and axial shear moduli converge to the same values for both cylindrical orthotropy types, the homogenized moduli associated with transverse non-asymmetric loading (E_T^*, v_T^* and G_T^*) converge to values that depend on the orthotropy type. Regardless of the orthotropy type, the convergence is also rapid in these cases, and similar to that observed for E_T^* in Fig. 3.17. The differences in the converged moduli due to array type are most pronounced for the transverse Young's modulus E_T^*.

3.3.3 Applicability of the Fiber Moduli Replacement Scheme

In this section we first compare homogenized moduli of radially and circumferentially orthotropic fiber composites generated as a function of fiber volume fraction using the locally-exact theory with those of obtained from the composite cylinder assemblage (CCA) model based on equivalent transversely isotropic properties of cylindrically orthotropic graphite fibers. Hashin (1990) provides four of five equivalent transversely isotropic moduli for cylindrically orthotropic fibers employed in the calculation of composite homogenized moduli under axisymmetric and axial shear loading. Christensen (1994) provides formula for all five equivalent fiber homogenized moduli which, however, are not used in the calculation of homogenized moduli. Both authors used an energy-based replacement scheme for cylindrically orthotropic fibers by the corresponding transversely isotropic moduli that produce the same energy in the fiber under boundary conditions used to determine the particular modulus. The five transversely isotropic moduli are $E_A^{(f)}$, $\nu_A^{(f)}$, $k_T^{(f)}$, $\mu_A^{(f)}$ and $\mu_T^{(f)}$. Closed-form expressions

for the first four moduli were obtained in terms of the cylindrically orthotropic moduli listed by Christensen (1994) as follows,

$$E_A = C_{zz} - \frac{(2+\sqrt{\alpha})C_{\theta z}^2 + 2\sqrt{\alpha}C_{\theta z}C_{zr} + (2\alpha+\sqrt{\alpha})C_{zr}^2}{(\sqrt{\alpha}+1)^2(\sqrt{\alpha}C_{rr}+C_{r\theta})} - \frac{C_{r\theta}(C_{\theta z}-C_{zr})^2}{(\sqrt{\alpha}+1)^2 C_{rr}(\sqrt{\alpha}C_{rr}+C_{r\theta})}$$

$$\nu_A = \frac{C_{\theta z}+\sqrt{\alpha}C_{zr}}{(\sqrt{\alpha}+1)(\sqrt{\alpha}C_{rr}+C_{r\theta})}$$

$$K_T^f = \frac{1}{2}(\sqrt{C_{rr}C_{\theta\theta}}+C_{r\theta})$$

$$\mu_A = \sqrt{\mu_{zr}\mu_{z\theta}} \tag{3.4}$$

where $\alpha = \sqrt{C_{\theta\theta}/C_{rr}}$. The equivalent transverse shear modulus $\mu_T^{(f)}$ is obtained from the solution of a quadratic equation from the associated self-consistent scheme

$$\mu_T^2 + \beta\mu_T + \gamma = 0 \tag{3.5}$$

where the lengthy parameters β are γ are given by Christensen (1994). The expressions in two extreme conditions, in which the contrasts between cylindrical and circumferential properties become huge, are

$$\mu_T^{R-O} \to \frac{1}{2}\sqrt{\frac{C_{rr}C_{\theta\theta}}{1+4C_{\theta\theta}/\mu_{r\theta}}} \qquad \frac{C_{\theta\theta}}{C_{rr}} : \frac{C_{r\theta}}{C_{rr}} : \frac{\mu_{r\theta}}{C_{rr}} = 0(\varepsilon)$$

$$\mu_T^{C-O} \to \frac{1}{2}\left[1+(1+4\frac{C_{rr}}{\mu_{r\theta}})^{1/2}\right]\mu_{r\theta} \qquad \frac{C_{rr}}{C_{\theta\theta}} : \frac{C_{r\theta}}{C_{\theta\theta}} : \frac{\mu_{r\theta}}{C_{\theta\theta}} = 0(\varepsilon) \tag{3.6}$$

Christensen also provides asymptotic closed-form expressions for the equivalent transversely shear moduli of radially and circumferentially orthotropic fiber with large moduli contrasts which, however, exhibit very slow convergence. Hence the equivalent transversely isotropic moduli of radially and circumferentially orthotropic graphite fibers reported in Table 3.10 were obtained using the above equations. We also use these equivalent transversely isotropic fiber moduli in the locally-exact homogenization theory to calculate the resulting composite homogenized moduli as a function of fiber volume fraction for comparison with the calculations that explicitly account for the cylindrical orthotropy of graphite fibers.

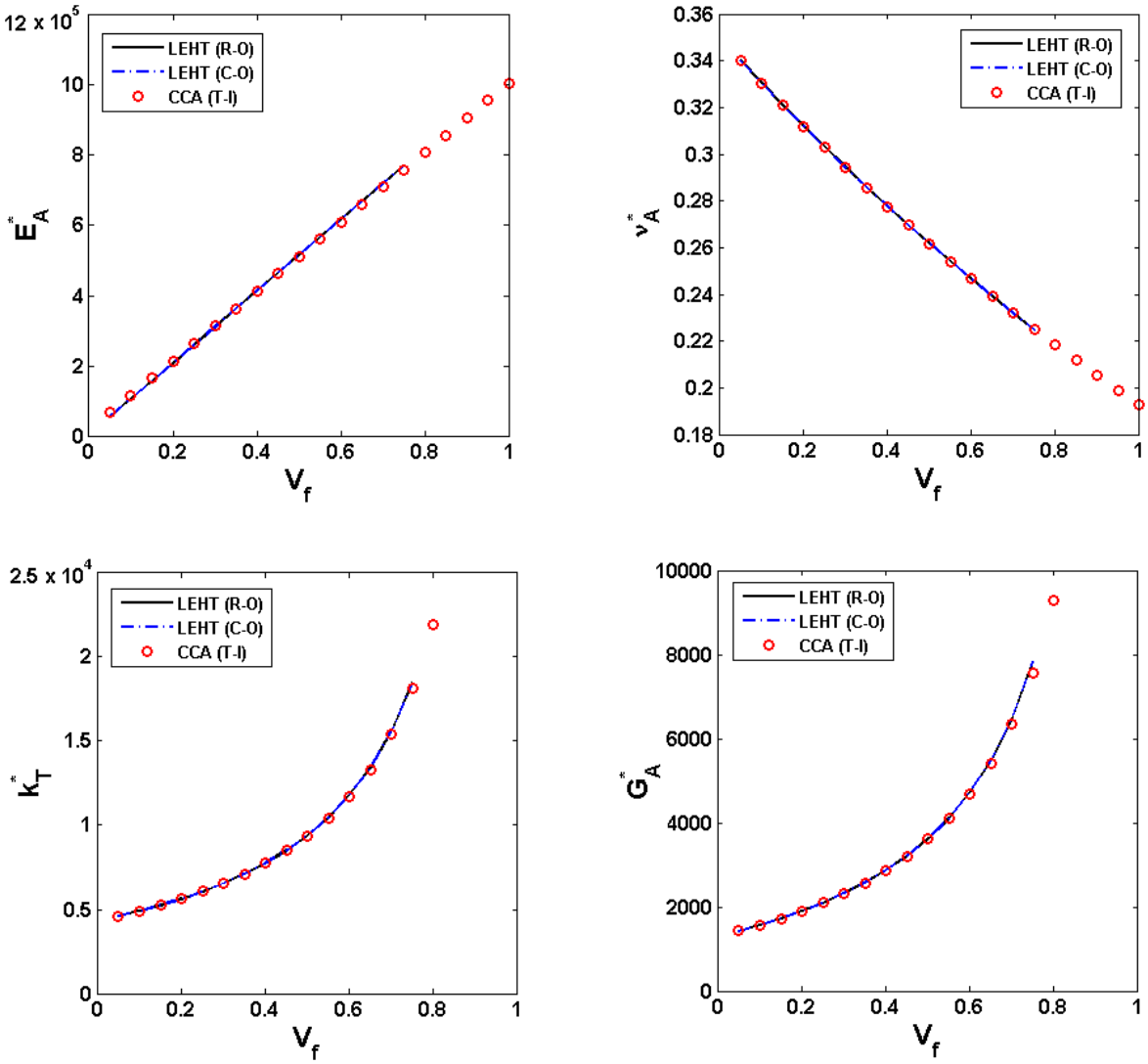

Figure 3.18 Comparison of homogenized moduli of a unidirectional graphite/epoxy composite with cylindrically orthotropic (both radially and circumferentially orthotropic) fibers predicted by the locally-exact theory and Hashin's CCA model based on equivalent transversely isotropic fiber moduli.

Figure 3.18 illustrates comparison of four of the five homogenized moduli of a unidirectional graphite/epoxy composite comprised of radially and circumferentially orthotropic fibers with elastic moduli given in Table 3.9 predicted by the locally-exact theory and Hashin's CCA moduli based on equivalent transversely isotropic fiber moduli given in Table 3.10. The same homogenized moduli are obtained from the locally-exact homogenization theory for both radially and circumferentially orthotropic fibers under axisymmetric and axial shear loading. As will be shown in the sequel, these moduli are also the same as the corresponding moduli obtained using the equivalent transversely isotropic fiber moduli. Moreover, practically no differences are observed between moduli generated under axisymmetric loading, namely E_A^*, ν_A^* and k_T^*, as well as under axial shear loading, μ_A^* or G_A^*, by the two homogenization approaches despite differences in the microstructural representation of the unidirectional composite. This remarkable result is rooted in the small differences in the stress fields in the matrix phase of both models and similar values of the average fiber stresses under axisymmetric and axial shear loading despite the absence of explicit adjacent fiber interactions in the CCA model. Figure 3.19 illustrates this point for the homogenized axial shear modulus μ_A^* through comparison of the axial shear stress fields in the hexagonal unit cell and the CCA model containing the same fiber volume fraction and subjected to pure shear loading by $\bar{\sigma}_{12} \neq 0$. Radially orthotropic fiber moduli were used in the locally-exact theory calculations. A higher fiber volume fraction was used for comparison to highlight the effect of adjacent fiber interaction, namely $\nu^{(f)} = 0.65$. Comparable axial shear stress distributions are observed throughout the matrix phase of both the hexagonal unit cell that accounts for adjacent fiber interaction through the periodicity conditions, and in the matrix phase of the CCA model. Given comparable average axial shear stresses in the fiber phases of the hexagonal unit cell and the CCA model, comparable homogenized axial shear moduli are obtained as observed in Fig. 3.18.

Figure 3.20 illustrates results for the homogenized plane strain bulk, axial and transverse shear moduli generated solely with the locally-exact homogenization theory using both radially and circumferentially orthotropic fiber moduli taken from Table 3.9 and their transversely isotropic counterparts from Table 3.10. No differences are observed between the homogenized axisymmetric and axial shear moduli obtained from the four sets of cylindrically orthotropic fiber moduli and their transversely isotropic equivalents. In the case of the homogenized

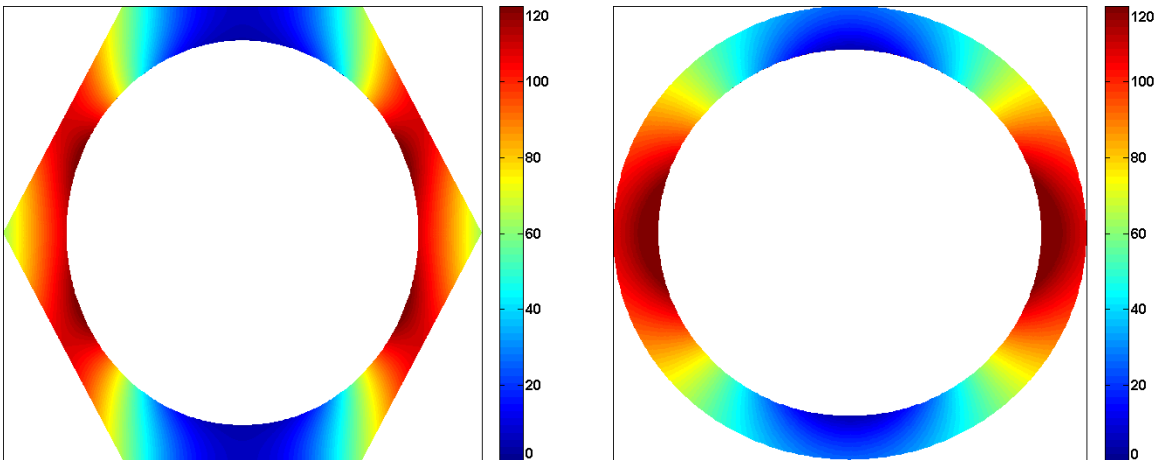

(a) $\sigma_{12}(y_2, y_3)$

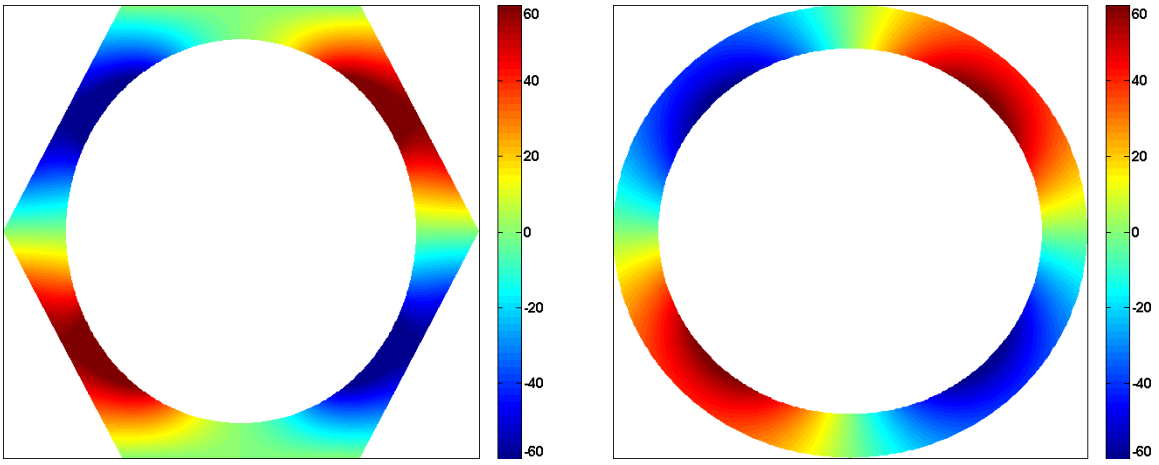

(b) $\sigma_{13}(y_2, y_3)$

Figure 3.19 Comparison of stress fields in the matrix phase of the hexagonal unit cell with a radially orthotropic fiber and the CCA model with an equivalent transversely isotropic fiber of a unidirectional composite with the fiber volume fraction $v_f = 0.65$ under pure axial shear loading by $\bar{\sigma}_{12} \neq 0$ at the applied axial shear strain of $\bar{\varepsilon}_{12} = 0.01$. Color bar in MPa.

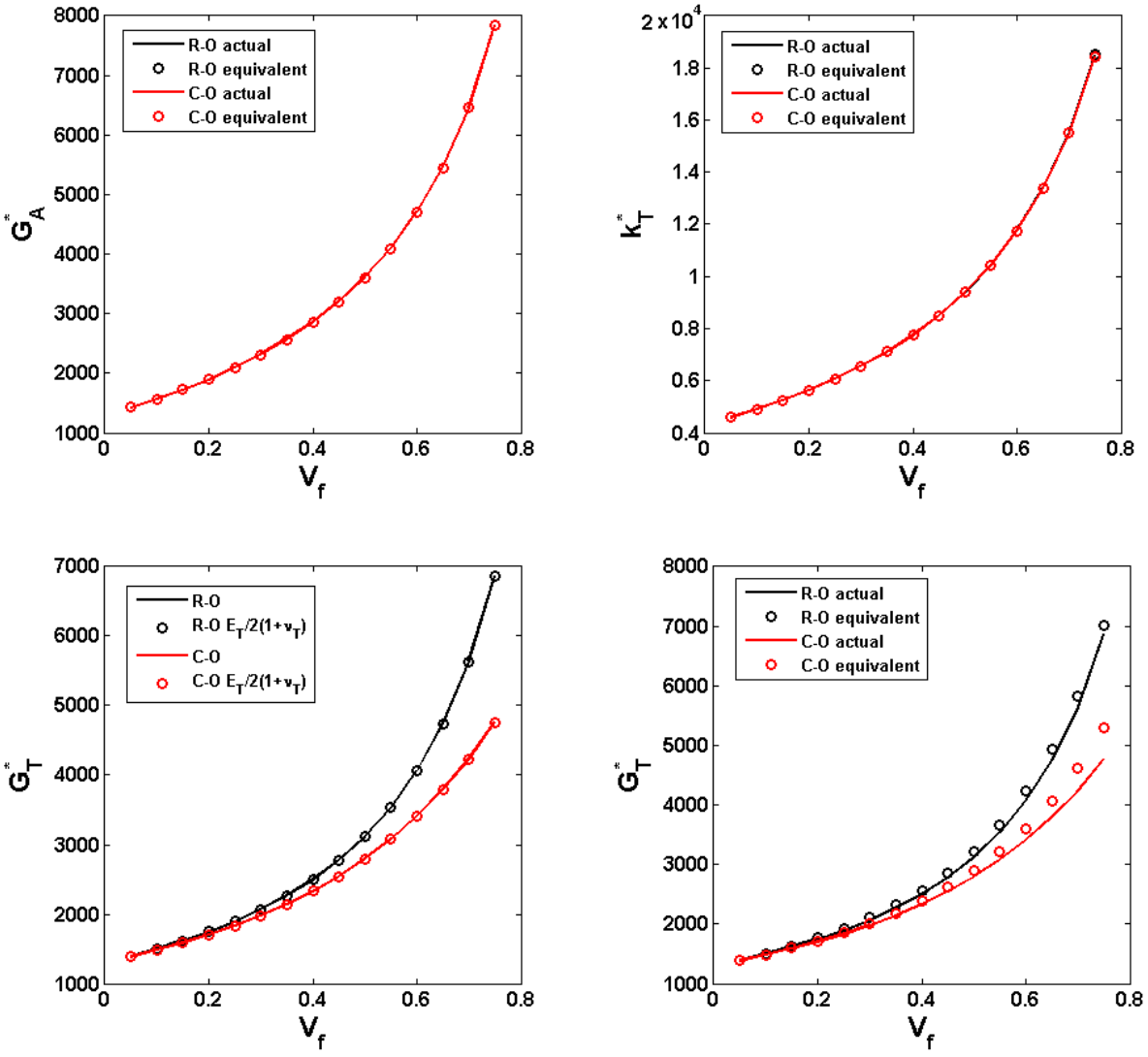

Figure 3.20 Transverse shear moduli predicted by the locally-exact theory based on cylindrically orthotropic graphite fibers: verification of transverse isotropy retention (left), and comparison with predictions based on equivalent transversely isotropic graphite fiber moduli (right).

transverse shear modulus μ_T^* or G_T^*, differences are expected and observed between the predictions based on radially and circumferentially orthotropic moduli, with the radially orthotropic fibers yielding noticeable greater homogenized transverse moduli than the circumferentially orthotropic fibers at large fiber volume fractions. An additional check on the correctness of the results is provided by comparing the homogenized transverse shear moduli obtained from the direct calculation with the results based on the transversely isotropic relation $G_T^* = E_T^* / 2(1+\nu_T^*)$. These results are included in Fig. 3.20 with no differences observed. Moreover, the homogenized transverse shear moduli based on cylindrically orthotropic fiber moduli are somewhat more compliant than the corresponding moduli based on the transversely isotropic fiber counterparts taken from Table 3.10, with greater differences observed for the circumferentially orthotropic fibers at larger fiber volume fractions.

The differences in the homogenized transverse shear moduli are rooted in the matrix and fiber transverse shear stress fields under pure shear loading by $\bar{\varepsilon}_{23} = 0.01$ shown in Figs. 3.21 and 3.22, respectively, for both radially and circumferentially orthotropic fibers and their transversely isotropic equivalents. The distributions were generated for a hexagonal unit cell with the fiber volume fraction of $\nu^{(f)} = 0.65$ where noticeable differences in the homogenized transverse shear moduli are observed. The average matrix and fiber transverse shear stresses calculated from these distributions are listed in Table 3.13 and reflect the differences in the homogenized transverse shear moduli based on the four sets of cylindrically orthotropic fiber moduli. Included in the table are the corresponding results for both $\nu^{(f)} = 0.10$ and $\nu^{(f)} = 0.65$ where little differences in the homogenized transverse shear moduli are observed based on the four sets of fiber moduli.

	$\nu_f = 0.10$				$\nu_f = 0.65$			
	RO → TI		CO → TI		RO → TI		CO → TI	
Fiber (MPa)	44.16	44.93	42.45	43.03	113.77	117.99	88.25	95.83
Matrix (MPa)	28.44	28.54	28.20	28.28	59.55	62.52	52.70	54.52

Table 3.13 Average transverse shear stresses in the fiber and matrix phases of a hexagonal unit cell under pure transverse shear loading.

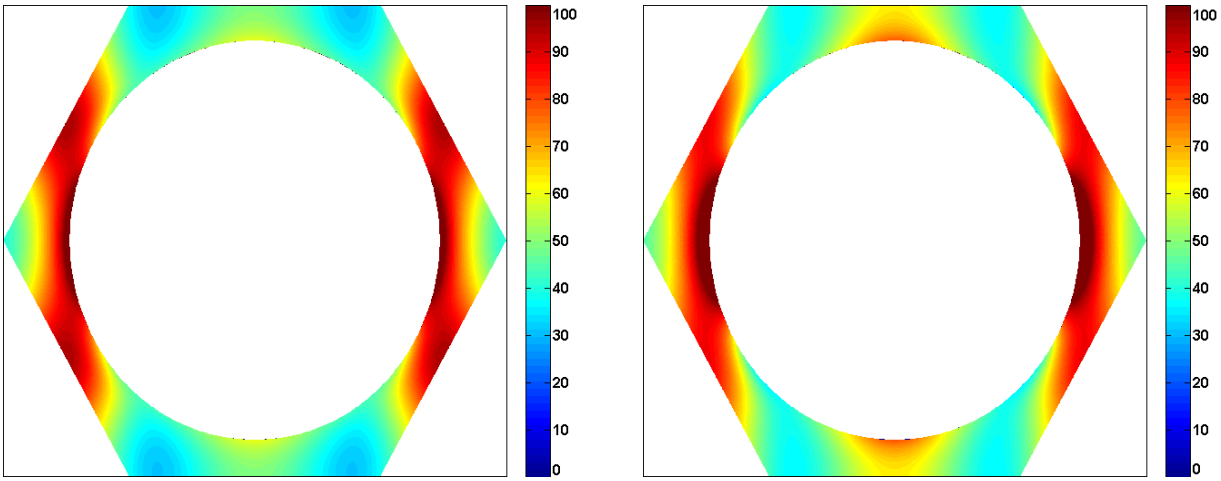

(a) Radially orthotropic fiber and transversely isotropic equivalent

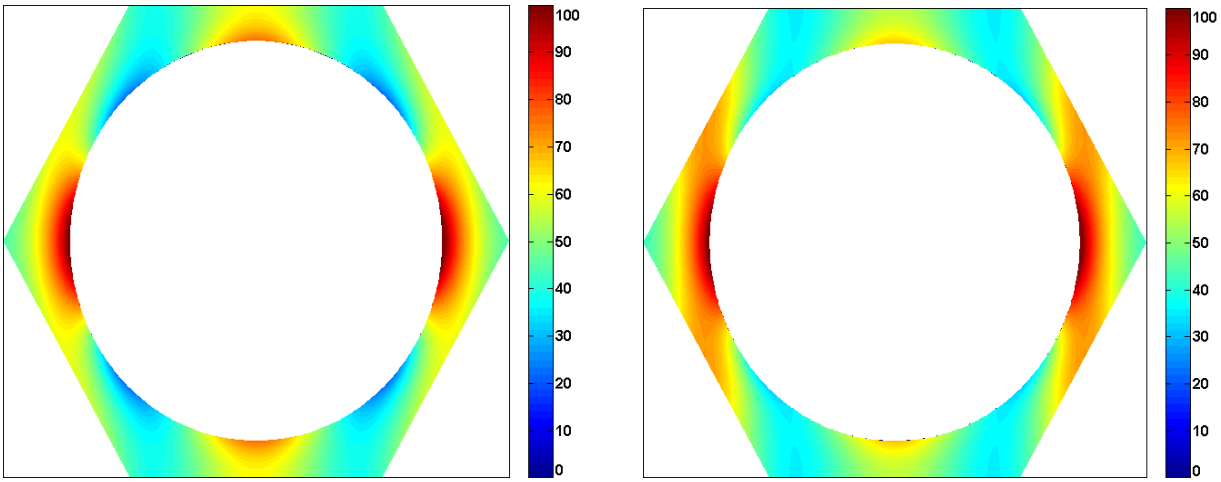

(b) Circumferentially orthotropic fiber and transversely isotropic equivalent

Figure 3.21 Matrix transverse shear stress fields $\sigma_{23}(y_2, y_3)$ predicted by the locally-exact theory based on cylindrically orthotropic graphite fibers (left) and their transversely isotropic equivalents (right) in a unidirectional composite with the fiber volume fraction $v^{(f)} = 0.65$ under pure transverse shear loading by $\bar{\sigma}_{23} \neq 0$ at the applied transverse shear strain of $\bar{\varepsilon}_{23} = 0.01$. Color bar in MPa.

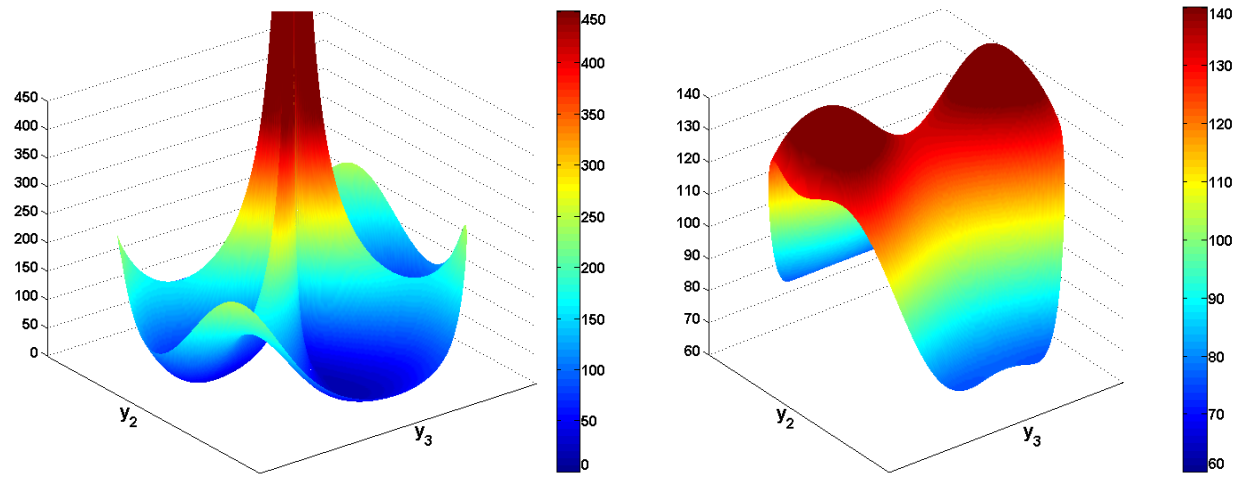

(a) Radially orthotropic fiber and transversely isotropic equivalent

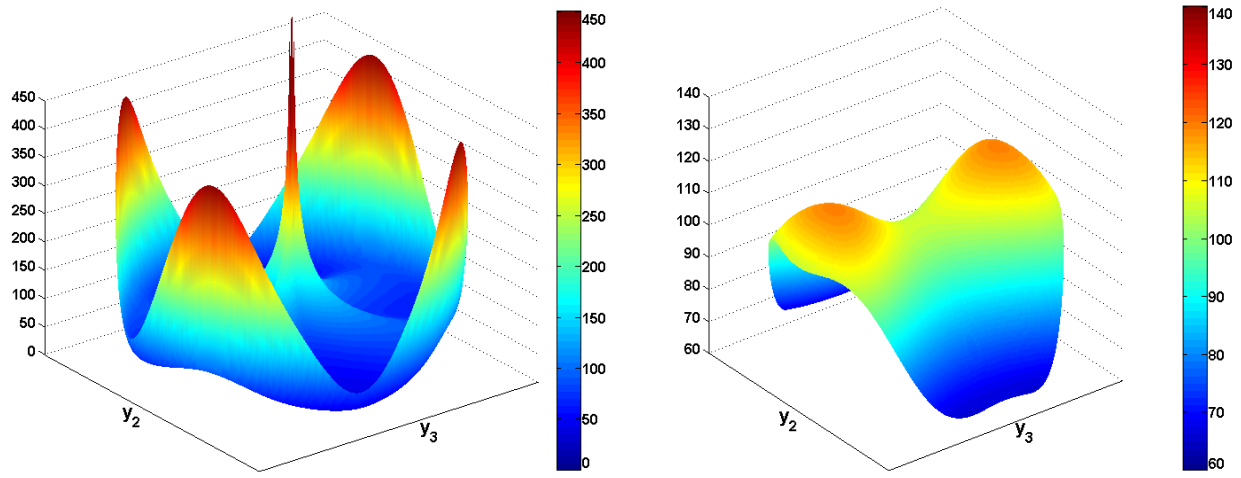

(b) Circumferentially orthotropic fiber and transversely isotropic equivalent

Figure 3.22 Fiber transverse shear stress fields $\sigma_{23}(y_2, y_3)$ predicted by the locally-exact theory based on cylindrically orthotropic graphite fibers (left) and their transversely isotropic equivalents (right) in a unidirectional composite with the fiber volume fraction $v^{(f)} = 0.65$ under pure transverse shear loading by $\bar{\sigma}_{23} \neq 0$ at the applied transverse shear strain of $\bar{\varepsilon}_{23} = 0.01$. Color bar in MPa.

Finally, we demonstrate the effect of fiber array on the homogenized moduli of cylindrically orthotropic fiber unidirectional composites. Figure 3.23 presents comparison of G_A^*, G_T^*, E_T^* and ν_T^* moduli of hexagonal and square arrays of radially and circumferentially orthotropic graphite fibers generated using the locally-exact homogenization theory. The axial moduli E_A^* and ν_A^* are not included as the effect of fiber array type is minimal in this case.

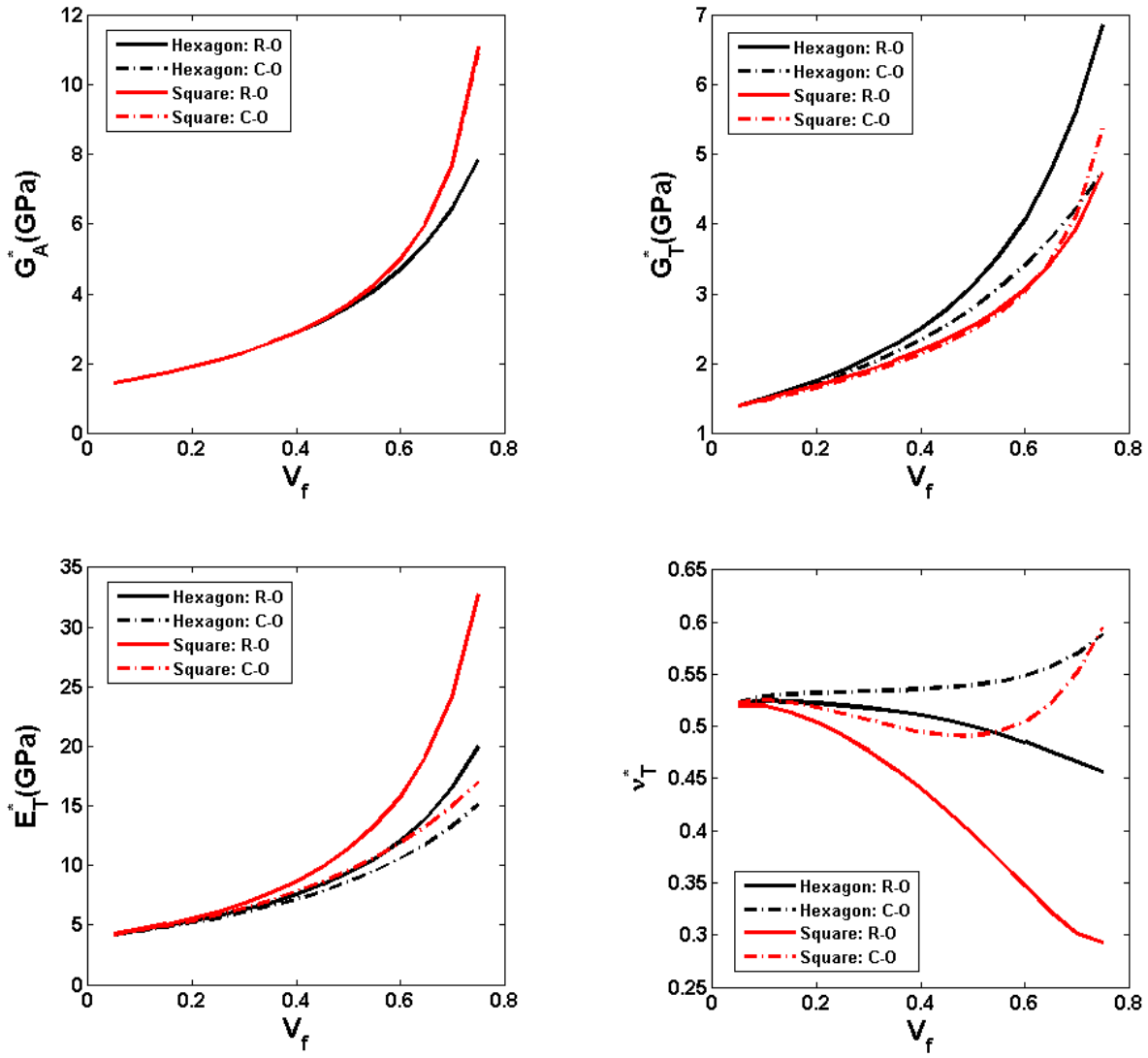

Figure 3.23 Comparison of homogenized moduli of hexagonal and square arrays predicted by the locally-exact theory.

3.4 Remarks

The convergence study of both two-phase (fiber/matrix) and three-phase (fiber/coating/matrix) unidirectional composites has been firstly studied and compared with other classical theories, by covering a wide range of fiber volume fractions. The theory has been validated for different microstructural array types and material constituents, which proves the robustness of the LEHT against other micromechanics models. Some extreme cases are employed to show the advantage of the present theory. For instance, the converged homogenized moduli and stress distributions of three-phase composites with very thin coatings are generated to compare with the ones without any coatings.

Also, the extension of the locally exact homogenization theory to accommodate cylindrically orthotropic fibers in periodic unidirectional composites with hexagonal and square microstructures enables rapid identification of the effects of fiber orthotropy on homogenized moduli and local stress fields. The efficiency with which the calculations are performed is rooted in the balanced variational principle which ensures stable and very accurate solution with relatively few terms in the Fourier series representation of the displacement fields in the cylindrically orthotropic fiber and matrix phases of the unit cell representative of the composite's microstructures. Hence the results may be used as a gold standard to assess the accuracy of other homogenization approaches. Herein, we have shown that the previously proposed replacement scheme for cylindrically orthotropic fibers with very large moduli contrast by their transversely isotropic homogenized equivalents implemented within the CCA model produces remarkably accurate results for four of the five homogenized moduli associated with axisymmetric and axial shear loading. These moduli differ very little from the corresponding moduli obtained by the locally exact homogenization theory that explicitly accounts for radially and circumferentially orthotropic graphite fibers. The advantage of the locally exact theory lies in its ability to generate both the homogenized moduli and local stress fields that explicitly account for the cylindrically orthotropic nature of graphite fibers within the same framework with great efficiency.

Perhaps most importantly, the unexplored effect of the fifth remaining modulus, namely the equivalent transverse modulus of cylindrically orthotropic fibers, on the homogenized transverse shear modulus of unidirectional composites has also been assessed using the self-consistent based replacement scheme proposed by Christensen (1994). Unlike the equivalent axisymmetric and axial shear fiber moduli, this replacement scheme produces equivalent transverse shear

moduli for radially and circumferentially orthotropic graphite fibers that may differ substantially. These differences translate into differences in the homogenized transverse shear moduli of the unidirectional composite which increase with the fiber volume fraction, with radially orthotropic fibers yielding stiffer response. Remarkably, Christensen's replacement scheme produces homogenized transverse shear moduli that closely follow the actual values based on cylindrically orthotropic fiber moduli, with larger differences observed for circumferentially orthotropic fibers.

Chapter 4

Numerical Results and Applications

4.1 Numerical Results

4.1.1 Two-Phase Composites: Homogenized Moduli vs Fiber Volume Fraction

In this section we employ the locally-exact homogenization theory to calculate homogenized moduli of unidirectional composites comprised of constituents with different moduli contrast in a wide fiber volume fraction range. These systems include graphite/epoxy, glass/epoxy, boron/aluminum and aluminum with cylindrical porosities. Both hexagonal and square arrays are employed and the results are compared with the FVDAM theory calculations as well as the widely employed Mori-Tanaka scheme. We also discuss execution time for these calculations and data file construction. Because some homogenized moduli exhibit behavior with inclusion/porosity volume fraction which is not intuitive, we verify that the results do not violate thermodynamic bounds.

We start with three of the five homogenized moduli, E_T^*, ν_T^*, G_A^*, calculated as a function of the fiber volume fraction for the graphite/epoxy material system. The axial modulus E_A^* is not shown as it is approximated very well by the familiar rule-of-mixtures formula, with similar result for the axial Poisson's ratio ν_A^*. The results are generated for hexagonal, square and tetragonal arrays in the fiber volume interval [0.05,0.75] using increments of 0.05, normalized by the corresponding matrix moduli in the case of the transverse Young's modulus and axial shear modulus, and compared with the corresponding results obtained from FVDAM and Mori-Tanaka calculation in Fig. 4.1. As observed, there is no difference between the locally exact analytical and FVDAM predictions for both hexagonal and square arrays. The array type only affects moduli associated with transverse loading, E_T^* and ν_T^*, with very little difference observed in the axial shear moduli G_A^* in most of the realistic fiber volume fraction range, and no difference

in the axial Poisson's ratio ν_A^*. The Mori-Tanaka results are close to the hexagonal array predictions as would be expected from the model's transversely isotropic framework. Fig. 4.2 presents the corresponding predictions for the glass/epoxy material system. The constituent moduli contrast in glass/epoxy system is greater than for the graphite/epoxy composite, thereby resulting in greater differences in the homogenized moduli for the hexagonal, square and tetragonal arrays. The locally-exact analytical moduli and the FVDAM predictions are virtually identical, but greater differences are now observed between the hexagonal array transverse moduli and the corresponding Mori-Tanaka predictions. Since the angle between adjacent two sides of the tetragonal array is chosen as $\varphi = \pi/3$, resembling hexagonal array, the homogenized moduli are identical to those of hexagonal array.

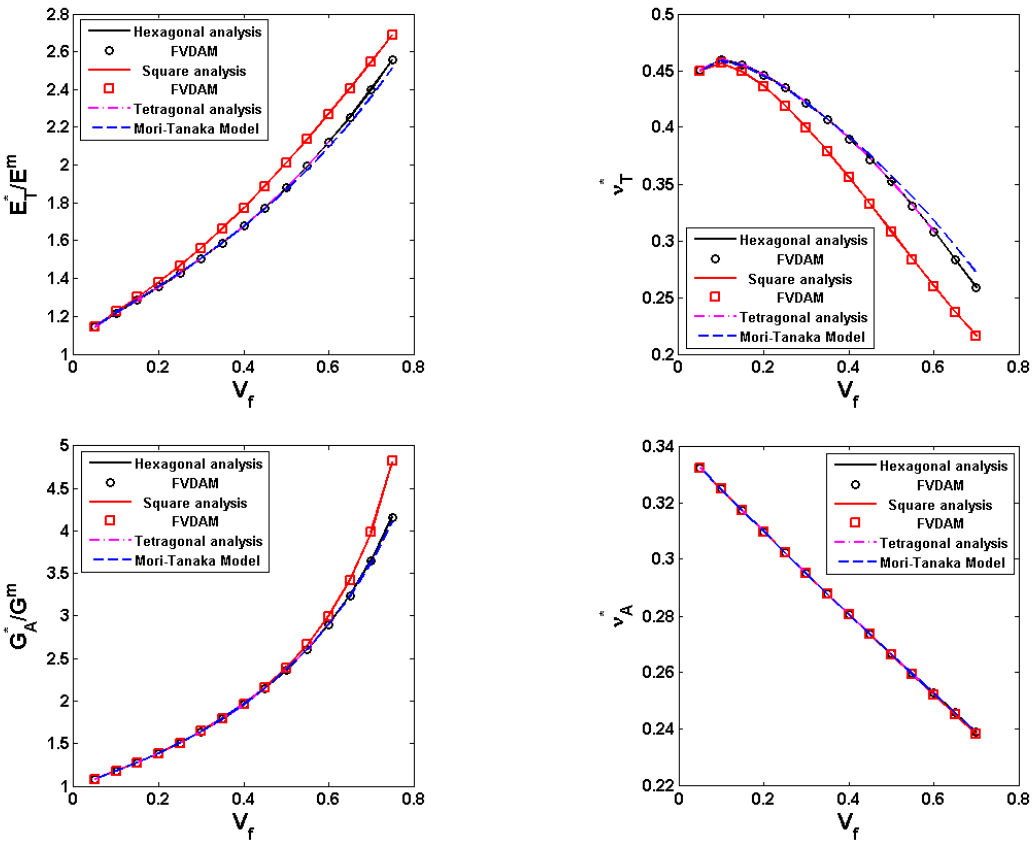

Figure 4.1 Homogenized moduli as a function of fiber volume fraction for a graphite/epoxy composite with hexagonal, square and tetragonal architectures. Comparison with FVDAM predictions and the Mori-Tanaka method.

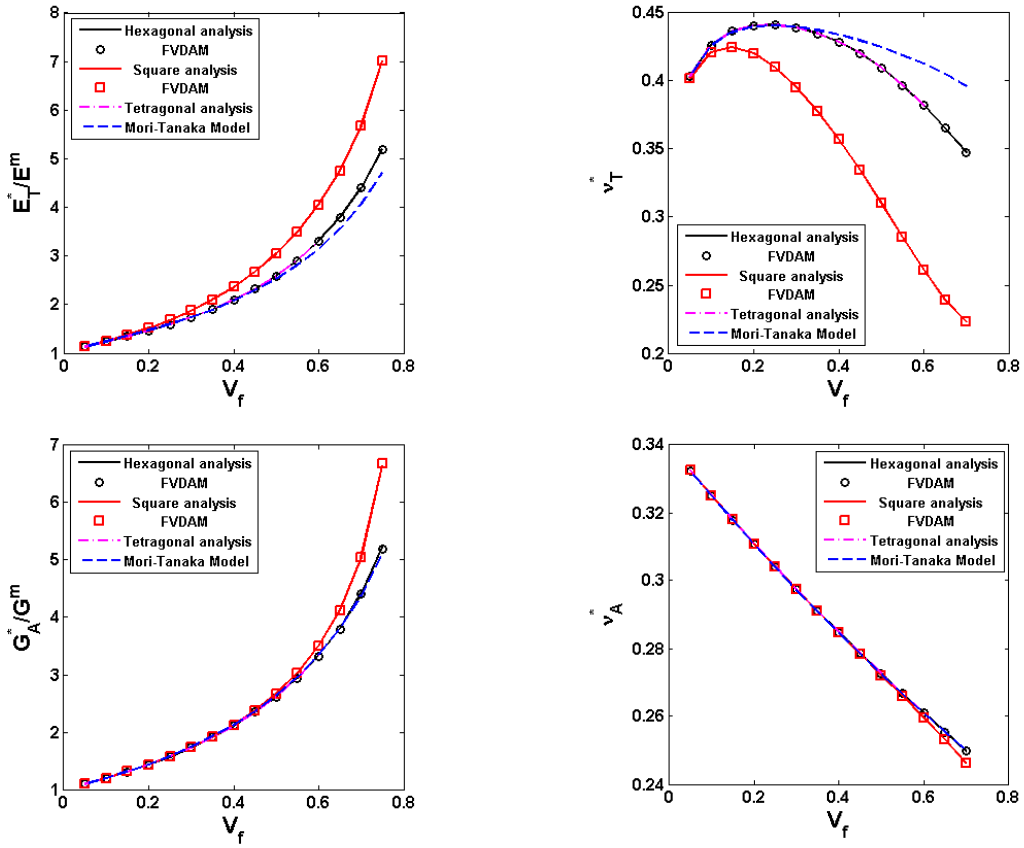

Figure 4.2 Homogenized moduli as a function of fiber volume fraction for a glass/epoxy composite with hexagonal, square and tetragonal architectures. Comparison with FVDAM predictions and the Mori-Tanaka method.

Finally, we illustrate the effect of fiber/matrix moduli mismatch on the homogenized moduli of graphite/epoxy, glass/epoxy, boron/aluminum and porous aluminum composites generated by the locally exact homogenization theory as a function of the inclusion/porosity content in Fig. 4.3. The results have been generated for hexagonal arrays. The homogenized transverse Young's and axial shear moduli trends with the fiber content reflect the respective fiber/matrix moduli mismatch for the three fiber-reinforced composites. In the case of cylindrical porosities in aluminum matrix, the results are expected with the exception of the transverse Poisson's ratio which increases above the value of 0.5 for porosity volume fractions greater than approximately 0.6. This counter-intuitive result, however, is consistent with the thermodymanic constraint $\nu_T^* < 1 - 2\nu_A^* \times (E_T^*/E_A^*)$ obtained by requiring that the homogenized compliance tensor $\mathbf{S}^*$ be positive-definite as dictated by the positive-definite constraint on the homogenized complementary energy. In contrast, the homogenized transverse Poisson's ratio ν_T^* for

cylindrical porosities in a square array (not shown) decreases with increasing porosity content.

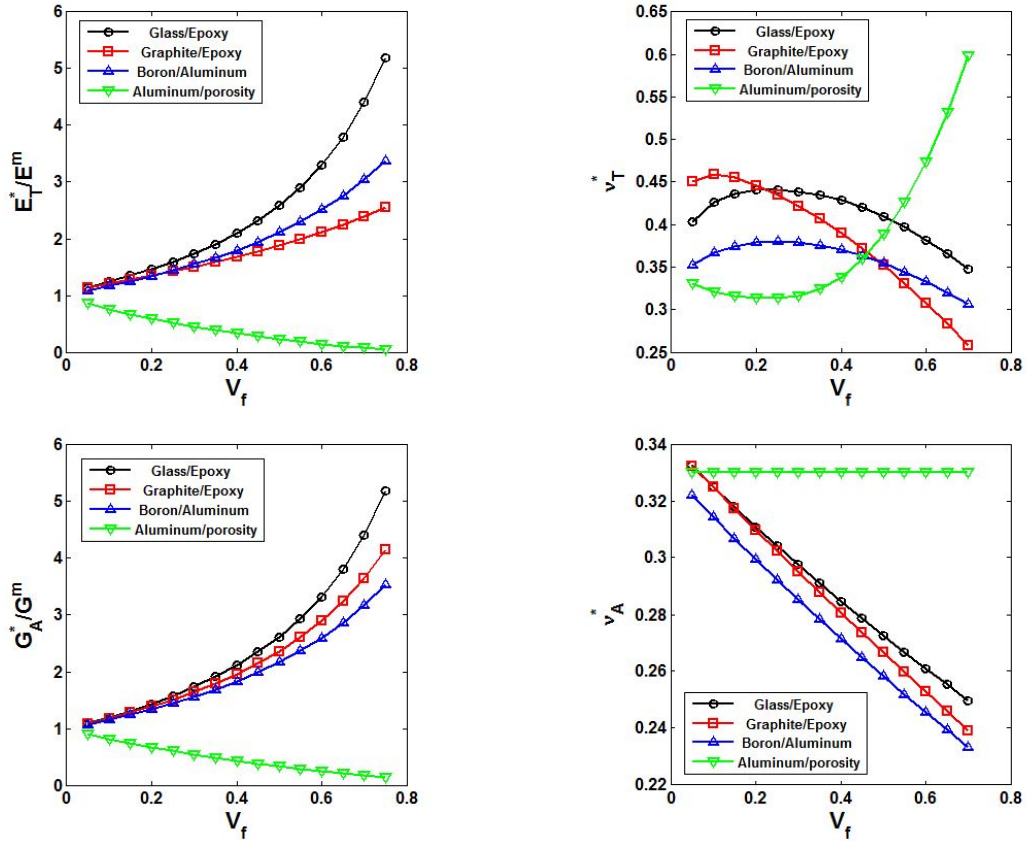

Figure 4.3 Homogenized moduli as a function of fiber/porosity volume fraction for unidirectional composites with hexagonal architectures with different constituent moduli contrast.

The quick convergence of the developed analytical solution to the unit cell boundary-value problem with relatively small number of harmonics makes the locally exact homogenization theory extremely efficient in execution. This is demonstrated in Fig. 4.4 for the graphite/epoxy composite wherein execution time needed to calculate the entire set of homogenized moduli or 0.6 fiber volume fraction have been recorded as a function of harmonic number for square and hexagonal arrays. These calculations were performed on a PC platform running Windows 7 Ultimate 64-bit operating system with 16 GB RAM and Intel(R) Core(TM) i5-3320M CPU @2.6 GHz. As observed, hexagonal arrays are somewhat more computationally demanding because the balanced variational principle is employed on six faces of the hexagonal unit cell instead of just four faces for the square array. Nonetheless, the locally exact homogenization theory is very

efficient, consuming less than one second to calculate the entire set of homogenized moduli for a single volume fraction with very good accuracy using 15 harmonics. Similarly, less than 15s are needed to calculate the entire set of homogenized moduli using 15 harmonics in the fiber volume fraction range [0.05,0.75] with an increment of 0.05. Moreover, the negligible effort required to construct an input data file describing the unit cell geometry (rectangular vs hexagonal), fiber placement and radius which defines the fiber volume fraction, and the constituent elastic moduli contributes to the method's overall efficiency as well as accessibility by specialist and not-specialist alike.

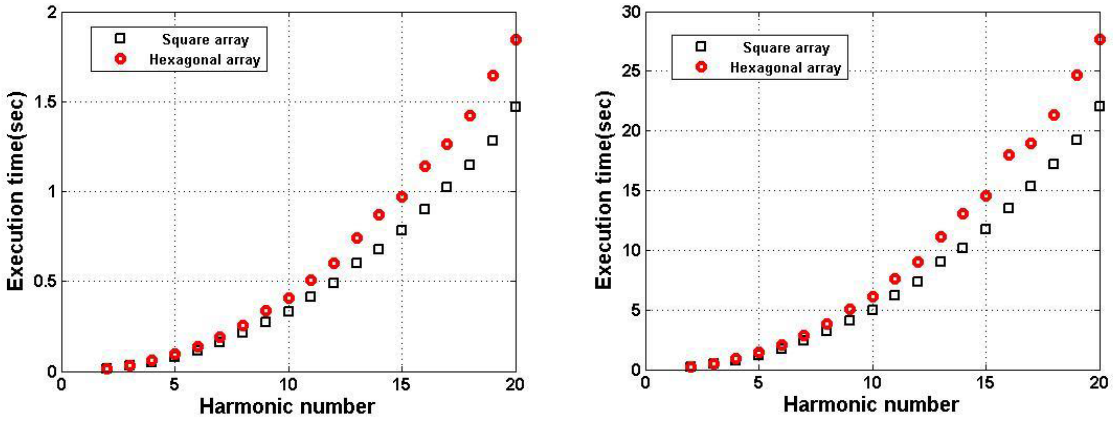

(a) (b)

Figure 4.4 Comparison of execution times as a function of harmonic number to generate one set of homogenized moduli for hexagonal and square arrays: (a) single fiber volume fraction of 0.6; (b) fiber volume fraction range [0.05-0.75] with an increment of 0.05.

4.1.2 Evaluation of Effective Material Properties for Composites with Rhombic or Parallelogram Fiber Arrangements

The homogenized moduli of the composites generated by LEHT are compared with another analytical technique – asymptotic homogenization method (AHM) and numerical method (FEM) (Rodríguez-Ramos et al., 2012) in Tables 4.1 – 4.5. The calculation by AHM are studied for N_0=10, where N_0 denotes the number of equations considered in the solution of the algebraic system. The Young's moduli and Poisson's ratio employed in most of the tables (except Table 4.3) are artificial values: $E^{(f)} = 312\text{GPa}$, $\nu^{(f)} = 0.3$; $E^{(m)} = 2.6\text{GPa}$, $\nu^{(m)} = 0.3$.

Angle θ	V_f	C_{11}^*			C_{22}^*			C_{33}^*			C_{23}^*		
		LEHT	AHM	FEM	LEHT	AHM	FEM	LEHT	AHM	FEM	LEHT	AHM	FEM
30°	0.1	34.579	34.579	34.576	4.0379	4.0376	4.0384	4.1118	4.1106	4.1123	1.6974	1.6980	1.6977
	0.2	65.702	65.701	65.700	4.6548	4.6551	4.6567	5.1230	5.0999	5.1189	1.9046	1.9075	1.9047
	0.3	96.948	96.920	96.940	5.3499	5.3531	5.3559	7.3099	7.0091	7.2488	2.1603	2.1539	2.1554
50°	0.1	34.578	34.578	34.577	4.0494	4.0494	4.0505	4.0573	4.0572	4.0582	1.7145	1.7145	1.7149
	0.3	96.853	96.853	96.851	5.5696	5.5696	5.5757	5.7070	5.7018	5.7117	2.3217	2.3232	2.3204
	0.5	159.47	159.46	159.46	8.1646	8.1740	8.1918	9.1781	8.9916	9.1903	3.3691	3.3977	3.3528
70°	0.1	34.578	34.578	34.577	4.0609	4.0609	4.0615	4.0594	4.0595	0.0600	1.7076	1.7075	1.7074
	0.3	96.851	96.851	96.850	5.7237	5.7209	5.7248	5.7002	5.6993	5.7027	2.2401	2.2425	2.2409
	0.5	159.44	159.44	159.44	8.9680	8.9147	8.9571	8.8064	8.7726	8.8087	3.0084	3.0557	3.0137

Table 4.1 Comparison of the homogenized moduli between LEHT, AHM and FEM with rhombic periodic cells C_{11}^*, C_{22}^*, C_{33}^*, C_{23}^*:

Angle θ	V_f	C_{14}^*			C_{24}^*			C_{34}^*			C_{44}^*		
		LEHT	AHM	FEM	LEHT	AHM	FEM	LEHT	AHM	FEM	LEHT	AHM	FEM
30°	0.1	-0.0064	-0.0063	-0.0061	0.0125	0.0124	0.0132	-0.0339	-0.0335	-0.0337	1.1620	1.1616	1.1622
	0.2	-0.0405	-0.0385	-0.0404	0.0442	0.0416	0.4346	-0.1792	-0.1699	-0.1783	1.3632	1.3629	1.3660
	0.3	-0.1694	-0.1434	-0.1643	0.0680	0.0635	0.0627	-0.6326	-0.5416	-0.6108	1.6806	1.6642	1.6868
50°	0.1	-0.0014	-0.0014	-0.0013	0.0056	0.0056	0.0054	-0.0102	-0.0103	-0.0098	1.1722	1.1722	1.1725
	0.3	-0.0244	-0.0236	-0.0244	0.0499	0.0479	0.0487	-0.1313	-0.1267	-0.1300	1.6904	1.6870	1.6928
	0.5	-0.1807	-0.1461	-0.1778	0.0854	0.0753	0.0755	-0.6876	-0.5624	-0.6693	2.7931	2.7050	2.8006
70°	0.1	0.0006	0.0006	0.0008	-0.0038	-0.0038	-0.0038	0.0057	0.0057	0.0060	1.1651	1.1651	1.1653
	0.3	0.0089	0.0089	0.0090	-0.0378	-0.0378	-0.0379	0.0675	0.0674	0.0681	1.6094	1.6085	1.6104
	0.5	0.0616	0.0586	0.0622	-0.0985	-0.0987	0.1014	0.3039	0.2939	0.3089	2.4424	2.4261	2.4466

Table 4.2 Comparison of the homogenized moduli between LEHT, AHM and FEM with rhombic periodic cells C_{14}^*, C_{24}^*, C_{34}^*, C_{44}^*.

$C_{55}^{(f)}/C_{55}^{(m)}$	V_f	$C_{55}^*/C_{55}^{(m)}$				$C_{56}^*/C_{55}^{(m)}$				$C_{66}^*/C_{55}^{(m)}$			
		LEHT	G&N	AHM	FEM	LEHT	G&N	AHM	FEM	LEHT	G&N	AHM	FEM
20	0.3	1.74	1.74	1.74	1.74	0.02	0.02	0.02	0.02	1.75	1.75	1.75	1.75
	0.5	2.66	2.66	2.66	2.67	0.08	0.08	0.08	0.08	2.70	2.70	2.70	2.71
	0.7	4.83	4.83	4.83	4.82	0.34	0.34	0.34	0.35	5.00	5.00	5.00	4.99
120	0.3	1.83	1.83	1.83	1.84	0.02	0.02	0.02	0.02	1.84	1.84	1.84	1.85
	0.5	2.96	2.96	2.96	2.97	0.11	0.11	0.11	0.11	3.01	3.01	3.01	3.02
	0.7	6.16	6.16	6.16	6.15	0.60	0.60	0.60	0.60	6.47	6.47	6.47	6.43

Table 4.3 Comparison of axial shear homogenized moduli between different approaches with rhombic periodic cell and $\theta = \arccos(1/4)$.

L/H	V_f	C_{22}^*			C_{23}^*			C_{33}^*			C_{44}^*		
		LEHT	AHM	FEM	LEHT	AHM	FEM	LEHT	AHM	FEM	LEHT	AHM	FEM
0.980	0.1	4.0623	4.0621	4.0651	1.7086	1.7086	1.7091	4.0561	4.0561	4.0585	1.1657	1.1657	1.1671
	0.3	5.7484	5.7327	5.7547	2.2569	2.2659	2.2535	5.6471	5.6394	5.6557	1.6125	1.6077	1.6200
	0.5	9.1818	8.9137	9.1901	3.0693	3.2075	3.0613	8.4733	8.3894	8.4835	2.4600	2.3723	2.4609
1.146	0.1	4.0742	4.0741	4.0755	1.7026	1.7026	1.7010	4.0565	4.0565	4.0594	1.1612	1.1607	1.1616
	0.3	5.9451	5.9190	5.9508	2.1818	2.1924	2.1829	5.6288	5.6245	5.6339	1.5739	1.5625	1.5701
	0.5	10.6786	10.0040	10.6754	2.7888	2.9316	2.7725	8.2374	8.2009	8.2491	2.3076	2.2560	2.3045
1.308	0.1	4.0862	4.0861	4.0889	1.6977	1.6978	1.6991	4.0551	4.0551	4.0572	1.1585	1.1570	1.1578
	0.3	6.1826	6.1396	6.1886	2.1199	2.1311	2.1195	5.5898	5.5872	5.5945	1.5539	1.5344	1.5409
	0.5	**13.5180**	**11.7480**	**13.4746**	2.5729	2.6968	2.5605	7.9532	7.9427	7.9665	2.2709	2.2087	2.2340

Table 4.4 Comparison of the in-plane homogenized moduli with parallelogram periodic cells for different ratios L/H and fiber volume fractions.

L/H	V_f	$C_{55}^*/C_{55}^{(m)}$				$C_{66}^*/C_{55}^{(m)}$			
		LEHT	G&N	AHM	FEM	LEHT	G&N	AHM	FEM
0.980	0.3	1.8657	1.87	1.8657	1.8678	1.8110	1.81	1.8110	1.8130
	0.5	3.1087	3.11	3.1088	3.1110	2.8088	2.81	2.8088	2.8095
	0.6	4.3277	4.33	4.3300	4.3334	3.6258	3.63	3.6269	3.6273
1.146	0.3	1.9245	1.92	1.9245	1.9255	1.7675	1.77	1.7674	1.7688
	0.5	3.5514	3.55	2.5288	2.5294	2.6197	2.62	2.6195	2.6207
1.138	0.3	1.9998	2.00	1.9998	2.0032	1.7252	1.72	1.7252	1.7258
	0.5	4.4012	4.40	4.4001	4.4188	2.4583	2.46	2.4578	2.4617

Table 4.5. Comparison of the out-of-plane homogenized moduli with parallelogram periodic cells for different ratios L/H and fiber volume fractions.

The results calculated by LEHT, AHM and FEM coincide in many different cases. Tables 4.1-4.3 exhibit composite materials with rhombic periodic unit cells. Tables 4.1-4.2 show the inplane homogenized moduli and Table 4.3 shows out-of-plane homogenized moduli according to three different fiber volume fractions. The composites shown belong to the monoclinic material of symmetry. For instance, the C_{14}^{*}, C_{24}^{*}, C_{34}^{*} in Table 4.3 are non-zero terms in comparison with hexagonal or tetragonal unit cells. In order to validate the effect of the ratio of $C_{44}^{(f)}/C_{44}^{(m)}$ on the out-of-plane homogenized moduli, three different fiber volume fractions are used to cover a wide range of the fiber arrangement at a fixed angle $\varphi = \arccos(1/4)$. A new set of results calculated using G&N (Golovchan and Nikityuk, 1981) are included to prove more confidence of the new proposed method. An excellent agreement between all the approaches can be observed.

Tables 4.4-4.5 study the homogenized moduli of composites with parallelogram arrays by letting $H = 1$ and $\theta = \arccos(0.5/L)$ with different values of L listed in the tables. As is well noticed in the tables, the out-of-plane homogenized moduli are well matched between different methods. However, smaller discrepancies are observed between LEHT and FEM than AHM, especially when the fiber volume fraction is set to be high for different angles. For example, LEHT provides much closer results compared with FEM than AHM for C_{22}^{*} corresponding to $L/H = 1.4$ and $V_f = 0.5$ in Table 4.4.

4.1.3 A Parametric Study for Composites with Coated Fibers

We illustrate the effects of coating's thickness and stiffness for three of the five homogenized moduli which exhibit the greatest sensitivity to these parameter variations, namely E_T^{*}, ν_T^{*} and G_A^{*}, calculated as a function of the fiber volume fraction for the graphite/epoxy material system. Fig. 4.5 illustrates the effect of coating thickness represented by the ratios $b/a = 1.0$, 1.01 and 1.10, see Fig. 2.2, on the three homogenized moduli for the coating/epoxy modulus contrast $E^{(c)}/E^{(m)} = 1.5$. The results were generated in the fiber volume interval [0.05,0.75] using increments of 0.05, normalized by the corresponding matrix moduli in the case of the transverse Young's and axial shear moduli. The fiber volume fraction was incremented by changing the unit cell dimensions in order to keep the coating thickness fixed. At this modulus contrast, measurable increases in the homogenized transverse Young's and axial shear moduli

are observed for the largest ratio $b/a = 1.1$, with a decrease observed in the transverse Poisson's ratio. The effect of coating increases with increasing fiber volume fraction, and appears to be comparable for both arrays, accounting for the greater Young's and axial shear moduli exhibited by the square array at each fiber volume fraction. Within each array type, the coating tends to enhance the axial shear modulus G_A^* to a somewhat greater extent than the transverse Young's modulus E_T^* for the considered coating/epoxy modulus contrast, suggesting more efficient stress transfer mechanism into the coated fiber discussed in the sequel.

Next, we choose coating thickness with the largest ratio $b/a = 1.1$ and investigate the effect of both fiber volume fraction and coating stiffness on the homogenized transverse Young's and axial shear moduli. The results are presented in Fig. 4.6 as three-dimensional carpet plots, highlighting the efficiency of generating homogenized moduli with our elasticity-based approach. These results have been generated for hexagonal arrays and normalized by the respective moduli of the matrix phase. Consistent with expectation, the effect of increasing coating's Young's modulus on the homogenized moduli increases with increasing fiber volume fraction as the coating volume fraction also increases even if the coating thickness remains fixed. Included in the figure are two-dimensional projections of the carpet plots in a small range of $E^{(c)}/E^{(m)}$ ratios, namely [0.0, 0.275], wherein rapid changes in the homogenized moduli values are observed in the carpet plots. These projections illustrate the minimum values of the coating Young's modulus as a function of the fiber volume fraction which yield homogenized moduli greater than the matrix modulus. This information may be useful in the design of engineered coatings.

What needs to be mentioned is that less than 1.5 s was needed to generate the full set of homogenized moduli with coated fibers as compared to less than 0.5s without the coating using 10 harmonics and a PC platform running Windows 7 Ultimate 64-bit operating system with 16GB RAM and Intel(R) Core(TM) i5-3320M CPU @2.6 GHz.

As observed in Fig. 4.5 and 4.6, the loading direction influences the effectiveness of fiber reinforcement vis-à-vis respective homogenized moduli. For both arrays, the axial shear modulus G_A^* increases faster with fiber volume fraction relative to the matrix than the transverse Young's modulus E_T^*, with the concomitant effectiveness increase of the coating. Fig. 4.7 illustrates the effectiveness of stress transfer from the matrix into the fiber under uniaxial loading by transverse

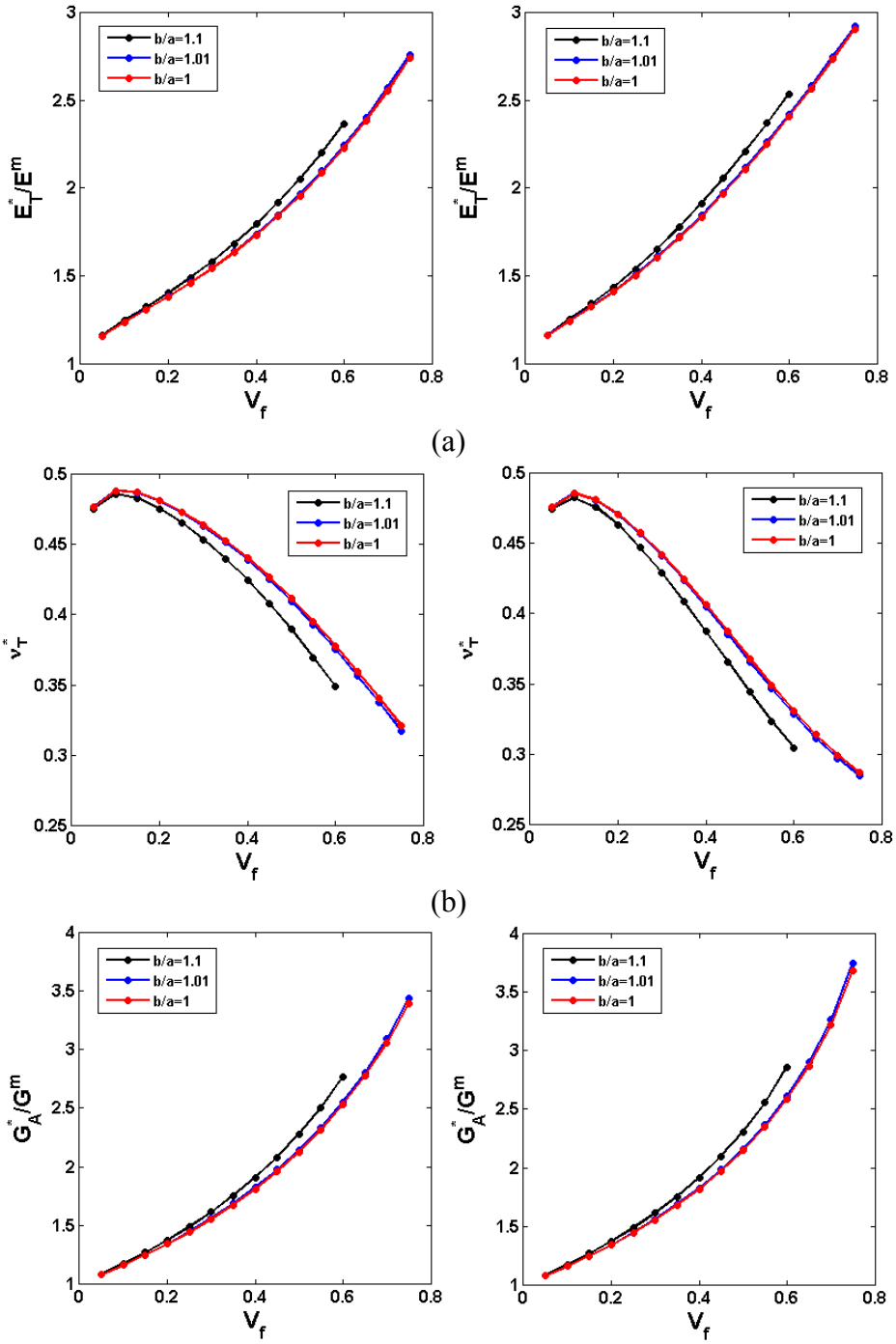

Figure 4.5 Homogenized moduli as a function of fiber volume fraction for a graphite/epoxy composite with hexagonal and square architectures and modulus contrast $E^{(c)}/E^{(m)}=1.5$, demonstrating the effect of coating thickness.

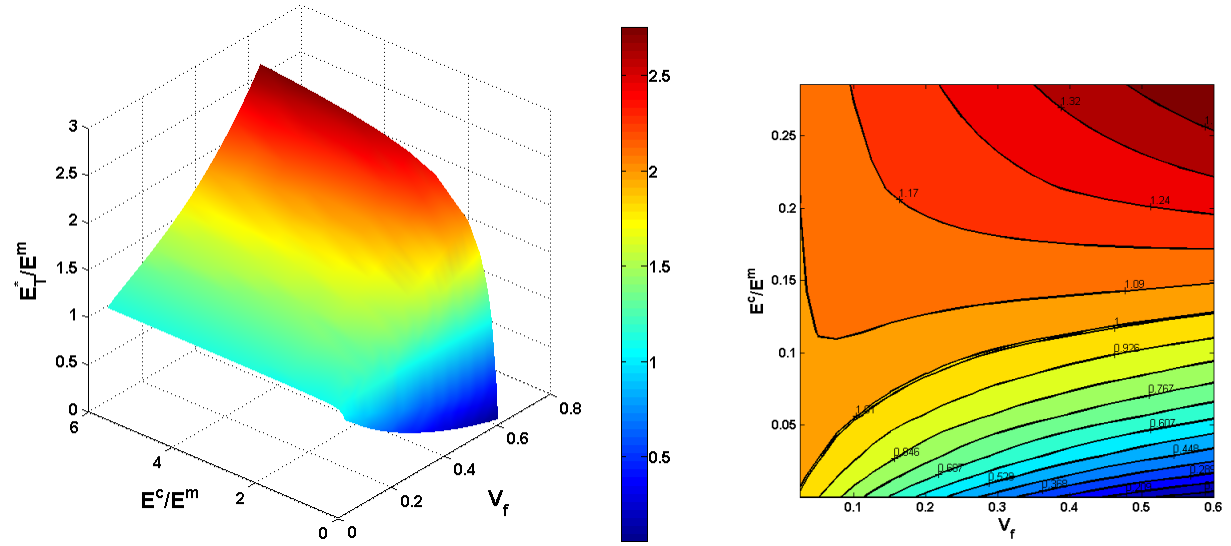

(a)

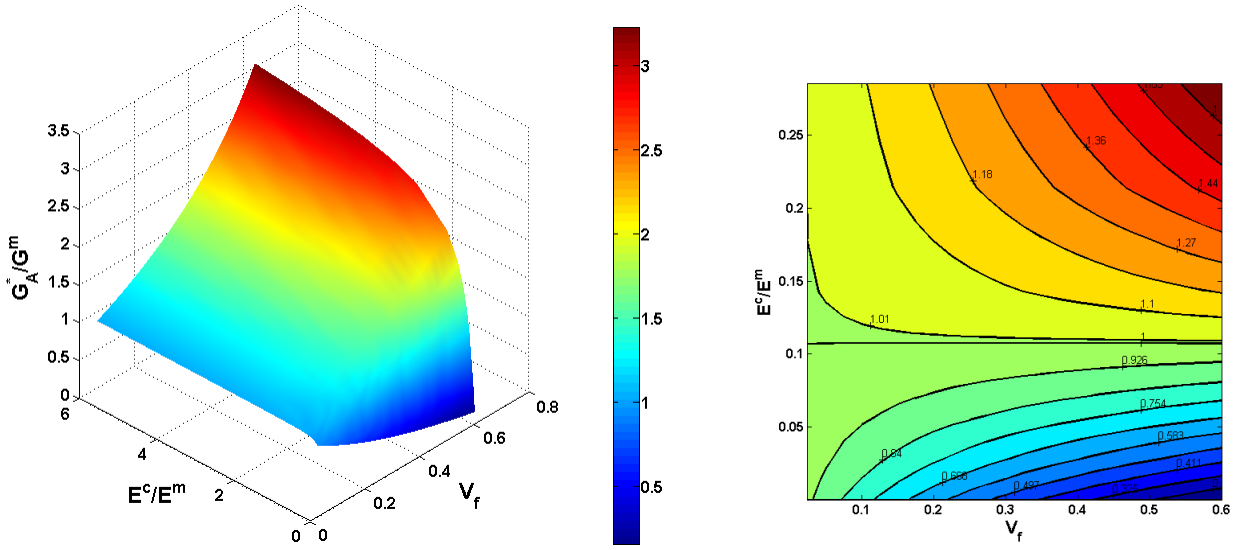

(b)

Figure 4.6 Homogenized moduli as a function of fiber volume fraction for a graphite/epoxy composite with hexagonal architecture and fiber/matrix radius ratio $b/a = 1.1$, demonstrating the effect of coating stiffness.

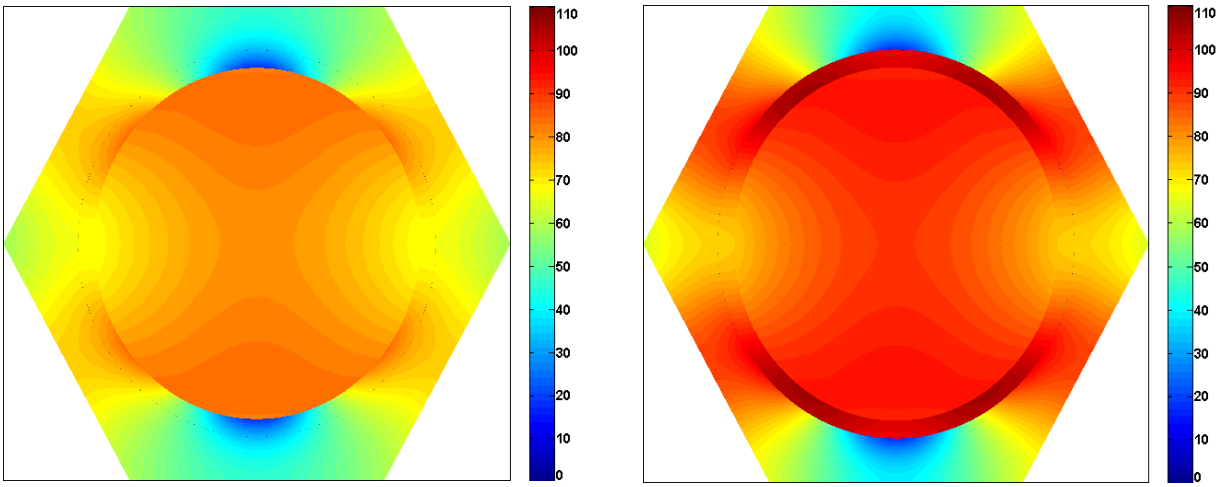

(a) $\sigma_{22}(y_2, y_3)$

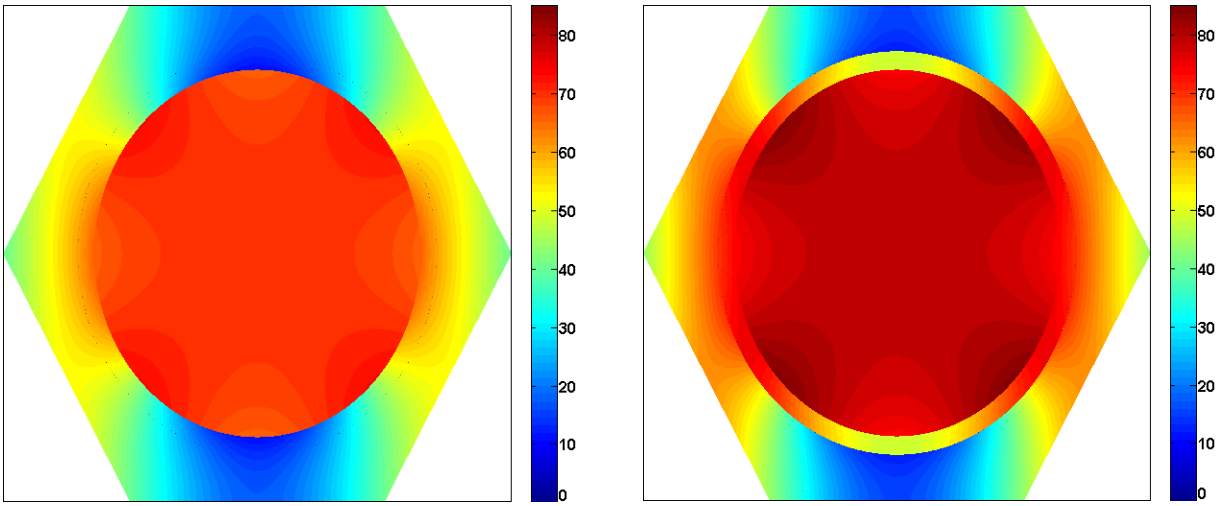

(b) $\sigma_{12}(y_2, y_3)$

Figure 4.7 Transverse normal and axial shear stress distributions in hexagonal unit cells of a graphite/epoxy composite with fiber volume fraction 0.60 subjected to uniaxial loading $\bar{\sigma}_{22} \neq 0$ and $\bar{\sigma}_{12} \neq 0$ at the applied strains $\bar{\varepsilon}_{22} = 0.01$ and $\bar{\varepsilon}_{12} = 0.01$, respectively, illustrating the effect of modulus contrasts $E^{(c)}/E^{(m)} = 1.0$ (left) and $E^{(c)}/E^{(m)} = 1.5$ (right) on stress transfer mechanism for $b/a = 1.0$ (left) and $b/a = 1.1$ (right).

tension and axial shear in the presence of coating with the $E^{(c)}/E^{(m)} = 4.0$ ratio relative to the uncoated fiber when the fiber volume fraction is 0.6. The stress fields were calculated for the respective macroscopic strains of 0.01 or 1% under corresponding unidirectional loading. Under transverse tension, the coating experiences substantially larger normal stress $\sigma_{22}(y_2, y_3)$ than the fiber in the angular sectors away from the applied load, producing a uniform stress field throughout most of the fiber which is greater relative to the uncoated fiber. In contrast, under axial shear loading, the coating experiences smaller axial shear stress $\sigma_{12}(y_2, y_3)$ than the fiber. Nonetheless, the axial shear stress in the fiber is substantially enhanced by the coating's presence relative to the uncoated fiber, producing a concomitant increase in the homogenized axial shear modulus G_A^*. Overall, for the chosen parameters, the coating tends to promote greater stress transfer into the fiber under axial shear loading relative to transverse normal loading.

4.2 Examples and Applications

4.2.1 Local Stress Recovery in a Multiscale FGM Application – Composite Cylinder

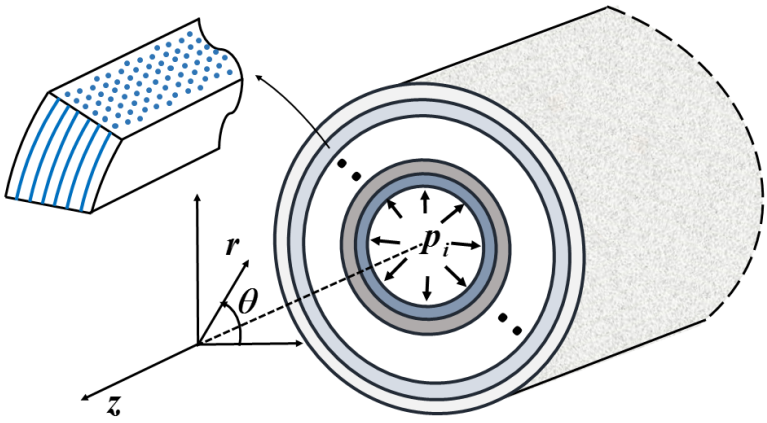

Fig 4.8 Circumferentially wound and functionally graded boron/aluminum cylinder subjected to internal pressure.

The locally exact theory's computational efficiency facilitates its use in multiscale applications. Herein, we demonstrate this capability by embedding the theory into the structural analysis of a functionally graded metal matrix composite cylinder subjected to internal pressure in order to generate homogenized and local stress fields. Specifically, we consider a thick-walled aluminum cylinder reinforced by circumferentially wound born fibers with an inner radius of 0.025 m, outer radius of 0.050m and 100 MPa applied internally, and investigate how grading may enhance the cylinder's loading bearing capacity in the elastic region. The grading is accomplished in a piece-wise fashion by dividing the cylinder into 10 sublayers with a constant boron fiber volume fraction in each year, Fig. 4.8. Because the boron fiber diameter is small relative to sublayer's thickness, each sublayer may be homogenized for structural analysis.

The analysis proceeds as follows. First, the elastic moduli in each sublayer of the cylinder are determined using the locally exact homogenization theory. These moduli are employed to solve the Navier's equations for the displacement field in each homogenized sublayer, which reduce to the following equation for the axisymmetric radial displacement with $\bar{u}_\theta = 0$, cf. Pindera and Freed (1994),

$$\frac{d^2\bar{u}_r}{dr^2} + \frac{1}{r}\frac{d\bar{u}_r}{dr} - \frac{C^*_{\theta\theta}}{C^*_{rr}}\frac{\bar{u}_r}{r^2} = 0 \tag{4.2}$$

where $C^*_{\theta\theta} > C^*_{rr}$ in the light of the circumferential reinforcement by boron fibers. We consider the plane strain case so that $\bar{u}_z = 0$. The solution for the radial displacement field in each sublayer takes the form

$$\bar{u}_r(r) = A_k r^\lambda + B_k r^{-\lambda} \tag{4.2}$$

where $\lambda = (C^*_{\theta\theta}/C^*_{rr})^{1/2}$ and the unknown coefficients A_k, B_k in each layer are obtained from the external boundary conditions

$$u_r^{(k)}(r_k) = u_r^{(k+1)}(r_k),\ \sigma_{rr}^{(k)}(r_k) = \sigma_{rr}^{(k+1)}(r_k),\ \ k = 1,...,n-1 \tag{4.3}$$

where n is the number of sublayers, and r_k is the distance to the kth interface. The above boundary and continuity conditions produce twenty equations for the unknown coefficients A_k, B_k. The expressions for the homogenized radial, circumferential and axial stress components are obtained from the Hooke's law

$$\begin{aligned}\sigma_{rr} &= C^*_{rr}\varepsilon_{rr} + C^*_{r\theta}\varepsilon_{\theta\theta} \\ \sigma_{\theta\theta} &= C^*_{r\theta}\varepsilon_{rr} + C^*_{\theta\theta}\varepsilon_{\theta\theta} \\ \sigma_{zz} &= C^*_{zr}\varepsilon_{rr} + C^*_{z\theta}\varepsilon_{\theta\theta}\end{aligned} \tag{4.4}$$

where $\bar{\varepsilon}_{rr} = d\bar{u}_r/dr$ and $\bar{\varepsilon}_{\theta\theta} = \bar{u}_r/r$. The following equivalence relations hold between the homogenized moduli in the cylindrical coordinate system associated with the composite tube and the Cartesian coordinate system of the unit cell used in the homogenization analysis,

$$\begin{aligned}&C^*_{11} \to C^*_{\theta\theta},\ \ C^*_{22} \to C^*_{rr},\ \ C^*_{33} \to C^*_{zz} \\ &C^*_{12} \to C^*_{r\theta},\ \ C^*_{13} \to C^*_{\theta z},\ \ C^*_{23} \to C^*_{rz}\end{aligned} \tag{4.5}$$

The solution for the unknown coefficients produces homogenized strains at each radial position in the composite cylinder that may be used to calculate the local fields within the unit cell representative of the sublayer's microstructure.

We consider composite cylinder with two grading patterns. First, we grade by decreasing the boron volume fraction from 0.50 at the inner sublayer to 0.05 at the outer sublayer. Then we reverse the grading pattern and compare the stress distributions produced by the two patterns with the corresponding distributions in a pure aluminum cylinder. Both homogenized and constituent phase stress distributions have been calculated. The homogenized stresses are calculated from Eqs. (4.3) and (4.4) upon solving for the displacement field in each homogenized sublayer of the graded cylinder. The displacement field produces homogenized strains at different radial locations that serve as input to the unit cell boundary-value problem solved using the locally-exact homogenization theory described in Chapter 2. The unit cell solution produces local stress fields in the fiber and matrix phases that vary along the graded cylinder's radius. The local stresses of interest are the fiber axial stress (or the circumferential stress in the cylinder's coordinate system) that may produce fiber fracture, as well as the effective stress $\sigma^m_{eff} = (3/2 s_{ij}s_{ij})^{1/2}$, $s_{ij} = \sigma_{ij} - 1/3\sigma_{kk}\delta_{ij}$, in the matrix phase that governs local matrix yielding.

Fig. 4.9 presents comparison of the radial, circumferentially, axial and effective stress distributions in the graded and pure aluminum cylinders. Grading from high to low reduces the homogenized radial stress relative to that in the pure aluminum cylinder with the opposite effect for the reverse grading pattern. The importance of recovering local constituent stresses is illustrated in the circumferential stress distribution. For this stress component, grading the cylinder from low to high produces a nearly uniform homogenized stress which is substantially lower than in the pure aluminum cylinder from low to high produces a nearly uniform

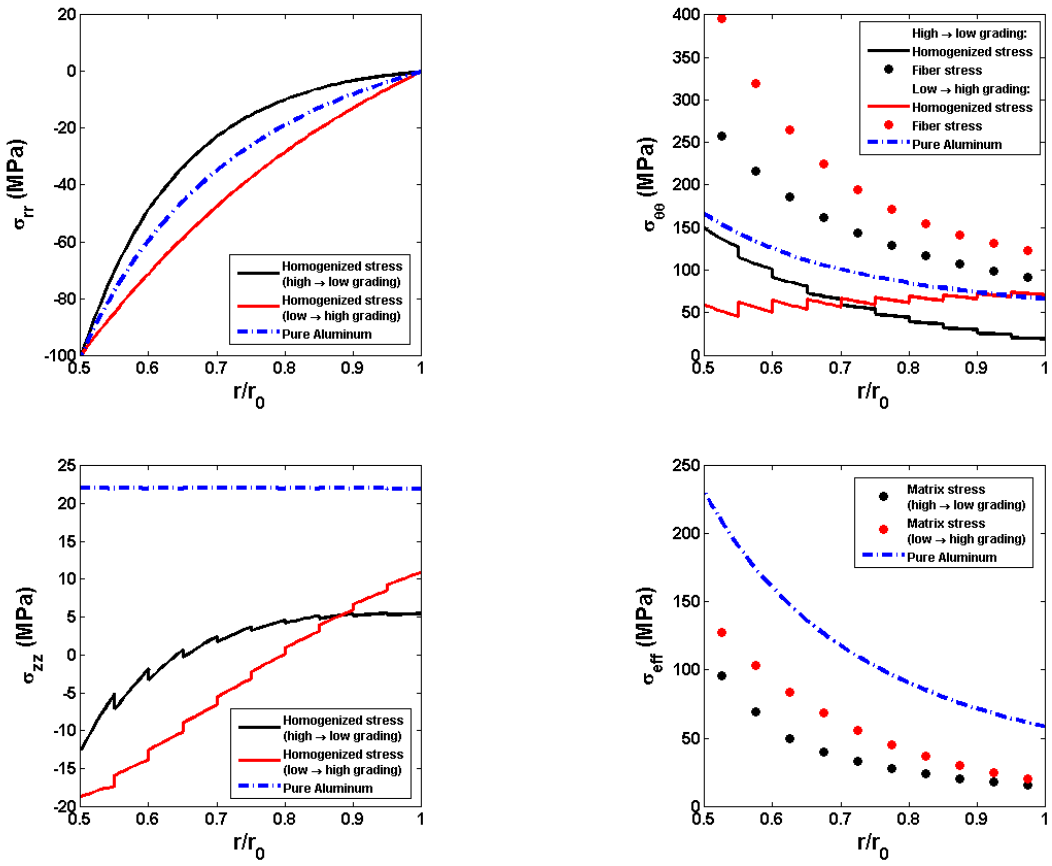

Figure 4.9 Homogenized and local stress distributions as a function of the graded cylinder's radial coordinate.

homogenized stress which is substantially lower than in the pure aluminum cylinder in the inner radius region, with the difference decreasing with increasing radial distance. In contrast, grading from high to low produces a small reduction in the homogenized circumferential stress relative to the pure aluminum case at the inner radius, which increases with increasing radial distance. The substantial reduction in the homogenized stress due to grading from low to high vs high to low, however, comes at the coat of large axial fiber stress in the inner radius region of the cylinder which may potentially produce fiber fracture. The smaller homogenized elastic modulus $C^*_{\theta\theta}$ in the low boron volume fraction range produces large circumferential strains which lead to high axial fiber stresses. Conversely, small axial fiber stress is observed in the inner radius region of the high to low grading pattern because of larger values of $C^*_{\theta\theta}$ due to larger boron volume fractions, and hence smaller circumferential strains. The benefit of the high to low grading

pattern is also observed in the effective stress distribution in the matrix phase where substantially lower maximum effective stress is observed in the inner radius region relative to both the pure aluminum cylinder and the low to high grading pattern. Grading in this manner will enhance the cylinder's pressurization capacity in the elastic region while ensuring that the axial fiber stress is not excessively large to cause fracture.

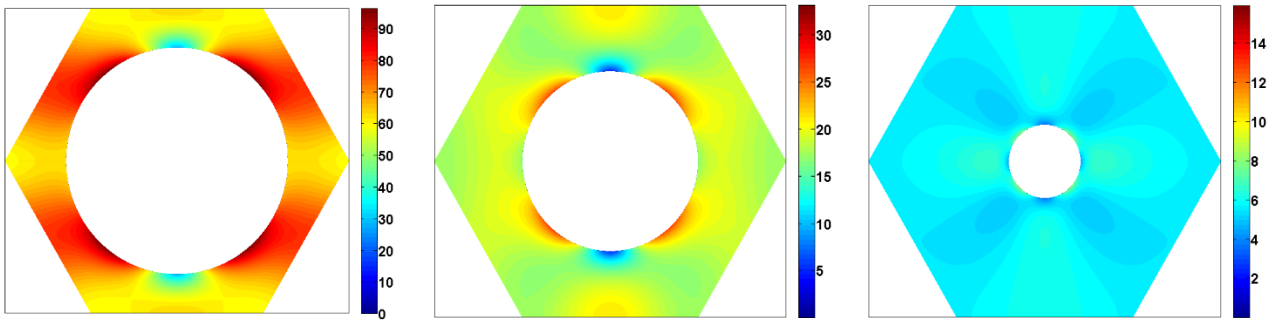

(a) Grading the boron fiber content from high to low

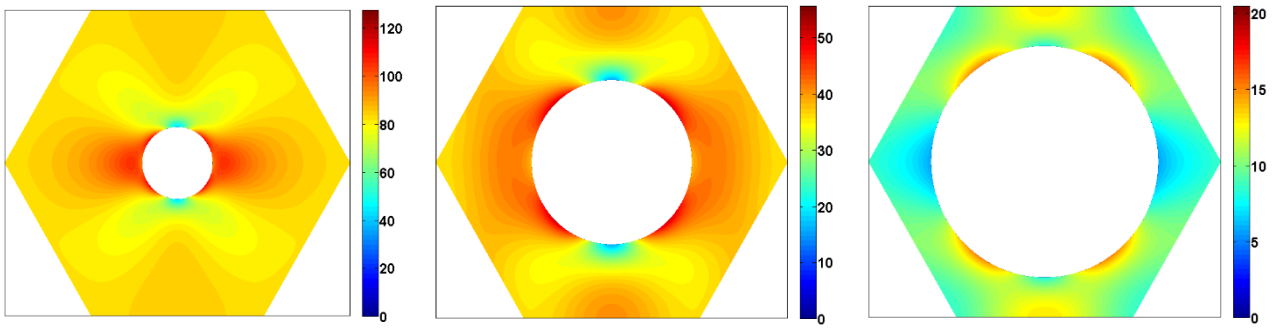

(b) Grading the boron fiber content from low to high

Fig 4.10 Effective stress distributions in the matrix phase of functionally graded B/Al cylinder in the center of the inner layer (left column), middle layer (center column) and outer layer (right column)

The constituent phase stress distributions illustrated in Fig. 4.9 were determined at the center of each sublayer from the unit cell analysis. These local stresses are the maximum axial fiber and effective matrix stresses that occur within the analyzed unit cells at each radial location. While the axial fiber stress remains nearly uniform at each radial location, the effective matrix stress varies substantially within the unit cell. These variation are shown in Fig. 4.10 in the center of the inner, middle and outer sublayers for both grading patterns, and illustrate local stress recovery capability in a multiscale analysis setting of the locally-exact homogenization theory. Examination of the effective stress fields suggests greater capacity of the high to low

grading pattern to support internal pressure before the aluminum matrix is fully plasticized. This observation provides guidance and motivation for further investigation by an elastic-plastic analysis using other means.

4.2.2 Local Stress Recovery in a Multiscale Application – Laminate

Herein, we demonstrate this capability by embedding the theory into a laminate analysis algorithm to generate the homogenized plate response and local stress fields under combined inplane loading. Specifically, we consider a quasi-isotropic $[0^o/\pm 45^o/90^o]_2$ laminate laid up with unidirectional graphite/epoxy plies containing 0.6 fiber volume fraction. The homogenized elastic moduli of the unidirectional plies are calculated using the locally-exact homogenization theory based on the constituent moduli given in Table 3.1. They are then employed to calculated the reduced stiffness moduli Q_{ij} of the plies used in constructing the laminate constitutive equation in the form

$$\begin{bmatrix} \bar{\sigma}_{xx} \\ \bar{\sigma}_{yy} \\ \bar{\sigma}_{xy} \end{bmatrix} = \begin{bmatrix} a_{11} & a_{12} & a_{16} \\ a_{12} & a_{22} & a_{26} \\ a_{16} & a_{26} & a_{66} \end{bmatrix} \begin{bmatrix} \varepsilon^0_{xx} \\ \varepsilon^0_{yy} \\ \gamma^0_{xy} \end{bmatrix} \tag{4.6}$$

where $a_{ij} = \frac{1}{2H}\sum_{k=1}^{n} \bar{Q}_{ij}(\theta) t_k$, t_k is the ply thickness, $2H$ is the laminate thickness, $\bar{Q}_{ij}(\theta)$ are transformed reduced stiffness moduli in the laminate coordinate system, and $\varepsilon^o_{xx}, \varepsilon^o_{yy}, \gamma^o_{xy}$ are the uniform laminate strains that arise due to the uniform inplane laminate stress $\bar{\sigma}_{xx}, \bar{\sigma}_{yy}, \bar{\sigma}_{xy}$. The uniform inplane laminate strains obtained from the above equation are then transformed to the principle material coordinate system of each ply, which then play the role of homogenized strains employed in the calculation of local fields within the unit cell representative of the ply's microstructure. The missing homogenized strain normal to the laminate's plane for each ply is obtained from the homogenized Hooke's law for the ply under the constraint of plane stress.

As an illustration, selected local stress fields in the 0^o, $\pm 45^o$ and 90^o plies of the considered quasi-isotropic laminate produced by the laminate stress vector $[100, 50, 25]^T$ MPa are presented in Fig. 4.11 in the principal material coordinate system of each ply. These include two inplane stresses $\sigma_{22}(y_2, y_3)$ and $\sigma_{12}(y_2, y_3)$, and two out-of-plane stresses $\sigma_{23}(y_2, y_3)$

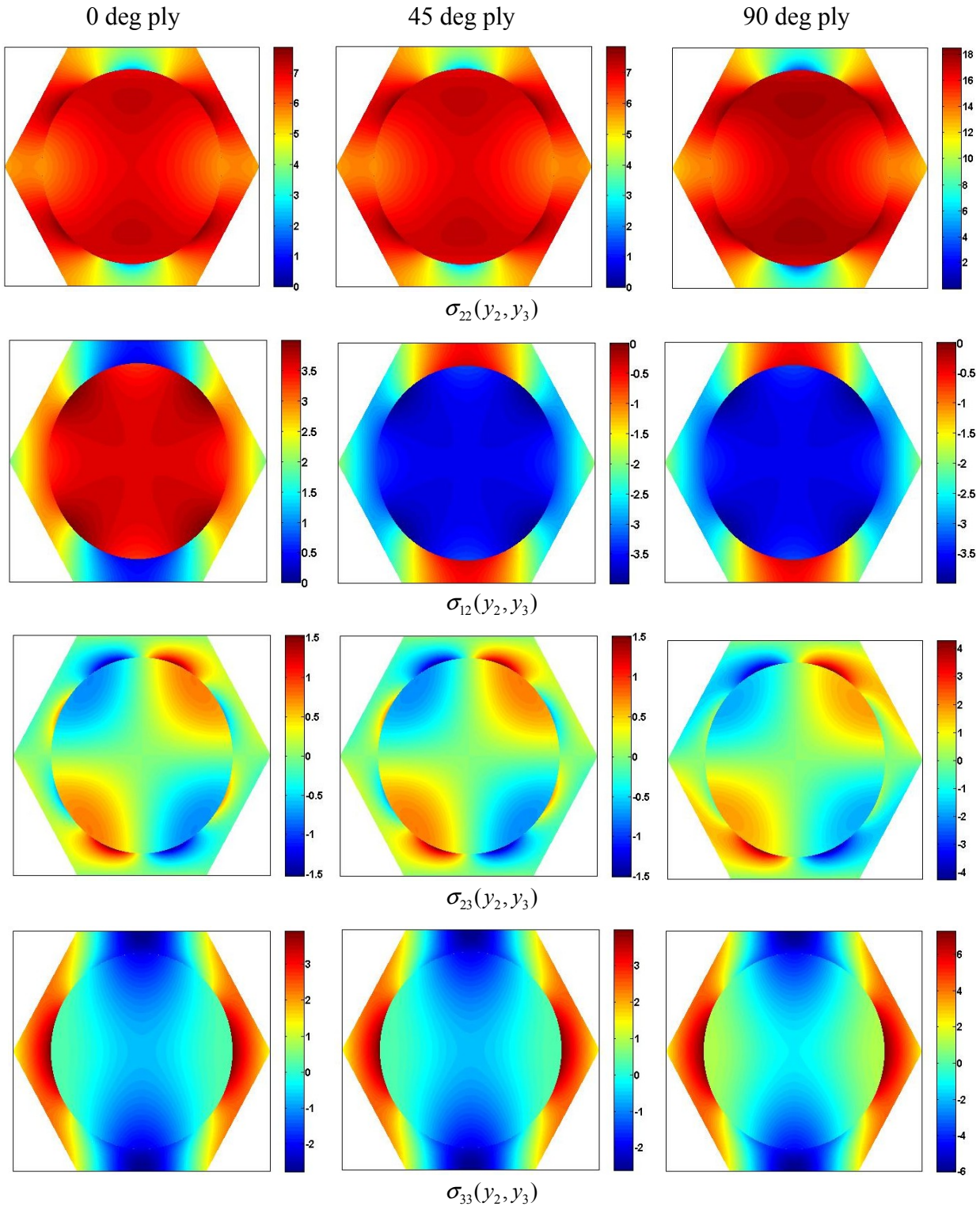

Figure 4.11 Local stress fields $\sigma_{22}(y_2, y_3)$, $\sigma_{12}(y_2, y_3)$, $\sigma_{23}(y_2, y_3)$ and $\sigma_{33}(y_2, y_3)$ in the principal material coordinate system of the individual plies in a symmetric quasi-isotropic laminate subjected to combined inplane state of stress $\bar{\sigma}_{xx} = 100$, $\bar{\sigma}_{yy} = 50$ and $\bar{\sigma}_{xy} = 25$ MPa.

and $\sigma_{33}(y_2, y_3)$ which are not insignificant. The local stress fields may be used in a failure criterion to efficiently generate homogenized laminate failure envelopes which account for the three-dimensional stress state in the individual plies.

4.2.3 Efficiency of Nanotube Reinforcement

The developed solution (Chapter 2) may be specialized to composites reinforced by hollow tubes by treating the coating as a hollow fiber upon setting the elastic moduli of the solid core to very small values. This also demonstrates the method's ruggedness. Hollow fiber reinforcement of traditional composites has not been attempted on a large scale due to fabrication difficulties. Fabrication techniques developed during the past decade for nanotechnology applications, however, make possible reinforcement of different types of matrix materials by inorganic nanotubes with precisely-controlled diameters, wall thickness and placement, such as hexagonally-arrayed alumina nanotubes, that have potential applications in microelectronics, nanofluidics, drug delivery and optical devices, amongst others. In light of the emerging applications of these nanostructures, little data is available on their homogenized properties.

Herein, we illustrate the extended theory's applicability by calculating homogenized moduli of an epoxy resin reinforced by atomic layer deposited (ALD) alumina nanotubes arranged in a hexagonal array. In particular, we consider alumina nanotubes 70 nm in diameter with wall thickness ranging from 6 nm to 15 nm, fabricated successfully by Yang et al. (2012), and calculate homogenized moduli as a function of effective nanotube volume fraction. Only mechanical reinforcement effects are considered given that the present extension does not include surface-energy effects that are important at very small scales. These will be incorporated in our future work. We note, however, that Duan et al. (2006) did not find significant effect of surface energy on homogenized plain strain and axial and transverse shear moduli of nano-porous aluminum with cylindrical porosities having radii greater than 10 nm using the CCA and GSC models. Hence continuum-level calculations remain valid for the considered size ranges, with interaction effects from neighboring nanotubes afforded by our locally-exact homogenization. The elastic moduli of the alumina nanotubes and epoxy matrix used in the present calculations were: $E_{\mathrm{Al_2O_3}} = 166\mathrm{GPa}$, $\nu_{\mathrm{Al_2O_3}} = 0.20$ and $E_m = 4\mathrm{GPa}$, $\nu_m = 0.34$, with the former taken from (Lyytinen et al., 2014). The Young's modulus and Poisson's ratio of the solid were $E_{\mathrm{core}} = 10^{-3}\mathrm{GPa}$ and $\nu_{\mathrm{core}} = 0.34$. These properties effectively produced a porosity in the

region occupied by the solid core which plays the role of the fiber in the analytical solution.

Fig. 4.12 presents homogenized transverse Young's and shear moduli E_T^* and G_T^* normalized by the respective moduli of the epoxy matrix for alumina nanotubes with three wall thickness as a function of the volume fraction of an equivalent solid nanocylinder of the same radius as the nanotube. The chosen mode of data display was motivated by the actual nanotube dimensions that had been successfully realized using the ALD method. The results may also be displayed as a function of the porosity volume fraction. As expected, the homogenized moduli increase with increasing alumina nanotube wall thickness for a fixed volume fraction of an equivalent solid nanocylinder. What is less expected, however, are the very small changes in the homogenized moduli over a large nanotube volume fraction relative to the epoxy matrix modulus when the nanotube wall thickness is 6 nm. In fact, while the transverse Young's modulus increases slightly, the transverse shear modulus initially decreases. In both instances the ratios E_T^*/E_m and G_T^*/G_m remain in the vicinity of unity over a large volume fraction range. This suggests that materials with enhanced functionality due to the presence of thin-walled tubes of varying dimensions may be designed without altering the elastic moduli of the base material.

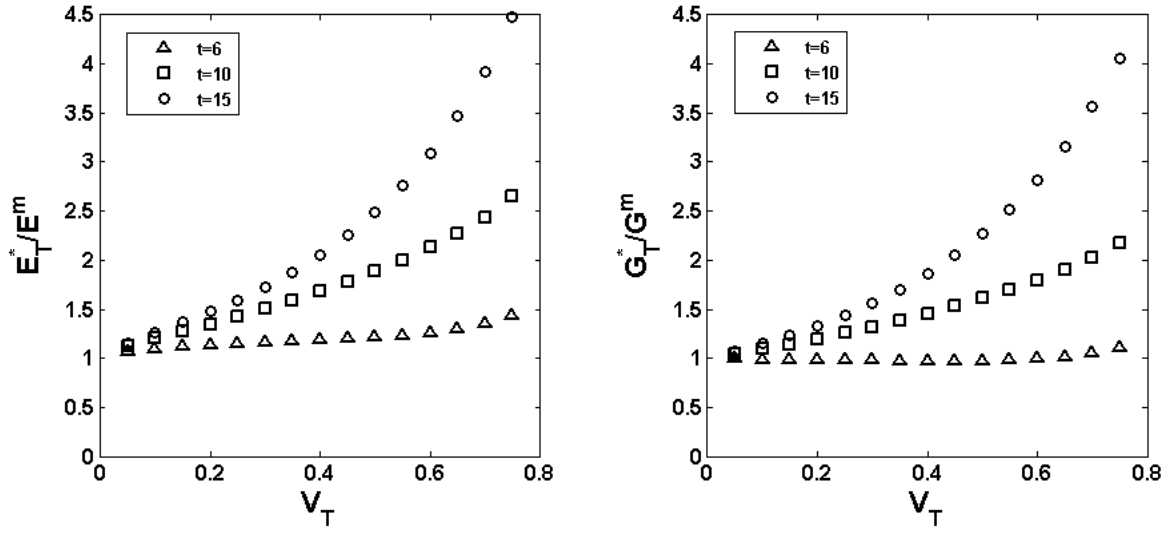

Figure 4.12 Homogenized moduli of alumina nanotube-reinforced epoxy matrix as a function of the nanotube's apparent volume fraction based on the outer radius of 70 nm for different tube thicknesses.

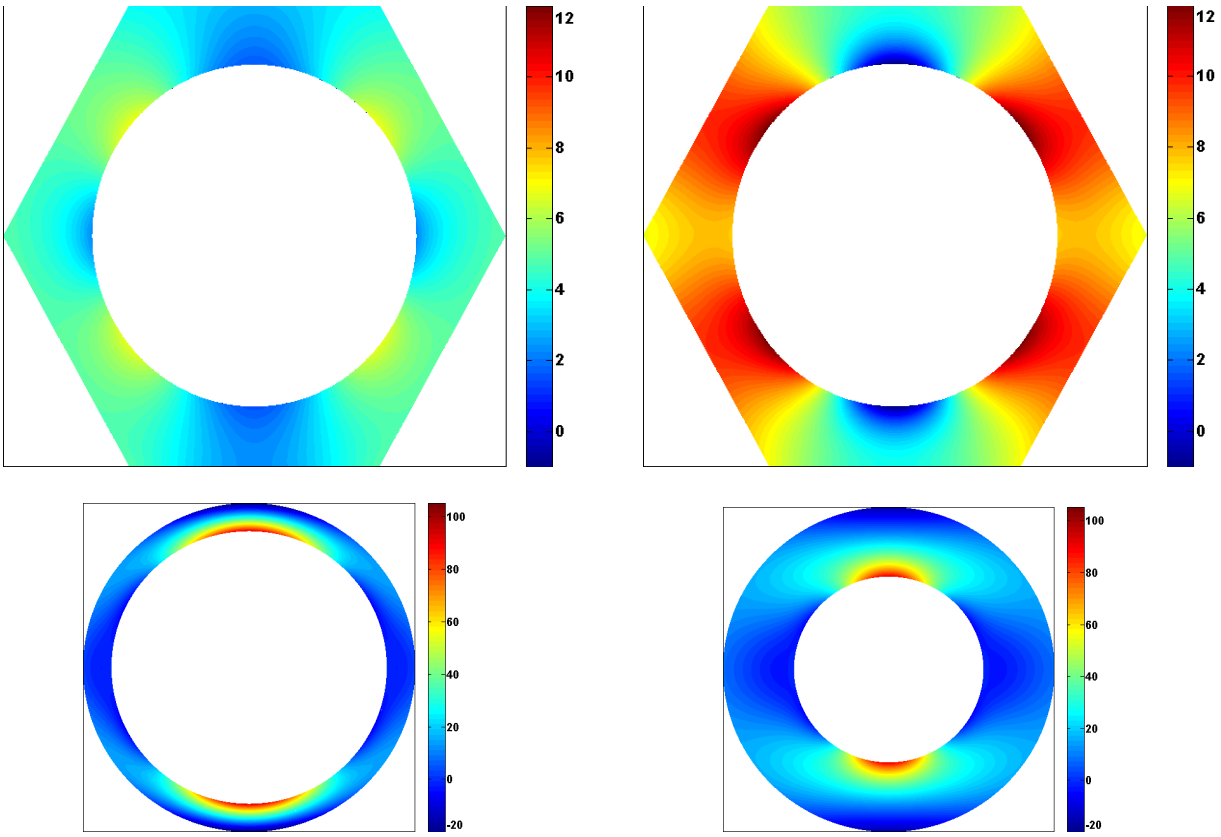

Figure 4.13 Normal stress fields $\sigma_{22}(y_2, y_3)$ in the epoxy matrix and alumina nanotubes of different thickness under uniaxial loading by $\overline{\sigma}_{22} \neq 0$ at the applied strain $\bar{\varepsilon}_{22} = 0.01$.

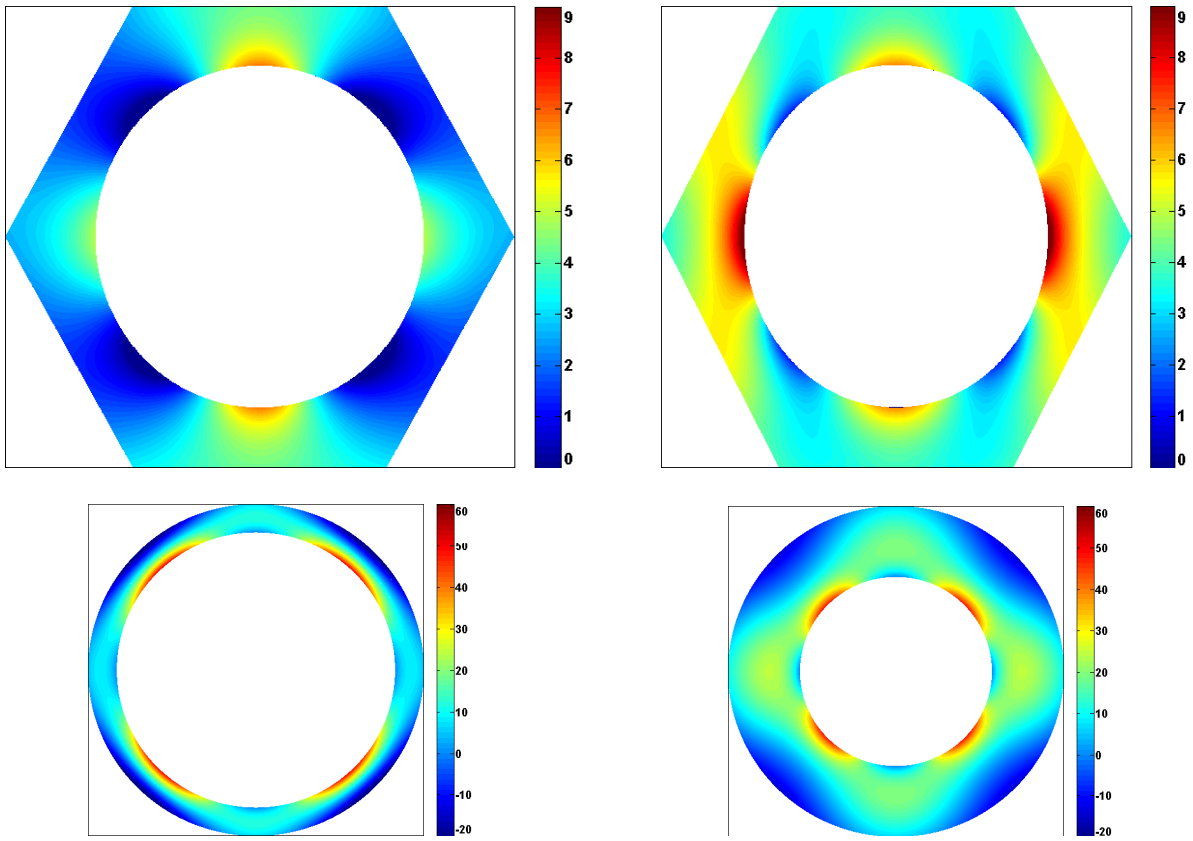

Figure 4.14 Tranverse shear stress fields $\sigma_{23}(y_2, y_3)$ in the epoxy matrix and alumina nanotubes of different thickness under uniaxial loading by $\bar{\sigma}_{23} \neq 0$ at the applied strain $\bar{\varepsilon}_{23} = 0.01$.

Figs. 4.13 and 4.14 illustrate the normal and transverse shear stress fields that arise in the nanotube reinforcement and epoxy matrix under respective uniaxial loadings in the case of nanotubes with the smallest and largest wall thickness at the apparent volume fraction of 0.60 While the maximum normal and transverse shear stresses are comparable in the thick and thin walled nanotubes, the wall thickness dramatically alters the epoxy matrix stress fields, thereby producing large differences in the homogenized moduli seen in Fig. 4.12.

4.3 Summary

In this chapter, we use locally exact homogenization theory to investigate several numerical results and applications of unidirectional composites. The homogenized moduli of both two-phase and three-phase composites with constituents of different moduli contrast are generated via a wide range of fiber volume fractions, and compared with FVDAM, FEM, and other analytical results. The study of the quick convergent moduli and respective stress distribution, as well as the execution time shows that the LEHT is an efficient and stable theory that can be applied into other problems, such as multiscale modeling, nanotube applications…

Thus, three applications are then employed to illustrate the theory's applicability: composite cylinder, laminate, and nanotube reinforcement. The first two multiscale modeling applications prove that LEHT is very efficient in the local stress recovery given certain loading circumstances. Different patterns of structural designs can be accomplished by manipulating the material constituents and geometrical properties of layers of composite cylinder and laminate. Composites with hollow nanotubes that can be fabricated using atomic layer deposition technique are also investigated. Avoiding the large detailed mesh discretization, the theory can easily predict the effects of the thickness of coating/interphase on the homogenized moduli and stress fields, giving researchers more insight about the composites with nanoscale.

The theory can be extended to a more robust tool by including more capabilities: viscoelasticity is one of the most important perspectives. Thus, the LEHT with the consideration of viscoelasticity is introduced in the next chapter to study the long-term behavior, especially for the polymeric composites.

Chapter 5

Locally Exact Homogenization of Viscoelastic Unidirectional Composites

5.1 Introduction

The elasticity-based locally-exact homogenization theory for periodic materials with hexagonal and tetragonal symmetries is extended to accommodate linearly viscoelastic phases via the correspondence principle. The theory employs Fourier series representations for fiber and matrix displacement fields in the cylindrical coordinate system that satisfy exactly equilibrium equations and continuity conditions in the interior of the unit cell. The inseparable exterior problem requires satisfaction of periodic conditions efficiently accomplished using previously introduced balanced variational principle which ensures rapid displacement and stress field convergence in the presence of linearly viscoelastic phases with relatively few harmonic terms. The solution's stability and efficiency, with concomitant simplicity of input data construction, facilitates rapid identification of the impact of phase viscoelasticity and array type on homogenized moduli and local fields in wide ranges of fiber volume fractions. We illustrate the theory's utility by investigating the impact of fiber array type and matrix viscoelastic response (constant Poisson's ratio vs constant bulk modulus) on the homogenized response and local stress fields, reporting previously undocumented differences. Specially, we show that initially small differences between hexagonal and square arrays are magnified substantially by viscoelasticity. New results on the transmission of matrix viscoelastic features to the macroscale are also generated in support of construction of homogenized viscoelastic functions from experimental data.

Section 5.2 describes the locally-exact homogenization theory's extension which is validated in Section 5.3. In section 5.4 we investigate the combined effects of array type and

phase relaxation moduli on the homogenized viscoelastic response and local stress fields, reporting new results, as well as the transmissibility of phase response across scales which is useful in the construction of homogenized response functions from experimental data. Specially, we address the question whether the homogenized creep compliance elements of a unidirectional composite comprised of a viscoelastic matrix that exhibits power-law creep also exhibit power-law creep response in a wide range of fiber volume fractions. Conclusions are presented in Section 5.5.

5.2 Locally-Exact Homogenization via Correspondence Principle

We employ the elastic-viscoelastic correspondence principle to transform the solution for the unit cell problem obtained using the locally-exact homogenization theory for periodic composites with transversely isotropic elastic phases to the viscoelastic solution in the Laplace transform domain, cf. Christensen (1971). Then we use an efficient inversion method proposed by Zakian (1969, 1970), see also Halsted and Brown (1972), to obtain the solution for the homogenized relaxation moduli and creep compliances in the time domain. The alternative approach is to solve the problem in the time domain directly, as for instance of the present approach is that it applies to viscoelasic functions with non-separable and separable kernels alike. The approach, however, depends on the accuracy and efficiency of the chosen Laplace inversion scheme which the Zakian method affords, (Hassanzadeh and Pooladi-Darvish, 2007).

The transformed problem is obtained by replacing the displacement, strain and stress variables in the elastic solution by their Laplace transforms, $u_i \to \hat{u}_i(s)$, $\varepsilon_{ij} \to \hat{\varepsilon}_{ij}(s)$, $\sigma_{ij} \to \hat{\sigma}_{ij}(s)$, and the elastic stiffness matrix elements by their Carson transforms $C_{ijkl} \to s\hat{C}_{ijkl}(s)$, where

$$\hat{C}_{ijkl}(s) = \int_0^s C_{ijkl}(t) e^{-st} dt \tag{5.1}$$

The solution to the unit cell problem in the Laplace-transform domain yields Hill's localization relation, (Hill, 1963), between transformed average strains in the fiber and matrix phases ($k = f, m$) and the transformed homogenized strains in the form

$$\hat{\bar{\boldsymbol{\varepsilon}}}^{(k)} = \hat{\mathbf{A}}^{(k)}(s\hat{\mathbf{C}}^{(f)}, s\hat{\mathbf{C}}^{(m)}, v_f)\hat{\bar{\boldsymbol{\varepsilon}}} \tag{5.2}$$

which are employed in the construction of the homogenized Hooke's law in the transformed

domain. The specified macroscopic strain employed in the determination of the relaxation moduli is $\bar{\varepsilon}(t) = H(t)\bar{\varepsilon}^0$ whose Laplace transform is $\hat{\bar{\varepsilon}}(s) = \bar{\varepsilon}^0/s$. The homogenized Hooke's law in the transform domain is obtained by averaging local constitutive equations in each phase,

$$\hat{\bar{\sigma}} = \frac{1}{V}\sum_k \int s\hat{\mathbf{C}}^{(k)}\hat{\varepsilon}^{(k)} dV_k = \sum_k v_k s\hat{\mathbf{C}}^{(k)}\hat{\bar{\varepsilon}}^{(k)} \tag{5.3}$$

where the phase volume fractions obey the relationship $\sum_k v_k = 1$. Upon use of Eq. (5.2), the homogenized relationship between stress and strain averages then becomes

$$\hat{\bar{\sigma}} = \sum_k v_k s\hat{\mathbf{C}}^{(k)}\hat{\mathbf{A}}^{(k)}\hat{\bar{\varepsilon}} = s\hat{\mathbf{C}}^*\hat{\bar{\varepsilon}} \tag{5.4}$$

where $\hat{\mathbf{C}}^* = \sum_k v_k \hat{\mathbf{C}}^{(k)}\hat{\mathbf{A}}^{(k)}$. In light of the phase volume fraction relationship above, the homogenized relaxation functions for the unit cell in the Laplace transform domain may be written,

$$\hat{\mathbf{C}}^* = \hat{\mathbf{C}}^{(m)} + v_f[\hat{\mathbf{C}}^{(f)} - \hat{\mathbf{C}}^{(m)}]\hat{\mathbf{A}}^{(f)} \tag{5.5}$$

j	K_j	α_j
1	–36902.08210 + 196990.4257i	12.83767675 + 1.666063445i
2	+61277.02524 + 95408.62551i	12.22613209 + 5.012718792i
3	–28916.56288 + 18169.18531i	10.93430308 + 8.409673116i
4	+4655.361138 – 1.901528642i	8.776434715 + 11.92185389i
5	+118.7414011 – 141.3036911i	5.225453361 + 15.72952905i

Table 5.1. Complex coefficients employed in Zakian's inversion formula, Eq. (5.6), from Laplace transform to time domain.

The inversion of the homogenized relaxation functions to the time domain is accomplished by dividing the desired time interval into increments $t = [t_1, t_2, t_3, ..., t_N]$ at which the unit cell problem in the Laplace transform domain is solved through the assignment $s(j) = \alpha_j/t_i$ for $j = 1, 2, ...5$, where the complex values of α_j are given in Table 5.1. The solution of the unit cell problem at the given time enables calculation of the strain concentration matrix for the fiber phase, $\hat{\mathbf{A}}^{(f)}$, in the above equation. The homogenized relaxation functions at the given time are subsequently calculated according to,

$$\mathbf{C}^*(t_i) = \frac{2}{t_i}\sum_{j=1}^{5} \mathrm{Re}[K_j \hat{\mathbf{C}}^*(\alpha_j / t_i)] \tag{5.6}$$

where the complex coefficients K_j are included in Table 5.1. The inversion process can also be referred to the flowchart on next page. The following section provides an overview of the unit cell solution in the Laplace transform domain that enables calculation of the time-domain relaxation functions based on the above inversion method.

5.2.1 Unit Cell Solution Overview

The solution to the elastic unit cell problem representative of periodic hexagonal and square arrays of transversely isotropic fibers embedded in (transversely) isotropic matrix, Fig. 2.1, has been provided by Wang and Pindera (2015, 2016). Here we summarize the main results in order to make the employed replacement scheme and the calculation of the strain concentration matrices in the transformed domain transparent.

The solution for the displacement field in the fiber and matrix phases of the unit cell, which leads to the determination of local strains, stresses and the homogenized moduli, is carried out within the homogenization theory's framework wherein the global coordinates $\mathbf{x} = (x_1, x_2, x_3)$ describe the average response of the entire periodic array, and the local coordinates $\mathbf{y} = (y_1, y_2, y_3)$ describe the interior unit cell response, (Papanicolau et al., 1978; Suquet, 1985). Accordingly, a two-scale displacement field representation is employed in the individual phases whose Laplace transform is

$$\hat{u}_i^{(k)}(\mathbf{x}, \mathbf{y}, s) = \hat{\bar{\varepsilon}}_{ij}(s) x_j + \hat{u}_i'^{(k)}(\mathbf{y}, s) \tag{5.7}$$

where the fluctuating transformed displacement components $\hat{u}_i'^{(k)}$ caused by the material's heterogeneity are functions of the local coordinates (y_2, y_3, t) given the unidirectional constraint along the x_1 direction by continuous reinforcement. The above displacement field generates the local strains

$$\hat{\varepsilon}_{ij}^{(k)}(\mathbf{y}, s) = \hat{\bar{\varepsilon}}_{ij}(s) + \hat{\varepsilon}_{ij}'^{(k)}(\mathbf{y}, s) \tag{5.8}$$

from which local stresses follow, with continuous reinforcement yielding the constraint $\hat{\bar{\varepsilon}}_{11}^{(k)} = \hat{\bar{\varepsilon}}_{11}$. The solution for the fluctuating displacement field in the fiber and matrix phases is obtained from the Navier's equations in the transformed domain in cylindrical coordinates

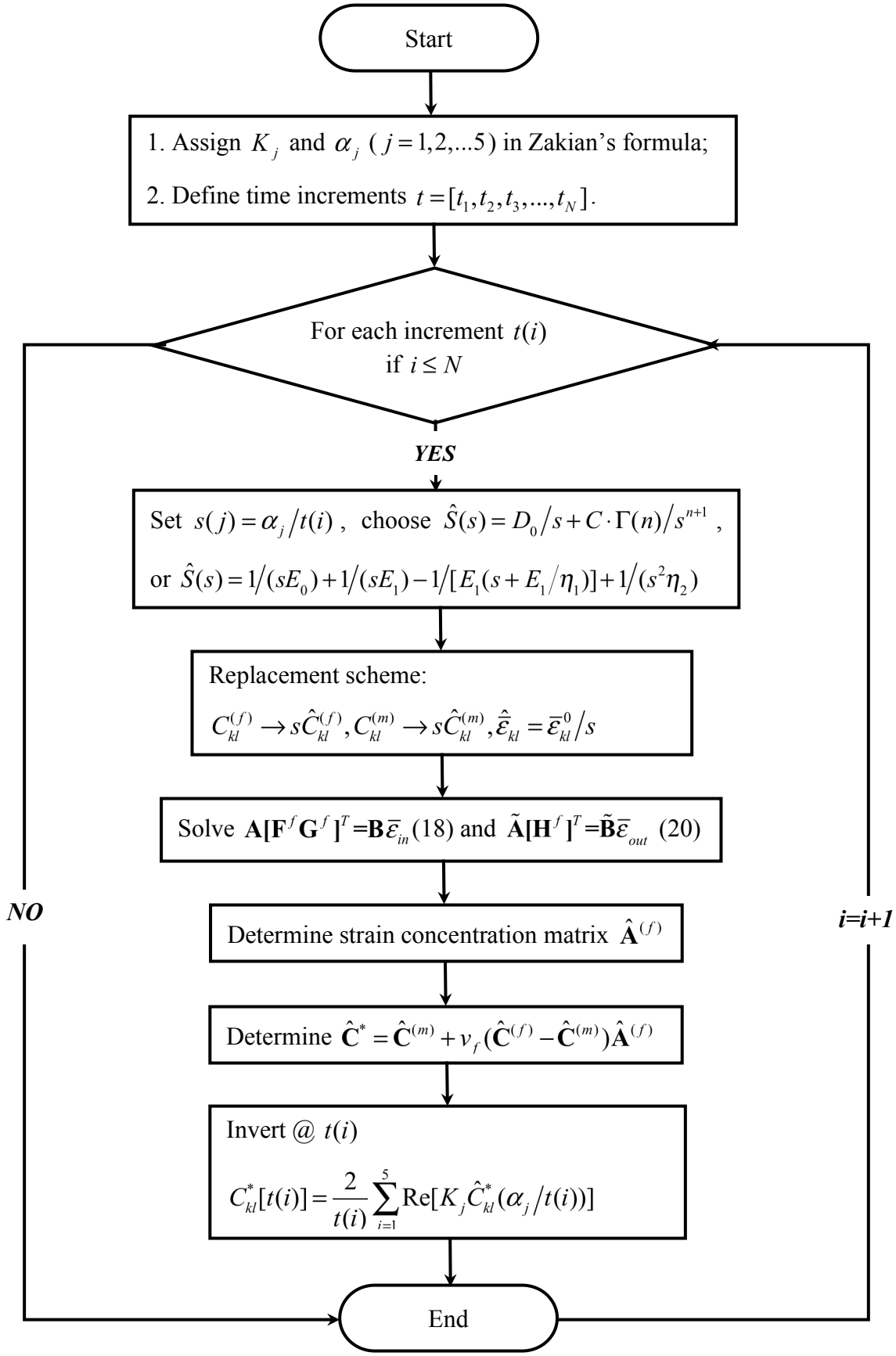
Start
1. Assign K_j and α_j ($j=1,2,...5$) in Zakian's formula;
2. Define time increments $t=[t_1,t_2,t_3,...,t_N]$.
For each increment $t(i)$
if $i \le N$
YES
Set $s(j)=\alpha_j/t(i)$, choose $\hat{S}(s)=D_0/s+C\cdot\Gamma(n)/s^{n+1}$,
or $\hat{S}(s)=1/(sE_0)+1/(sE_1)-1/[E_1(s+E_1/\eta_1)]+1/(s^2\eta_2)$
Replacement scheme:
$C_{kl}^{(f)}\to s\hat{C}_{kl}^{(f)}, C_{kl}^{(m)}\to s\hat{C}_{kl}^{(m)}, \hat{\bar{\varepsilon}}_{kl}=\bar{\varepsilon}_{kl}^0/s$
Solve $\mathbf{A}[\mathbf{F}^f\mathbf{G}^f]^T=\mathbf{B}\bar{\varepsilon}_{in}$ (18) and $\tilde{\mathbf{A}}[\mathbf{H}^f]^T=\tilde{\mathbf{B}}\bar{\varepsilon}_{out}$ (20)
NO
Determine strain concentration matrix $\hat{\mathbf{A}}^{(f)}$
i=i+1
Determine $\hat{\mathbf{C}}^*=\hat{\mathbf{C}}^{(m)}+v_f(\hat{\mathbf{C}}^{(f)}-\hat{\mathbf{C}}^{(m)})\hat{\mathbf{A}}^{(f)}$
Invert @ $t(i)$
$C_{kl}^*[t(i)]=\frac{2}{t(i)}\sum_{i=1}^{5}\mathrm{Re}[K_j\hat{C}_{kl}^*(\alpha_j/t(i))]$
End

$$\frac{\partial^2 \hat{u}_z'}{\partial r^2}+\frac{1}{r}\frac{\partial \hat{u}_z'}{\partial r}+\frac{1}{r^2}\frac{\partial^2 \hat{u}_z'}{\partial \theta^2}=0$$

$$\hat{C}_{22}\left(\frac{\partial^2 \hat{u}_r'}{\partial r^2}+\frac{1}{r}\frac{\partial \hat{u}_r'}{\partial r}-\frac{\hat{u}_r}{r^2}\right)+\frac{\hat{C}_{22}-\hat{C}_{23}}{2r^2}\frac{\partial^2 \hat{u}_r'}{\partial \theta^2}+\frac{\hat{C}_{22}+\hat{C}_{23}}{2r}\frac{\partial^2 \hat{u}_\theta'}{\partial r\partial \theta}-\frac{3\hat{C}_{22}-\hat{C}_{23}}{2r^2}\frac{\partial \hat{u}_\theta'}{\partial \theta}=0 \tag{5.9}$$

$$\frac{\hat{C}_{22}-\hat{C}_{23}}{2}\left(\frac{\partial^2 \hat{u}_\theta'}{\partial r^2}+\frac{1}{r}\frac{\partial \hat{u}_\theta'}{\partial r}-\frac{\hat{u}_\theta'}{r^2}\right)+\frac{\hat{C}_{22}}{r^2}\frac{\partial^2 \hat{u}_\theta'}{\partial \theta^2}+\frac{\hat{C}_{22}+\hat{C}_{23}}{2r}\frac{\partial^2 \hat{u}_r'}{\partial r\partial \theta}+\frac{3\hat{C}_{22}-\hat{C}_{23}}{2r^2}\frac{\partial \hat{u}_r'}{\partial \theta}=0$$

which facilitate exact enforcement of displacement and traction continuity at the fiber/matrix interface one harmonic at a time. This is referred to as the interior problem. The inseparable exterior problem involves satisfaction of the periodicity conditions in Cartesian coordinates,

$$\hat{u}_i(\mathbf{x}_0+\mathbf{d},s)=\hat{u}_i(\mathbf{x}_0,s)+\hat{\bar{\varepsilon}}_{ij}d_j,\ \hat{t}_i(\mathbf{x}_0+\mathbf{d},s)=-\hat{t}_i(\mathbf{x}_0,s) \tag{5.10}$$

where $(\mathbf{x_o},\mathbf{x_o}+\mathbf{d})\in S$, S is the unit cell boundary, $\mathbf{d}$ is a characteristic distance that defines the unit cell array microstructure, and $\hat{t}_i=\hat{\sigma}_{ji}n_j$ from Cauchy's relation, with n_j denoting the jth component of the unit normal to the boundary. Solution of the exterior problem which cannot be solved one harmonic at a time entails minimization of a functional leading to the balanced variational principle in the final form

$$\int_{S_T}\delta\hat{u}_i(\hat{t}_i-\hat{t}_i^o)dS+\int_{S_u}\delta\hat{t}_i(\hat{u}_i-\hat{u}_i^o)dS=0 \tag{5.11}$$

where $\hat{\mathbf{t}}=\hat{\mathbf{t}}^{\mathbf{o}}$ and $\hat{\mathbf{u}}=\hat{\mathbf{u}}^{\mathbf{o}}$ are periodic traction and displacement constraints imposed on S_t and S_u, respectively. The displacement and traction components on the six and four surfaces of hexagonal and rectangular unit cells, respectively are related through the periodicity conditions, Eqs. (5.10).

5.2.2 Displacement and Stress Fields in the Transform Domain

The solution for the transformed fluctuating out-of-plane and in-plane displacements $\hat{u}_z'$ and $\hat{u}_r'$, $\hat{u}_\theta'$, respectively, in the fiber and matrix phases is obtained in the form

$$\begin{aligned}
\hat{u}_z' &= \sum_{n=1}^{\infty} a\left[\left(\xi^n\hat{H}_{n1}^{(k)}+\xi^{-n}\hat{H}_{n3}^{(k)}\right)\cos n\theta+\left(\xi^n\hat{H}_{n2}^{(k)}+\xi^{-n}\hat{H}_{n4}^{(k)}\right)\sin n\theta\right]\\
\hat{u}_r' &= \hat{F}_{01}^{(k)}a\xi+\hat{F}_{02}^{(k)}a\xi^{-1}+\sum_{n=2}^{\infty}\sum_{j=1}^{4}a\xi^{p_{nj}}\left[\hat{F}_{nj}^{(k)}\cos n\theta+\hat{G}_{nj}^{(k)}\sin n\theta\right]\\
\hat{u}_\theta' &= \sum_{n=2}^{\infty}\sum_{j=1}^{4}a\beta_{nj}\xi^{p_{nj}}\left[\hat{F}_{nj}^{(k)}\sin n\theta-\hat{G}_{nj}^{(k)}\cos n\theta\right]
\end{aligned} \tag{5.12}$$

where rigid body terms associated with $n=0$ term in the expression for $\hat{u}_z'$, and $n=1$ terms in the expressions for $\hat{u}_r'$, $\hat{u}_\theta'$ have been excluded by fixing the fiber at the origin. $\hat{H}_{nj}^{(k)}, \hat{F}_{nj}^{(k)}, \hat{G}_{nj}^{(k)} (j=1,2,3,4)$ are unknown coefficients, $\xi = r/a$ is the nondimensionalized radial coordinate with respect to the fiber radius a, and the four eigenvalues p_{nj} are $p_{n1}=n+1$, $p_{n2}=n-1$, $p_{n3}=-(n+1)$, $p_{n4}=-(n-1)$ with the corresponding eigenvectors $\beta_{nj}^{(k)}$ given by

$$\hat{\beta}_{nj} = \frac{2\hat{C}_{22}(1-p_{nj}^2)+(\hat{C}_{22}-\hat{C}_{23})n^2}{n\cdot[(\hat{C}_{22}+\hat{C}_{23})p_{nj}-3\hat{C}_{22}+\hat{C}_{23}]}$$

To ensure that the displacements remain bounded in the fiber, we set $\hat{H}_{n3}^{(f)} = \hat{H}_{n4}^{(f)} = 0$ for $n \geq 1$ in the case of the out-of-plane displacement, and $\hat{F}_{02}^{(f)} = 0$ and $\hat{F}_{n3}^{(f)} = \hat{F}_{n4}^{(f)} = 0$, $\hat{G}_{n3}^{(f)} = \hat{G}_{n4}^{(f)} = 0$ for $n \geq 2$ in the case of the in-plane displacements. The remaining coefficients $\hat{H}_{nj}^{(k)}, \hat{F}_{nj}^{(k)}, \hat{G}_{nj}^{(k)}$ in the matrix phase ($k=m$) are subsequently obtained in terms of the fiber coefficients $\hat{H}_{nj}^{(f)}$, $\hat{F}_{nj}^{(f)}$ and $\hat{G}_{nj}^{(f)}$ from the interfacial fluctuating displacement and traction continuity conditions are the fiber/matrix interphase. The interfacial traction components are obtained from Hooke's law and strain-displacement relations,

$$\begin{aligned}
\hat{\sigma}_{zr} &= 2s\hat{C}_{66}^{(k)}\hat{\bar{\varepsilon}}_{zr} + s\hat{C}_{66}^{(k)}\sum_{n=1}^{\infty} n\left[\left(\xi^{n-1}\hat{H}_{n1}^{(k)} - \xi^{-n-1}\hat{H}_{n3}^{(k)}\right)\cos n\theta + \left(\xi^{n-1}\hat{H}_{n2}^{(k)} - \xi^{-n-1}\hat{H}_{n4}^{(k)}\right)\sin n\theta\right] \\
\hat{\sigma}_{rr} &= s\hat{C}_{12}^{(k)}\bar{\varepsilon}_{zz} + s\hat{C}_{22}^{(k)}\bar{\varepsilon}_{rr} + s\hat{C}_{23}^{(k)}\bar{\varepsilon}_{\theta\theta} + s(\hat{C}_{22}^{(k)}+\hat{C}_{23}^{(k)})\hat{F}_{01} - s(\hat{C}_{22}^{(k)}-\hat{C}_{23}^{(k)})\hat{F}_{02}\xi^{-2} \\
&\quad + s\sum_{n=2}^{\infty}\sum_{j=1}^{4}\hat{P}_{nj}^{(k)}\xi^{p_{nj}-1}\left(\hat{F}_{nj}^{(k)}\cos n\theta + \hat{G}_{nj}^{(k)}\sin n\theta\right) \\
\hat{\sigma}_{r\theta} &= s(\hat{C}_{22}^{(k)}-\hat{C}_{23}^{(k)})\hat{\bar{\varepsilon}}_{r\theta} + s\sum_{n=2}^{\infty}\sum_{j=1}^{4}\hat{R}_{nj}^{(k)}\xi^{p_{nj}-1}\left(\hat{F}_{nj}^{(k)}\sin n\theta - \hat{G}_{nj}^{(k)}\cos n\theta\right)
\end{aligned} \tag{5.13}$$

in which $\hat{P}_{nj}^{(k)} = \hat{C}_{22}^{(k)}p_{nj} + \hat{C}_{23}^{(k)}(1+n\hat{\beta}_{nj}^{(k)})$, and $\hat{R}_{nj}^{(k)} = (\hat{C}_{22}^{(k)}-\hat{C}_{23}^{(k)})/2\cdot\left[(p_{nj}-1)\hat{\beta}_{nj}^{(k)} - n\right]$.

5.2.3 Interfacial Continuity

The axial shear problem is decoupled from the transverse normal and shear problems. Hence applying the two interfacial continuity conditions on the axial displacement and axial shear stress

at $r=a$ and using the orthogonality of $\cos n\theta$ and $\sin n\theta$ terms, we obtain the following relations between coating and fiber coefficients associated with different-order harmonic terms for $n\geq 1$,

$$\hat{\mathbf{H}}_n^{(m)}=\hat{\mathbf{c}}_1\hat{\mathbf{H}}_n^{(f)}+\delta_{n1}\hat{\mathbf{c}}_2[2\hat{\bar{\varepsilon}}_{12}\ \ 2\hat{\bar{\varepsilon}}_{13}]^T \tag{5.14}$$

where $\hat{\mathbf{H}}_n^{(f)}=[\hat{H}_{n1}^{(f)},\hat{H}_{n2}^{(f)}]^T$, $\hat{\mathbf{H}}_n^{(m)}=[\hat{H}_{n1}^{(m)},\hat{H}_{n2}^{(m)},\hat{H}_{n3}^{(m)},\hat{H}_{n4}^{(m)}]^T$, and the matrices $\hat{\mathbf{c}}_1,\hat{\mathbf{c}}_2$ are given below. The Kronecker delta term δ_{n1} is present because the average strains are introduced only through the $n=1$ terms $\cos\theta$ and $\sin\theta$. Eq. (5.14) can be expressed explicitly as follows:

$$\begin{bmatrix}\hat{H}_{n1}\\ \hat{H}_{n2}\\ \hat{H}_{n3}\\ \hat{H}_{n4}\end{bmatrix}^{(m)}=\begin{bmatrix}\hat{c}_1 & 0\\ 0 & \hat{c}_1\\ \hat{c}_2 & 0\\ 0 & \hat{c}_2\end{bmatrix}\begin{bmatrix}\hat{H}_{n1}\\ \hat{H}_{n2}\end{bmatrix}^{(f)}+\delta_{n1}\hat{c}_2\begin{bmatrix}-1 & 0\\ 0 & -1\\ 1 & 0\\ 0 & 1\end{bmatrix}\begin{bmatrix}2\hat{\bar{\varepsilon}}_{12}\\ 2\hat{\bar{\varepsilon}}_{13}\end{bmatrix} \tag{5.15}$$

where $\hat{c}_1=(\hat{C}_{66}^{(m)}+\hat{C}_{66}^{(f)})\big/2\hat{C}_{66}^{(m)}$, and $\hat{c}_2=1-\hat{c}_1$.

The transverse normal and shear problems in the $r-\theta$ plane are coupled. Hence applying the four interfacial continuity conditions, and using orthogonality of $\cos n\theta$ and $\sin n\theta$ terms, we obtain the following relations between coating and fiber coefficients for $n=0$

$$\hat{\mathbf{F}}_0^{(m)}=\hat{\mathbf{b}}_0\hat{F}_{01}^{(f)}+\hat{\mathbf{c}}_0\hat{\bar{\varepsilon}}_{11}+\hat{\mathbf{d}}_0(\hat{\bar{\varepsilon}}_{22}+\hat{\bar{\varepsilon}}_{33}) \tag{5.16}$$

where $\hat{\mathbf{F}}_0^{(m)}=[\hat{F}_{01}^{(m)},\hat{F}_{02}^{(m)}]^T$, and the matrices $\hat{\mathbf{b}}_0,\hat{\mathbf{c}}_0$ and $\hat{\mathbf{d}}_0$ are given below.

$$\begin{aligned}&\hat{b}_{01}=\frac{(\hat{C}_{22}^{(f)}+\hat{C}_{23}^{(f)})+(\hat{C}_{22}^{(m)}-\hat{C}_{23}^{(m)})}{2\hat{C}_{22}^{(m)}},\quad \hat{c}_{01}=\frac{\hat{C}_{12}^{(f)}-\hat{C}_{12}^{(m)}}{2\hat{C}_{22}^{(m)}},\quad \hat{d}_{01}=-\frac{1}{2}\hat{b}_{02}\\ &\hat{b}_{02}=\frac{(\hat{C}_{22}^{(m)}+\hat{C}_{23}^{(m)})-(\hat{C}_{22}^{(f)}+\hat{C}_{23}^{(f)})}{2\hat{C}_{22}^{(m)}},\quad \hat{c}_{02}=-\hat{c}_{01},\qquad \hat{d}_{02}=-\hat{d}_{01}\end{aligned} \tag{5.17}$$

For $n\geq 2$,

$$\begin{aligned}\hat{\mathbf{A}}_n^{(m)}\hat{\mathbf{F}}_n^{(m)}&=\hat{\mathbf{A}}_n^{(f)}\hat{\mathbf{F}}_n^{(f)}+\delta_{n2}\hat{\mathbf{A}}_0(\hat{\bar{\varepsilon}}_{22}-\hat{\bar{\varepsilon}}_{33})\\ \hat{\mathbf{A}}_n^{(m)}\hat{\mathbf{G}}_n^{(m)}&=\hat{\mathbf{A}}_n^{(f)}\hat{\mathbf{G}}_n^{(f)}+\delta_{n2}\hat{\mathbf{A}}_0 2\hat{\bar{\varepsilon}}_{23}\end{aligned} \tag{5.18}$$

where $\hat{\mathbf{F}}_n^{(m)}=[\hat{F}_{n1}^{(m)},\hat{F}_{n2}^{(m)},\hat{F}_{n3}^{(m)},\hat{F}_{n4}^{(m)}]^T$, $\hat{\mathbf{F}}_n^{(f)}=[\hat{F}_{n1}^{(f)},\hat{F}_{n2}^{(f)}]^T$, $\hat{\mathbf{G}}_n^{(m)}=[\hat{G}_{n1}^{(m)},\hat{G}_{n2}^{(m)},\hat{G}_{n3}^{(m)},\hat{G}_{n4}^{(m)}]^T$, $\hat{\mathbf{G}}_n^{(f)}=[\hat{G}_{n1}^{(f)},\hat{G}_{n2}^{(f)}]^T$, and the matrices $\hat{\mathbf{A}}_n^{(m)},\hat{\mathbf{A}}_n^{(f)}$ and $\hat{\mathbf{A}}_0$ are given below:

$$\hat{A}_n^{(m)} = \begin{bmatrix} 1 & 1 & 1 & 1 \\ \hat{\beta}_{n1} & \hat{\beta}_{n2} & \hat{\beta}_{n3} & \hat{\beta}_{n4} \\ \hat{P}_{n1} & \hat{P}_{n2} & \hat{P}_{n3} & \hat{P}_{n4} \\ \hat{R}_{n1} & \hat{R}_{n2} & \hat{R}_{n3} & \hat{R}_{n4} \end{bmatrix}^{(m)}, \quad \hat{A}_n^{(f)} = \begin{bmatrix} 1 & 1 \\ \hat{\beta}_{n1} & \hat{\beta}_{n2} \\ \hat{P}_{n1} & \hat{P}_{n2} \\ \hat{R}_{n1} & \hat{R}_{n2} \end{bmatrix}^{(f)}, \quad \hat{A}_0 = \frac{1}{2} \begin{bmatrix} 0 \\ 0 \\ (\hat{C}_{22}^{(f)} - \hat{C}_{23}^{(f)}) - (\hat{C}_{22}^{(m)} - \hat{C}_{23}^{(m)}) \\ (\hat{C}_{22}^{(m)} - \hat{C}_{23}^{(m)}) - (\hat{C}_{22}^{(f)} - \hat{C}_{23}^{(f)}) \end{bmatrix} \tag{5.19}$$

The Kronecker delta term δ_{n2} is present because the average strains are introduced only through the $n=2$ terms $\cos 2\theta$ and $\sin 2\theta$.

5.2.4 Periodic Boundary Conditions

The unknown coefficients $\hat{\mathbf{H}}_n^{(f)}, \hat{\mathbf{F}}_n^{(f)}, \hat{\mathbf{G}}_n^{(f)}$ are determined by applying the variational principle, Eq. (5.11), with the surface displacements and tractions on the opposite faces of the unit cell related through the periodic boundary conditions. Use of the two-scale displacement representation given by Eq. (5.7) in the periodic displacement boundary conditions, Eq. (5.10), reduces these periodicity conditions to constraints on the fluctuating displacement components. Since the out-of-plane and inplane problems are uncoupled, the coefficients $\hat{\mathbf{F}}_n^{(f)}, \hat{\mathbf{G}}_n^{(f)}$ are found independently of the coefficients $\hat{\mathbf{H}}_n^{(f)}$ upon utilizing the reduced periodicity conditions in the variational principle. Implementing the reduced periodicity conditions for the inplane problem in the variational principle, we have following system of equations for the unknown coefficients $\hat{\mathbf{F}}_n^{(f)}, \hat{\mathbf{G}}_n^{(f)}$,

$$\hat{\mathbf{A}}_{in}[\hat{\mathbf{F}}^{(f)}\hat{\mathbf{G}}^{(f)}] = \hat{\mathbf{B}}_{in}\hat{\bar{\boldsymbol{\varepsilon}}}_{in} \tag{5.20}$$

where $\hat{\bar{\boldsymbol{\varepsilon}}}_{in} = [\hat{\bar{\varepsilon}}_{11}, \hat{\bar{\varepsilon}}_{22}, \hat{\bar{\varepsilon}}_{33}, 2\hat{\bar{\varepsilon}}_{23}]^T$, and $\hat{\mathbf{F}}^{(f)} = [\hat{F}_1^{(f)}, ...\hat{F}_{N_{\max}}^{(f)}]$, $\mathbf{G}^{(f)} = [\hat{G}_1^{(f)}, ...\hat{G}_{N_{\max}}^{(f)}]$. Similarly, for the out-of-plane loading, the variational principle yields the system of equations for the unknown coefficients $\hat{\mathbf{H}}_n^{(f)}$,

$$\hat{\mathbf{A}}_{out}\hat{\mathbf{H}}^{(f)} = \hat{\mathbf{B}}_{out}\hat{\bar{\boldsymbol{\varepsilon}}}_{out} \tag{5.21}$$

where $\hat{\bar{\boldsymbol{\varepsilon}}}_{out} = [2\hat{\bar{\varepsilon}}_{12}, 2\hat{\bar{\varepsilon}}_{13}]^T$ and $\hat{\mathbf{H}}^{(f)} = [\hat{H}_1^{(f)}, ...\hat{H}_{N_{\max}}^{(f)}]$. The elements of the matrices $\hat{\mathbf{A}}_{in}, \hat{\mathbf{A}}_{out}$ and $\hat{\mathbf{B}}_{in}, \hat{\mathbf{B}}_{out}$ are obtained in terms of surface integrals along the six sides $S_1, ...S_6$ of the unit cell. Similar results are obtained for rectangular or square unit cells with four exterior surfaces, see (Wang and Pindera, 2015) for details.

5.2.5 Strain Concentration Matrix Determination

To determine the fiber strain concentration matrix, the average fiber strains are obtained in closed form upon integrating the local expressions over the phase cross section. The resulting expressions contain only the applied average strains and the displacement coefficients associated with the $n=1$ harmonic in the case of axial shear strains, and the $n=0,2$ harmonics in the case of transverse normal and shear strains

$$\begin{aligned}
\hat{\bar{\varepsilon}}_{22}^{(f)} &= \hat{\bar{\varepsilon}}_{22} + \hat{F}_{01}^{(f)} + \frac{3(\hat{C}_{22}^{(f)} + \hat{C}_{23}^{(f)})}{4\hat{C}_{22}^{(f)}} \hat{F}_{21}^{(f)} + \hat{F}_{22}^{(f)} & \qquad \hat{\bar{\varepsilon}}_{11}^{(f)} &= \hat{\bar{\varepsilon}}_{11} \\
\hat{\bar{\varepsilon}}_{33}^{(f)} &= \hat{\bar{\varepsilon}}_{33} + \hat{F}_{01}^{(f)} - \frac{3(\hat{C}_{22}^{(f)} + \hat{C}_{23}^{(f)})}{4\hat{C}_{22}^{(f)}} \hat{F}_{21}^{(f)} - \hat{F}_{22}^{(f)} & \qquad \hat{\bar{\varepsilon}}_{12}^{(f)} &= \hat{\bar{\varepsilon}}_{12} + \frac{1}{2}\hat{H}_{11}^{(f)} \\
\hat{\bar{\varepsilon}}_{23}^{(f)} &= \hat{\bar{\varepsilon}}_{23} + \frac{3(\hat{C}_{22}^{(f)} + \hat{C}_{23}^{(f)})}{4\hat{C}_{22}^{(f)}} \hat{G}_{21}^{(f)} + \hat{G}_{22}^{(f)} & \qquad \hat{\bar{\varepsilon}}_{13}^{(k)} &= \hat{\bar{\varepsilon}}_{13} + \frac{1}{2}\hat{H}_{12}^{(k)}
\end{aligned} \tag{5.22}$$

in which $\hat{\bar{\varepsilon}}_{11}^{(f)} = \hat{\bar{\varepsilon}}_{11}$ is because uniaxial reinforcement.

The column of the fiber strain matrix $\hat{\mathbf{A}}^{(f)}$ are generated by solving the unit cell problem for one non-zero average strain applied at a time, with the remaining average strains kept zero. The solution produces the unknown coefficients $\hat{\mathbf{F}}_n^{(f)}, \hat{\mathbf{G}}_n^{(f)}$ or $\hat{\mathbf{H}}_n^{(f)}$ for the applied loading, and thus the average fiber strains. The elements of the strain concentration matrix occupying the column that corresponds to the applied non-zero average strain are then obtained by taking the ratios of the averaged strain in the fiber phase and the average applied strain.

5.3 Validation

We validate the solution by first demonstrating the rapid convergence of relaxation moduli and local stress fields with the number of harmonics, and then comparing the solution's predictions with those reported in the literature based on finite-volume calculations of comparable accuracy as the Q-9 based finite-element results. We also compare the locally-exact theory predictions with experimental response of off-axis graphite-epoxy tension specimens subjected to creep loading.

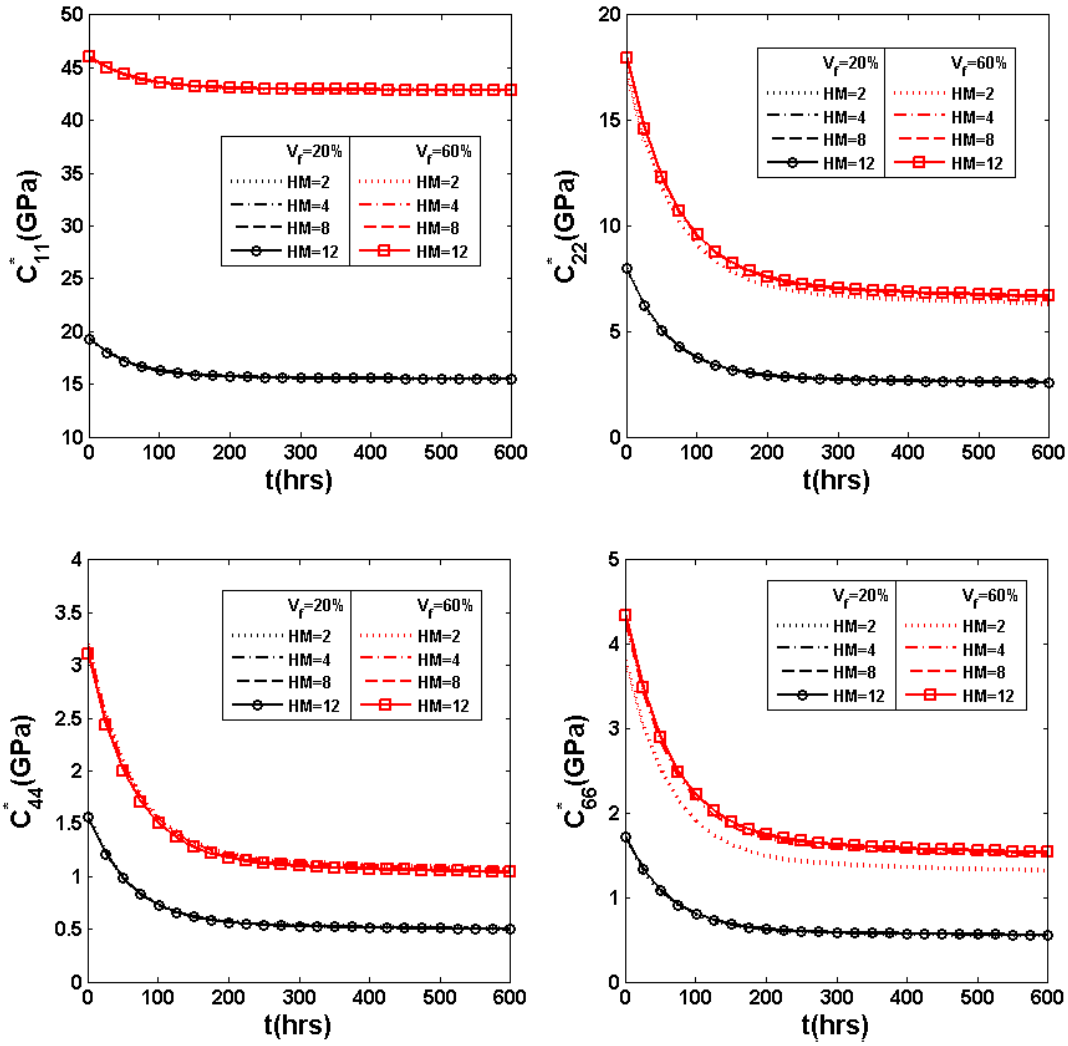

Figure 5.2 Convergence study of selected relaxation functions as a function number of harmonics for a glass/epoxy unidirectional composite with low and high fiber volume fraction.

5.3.1 Convergence Study

We consider hexagonal and square unit cells representative of a unidirectional composite comprised of a polymeric matrix reinforced by glass fibers employed by (Cavalcante and Marques, 2014) for validation of the generalized FVDAM theory with linearly viscoelastic phases. The glass fibers were taken as elastic and the polymeric matrix was modeled as an isotropic four-parameter fluid comprised of Maxwell and Kelvin elements connected in series. The creep compliance in tension for this model takes the form

$$S_{11}(t) = \frac{1}{E_0} + \frac{1}{E_1}(1 - e^{-(E_1/\eta_1)t}) + \frac{t}{\eta_2} \tag{5.23}$$

where $E_0 = 3.27\text{GPa}$, $E_1 = 1.8\text{GPa}$, $\eta_1 = 300\text{GPa}\cdot\text{h}$, $\eta_2 = 8000\text{GPa}\cdot\text{h}$. This was obtained from the generalized Kelvin model by setting the spring element stiffness in one of the Kevin elements to a very small value, $E_2 = 10^{-12}\text{GPa}$. The matrix Poisson's ratio was assumed to remain constant at $\nu = 0.38$. The fiber elastic moduli are $E = 68.77\text{GPa}$ and $\nu = 0.21$.

Using the above parameters, we investigate convergence of the homogenized moduli and local stress fields with the number of harmonics in the displacement field representation, see Eq. (5.12), for two non-dilute fiber volume fractions, namely 0.20 and 0.60. Figure 5.2 illustrates convergence behavior of the homogenized relaxation stiff elements $C^*_{11}(t)$, $C^*_{22}(t)$, $C^*_{44}(t)$ and $C^*_{66}(t)$ with the harmonics number as a parameter for *n*=2,4,8 and 12. While the convergence of these moduli is rapid at the low volume fraction, the high volume fraction requires somewhat greater number of harmonics for convergence in the considered time interval. The axial shear relaxation modulus $C^*_{66}(t)$ exhibits the slowest convergence, requiring 4 harmonics in the displacement field representation, followed by the tensile transverse relaxation modulus $C^*_{22}(t)$. In contrast, the convergence of the local stresses requires greater number of harmonics. For instance, the transverse shear stress field $\sigma_{23}(y_2, y_3, t)$ for the high fiber volume fraction converges with 8 harmonics under pure shear loading by $\bar{\varepsilon}_{23} = H(t)\varepsilon^o_{23}$ whereas the corresponding homogenized relaxation modulus requires fewer harmonics as seen in Fig. 5.2. Here, we illustrate the convergence of the axial shear stress field $\sigma_{12}(y_2, y_3, t)$ under pure axial shear loading by $\bar{\varepsilon}_{12} = H(t)\varepsilon^o_{12}$ at three different times for $n = 2$, 8 and 12 as this loading requires 4 harmonics to yield converged homogenized relaxation response observed in Fig. 5.2 at the high fiber volume fraction where interaction between fibers has greater impact than at the low fraction. Fig 5.3 illustrates the axial shear stress fields at the three different times $t = 0$, 150 and 600 hours for the three harmonics. For $n = 2$ harmonics, both the matrix and fiber shear stress fields are poorly predicted. Increasing the number of harmonics to 8 produces a stress field that differs little from that obtained using 12 harmonics at the considered times.

2 harmonics 8 harmonics 12 harmonics

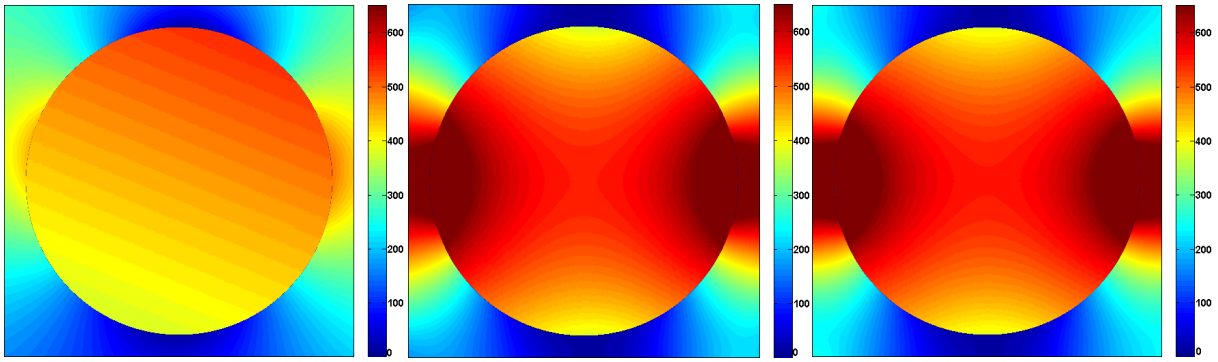

(a) Time = 0 hours

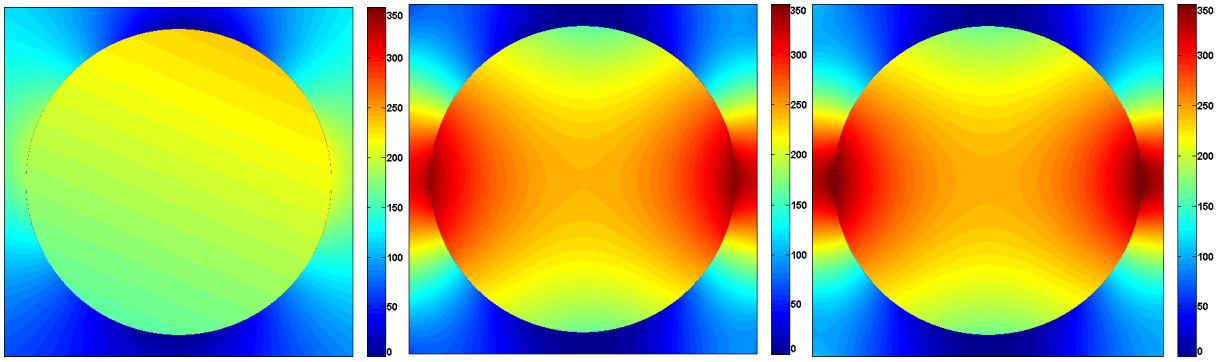

b) Time = 150 hours

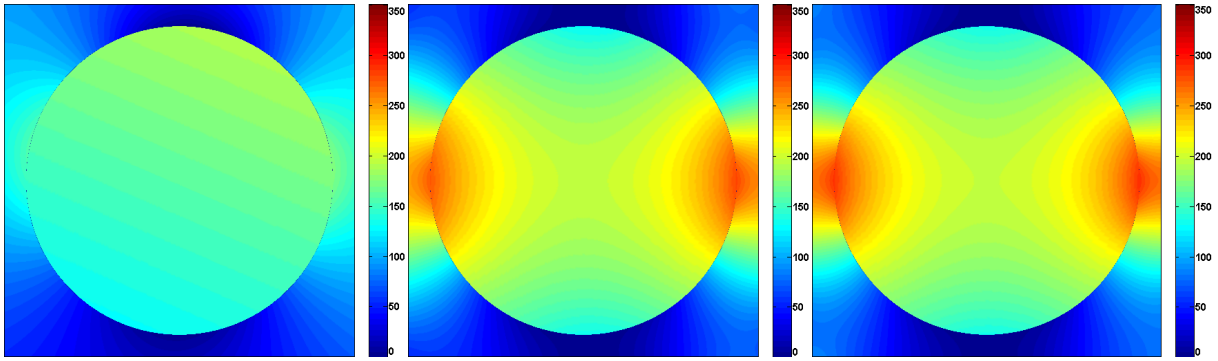

c) Time = 600 hours

Figure 5.3. Convergence study of $\sigma_{12}(y_2, y_3)$ stress fields for different numbers of harmonics in the displacement field representation during uniaxial loading by $\bar{\varepsilon}_{12} = \mathrm{H}(t)\varepsilon_{12}^{o}$.

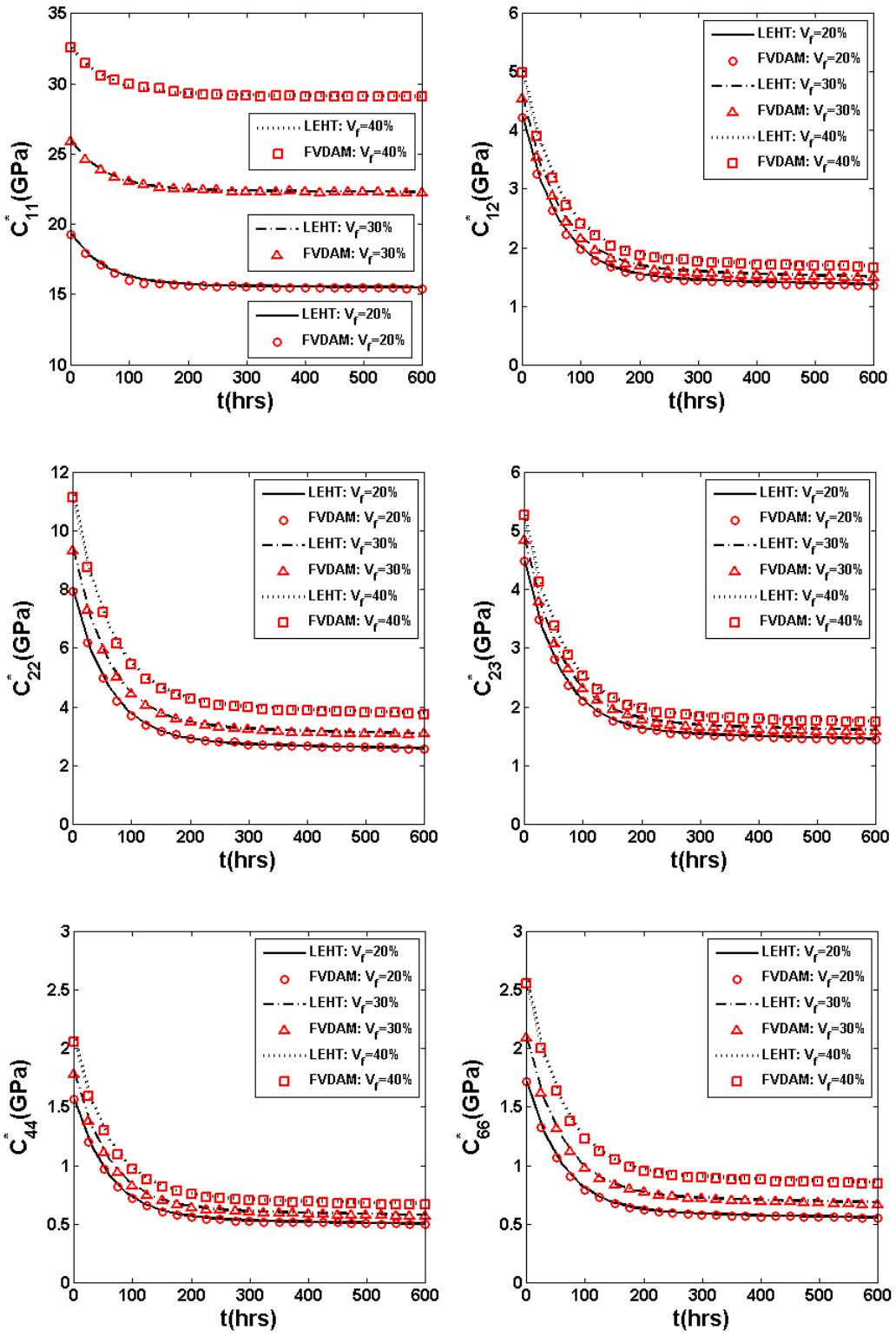

Figure 5.4. Comparison of the relaxation functions of a unidirectional glass/epoxy composite with different fiber volume fractions generated by the locally-exact theory with FVDAM predictions of Cavalcante and Marques (2014).

The rapid convergence of both the homogenized moduli and local stress fields sets our method apart from other elasticity-based solutions such as the eigenstrain expansion approach, cf. (Caporale et al., 2015), which require substantially greater number of harmonics for converged elastic stress fields, and hence by extension viscoelastic stress fields as well.

5.3.2 Comparison with Finite-Volume Results

Cavalcante and Marques (2014) extended the elastic version of the generated FVDAM theory of Cavalcante and Pindera (2013) to the linearly viscoelastic domain directly in the time domain, showing substantial improvement in the local stress field fidelity relative to the original version. The elastic version produces results of comparable accuracy relative to the Q-9 based finite-element method. The authors then compared the generated FVDAM predictions of the creep and relaxation moduli of a glass epoxy system containing different fiber volume fractions with the analytical solution of Luciano and Barbero (1995), showing exceptionally good correlation. The study of Cavalcante and Marques (2014) is one of the few studies where the local stress fields have also been generated during a relaxation history, in addition to the homogenized viscoelastic response functions. Herein, we use these results as a gold standard for comparison with our newly extended locally-exact theory. It is important to note that the solution method employed in the generated FVDAM and locally-exact approaches are totally different, lending credence to the locally-exact theory's rigorous validation, and the ensuing conclusions.

Figure 5.4 illustrates comparison of the complete set of relaxation moduli for the glass/epoxy system employed in the preceding section modelled as a square array of fibers in the epoxy matrix for the fiber volume fractions 0.20, 0.30 and 0.40. The correlation is seen to be excellent for the six relaxation moduli generated moduli generated at 25 times in the interval [0,600] hours using 8 harmonics. This contrasts with the 200 time steps employed in the generated FVDAM simulations required to obtain converged response directly in the time domain by solving the unit cell problem incrementally owing to the separable kernel representation of the linearly viscoelastic constitutive model used for the polymeric matrix. We also compare the local stress fields generated by Cavalcante and Marques (2014) under transverse shear loading $\bar{\varepsilon}_{23} = H(t)\varepsilon_{23}^{o}$ at $t = 600$ hours with the locally-exact predictions for the 0.20 fiber volume fraction. Eight harmonics were employed to generate the results shown in Fig. 5.5 which are compared with the generalized FVDAM results obtained using the Mesh B in

the author's paper. In both cases, converged stress distributions are obtained which are nearly identical.

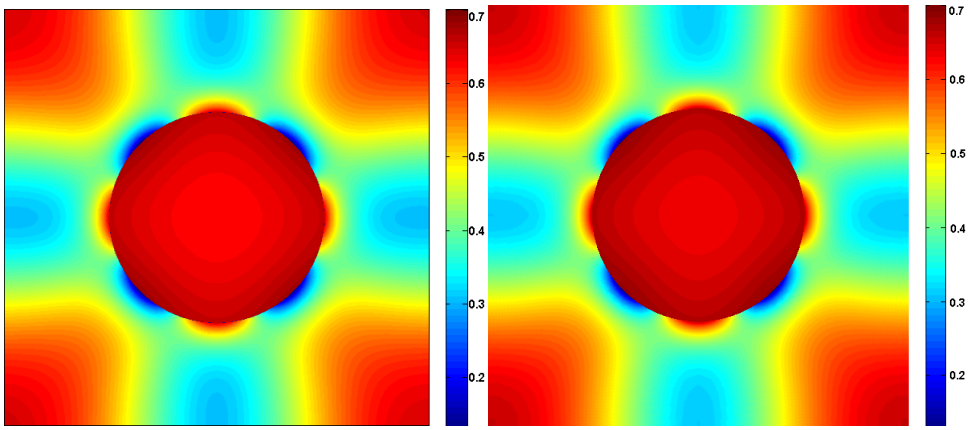

Figure 5.5. Comparison of transverse shear stress fields $\sigma_{23}(y_2, y_3)$ due to uniaxial loading $\bar{\varepsilon}_{23} = \mathrm{H}(t)\varepsilon_{23}^{o}$ in a square unit cell of a unidirectional glass/epoxy composite with 0.20 fiber volume fraction at t = 600 hrs generated by the locally-exact (left) and FVDAM (right) theory of Cavalcante and Marques (2014).

The above results were generated on a PC platform Windows 7 Ultimate 64-bit operating system with 16 GB RAM and Intel(R) Core(TM) i5-3320M CPU @ 2.6 GHz. Table 2 illustrates the execution time required to generate an entire set of relaxation functions in the considered time interval of [0,600] hours as a function of the number of harmonic terms employed in the displacement field representation in the unit cell solution.

Array type	Execution time (minutes)						
	$n=2$	$n=4$	$n=6$	$n=8$	$n=10$	$n=12$	$n=14$
Square	0.369	1.702	3.674	8.009	11.613	16.437	21.859
Hexagonal	2.443	4.042	6.409	11.011	17.736	24.125	29.431

Table 5.2. Execution times consumed in calculating the full set of the relaxation functions of a unidirectional glass/epoxy composite with 20% fiber volume fraction as a function of the number of harmonics used in the displacement field approximation.

5.3.3 Comparison with Experiment

The experimental creep data on off-axis graphite/epoxy specimens at room and elevated temperature generated by Yancey and Pindera (1990) is employed for comparison with the

locally-exact predictions. The T300 graphite fiber and 934 epoxy matrix moduli used in the comparison are given in Tables 5.3-5.4 at the two temperatures. While the fiber remains elastic in the considered temperature range, the epoxy matrix creep response is described very well by the power-law creep compliance

$$S_{11}(t) = D_0 + Ct^n \tag{5.24}$$

where the three parameters are included in Table 5.4. This representation of the creep compliance produces a non-separable kernel which is not readily amenable to an incremental solution of the unit cell problem in the time-domain, in contrast with the present solution approach independent of the type of viscoelastic function kernel in the hereditary integral representation of the viscoelastic behavior.

Temperature	E_A(GPa)	E_T(GPa)	G_A(GPa)	ν_A	ν_T
$22\,^{o}C$	202.82	25.30	44.12	0.443	0.05
$121\,^{o}C$	214.33	14.82	68.18	0.450	0.05

Table 5.3. Elastic moduli of transversely isotropic T300 graphite fiber at two temperatures.

Temperature	E(GPa)	ν	C(1/GPa-min)	n
22 °C	4.51	0.311	0.0135	0.17
121 °C	3.36	0.317	0.0250	0.20

Table 5.4. Elastic moduli and viscoelastic power-law parameters of 934 epoxy resin at two temperatures.

In the locally exact simulations the composite was taken as transversely isotropic and hence a hexagon unit cell was employed to generate the creep response of 10^o and 90^o off-axis specimens for comparison with the experimental results. Two sets of results were generated based on the assumption that either the Poisson's ratio or the bulk modulus of the epoxy matrix is constant. While constant Poisson's ratio of the matrix phase is often assumed in numerical simulations of the time-dependent composite material response due to unavailability of experimental data, the potentially time-independent response of polymeric matrices under hydrostatic loading may produce large differences in the response of specimens subjected to loading which produce large local hydrostatic stresses. One example is a 90^o specimen subjected to transverse loading that determines the transverse creep compliance $S_{22}^{*}(t)$. This will

be explored in greater detail in Section 5.4 in the context of the impact of fiber array type on the homogenized composite response.

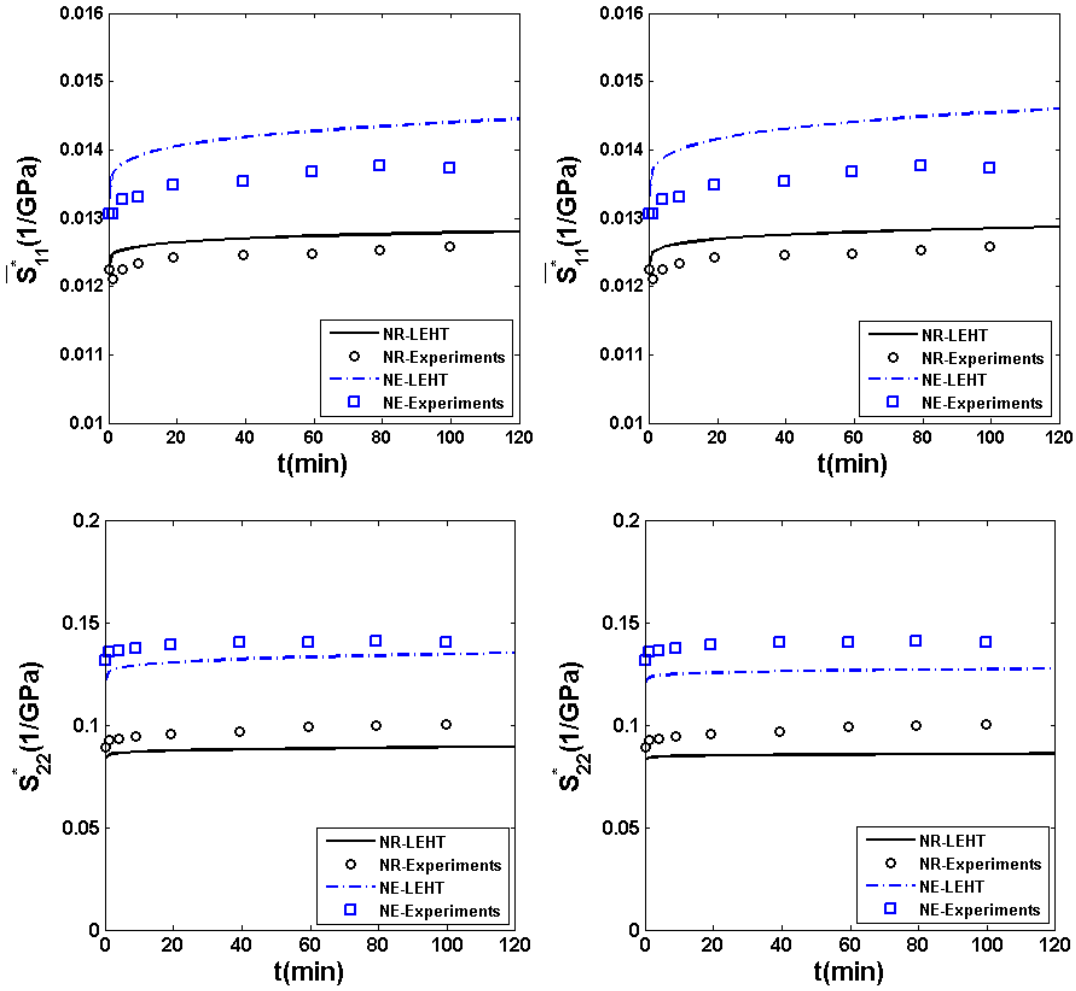

Figure 5.6. Comparison of the predicted creep compliances $\bar{S}_{11}(t)$ and $S_{22}(t)$ of 10° and 90° off-axis graphite/epoxy specimens under uniaxial creep loading at room and elavated temperatures with the experimental data of Yancey and Pindera (1990): constant Poisson's ratio of the epoxy matrix (left) and constant bulk modulus of the epoxy matrix (right).

Figure 5.6 illustrates comparison between the experimental results and locally exact predictions at the two temperatures and the two assumptions on the Poisson's ratio and bulk modulus of the epoxy matrix. The simulations of the 10^{o} off-axis specimen response were obtained from the transformation equations in terms of the calculated creep compliance functions in the principal material coordinate system. While the use constant Poisson's ratio or bulk modulus assumptions for the matrix phase produces little difference in the 10^{o} off-axis

specimen response, with good correlation with experiment in both cases, the predicted transverse response of the 90^o specimen is visibly affected by these assumptions. Specially, the assumption of time-independent matrix response under hydrostatic loading tends to suppress the creep component due to local hydrostatic matrix stresses that arise due to the fiber constraint. The creep suppression is consistent at both temperatures.

5.4 Numerical Results

We consider two important aspects of the viscoelastic response of polymeric matrix composites that have not been given much scrutiny. The first is the effect of fiber array on the time-dependent response under the assumption of either constant Poisson's ratio or bulk modulus. The second addresses the extent to which a particular creep compliance representation of the matrix phase percolates to the macroscopic scale. For instance, given a power-law representation of the matrix creep compliance, can a similar power-law representation be employed to construct the homogenized creep compliance of the composite?

5.4.1 Impact of Fiber Array and Matrix Relaxation Moduli

It is well known that the fiber array influences the elastic-plastic and creep response of metal matrix composites by altering the hydrostatic stress distributions in the matrix phase. In contrast, the elastic moduli, which are influenced by the stress transfer from the matrix to the fiber phase, are affected to a lesser extent by the fiber array for a given fiber shape. Herein, we employ the power-law creep compliance representation for the epoxy matrix of the preceding section to generate creep compliances of a unidirectional graphite/epoxy composite with the fiber volume fraction of 0.60 using two microstructural representations based on square and hexagonal fiber arrays.

Figure 5.7 illustrates the differences in the homogenized transverse normal and shear, and axial shear creep compliances $S_{22}^{*}(t)$, $S_{44}^{*}(t)$, $S_{66}^{*}(t)$ of hexagonal and square fiber arrays with constant matrix Poisson's ratio (left column) and constant bulk modulus (right column). For each matrix type, the effect of fiber array increases with time, with the initially small differences in the instantaneous elastic response substantially magnified with continued loading. Largest differences are observed in the transverse normal and shear creep compliances $S_{22}^{*}(t)$, $S_{44}^{*}(t)$, and smallest in the axial creep compliance. The assumption of purely elastic matrix response

under hydrostatic stress dramatically suppresses creep of the composite under transverse normal loading for both hexagonal and square fiber arrays. In contrast, under transverse shear loading the square fiber array creep is slightly enhanced while the hexagonal array creep is slightly suppressed. Under loading by axial shear, the matrix phase experiences only axial shear stresses, and hence no differences are observed for a given fiber array using either of the two assumptions on the matrix response. The differences arise because the shear modulus of the isotropic matrix, which depends on the Young's modulus and Poisson's ratio in the elastic domain, evolves differently in the time depending whether the matrix is assumed to respond elastically or in a time-dependent manner under hydrostatic loading.

Figure 5.8 presents the transverse shear stress distributions $\sigma_{23}(y_2, y_3)$ at the instant of applied loading $\bar{\sigma}_{23}(t) = H(t)\sigma_{23}^o$, $t = 0$, and at the terminal time of $t = 600$ hours, in support of increasing differences with time in the transverse creep compliance $S_{44}^*(t)$ of the hexagonal and square arrays with constant bulk modulus matrix observed in Fig. 5.7. The substantially greater load bearing capability of the fibers in the hexagonal array, which produces much stiffer response, is attributable in large measure to the array type. The additional contribution of the matrix type is rooted in the hydrostatic stress differences in the matrix phase produced by the two arrays, which are compared in Fig. 5.9. The substantially larger hydrostatic stress magnitudes in the matrix phase of the hexagonal array produce additional differences in the response of both arrays upon comparison with the corresponding results in Fig. 5.7 based on the constant Poisson's ratio assumption.

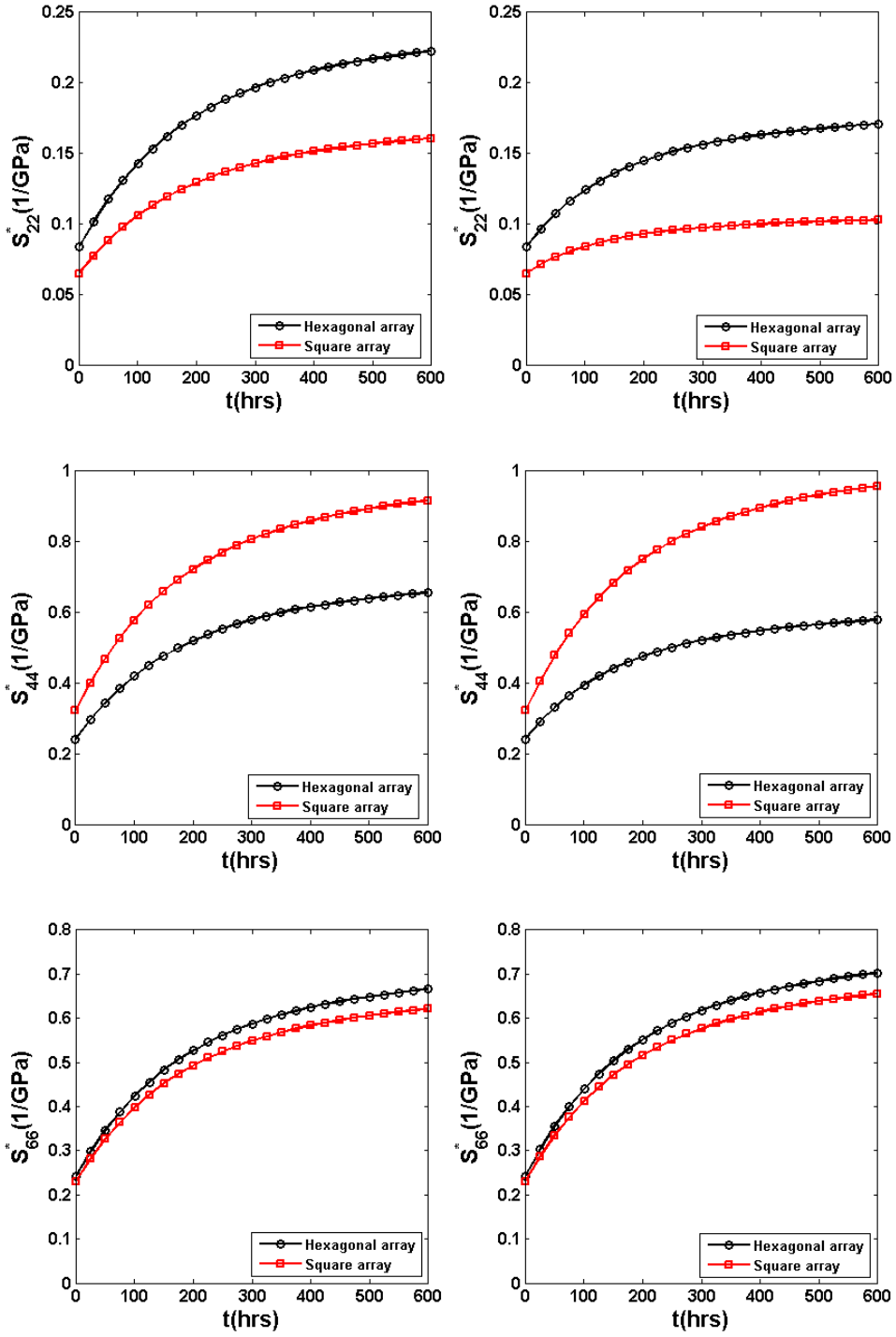

Figure 5.7 Comparison of the creep compliances $S_{22}(t)$, $S_{44}(t)$, $S_{66}(t)$ of hexagonal and square arrays of a glass/epoxy unidirectional composite predicted by the locally exact theory: constant Poisson's response of the epoxy matrix (left) and constant bulk modulus of the epoxy matrix (right).

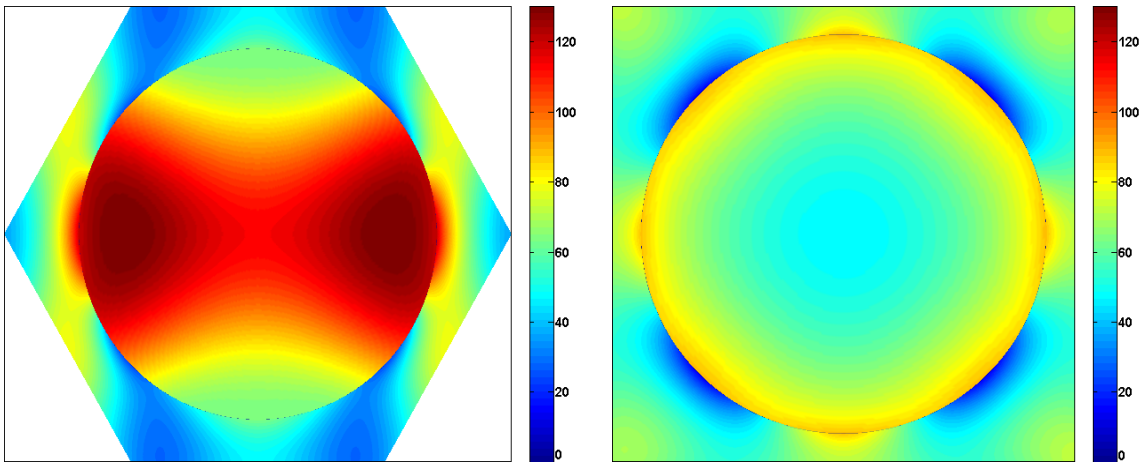

a) Time = 0 hr

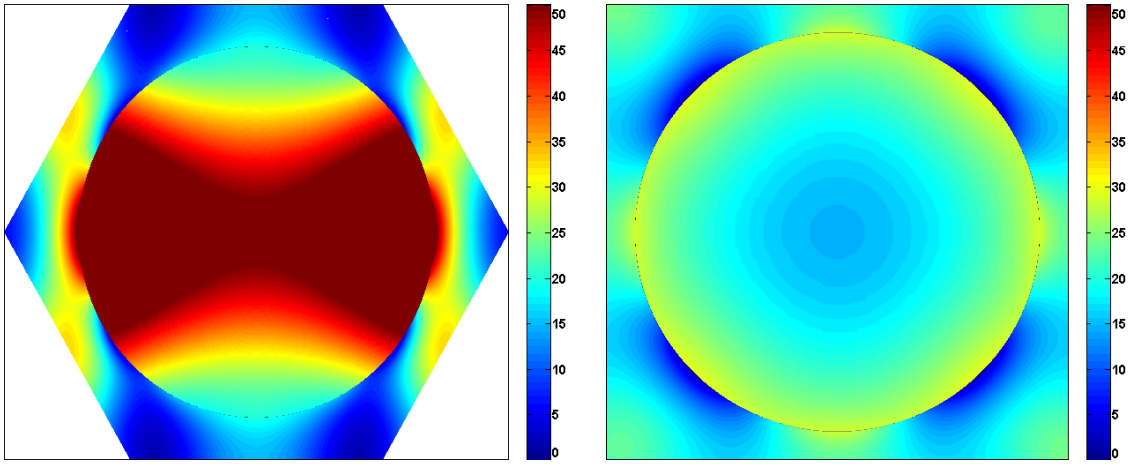

b) Time = 600 hr

Figure 5.8. Comparison of transverse shear stress fields $\sigma_{23}(y_2, y_3)$ in hexagonal and square arrays of a glass/epoxy unidirectional composite under pure creep loading $\bar{\varepsilon}_{23} = \mathrm{H}(t)\varepsilon_{23}^{o}$ predicted by the locally-exact theory when the bulk modulus of the epoxy matrix is assumed constant.

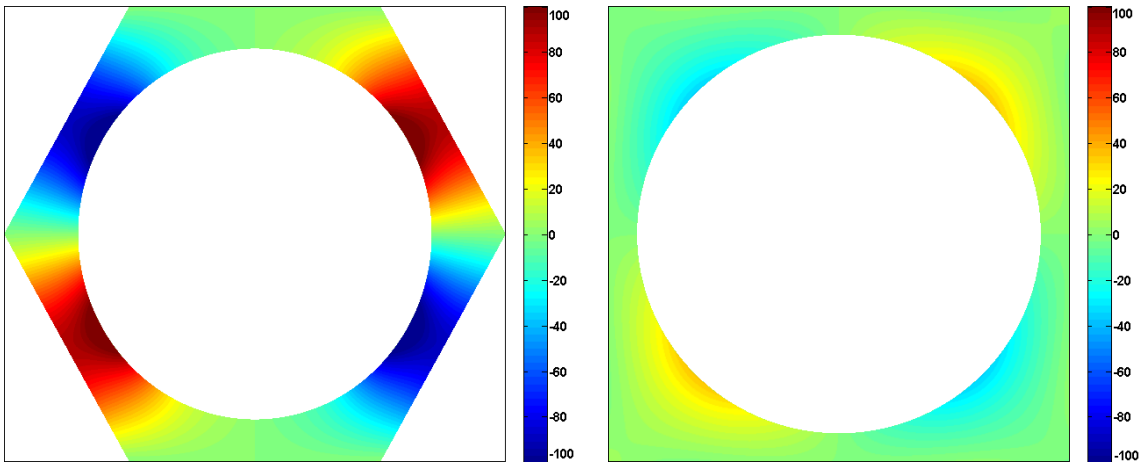

a) Time = 0 hr

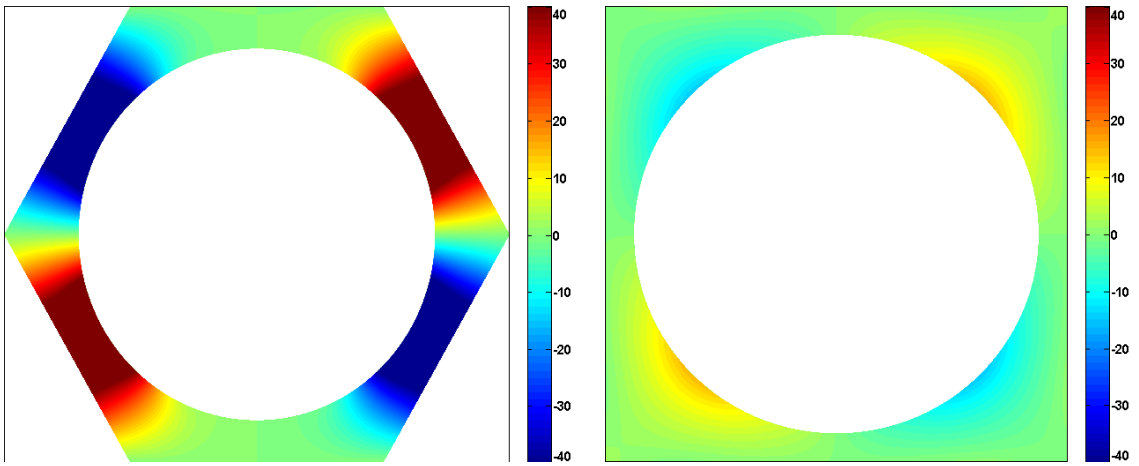

b) Time = 600 hr

Figure 5.9. Comparison of hydrostatic stress fields in the matrix phase of hexagonal and square arrays of a glass/epoxy unidirectional composite under pure creep loading $\bar{\varepsilon}_{23} = \mathrm{H}(t)\varepsilon^{\mathrm{o}}_{23}$ predicted by the locally-exact theory when the bulk modulus of the epoxy matrix is assumed constant.

5.4.2 Transmission of Matrix Response Features Across Scales

Construction of relaxation moduli or creep compliances of unidirectional composites with viscoelastic phases based on experimental data requires extensive tests to characterize all time-dependent functions. For transversely isotropic composites, five independent functions are required, some of which are difficult to obtain experimentally, e.g., $C_{44}^{*}(t)$ or $S_{44}^{*}(t)$. Moreover, once a set of relaxation moduli or creep compliances is experimentally obtained, the question arises with regard to the choice of functions that may be employed that produce best fit with experimental data. In this section we address this issue by investigating how the choice of a particular function that describes the linearly viscoelastic response of the matrix phase percolates to the homogenized level. Specifically, we use the power-law description of the creep compliance of the epoxy matrix reported by Yancey and Pindera (1990) at the elevated temperature to determine whether the homogenized response also obeys similar power-law descriptions with altered coefficients (which must depend on the fiber volume fraction, array type, and fiber moduli), and perhaps also altered power-law exponent(s). The larger exponent at the elevated temperature relative to that at room temperature, Table 5.3, produces greater creep, facilitating determination of the homogenized parameters with greater fidelity.

Using the locally-exact theory, homogenized creep compliances were generated for the considered graphite/epoxy system at three different fiber volume fractions, namely $v_f = 0.20,\ 0.40,\ 0.60$. The responses that exhibit the most pronounced time-dependent behavior dominated by the viscoelastic epoxy matrix, namely $S_{22}^{*}(t)$, $S_{44}^{*}(t)$ and $S_{66}^{*}(t)$ are illustrated in Fig. 5.10. To determine whether these responses are well-approximated by power-law functions, the time-dependent part of the response

$$S_{ij}^{*}(t) - S_{ij}^{0} = S_{ij}^{*ve}(t) \tag{5.25}$$

was plotted as a function of time on a log-log graph in order to extract power-law exponents and associated coefficients. In other words, assuming that these homogenized functions may be approximated by,

$$S_{ij}^{*}(t) = S_{ij}^{*(0)} + S_{ij}^{*(1)} t^{n_{ij}^{*}} \tag{5.26}$$

where $ij = 11, 12, 13, 22, 23, 33, 44, 55, 66$, they were post-processed according to

$$\ln(S_{ij}^{*}(t)-S_{ij}^{*(0)})=\ln S_{ij}^{*(1)}+n_{ij}^{*}\ln t \tag{5.27}$$

to identify observable linear regions with the related power-law slopes n_{ij}^{*} and coefficients $S_{ij}^{*(1)}$.

Table 5.5 reports the resulting power-law coefficients and exponents for the selected homogenized creep compliances obtained from the locally-exact theory simulations for the hexagonal array containing the three fiber volume fractions are two types of epoxy matrices characterized by either constant Poisson's ratio or constant bulk modulus. As anticipated, the power-law coefficients decrease with the fiber volume fraction at rates that depend on the particular creep compliance and matrix type. Regardless of the matrix type and creep compliance, however, the power-law exponents for the matrix-dominated homogenized creep compliances remain essentially the same as that of the epoxy matrix in the investigated fiber volume range. Comparison of the homogenized creep compliances based on the power-law fits of Eq. (5.26) with the locally-exact simulations are included in Fig. 5.10, illustrating excellent agreement.

Included in Table 5.5 are the corresponding results for the creep compliance $S_{11}^{*}(t)$ which is dominated by the elastic fibers, producing negligible time-dependent behavior in the considered fiber volume range characterized by very small magnitudes of the power-law coefficients. The power-law exponents, however, are nearly independent of the fiber volume fractions are consistently lower relative to the matrix-dominated creep compliance exponents.

v_f	$S_{11}^{*(1)}$	$S_{22}^{*(1)}$	$S_{44}^{*(1)}$	$S_{66}^{*(1)}$	n_{11}^{*}	n_{22}^{*}	n_{44}^{*}	n_{66}^{*}
$0.20(\nu=\nu_o)$	$1.086*10^{-4}$	0.0166	0.0478	0.0442	0.1650	0.1997	0.1998	0.2
$0.40(\nu=\nu_o)$	$2.201*10^{-5}$	0.0113	0.0321	0.0285	0.1650	0.1994	0.1996	0.2
$0.60(\nu=\nu_o)$	$6.717*10^{-6}$	0.0067	0.0183	0.0165	0.1650	0.1989	0.1990	0.2
$0.20(K=K_o)$	$1.098*10^{-4}$	0.0142	0.0532	0.0503	0.1645	0.1970	0.1988	0.2
$0.40(K=K_o)$	$2.250*10^{-5}$	0.0093	0.0347	0.0325	0.1645	0.1954	0.1972	0.2
$0.60(K=K_o)$	$6.931*10^{-6}$	0.0051	0.0189	0.0188	0.1645	0.1921	0.1939	0.2

Table 5.5 Power-law coefficients and exponents of homogenized creep compliances of a unidirectional T300 graphite/934 epoxy composite at $121^{\circ}\mathrm{C}$ containing different fiber volume fractions.

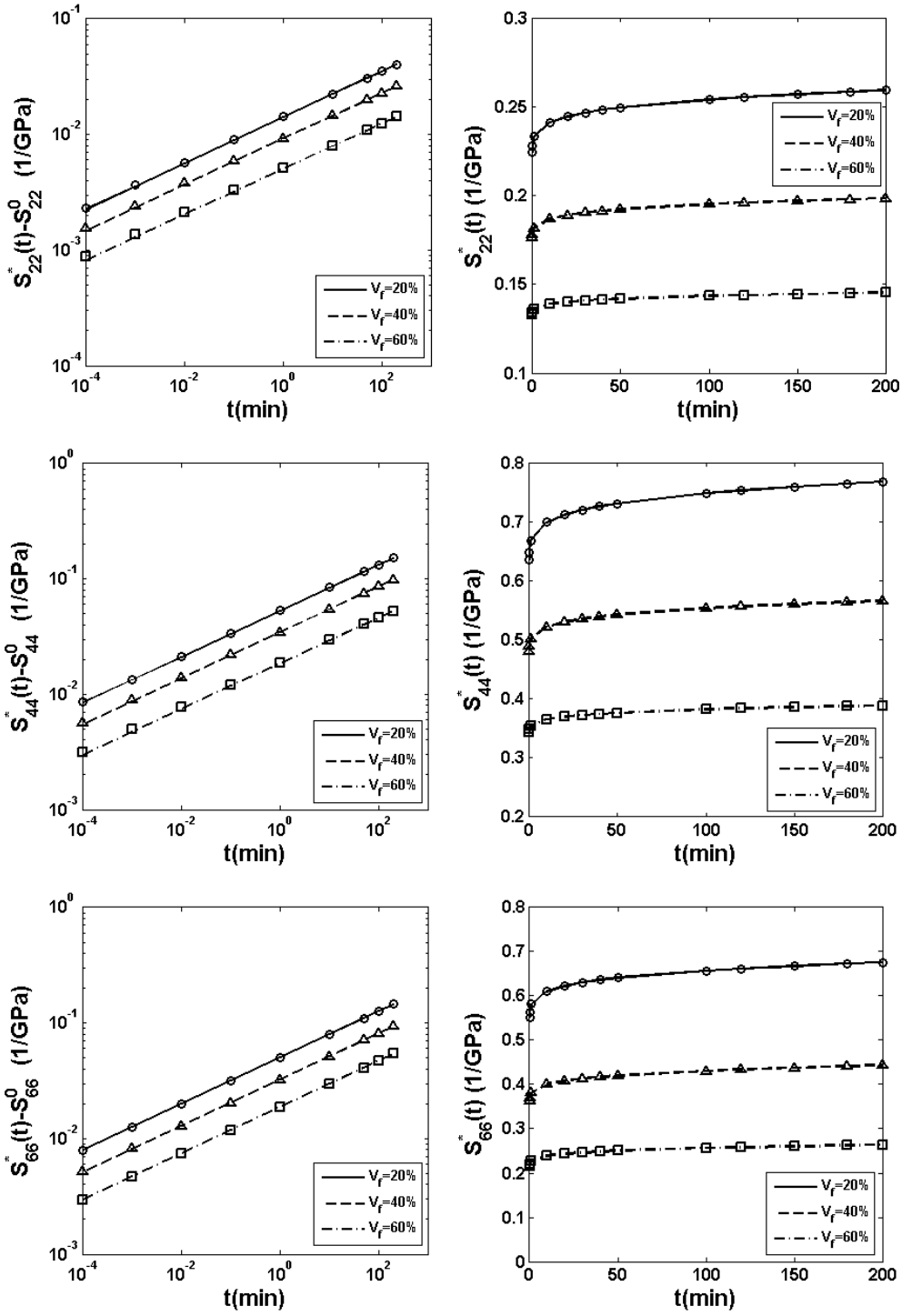

Figure 5.10. Time-dependent components of matrix-dominated homogenized creep compliances of a transversely isotropic graphite/epoxy composite displayed on a logarithmic scale (left). The matrix phase is characterized by a power-law creep compliance and constant bulk modulus while the fiber is elastic. Predictions based on power-law fits (symbols) are compared with locally-exact simulations (lines), (right).

5.5 Conclusions

The extension of the locally-exact homogenization theory to accommodate linearly viscoelastic phases in periodic unidirectional composites with hexagonal and square microstructures via the correspondence enables rapid identification of the effects of viscoelasticity, fiber array architecture and phase response on homogenized relaxation moduli and local stress fields. The success of the correspondence principle applied to the locally-exact theory depends on the efficiency and accuracy with which the Laplace-transformed unit cell solution is inverted to the time domain. The chosen inversion method proposed by Zakian (1969) proved to be an excellent vehicle towards this end. Because of the simple input data construction arising from the computationally stable analytical framework, the theory may be used efficiently by specialists and non-specialists alike to rapidly calculate both homogenized relaxation moduli or creep compliances and local stress fields in a wide fiber volume fraction range. The extended theory's success is rooted in the variational principle proposed by Drago and Pindera (2008) which facilitates rapid convergence of the unknown Fourier coefficients in the unit cell displacement field representation upon application of periodic boundary conditions, demonstated herein to also hold true in the Laplace-transform domain.

The theory's utility was highlighted by investigating the impact of fiber array type and matrix constitutive assumptions on the homogenized response of unidirectional composites. The results revealed previously undocumented importance of viscoelasticity on the homogenized response of unidirectional composites with hexagonal and square microstructures, illustrating that initially small differences in the instantaneous response are substantially magnified with time, while quantifying the effect of matrix viscoelastic incompressibility under hydrostatic loading. The theory was also employed to investigate how the time-dependent component of the matrix creep compliance affects the homogenized response. The results indicate that a power-law representation of the matrix creep compliance produces power-law homogenized response in the matrix-dominated directions with the same power-law exponent but fiber volume fraction dependent coefficients.

Chapter 6

Comparison: LEHT vs Classical Models

6.1 Review

Composite cylinder assemblage (CCA) model was proposed by Hashin (1962) based on isotropic constituent, which was later extended to transversely isotropic phases in terms of replacement schemes (Hashin, 1979). This is the classic model based on representative volume element (RVE) concept, which provides closed-form expressions for the four of five effective moduli for the response of unidirectional-reinforced composites. The axial Young's and shear modulus, axial Poisson's ratio, transverse bulk modulus can be expressed because a single composite cylinder still acts as a RVE, while the entire assemblage responds as same as a single cylinder under homogeneous traction and displacement boundary conditions for axisymmetric and axial shear loading. The fifth effective modulus – transverse shear modulus, can only be expressed as the upper and lower bounds using variational principle. The four actual expressions for homogenized moduli for CCA model (Hashin, 1979) are expressed for future reference:

$$
\begin{aligned}
E_A^* &= v_f E_A^{(f)} + v_m E_A^{(m)} + \frac{4 v_f v_m (\nu_A^{(f)} - \nu_A^{(m)})^2}{v_f / k_T^{(m)} + v_m / k_T^{(f)} + 1/G_T^{(m)}} \\
\nu_A^* &= v_f \nu_A^{(f)} + v_m \nu_A^{(m)} + \frac{v_f v_m (\nu_A^{(f)} - \nu_A^{(m)})(1/k_T^{(m)} - 1/k_T^{(f)})}{v_f / k_T^{(m)} + v_m / k_T^{(f)} + 1/G_T^{(m)}} \\
k_T^* &= k_T^{(m)} + \frac{v_f}{1/(k_T^{(f)} - k_T^{(m)}) + v_m/(k_T^{(m)} + G_T^{(m)})} \\
G_A^* &= G_A^{(m)} + \frac{v_f}{1/(G_A^{(f)} - G_A^{(m)}) + v_m/(2G_A^{(m)})}
\end{aligned}
\tag{6.1}
$$

while the upper and lower bounds for the transverse shear modulus G_T^* are

$$G_{T(+)}^{*}=G_{T}^{(m)}\{1+\frac{(1+\beta_m)v_f}{\rho-v_f[1+3v_m^2\beta_m^2/(1+\alpha v_f^3)]}\}$$
$$G_{T(-)}^{*}=G_{T}^{(m)}+\frac{v_f}{1/(G_T^{(f)}-G_T^{(m)})+v_m(k_T^{(m)}+2G_T^{(m)})/[2G_T^{(m)}(k_T^{(m)}+G_T^{(m)})]} \tag{6.2}$$

In addition, the bounds for the transverse normal modulus E_T^* can be expressed as follows

$$\frac{4}{E_{T\pm}^{*}}=\frac{1}{G_{T\pm}^{*}}+\frac{1}{k_T^{*}}+\frac{4\nu_A^{*2}}{E_A^{*}} \tag{6.3}$$

in which $\alpha=(\beta_m-\gamma\beta_f)/(1+\gamma\beta_f)$, $\rho=(\gamma+\beta_m)/(\gamma-1)$, $\beta_f=k_T^{(f)}/(k_T^{(f)}+2G_T^{(f)})$, $\beta_m=k_T^{(m)}/(k_T^{(m)}+2G_T^{(m)})$, $\gamma=G_T^{(f)}/G_T^{(m)}$. $E_A^{(k)},k_T^{(k)},\nu_A^{(k)},G_A^{(k)},G_T^{(k)}$ are the material properties while v_k stands for the volume fraction of fiber and matrix, respectively, and $k=f,m$.

Christensen and Lo (1979) provide the quadratic expression for the transverse shear modulus using an energy approach based on the three-phase model, which can be expressed as:

$$\left(G^{*}/G^{(m)}\right)^2 A+\left(G^{*}/G^{(m)}\right)B+D=0 \tag{6.4}$$

in which *A*, *B* and *D* are the functions of the material properties of composite cylinder assemblage, the details of which can be referred in the original literature.

The viscoelastic behavior was extended for heterogeneous media based on CCA models by Hashin and his colleagues, (Hashin, 1965; Hashin, 1966; Gottesman and Hashin, 1980). In the meantime, based on the assumption of average stress in the matrix phase, Mori and Tanaka (1973) provided another approach to evaluate effective stiffness matrix by firstly evaluating Eshelby-type problem, in which the fiber was imbedded into the matrix phase, and then applying far-field macroscopic strain to generate strain concentration matrix $\mathbf{A}_{m\infty}^{(f)}$ relating averaging fiber strain with averaging matrix strain $\bar{\varepsilon}_f=\mathbf{A}_{m\infty}^{(f)}\bar{\varepsilon}_m$. For any two-phase composite materials:

$$\bar{\varepsilon}=v_f\bar{\varepsilon}_f+v_m\bar{\varepsilon}_m \;\Rightarrow\; \bar{\varepsilon}=[v_f\mathbf{A}_{m\infty}^{(f)}+v_m\mathbf{I}]\bar{\varepsilon}_m \tag{6.5}$$

from which the strain concentration matrix relating the averaging fiber strain with the macroscopic average strain becomes

$$\mathbf{A}^{(f)}=\mathbf{A}_{m\infty}^{(f)}[v_f\mathbf{A}_{m\infty}^{(f)}+v_m\mathbf{I}]^{-1} \tag{6.6}$$

Then the final elastic stiffness matrix can be expressed as

$$\mathbf{C}^{*} = \mathbf{C}^{(m)} + v_f(\mathbf{C}^{(f)} - \mathbf{C}^{(m)})\mathbf{A}_{m\infty}^{(f)}[v_f\mathbf{A}_{m\infty}^{(f)} + v_m\mathbf{I}]^{-1} \tag{6.7}$$

The problem for Mori-Tanaka model is that the matrix phase is taken into account but only in an average sense, which leads to the overestimating of initial yielding in the presence matrix plasticity (Pindera et al., 2009).

Both CCA and Mori-Tanaka models have been among the most popular tools in investigating the micromechanical behavior of unidirectional composites in the past years. Both of them have their advantages over other micromechanics techniques: easily understandable and implemented, comparatively accurate predictions, et al. However, other problems are still looming: CCA model does not either consider fiber and fiber interaction, or provide the exact expression for the transverse shear (normal) modulus; Mori-Tanaka just consider matrix phase in an average sense…

In this chapter we systematically compare the elastic and viscoelastic response of unidirectional composite materials based on CCA model, Mori-Tanaka model as well as LEHT, the framework of which is introduced in Chapter 2. The comparison between LEHT and CCA model has been conducted for unidirectional composites with cylindrical orthotropic fibers in Chapter 3 for validation of the accuracy and efficiency of the present theory. Here the comparison is limited for composites with (transversely) isotropic constituents to show the advantage of the present theory against the classical models for both homogenized moduli and stress distributions.

6.2 Elastic Behavior

In this section, the converged elastic homogenized moduli and stress distributions are compared between the LEHT, proposed in this dissertation, and the classical CCA and Mori-Tanaka models, both of which has been validated and applied in many situations. The homogenized moduli are compared by using glass/epoxy (listed in Table 6.1) to highlight the stronger contrast of inplane moduli between fiber and matrix, and covering a wide range of fiber volume fraction [0.05-0.75] to suit to more demanding cases. The LEHT has been demonstrated by many other analytical and numerical techniques, and here we just want to show the advantages of the proposed method, which can be used as a gold standard against other micromechanics tools.

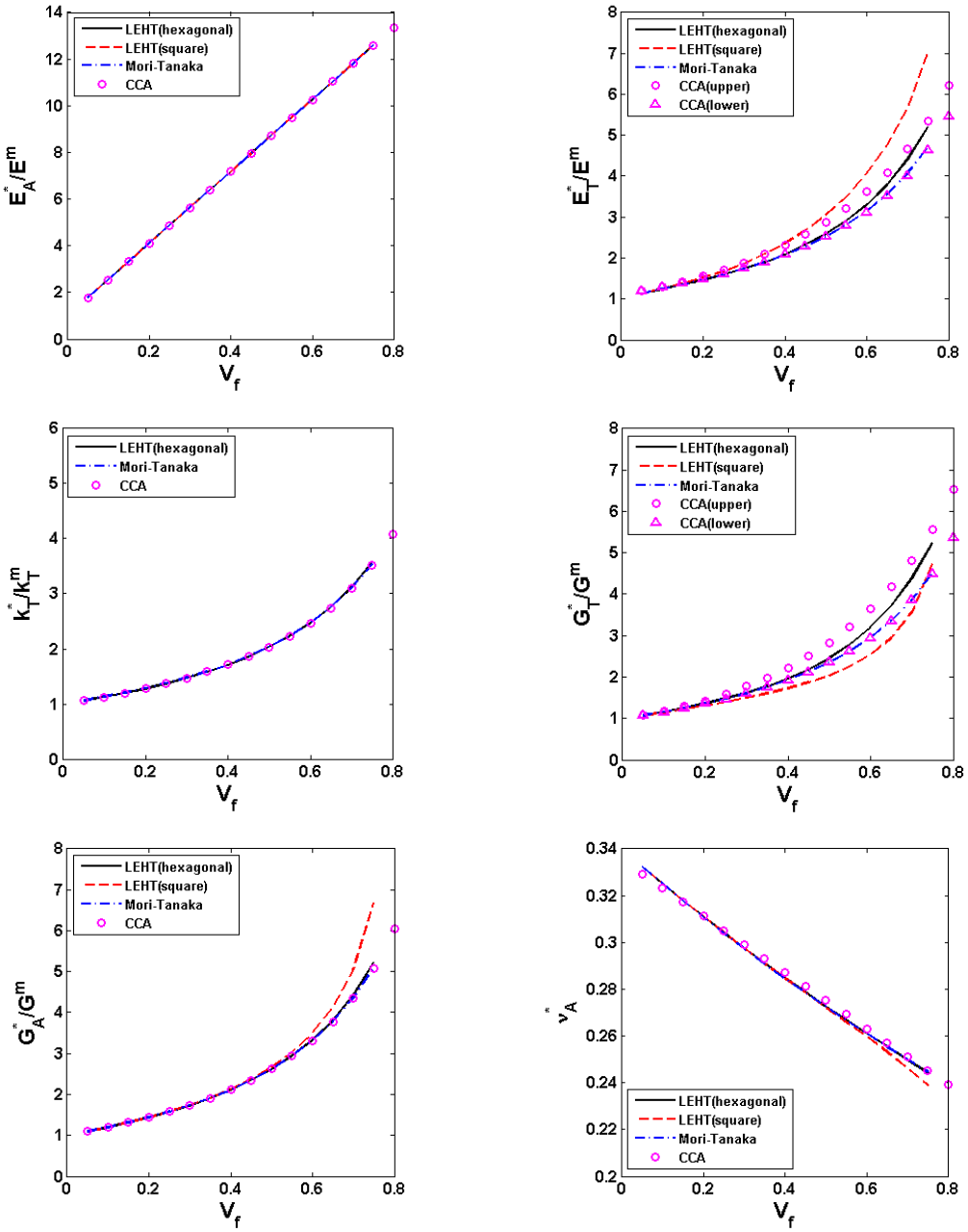

Fig. 6.1 Homogenized moduli as a function of fiber volume fraction for glass/epoxy composite based on different models.

The homogenized moduli generated using three different models are compared in Fig 6.1, most of which has been normalized by their corresponding moduli of matrix, except axial Poisson's ratio ν_A. As can be observed in the figure, the homogenized moduli $E_A^*, k_T^*, \nu_A^*, G_A^*$ are almost identical based on LEHT (hexagonal array), CCA model, as well as Mori-Tanaka model under axisymmetric and axial shear loading. While the respective moduli for square array based on LEHT analysis are almost same for most of the cases, except slight differences appear for G_A and ν_A when fiber volume fraction exceeds 55%. This is because the isotropic property characteristics still hold for the inplane problem for hexagonal array but not rectangular (square) array, and the fiber-fiber interactions turns to be more obvious when fiber volume fraction becomes larger. For the transverse normal and shear properties, only upper and lower bounds for E_T and G_T exist for CCA model, while Mori-Tanaka always gives the actual predictions for all of the homogenized moduli. In addition, the homogenized moduli of E_T^* and G_T^* based on LEHT for hexagonal array always lie between upper and lower bounds of their counterparts predicted by CCA model. In the meantime, Mori-Tanaka model gives almost the same transverse properties as the lower bounds of CCA model.

Material	E_A(GPa)	E_T(GPa)	μ_A(GPa)	μ_T(GPa)	ν_A
E-glass fiber	69.0	69.0	28.28	28.28	0.22
3501-6 epoxy	4.2	4.2	1.567	1.567	0.34

Table 6.1. Elastic fiber and matrix properties employed in the elastic analysis.

Next, we are going to show the stress distributions using LEHT analysis and CCA model under different types of loading conditions. First, the inplane axisymmetric loading is applied, in which $\bar{\varepsilon}_{22} = \bar{\varepsilon}_{33} = 0.01$ for the hexagonal array and $\bar{\varepsilon}_{rr} = 0.01$ for the CCA model, respectively. Two fiber volume fractions are employed, 30% and 65%, to illustrate the effect of fiber-fiber interaction on the stress distributions in the fiber area predicted by the two methods. Figs 6.2-6.3 illustrate the inplane stress distributions $\sigma_{22}(y_2, y_3)$, $\sigma_{33}(y_2, y_3)$, $\sigma_{23}(y_2, y_3)$ for comparison; out-of-plane stress field $\sigma_{11}(y_2, y_3)$ is not shown here because the fiber is dominant in taking most of the axial stress, which is not as interesting as well. For the fiber volume fraction of 0.30, the CCA model shows accurate predictions compared with the LEHT. However, when the fiber volume fraction increases to 0.65 in Fig 6.3, obvious stress disturbance can be observed in the

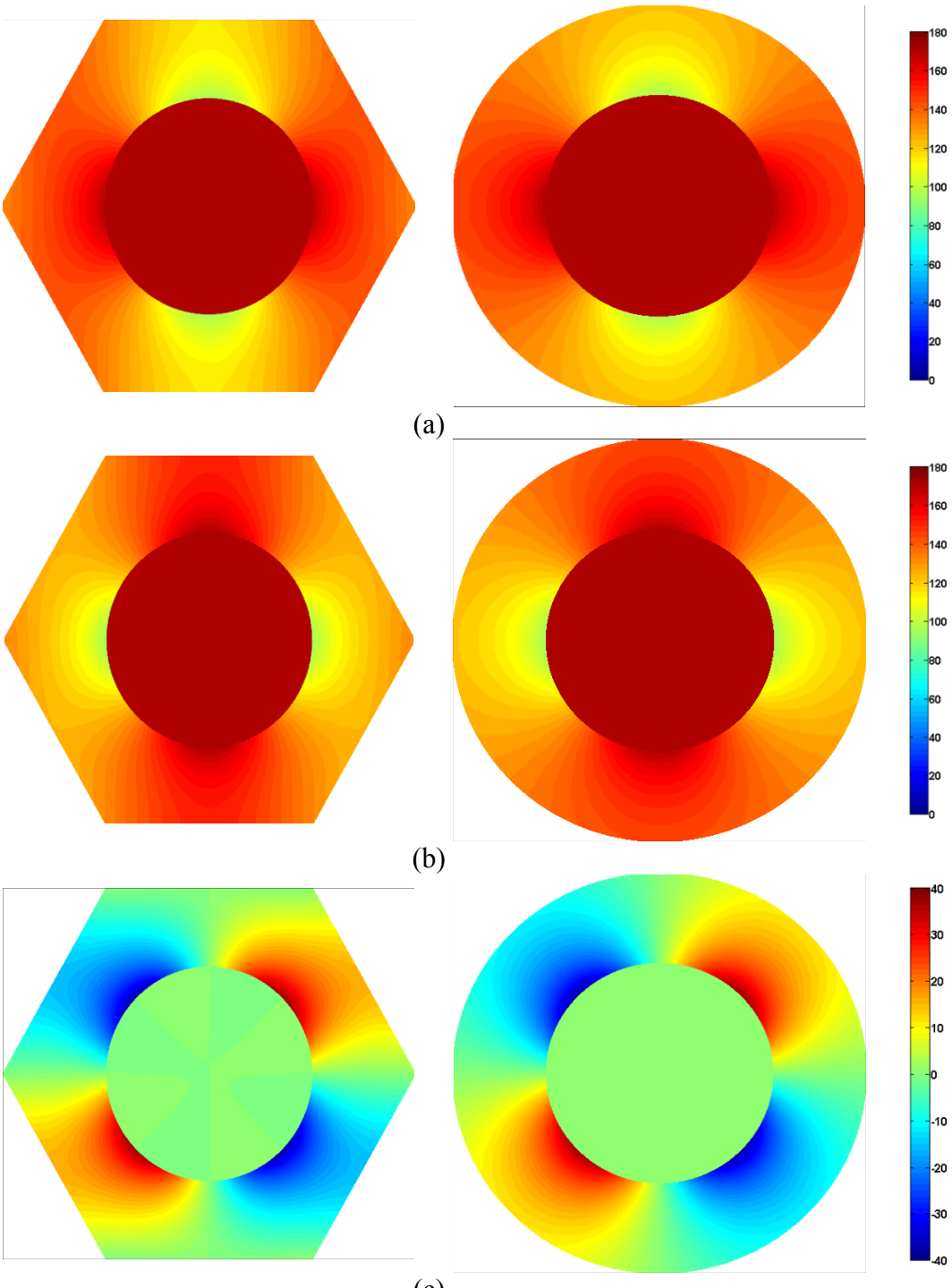

Fig. 6.2 Stress distribution comparisons of (a) σ_{22}; (b) σ_{33}; and (c) σ_{23} between LEHT analysis for hexaognal array (left) and CCA model (right) with the fiber volume fraction 0.30 subjected to the loading: $\bar{\varepsilon}_{22} = \bar{\varepsilon}_{33} = 0.01$ (left) and $\bar{\varepsilon}_{rr} = 0.01$ (right).

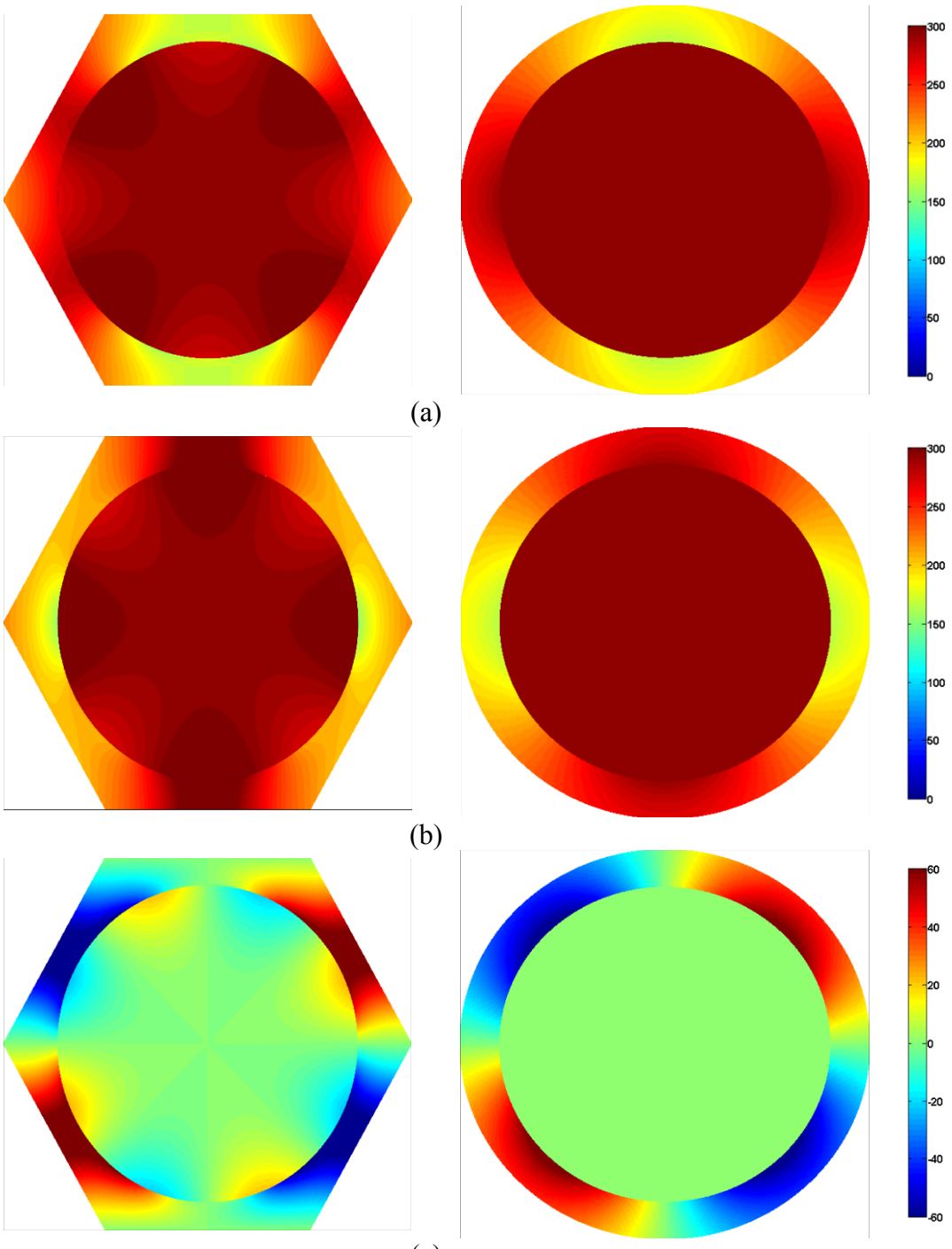

Fig. 6.3 Stress distribution comparisons of (a) σ_{22}; (b) σ_{33}; and (c) σ_{23} between LEHT analysis for hexaognal array (left) and CCA model (right) with the fiber volume fraction 0.65 subjected to the loading: $\bar{\varepsilon}_{22} = \bar{\varepsilon}_{33} = 0.01$(left) and $\bar{\varepsilon}_{rr} = 0.01$ (right).

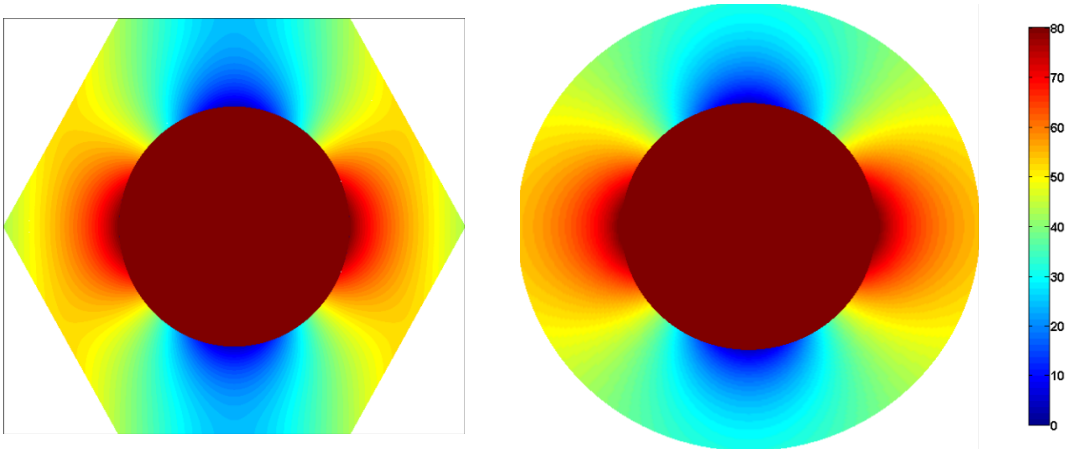

(a)

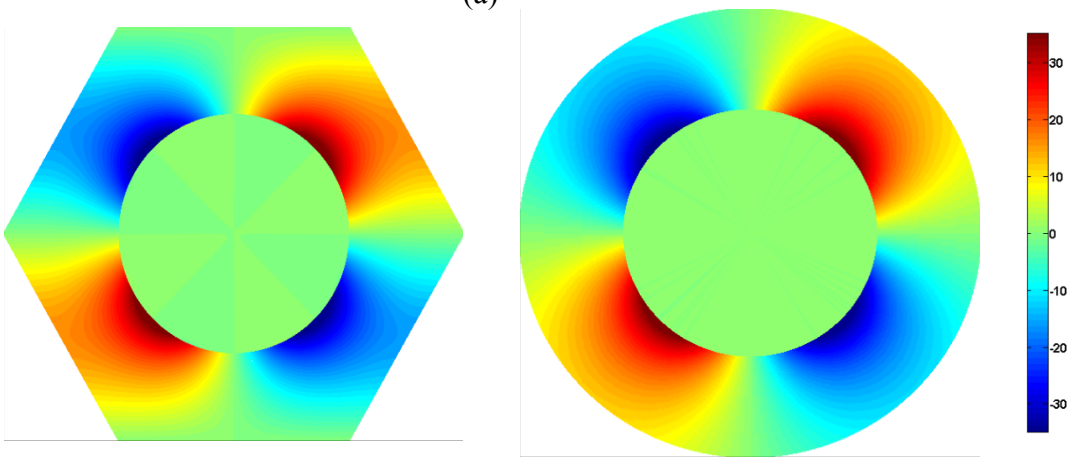

(b)

Fig. 6.4 Stress distribution comparisons of (a) σ_{12}; (b) σ_{13} between LEHT analysis for hexaognal array (left) and CCA model (right) with the fiber volume fraction 0.30 subjected to the loading: $\bar{\varepsilon}_{12} = 0.01$ (left) and $\bar{\varepsilon}_{zr} = 0.01$ (right).

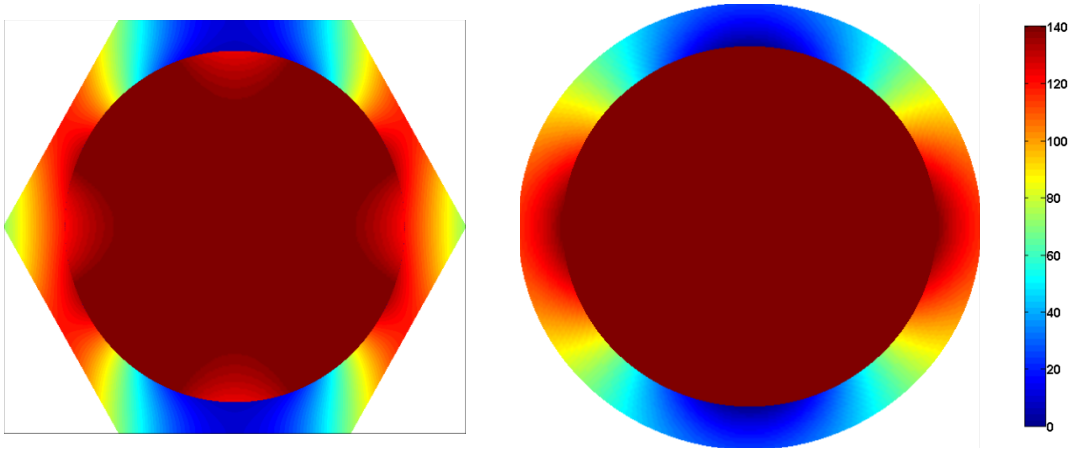

(a)

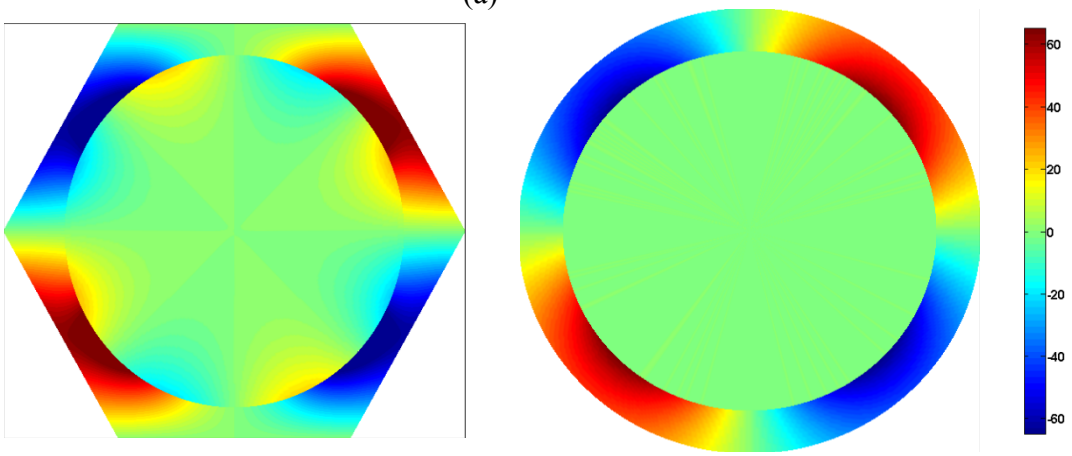

(b)

Fig. 6.5 Stress distribution comparisons of (a) σ_{12}; (b) σ_{13} between LEHT analysis for hexaognal array (left) and CCA model (right) with the fiber volume fraction 0.65 subjected to the loading: $\bar{\varepsilon}_{12} = 0.01$ (left) and $\bar{\varepsilon}_{zr} = 0.01$ (right).

fiber area in LEHT analysis but not in the CCA model, although the matrix phases still show similar distributions. The disturbance in the fiber is due to fiber-fiber interaction, which cannot be predicted by the CCA model, and can only be captured in the higher fiber volume fraction case by LEHT. Similar phenomenon also happens in the stress fields under axial shear loading conditions $\bar{\varepsilon}_{12} = 0.01$ (for hexagonal array) and $\bar{\varepsilon}_{zr} = 0.01$ (for CCA model) (Figs. 6.4-6.5), while the fiber disturbance still cannot be observed when fiber volume fraction is $V_f = 0.65$ by CCA model. However, CCA model still establishes accurate stress distributions in most cases, especially in the matrix phase, which cannot be illustrated by Mori-Tanaka model. In the next section, the viscoelasticity capability is implemented into LEHT (see Chapter 5 for details), as well as CCA and Mori-Tanaka models for comparison.

6.3 Viscoelastic Behavior

The viscoelastic behavior, based on the CCA model, was firstly studied by Hashin for unidirectional composites about half a century ago. Here we are trying to explain the viscoelastic behavior predicted by including LEHT, CCA model, as well as Mori-Tanaka model. The detailed process for solving the viscoelastic relaxation moduli or creep compliances by LEHT has been illustrated in Chapter 5, and are not going to be repeated here. However, the inversion technique for CCA and Mori-Tanaka models are explained in this section for future reference, both of which are using Zakian method, which has been proved to be a robust tool for many demanding cases, (Hassanzadeh and Pooladi-Darvish, 2007).

Since the explicit expressions of homogenized moduli are already given in Eqs. (6.1-6.2) for CCA model, what is needed to do is to replace the elastic moduli by their Carson transform, $E_A^{(k)}, k_T^{(k)}, \nu_A^{(k)}, G_A^{(k)}$ and $G_T^{(k)}$ → $s\hat{E}_A^{(k)}, s\hat{k}_T^{(k)}, s\hat{\nu}_A^{(k)}, s\hat{G}_A^{(k)}, s\hat{G}_T^{(k)}$, $k = f, m,$ or $*$. s is the Laplace variable which usually has the following relationship $s(j) = \alpha_j / t_i$ for $j = 1, 2, ...5,$ in which the time domain is essentially a vector by dividing the desired time interval into increments $t = [t_1, t_2, t_3, ..., t_N]$. α_j are complex values and can be referred to Table 5.1. The homogenized relaxation functions at the given time are subsequently calculated according to Eq. (5.6) using Zakian method for the inversion technique, which is

$$f^*(t_i) = \frac{2}{t_i} \sum_{j=1}^{5} \mathrm{Re}[K_j F^*(\alpha_j / t_i)] \tag{6.8}$$

in which f stands for the elastic moduli $E_A^{(k)}, k_T^{(k)}, \nu_A^{(k)}, G_A^{(k)}$ and $G_T^{(k)}$, while F denotes their respective relaxation moduli $\hat{E}_A^{(k)}, \hat{k}_T^{(k)}, \hat{\nu}_A^{(k)}, \hat{G}_A^{(k)}, \hat{G}_T^{(k)}$ in Laplace domain.

However, the scheme used for Mori-Tanaka model is somewhat more complicated. The replacement scheme is firstly employed by replacing the displacement, strain and stress fields in the elastic domain by their Laplace transforms $u_i \to \hat{u}_i,\ \varepsilon_{ij} \to \hat{\varepsilon}_{ij}(s),\ \sigma_{ij} \to \hat{\sigma}_{ij}(s)$, and the elastic stiffness matrix elements by their Carson transforms $C_{ijkl} \to s\hat{C}_{ijkl}(s)$. Then far-field macroscopic strain is applied to generate strain concentration matrix $\hat{\mathbf{A}}_{m\infty}^{(f)}$ relating averaging fiber strain with averaging matrix strain $\hat{\bar{\varepsilon}}_f = \hat{\mathbf{A}}_{m\infty}^{(f)}\left(s\hat{\mathbf{C}}^{(f)}, s\hat{\mathbf{C}}^{(m)}, v_f \to 0\right)\hat{\bar{\varepsilon}}_m$ in the Laplace domain. In addition, Eq. (6.5) can be re-expressed in Laplace domain as

$$\hat{\bar{\varepsilon}} = [v_f \hat{\mathbf{A}}_{m\infty}^{(f)} + v_m \mathbf{I}]\hat{\bar{\varepsilon}}_m \tag{6.9}$$

Then the final elastic stiffness matrix in the transform domain can be expressed as

$$\hat{\mathbf{C}}^* = \hat{\mathbf{C}}^{(m)} + v_f(\hat{\mathbf{C}}^{(f)} - \hat{\mathbf{C}}^{(m)})\hat{\mathbf{A}}_{m\infty}^{(f)}[v_f \hat{\mathbf{A}}_{m\infty}^{(f)} + v_m \mathbf{I}]^{-1} \tag{6.10}$$

Similar to the process applied to LEHT discussed in last chapter, the homogenized relaxation moduli obtained by Mori-Tanaka model, Eq. (6.10), can be inverted back as elastic moduli using Eq. (6.8).

Two material systems are employed to generate the relaxation moduli: Glass/ED-6 resin (Cavalcante and Marques, 2014), and T300 graphite/934 resin at elevated temperature (Yancey and Pindera, 1990). And the fiber volume fraction employed for the stress distributions in this section is 60% to highlight the fiber-fiber interaction.

Material	E_A(GPa)	E_T(GPa)	μ_A(GPa)	μ_T(GPa)	ν_A
Glass fiber	68.67	68.67	28.38	28.38	0.21
T300 graphite fiber	214.33	14.82	68.18	7.06	0.45

Table 6.2 Elastic fiber properties used in the calculations.

Material	E_0(GPa)	E_1(GPa)	η_E^1(GPa·h)	η_E^2(GPa·h)	C(1/GPa·min)	n	ν_m
ED-6	3.27	1.8	300	8000			0.38
934	3.36				0.025	0.20	0.317

Table 6.3 Viscoelastic four-parameter and power-law model parameters for the response of resin.

First, the relaxation moduli are generated using graphite/epoxy resin composite, and power law model is used to model the matrix response. The isotropic creep compliance $S(t)$, for the power law model is given by:

$$S(t) = D_0 + Ct^n \tag{6.11}$$

in which D_0 is the instantaneous elastic compliance, and $D_0 = 1/E_0$, where E_0 is the instantaneous elastic stiffness. C and n are experimentally measured parameters, and t is time. The parameters can be referred to Table. 6.3.

Fig. 6.6 illustrates the comparison of relaxation moduli up to 200 minutes between three models. Similar to Chapter 5, two popular assumptions are used for the consideration: (1) The hydrostatic response, in which the bulk modulus is assume to a constant (same value as the instantaneous response), and $K = \text{constant}$; (2) the Poisson's ratio is fixed as $\nu = \text{constant}$.

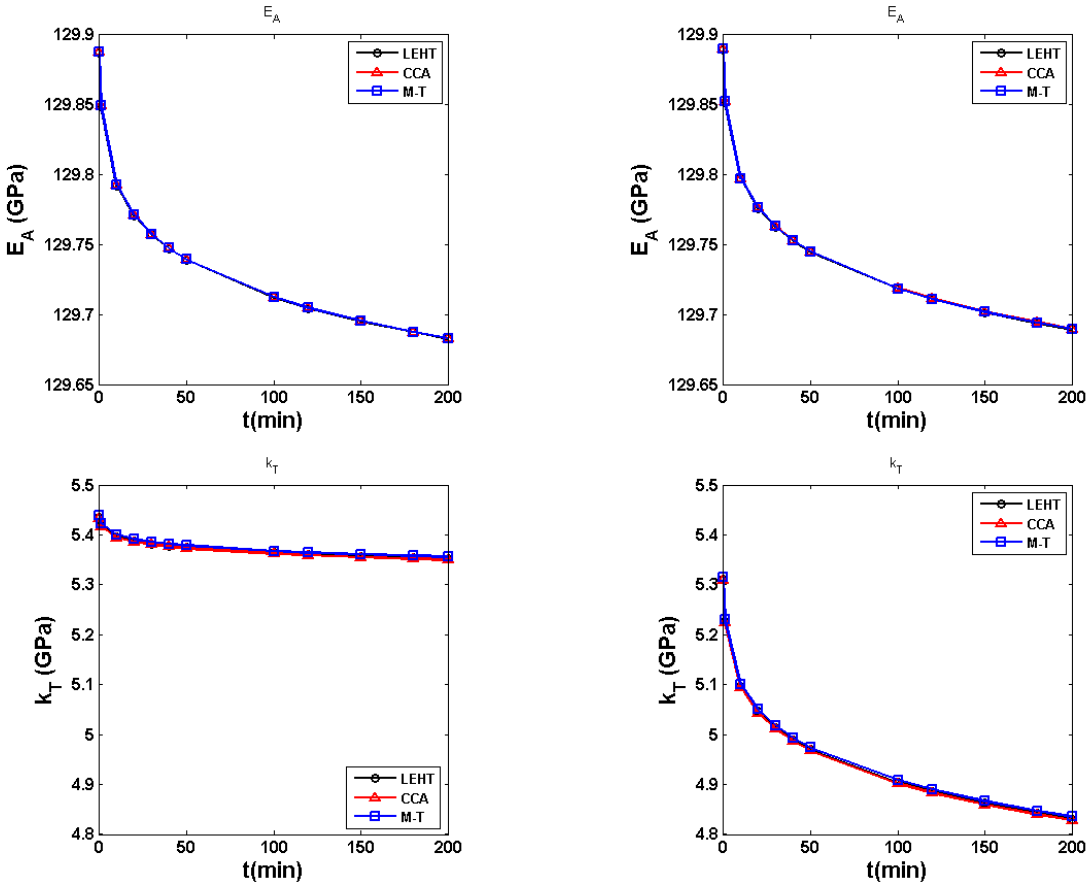

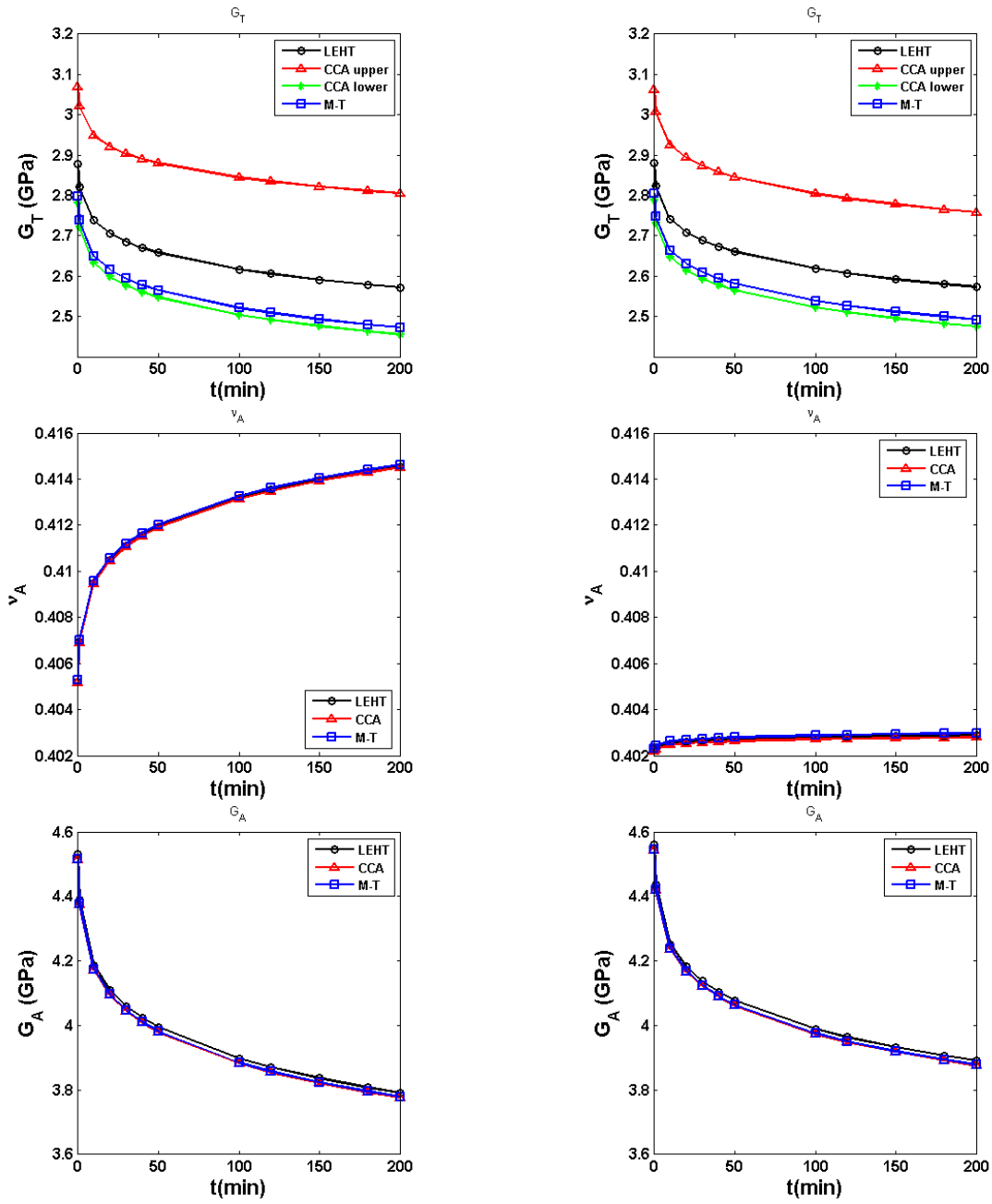

$K = \text{constant}$ $\nu = \text{constant}$

Fig. 6.6 Comparison of the relaxation moduli of graphite/934 resin for LEHT, CCA model and Mori-Tanaka model: constant bulk modulus of the epoxy matrix (left column) and constant Poission's ratio of epoxy matrix (right column).

As is noticed in the figure, all three models predict almost the same behavior under axisymmetric and axial shear loading, and $E_A(t)$, $k_T(t)$, $\nu_A(t)$, $G_A(t)$ are almost identical for different three models. Similar as elastic behavior, the transverse shear modulus G_T generated by LEHT in viscoelastic domain is also between upper and lower bounds of CCA model, while Mori-Tanaka model predicts G_T that is close enough to the lower bound of the CCA model. From the other perspective, slight difference can be observed for three of the five relaxation moduli $E_A(t)$, $G_A(t)$, $G_T(t)$ investigated in the figure under two different assumptions that model the response of the matrix. And big differences are found for k_T, ν_A, while inplane bulk modulus creep much less for the constant K case, and axial shear Poisson's ratio almost keep constant for the constant ν case.

Then the glass/resin system is used here to show higher inplane modulus contrast. The ED-6 resin employed here is modeled using four-parameter model, which is comprised by two springs and two dashpots, arranged as shown in Fig. 6.7,

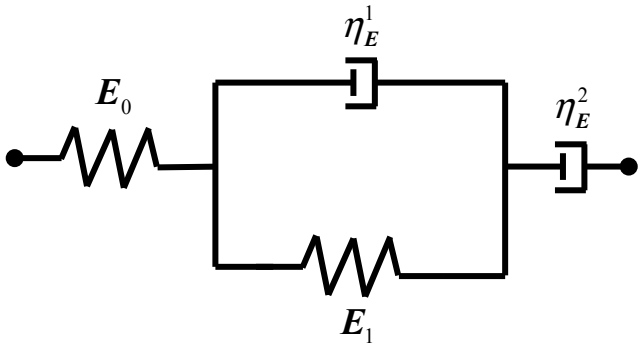

Figure 6.7 Mechanical representation of the four-parameter model

The creep compliance in tension for this model takes the following form

$$S(t) = \frac{1}{E_0} + \frac{1}{E_1}(1 - e^{-\frac{E_1}{\eta_E^1}t}) + \frac{t}{\eta_E^2} \tag{6.12}$$

and the parameters are listed in the Table. 6.3.

As we can see in the Fig. 6.8, the response of Axial Young's modulus is identical in both cases. The axial shear modulus is also same predicted by three models in each case, but small difference can be observed between the two assumptions. This is because for the out-of-plane

shear problem, the same Young's modulus of the matrix is firstly assumed based on different models, and then shear modulus G_m would be different based on different assumptions from the relationship $G_m = E_m/2(1+\nu_m)$.

As already observed in the moduli of graphite/resin in Fig. 6.6, the transverse shear modulus G_T predicted by LEHT lies between the upper and lower bounds of CCA model, while Mori-Tanaka model gives almost same results as lower bound of CCA model. It should be mentioned that LEHT has been validated by numerical technique FVDAM (Cavalcante and Marques, 2014) and another analytical technique in the work of Luciano and Barbero (1995), which are discussed in detailed in Chapter 5.

Similar phenomenon as Fig 6.6 also happens to the plain strain bulk modulus k_T and axial shear Poisson's ratio between the two assumptions when k_T creeps less in constant bulk modulus case and ν_A barely changes in the constant Poisson's ratio case.

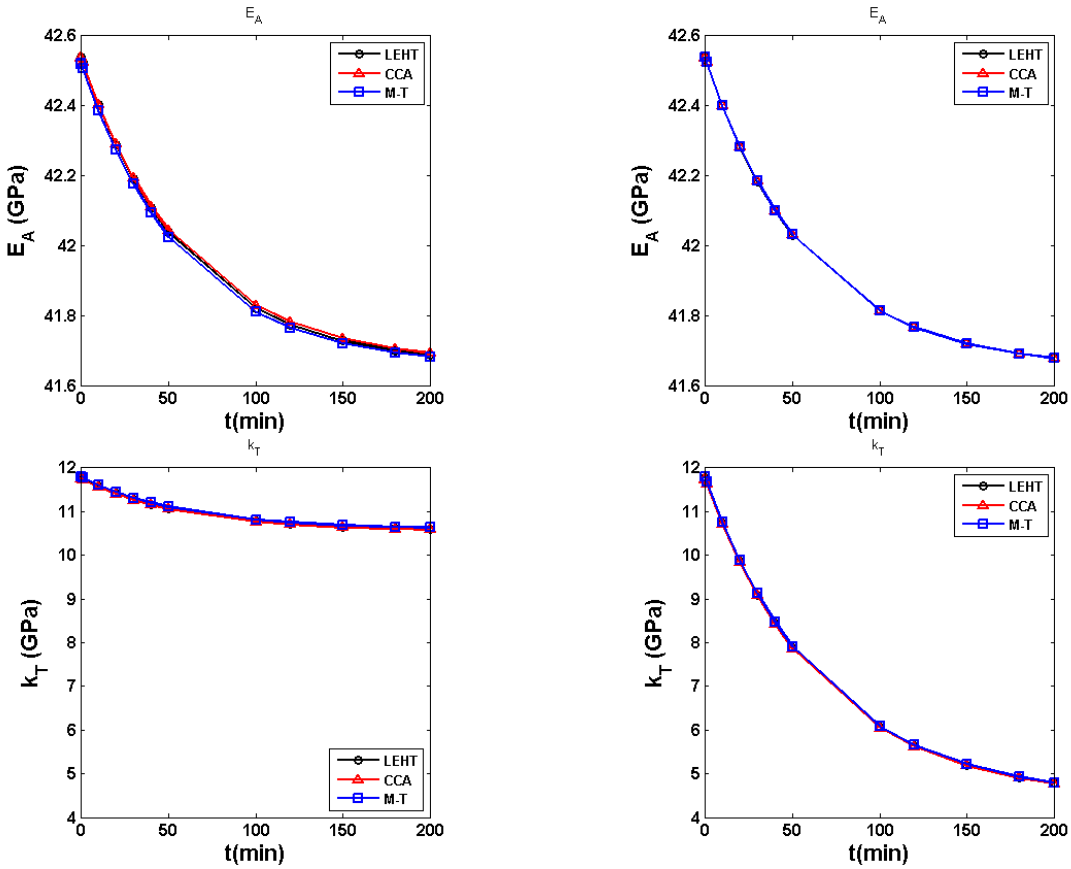

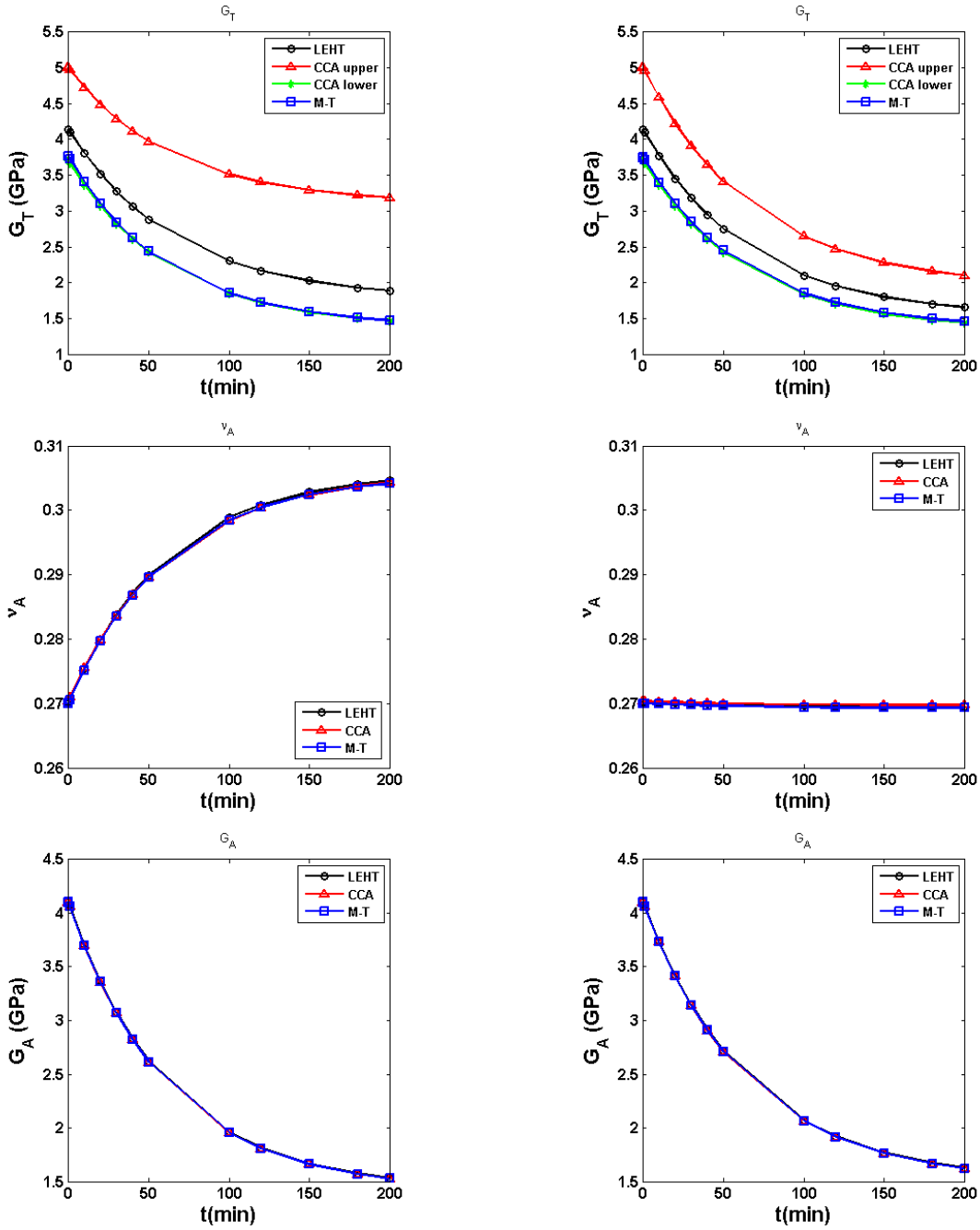

K = constant ν = constant

Fig. 6.8 Comparison of the relaxation moduli of glass/ED-6 resin for LEHT, CCA model and Mori-Tanaka model: constant bulk modulus of the epoxy matrix (left column) and constant Poission's ratio of epoxy matrix (right column).

Next, the stress distributions are compared between LEHT and CCA model to show the evolution of the material properties. The stress fields are generated by applying two different types of loading: transverse axisymmetric loading and axial shear loading, which are illustrated in Fig 6.9 and 6.10, respectively. Here the stress distributions are generated at $t = 0$, $t = 150\text{h}$ and $t = 600\text{h}$ (from left to right). As is observed, the stress fields are similar predicted by the two models. But the CCA model cannot capture the disturbance in the fiber region when the fiber-fiber interaction become obvious (fiber volume fraction is 60%), but it does show similar distributions in the matrix against LEHT, which cannot be illustrated by Mori-Tanaka model.

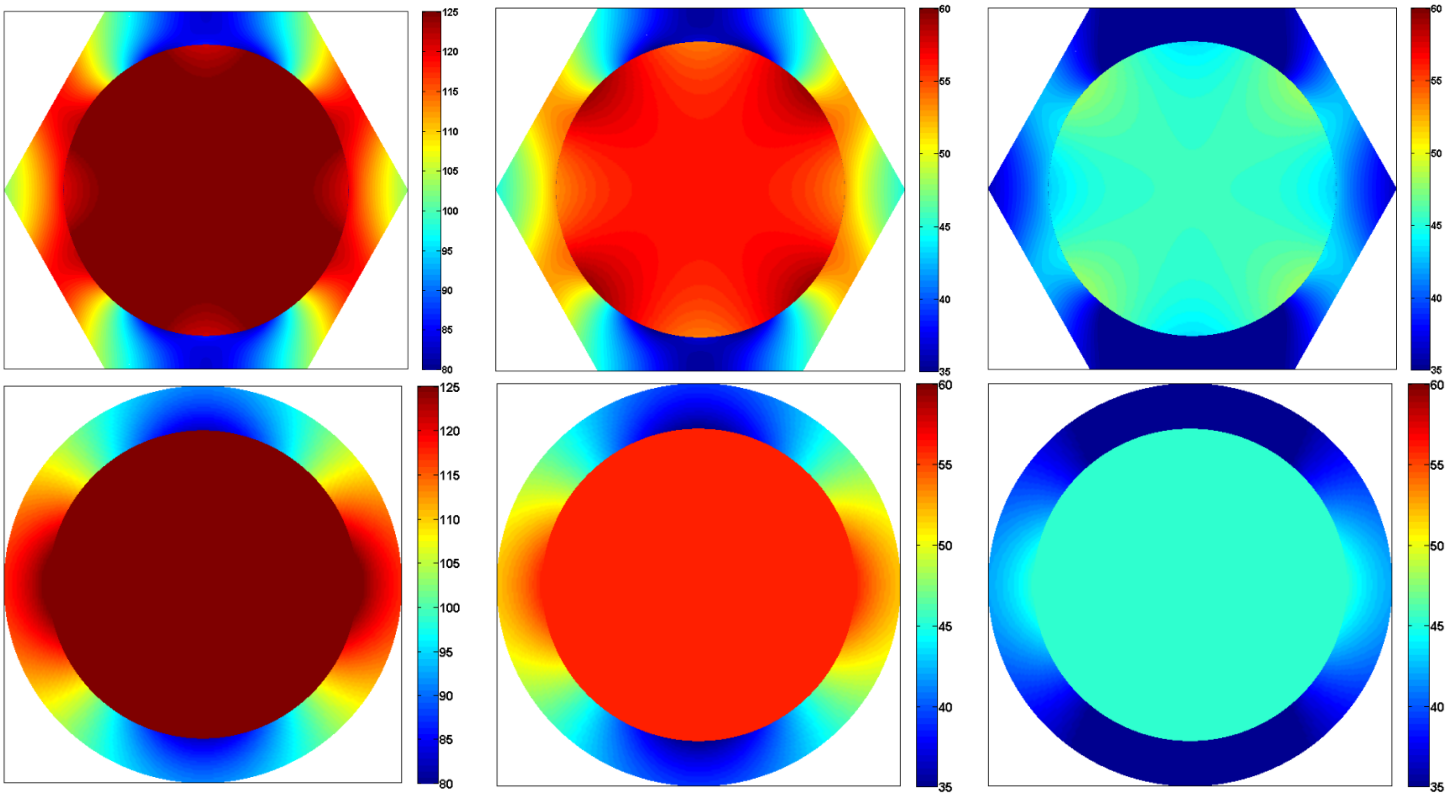

(a) $\sigma_{22}(y_2, y_3)$

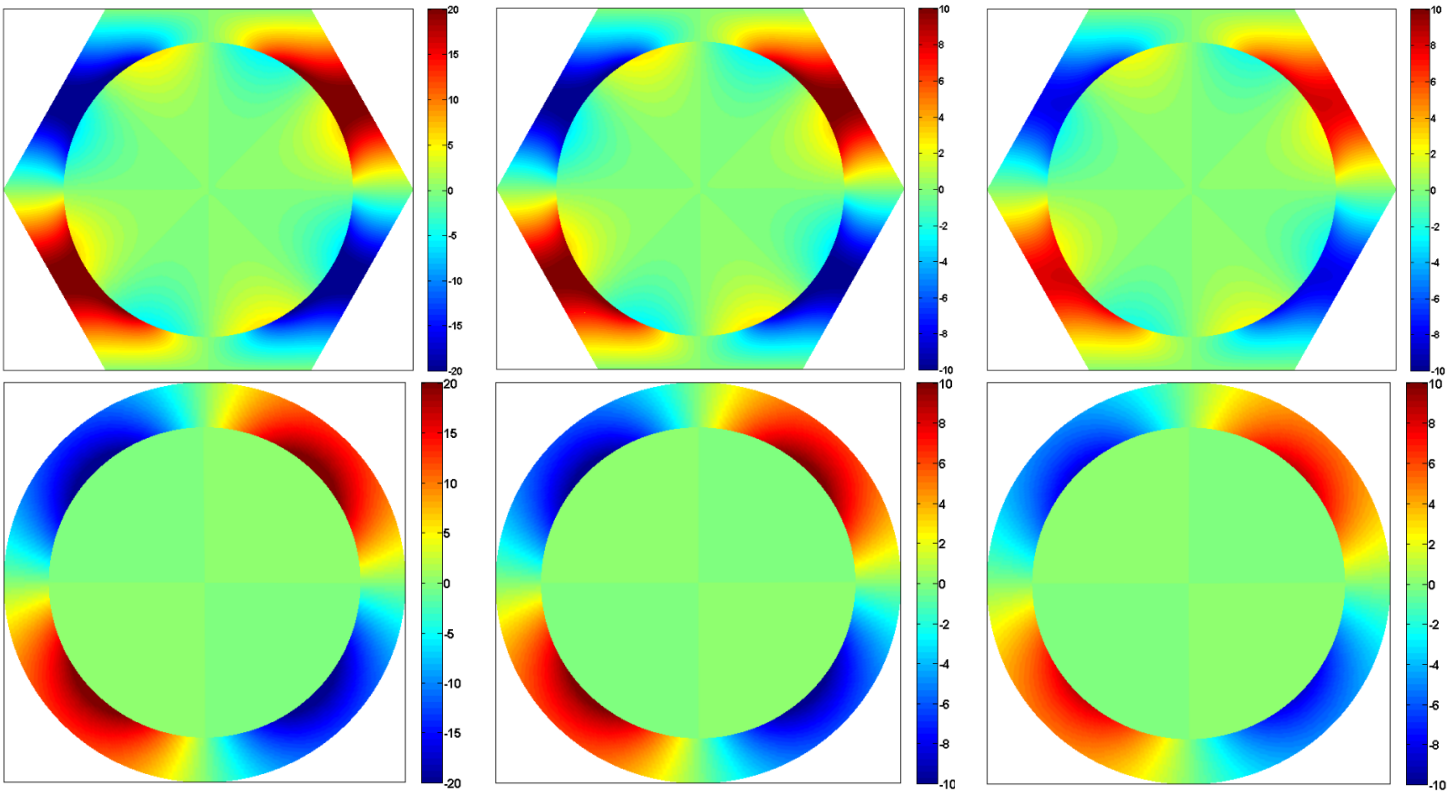

(b) $\sigma_{23}(y_2, y_3)$

Fig. 6.9 Comparison of the converged stress distributions σ_{22}, σ_{23} of glass/epoxy composite with the fiber volume fraction of 0.6 subjected to the axisymmetric loadings (1) $\bar{\varepsilon}_{22} = \bar{\varepsilon}_{33} = 0.005$ for hexagonal array (top); (2) $\bar{\varepsilon}_{rr} = 0.005$ for CCA model (bottom); at different time points: 0, 150h, 600h (from left to right).

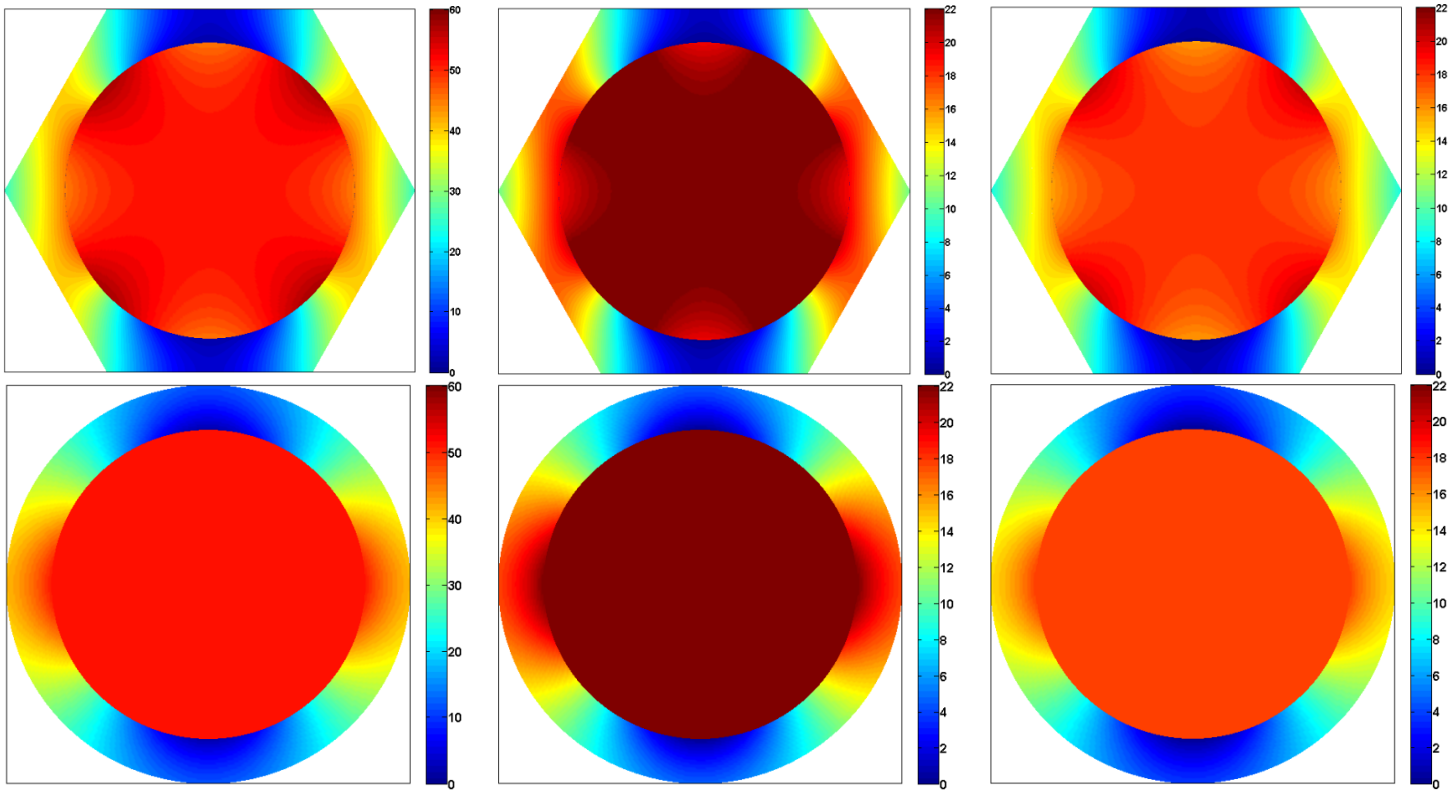

(a) $\sigma_{12}(y_2, y_3)$

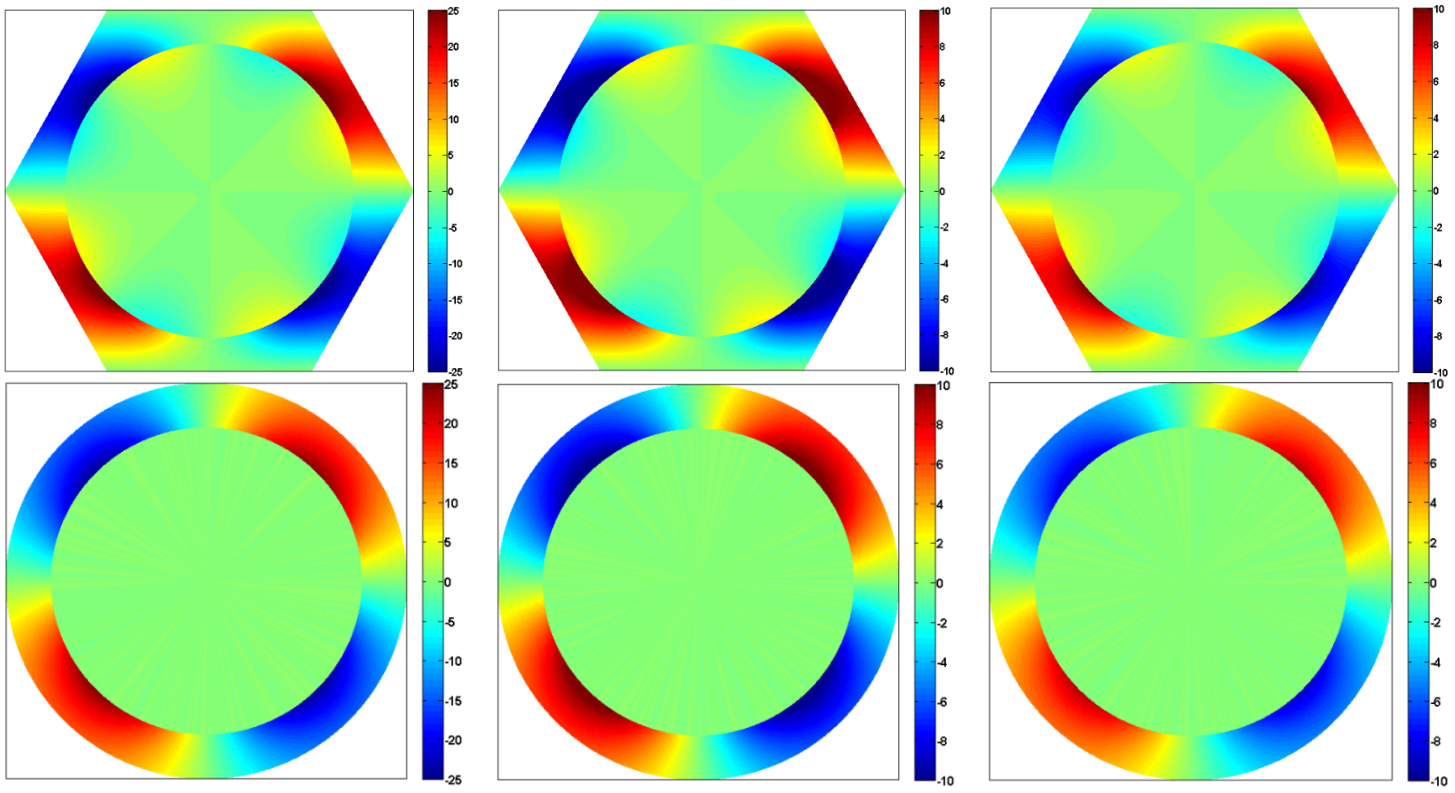

(b) $\sigma_{13}(y_2, y_3)$

Fig. 6.10 Comparison of the converged stress distributions σ_{12}, σ_{13} of glass/epoxy composite with the fiber volume fraction of 0.6 subjected to the axial shear loadings (1) $\bar{\varepsilon}_{12} = 0.005$ for hexagonal array (top); (2) $\bar{\varepsilon}_{zr} = 0.005$ for CCA model (bottom); at different time points: 0, 150h, 600h (from left to right).

6.4 Remarks

In this chapter, two of the most well cited models in micromechanics community, CCA and Mori-Tanaka models, are investigated and compared with the LEHT. Both the elastic and viscoelastic cases are studied. Based on the study of homogenized moduli and stress distributions. A few points can be used to conclude this chapter:

(1) CCA model is an easy-to-use and explicitly expressed analytical technique for the prediction of effective properties in microstructures. The model provides accurate predictions for four of the five transversely isotropic elastic effective properties (or viscoelastic relaxation moduli) – E_A, k_T, ν_A, G_A, but only gives upper and lower bounds for the fifth one: G_T. In addition, the fiber-fiber interaction is still an obstacle especially when the fiber volume fraction is large.

(2) Mori-Tanaka model is also a straightforward concept to be understood and employed, which is based on the assumption of averaged matrix stress distributions. Most of the predictions for the homogenized moduli are almost identical compared with LEHT and CCA, as well as Mori-Tanaka model. However, the transverse normal and shear moduli predicted by Mori-Tanaka model are almost identical as lower bound of the CCA model in both elastic case and viscoelastic case, which have obvious discrepancies against LEHT that has been validated by other techniques. Also, the stress distributions cannot be investigated using Mori-Tanaka model.

(3) Locally exact homogenization theory can be used as a standard against other models because it shows accurate predictions for the homogenized moduli, which is already discussed in previous chapters, and stress distributions in different geometrical microstructures, for both elastic and viscoelastic cases.

The accurate and efficient calculations of both homogenized moduli and stress distributions are mainly because of the balanced variaitional principle firstly proposed by Drago and Pindera (2008), which will be discussed and compared in details with another well known method for boundary conditions implementation – Jirousek's constrained variaitional approach.

Chapter 7

Effect of Boundary Conditions Implementation

7.1 Introduction

Convergence of the locally-exact homogenization theory for periodic materials was investigated in Chapter 4 for both hexagonal and square arrays, based on isotropic and transversely isotropic material properties. In the theoretical construction, the interior problem is solved exactly one harmonic at a time using Fourier series expansions for the displacement fields in the fiber and matrix phases which satisfy both the Navier's equations and continuity conditions. Alternatively, the non-separable exterior problem involving the implementation of periodic boundary conditions is solved approximately using a new balanced variational principle which leads to exceptionally fast and well-behaved convergence of the Fourier series coefficients. Jirousek (1978) proposed another variational principle derived from a constrained potential energy functional for finite-element solutions based on locally-exact elements, which motivated the development of the balanced variational principle that is employed in the locally-exact homogenization theory. Recently, Jirousek's constrained variational principle has been re-discovered by a number of researchers and applied to the homogenization of periodic materials, Yan et al. (2010), Yan and Jiang (2010), Yan et al. (2011, 2013), Guinovart-Díaz et al. (2012), Rodríguez-Ramos et al. (2013). The focus of these investigations was on homogenized thermo-electrical-mechanical moduli, with little mention of the convergence behavior or local field accuracy.

In this chapter, we compare the unit cell's solution convergence behavior based on the two different implementations of periodic boundary conditions, namely the constrained and balanced variational principles, in a wide range of fiber volume fraction, modulus contrasts and two array

types to demonstrate the latter principle's advantages. Such comparison is highly relevant and a major contribution to the literature given the gaining popularity of the recently re-discovered constrained variational principle.

7.2 Periodic Boundary Conditions

Upon solution of the Navier's equations in the individual phases of a unit cell, and enforcing the fiber/matrix interfacial continuity conditions on both tractions and displacements, the unknown coefficients associated with the displacement field in the matrix phase are expressed in terms of the unknown fiber coefficients $\mathrm{F}_n^{(f)}, \mathrm{G}_n^{(f)}, \mathrm{H}_n^{(f)}$, which are determined from the periodic traction and displacement boundary conditions. For the non-separable exterior problem, the two common ways of implementing periodic boundary conditions involved collocation and least squares methods. These two approaches, however, are not very stable, and often require large numbers of harmonics in the displacement field representation, as demonstrated by Drago (2008). Jirousek (1978) proposed a variational principle based on minimum potential energy for large-deformation problems solved using a locally-exact approach in the context of finite-element method. Motivated by this approach, Drago and Pindera (2008) developed the balanced variational principle for implementation of the periodic boundary conditions discussed in detail in Chapter 2.

The balanced variational principle is compared with Jirousek's constrained variational approach in the sequel to demonstrate the differences and similarities. These features enable straightforward implementation of the constrained variational principle into the locally-exact homogenization framework. The numerical results are limited to these two approaches as the collocation and least squares methods have been extensively discussed by Drago (2008), and proved to be unstable and inefficient techniques vis-à-vis homogenized moduli and stress distribution calculations.

Jirousek (1978) had proposed the following augmented functional in developing a finite-element procedure locally satisfying all field equations

$$H_J = \frac{1}{2}\int_V \sigma_{ij}\varepsilon_{ij}dV - \int_{S_t} \mathbf{t}_i^0 \mathbf{u}_i dS - \int_{S_u} \mathbf{t}_i(\mathbf{u}_i\text{-}\mathbf{u}_i^0)dS \tag{7.1}$$

This functional represents the potential energy (the first two terms) subject to the displacement constraint (third term) over S_u. In the context of the unit cell problem, $\mathbf{t}^0$ and

$\mathbf{u}^0$ are interpreted as periodic traction and displacement constraints imposed on S_t and S_u, respectively. Thus the additional term appearing in the variational principle represents a constraint on the periodic displacement boundary conditions over a portion of the RUC boundary.

Taking the first variation of H_J, and using the fact that our local elasticity solutions satisfy the stress equilibrium equations a *priori*, so that

$$\frac{1}{2}\int_V \sigma_{ij}\varepsilon_{ij}dV = \frac{1}{2}\int_S \mathbf{t}_i\mathbf{u}_i dS \tag{7.2}$$

After some manipulation, we obtain the variational principle in the final form

$$\int_{S_t} \delta\mathbf{u}_i(\mathbf{t}_i - \mathbf{t}_i^0)dS - \int_{S_u} \delta\mathbf{t}_i(\mathbf{u}_i - \mathbf{u}_i^0)dS = 0 \tag{7.3}$$

On the other hand, the proposed balanced variational principle is expressed as:

$$H_{D-P} = \frac{1}{2}\int_V \sigma_{ij}\varepsilon_{ij}dV - \int_{S_u} \mathbf{t}_i\mathbf{u}_i^0 dS - \int_{S_t} \mathbf{t}_i^0\mathbf{u}_i dS \tag{7.4}$$

which leads to the variational statement

$$\int_{S_t} \delta\mathbf{u}_i(\mathbf{t}_i - \mathbf{t}_i^0)dS + \int_{S_u} \delta\mathbf{t}_i(\mathbf{u}_i - \mathbf{u}_i^0)dS = 0 \tag{7.5}$$

Implementing periodic boundary conditions in the first variation of the functionals representing the two variational principles, we obtain the inplane expressions:

(a) Rectangular or parallelogram arrays

$$\begin{aligned}&\sum_{i=1}^{2}\int_{S_i}\left\{\delta T_2(S_i)\left[u_2'(S_i) - u_2'(S_{i+2})\right] + \delta T_3(S_i)\left[u_3'(S_i) - u_3'(S_{i+2})\right]\right\}dS \\ &\quad \mathrm{m}\sum_{i=3}^{4}\int_{S_i}\left\{\delta u_2'(S_i)\left[T_2(S_i) + T_2(S_{i-2})\right] + \delta u_3'(S_i)\left[T_3(S_i) + T_3(S_{i-2})\right]\right\}dS = 0\end{aligned} \tag{7.6}$$

(b) Hexagonal array

$$\begin{aligned}&\sum_{i=1}^{3}\int_{S_i}\left\{\delta T_2(S_i)\left[u_2'(S_i) - u_2'(S_{i+3})\right] + \delta T_3(S_i)\left[u_3'(S_i) - u_3'(S_{i+3})\right]\right\}dS \\ &\quad \mathrm{m}\sum_{i=4}^{6}\int_{S_i}\left\{\delta u_2'(S_i)\left[T_2(S_i) + T_2(S_{i-3})\right] + \delta u_3'(S_i)\left[T_3(S_i) + T_3(S_{i-3})\right]\right\}dS = 0\end{aligned} \tag{7.7}$$

and for the out-of-plane loading:

(a) Rectangular or parallelogram arrays

$$\sum_{i=1}^{2}\int_{S_i}\delta T_1(S_i)\left[u_1'(S_i)-u_1'(S_{i+2})\right]dS \mp \sum_{i=3}^{4}\int_{S_i}\delta u_1'(S_i)\left[T_1(S_i)+T_1(S_{i-2})\right]dS=0 \qquad (7.8)$$

(b) Hexagonal array

$$\sum_{i=1}^{3}\int_{S_i}\delta T_1(S_i)\left[u_1'(S_i)-u_1'(S_{i+3})\right]dS \mp \sum_{i=4}^{6}\int_{S_i}\delta u_1'(S_i)\left[T_1(S_i)+T_1(S_{i-3})\right]dS=0 \qquad (7.9)$$

Comparing the two variational principles we observe that the differences in the final equations lie in the "∓" signs between the terms involving the unit cell boundary summations. This feature makes it very easy to incorporate the constrained variational principle into the locally-exact homogenization theory's framework for comparison with the balanced principle.

7.3 Numerical Results

The main focus of the numerical study is to compare the locally-exact homogenization theory's convergence behavior as a function of the number of harmonics in the displacement field representation based on the implementation of periodic boundary conditions using the balanced and constrained variational principles. This is carried out by computing the homogenized engineering moduli and local stress fields as a function of the harmonic number for unit cells representative of glass/epoxy and graphite/epoxy unidirectional composites, as well as aluminum with cylindrical porosities. These material systems are characterized by a wide range of fiber/matrix modulus contrasts, and include both isotropic and transversely isotropic fibers, see Table 1. In the case of graphite/epoxy, coated fibers are also included in the convergence study for several coating thicknesses. Unit cells representative of hexagonal and square arrays are considered with fiber/porosity volume fractions of 0.20, 0.50 and 0.60. Convergence of homogenized moduli was investigated for unit cells with centered fibers, whereas local stress fields were computed at selected harmonic numbers for both centered and off-set fibers under uniaxial loading. The uniaxial loading was achieved by applying the correct ratios of the homogenized strains that produced the desired non-zero homogenized stress component. In the case of axial and transverse shear loading, it was sufficient to set the remaining homogenized strains to zero because of the absence of coupling between normal and shear strains. For loading by normal strains, the appropriate homogenized strain ratios necessary to achieve the desired non-zero homogenized stress were obtained from the homogenized Hooke's law.

The homogenized engineering moduli were computed using the elements of the

homogenized compliance matrix $\mathbf{S}^*$. This matrix is the inverse of the homogenized stiffness matrix $\mathbf{C}^*$ appearing in the homogenized Hooke's law in Eqs. (2.61)-(2.62). Given that the elements of $\mathbf{S}^*$ are expressed directly in terms of the engineering moduli, and $\mathbf{S}^* = [\mathbf{C}^*]^{-1}$, the six and five independent homogenized engineering moduli of square and hexagonal arrays, respectively, E_{11}^*, $E_{22}^* = E_{33}^*$, $\nu_{12}^* = \nu_{13}^*$, ν_{23}^*, $G_{12}^* = G_{13}^*$, G_{23}^* can readily be calculated. For instance, $E_{11}^* = 1/S_{11}^*$, $\nu_{12}^*/E_{22}^* = -S_{21}^*$, $G_{12}^* = 1/S_{66}^*$, etc.

In the sequel, the presentation of results is organized by material systems characterized by different fiber/matrix modulus contrasts.

Material	E_A(GPa)	E_T(GPa)	μ_A(GPa)	μ_T(GPa)	ν_A
E-glass fiber	69.0	69.0	28.28	28.28	0.22
3501-6 epoxy	4.2	4.2	1.567	1.567	0.34
Aluminum	69.0	69.0	25.94	25.94	0.33
Porosity	69.0e-6	69.0e-6	25.94e-6	25.94e-6	0.33
Graphite fiber	214	14	7	5.83	0.25
Epoxy	3.5	3.5	1.296	1.296	0.35
Coating	5.25	5.25	2.059	2.059	0.275

Table 7.1 Elastic fiber, coating, and matrix properties employed in the calculations.

7.3.1 Glass/Epoxy Composite

We start with the convergence of the three homogenized moduli E_{22}^*, G_{23}^* and G_{12}^* of a unidirectional glass/epoxy composite containing 0.20 fiber volume fraction. The fiber/matrix Young's modulus contrast for this system is approximately sixteen and a half. The chosen moduli are representative of the coupled and uncoupled systems of equations that must be solved to generate them. Unit cells with centered fibers were used in the computations. As observed in Fig. 7.1, the balanced variational principle produces converged homogenized moduli with as few harmonics as four and six for the hexagonal and square arrays, respectively. Greater number of harmonic terms is required for the constrained variational principle, where greater variations in the homogenized moduli are also observed at low harmonic numbers, in contrast with the balanced principle. For instance, the homogenized transverse shear modulus G_{23}^* requires eleven harmonics for convergence in the case of the hexagonal array.

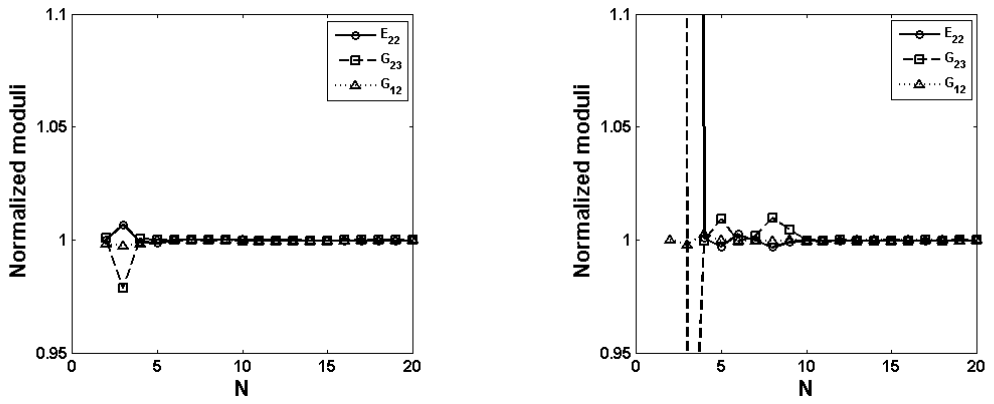

(a) Hexagonal array

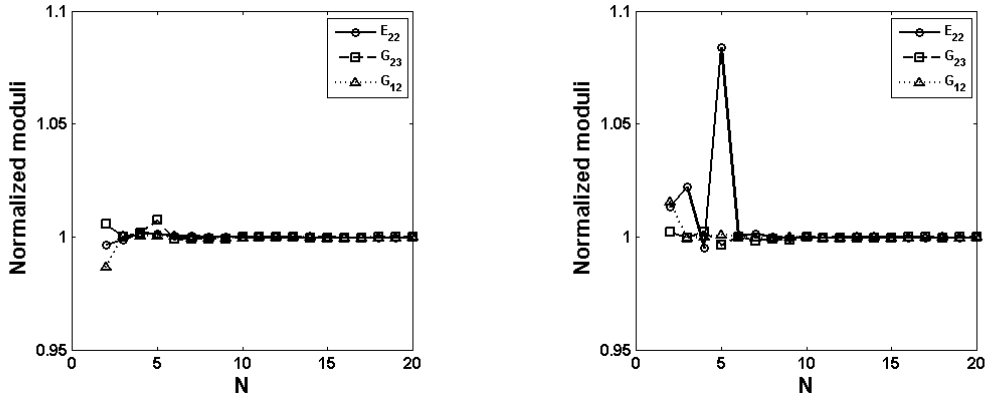

(b) Square array

Balanced variational principle Constrained variational principle

Figure 7.1 Convergence of homogenized moduli $E_{22}^{*}, G_{23}^{*}, G_{12}^{*}$ for unidirectional glass/epoxy, containing 0.20 fiber volume fraction, with the number of harmonics used in the displacement field representation.

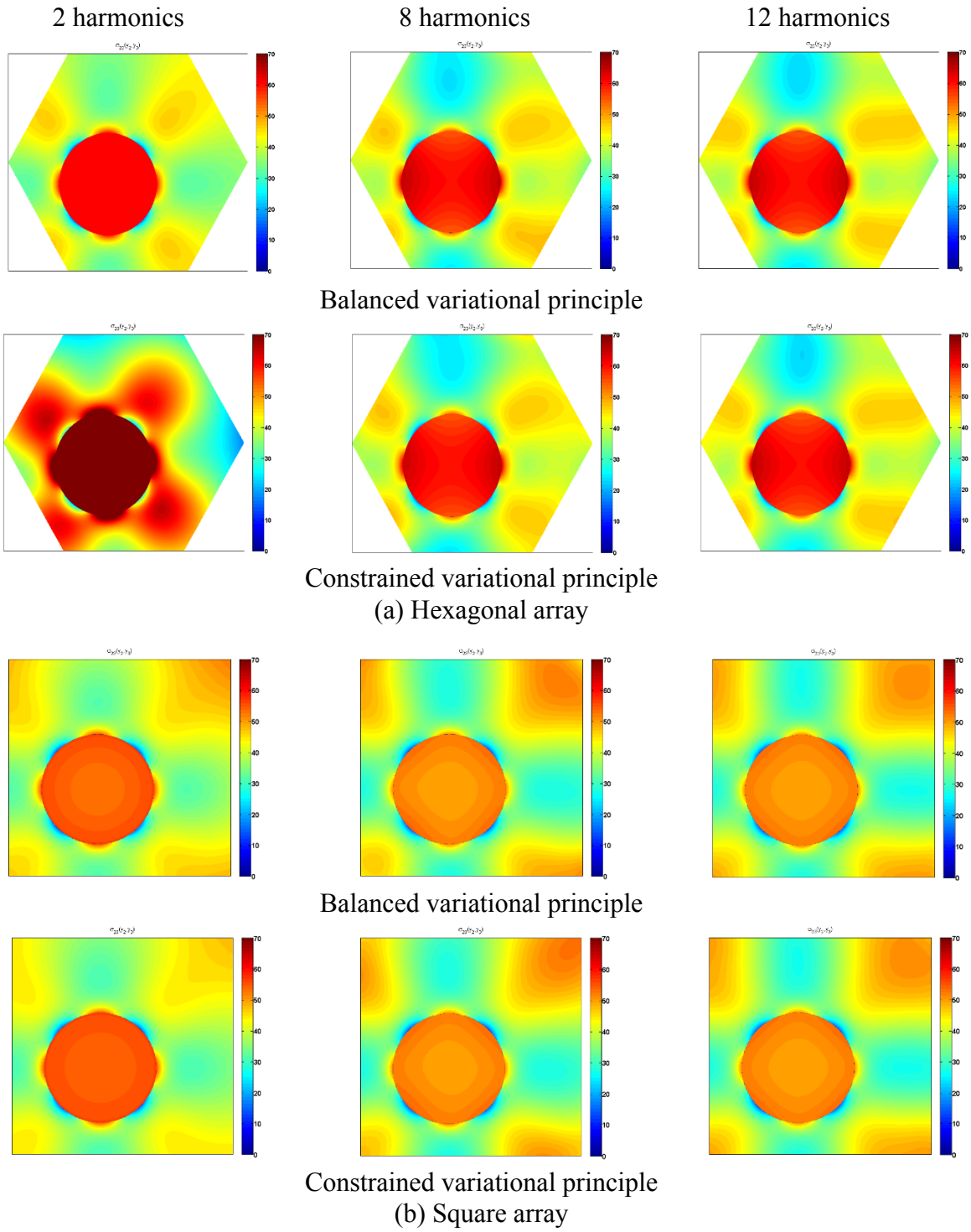

Figure 7.2 Comparison of $\sigma_{23}(y_2, y_3)$ stress fields in unidirectional glass/epoxy containing 0.20 fiber volume fraction for loading by $\bar{\varepsilon}_{23} = 0.01$ generated using 2, 8 and 12 harmonics by balanced and constrained variational approaches.

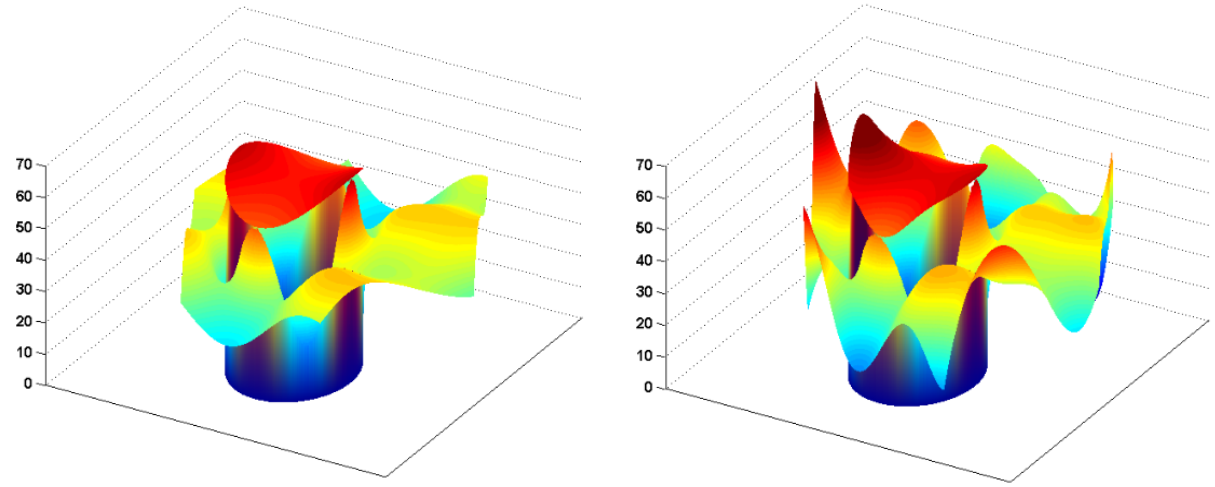

(a) Hexagonal array

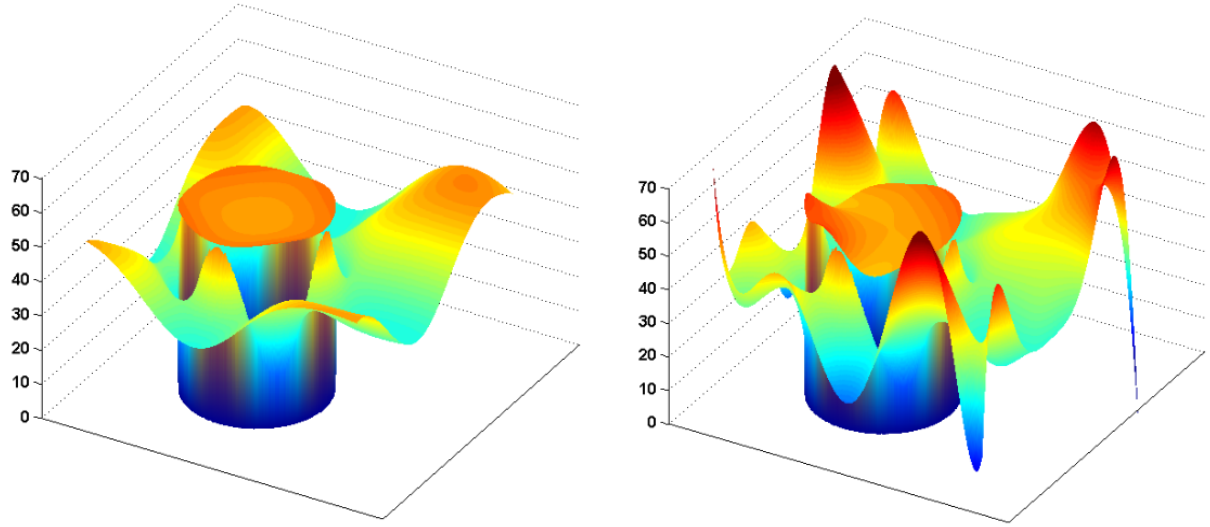

(b) Square array

Balanced variational principle Constrained variational principle

Figure 7.3 Comparison of $\sigma_{23}(y_2, y_3)$ stress fields in unidirectional glass/epoxy containing 0.20 fiber volume fraction for loading by $\bar{\varepsilon}_{23} = 0.01$ generated using 9 harmonics by balanced and constrained variational approaches.

The observed convergence behavior of the homogenized engineering moduli with harmonic number may also be used as a rough indicator of the convergence of local stress fields under uniaxial loading. It is certainly an accurate indicator of the convergence of the local stress fields to their integral or average values as the elements of the homogenized stiffness matrix may also be computed from the ratios of the average stresses and one non-zero homogenized strain component that produces them, rather than the strain concentration matrix approach employed in the present study. These ratios determine the elements of the column of the homogenized stiffness matrix that corresponds to the applied homogenized strain component. The results shown in Fig. 7.1 suggest that the balanced variational principle produces local stresses that converge to their homogenized values rapidly and generally smoothly with harmonic number. Moreover, the convergence is not greatly influenced by the fiber's placement which may be centered (which was used to compute the homogenized engineering moduli in Fig. 7.1), or offset from the center, nor array type. The point-wise convergence is also generally smooth and predictable. This is in contrast with the local stress convergence obtained from the constrained variational principle, which may be erratic and dependent on the fiber placement as demonstrated below.

Fig. 7.2 illustrates the convergence of the local stress fields $\sigma_{23}(y_2, y_3)$ at the applied transverse shear strain $\bar{\varepsilon}_{23} = 0.01$ in hexagonal and square unit cells of the glass/epoxy composite with off-set fibers generated using 2, 8 and 12 harmonics. The notable feature of the balanced variational principle is the ability to capture the essential details of the stress field with even two harmonics, which become continuously refined in a smooth fashion with increasing number of harmonics. For the hexagonal array, the transverse shear stress field generated using 8 harmonics is nearly converged, with 12 harmonics producing additional refinement and convergence. This contrasts with the constrained variational principle which exhibits slower and more erratic convergence. Fig. 7.3 highlights this point for both arrays whose local transverse shear stress fields were generated using 9 harmonics. The stress distributions were generated in three dimensions to highlight the differences and non-uniform convergence behavior of the constrained variational principle which produces distributions with large departures from those generated using 8 and 12 harmonics shown in Fig. 7.2. In contrast, the stress distributions for both arrays produced using the balanced variational principle shown in Fig. 7.3 conform to those of Fig. 7.2 with regard to smooth convergence.

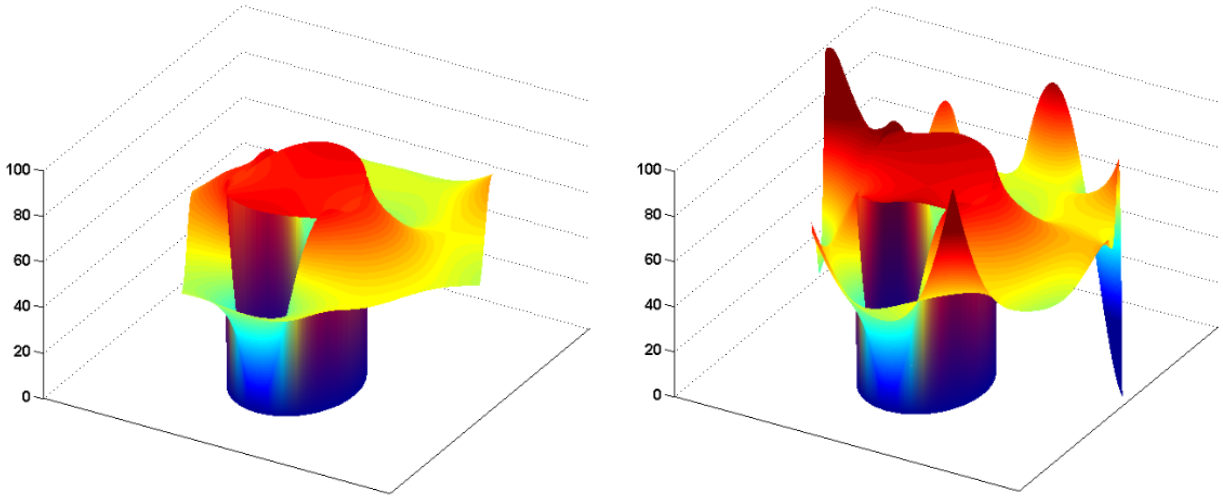

(a) Hexagonal array

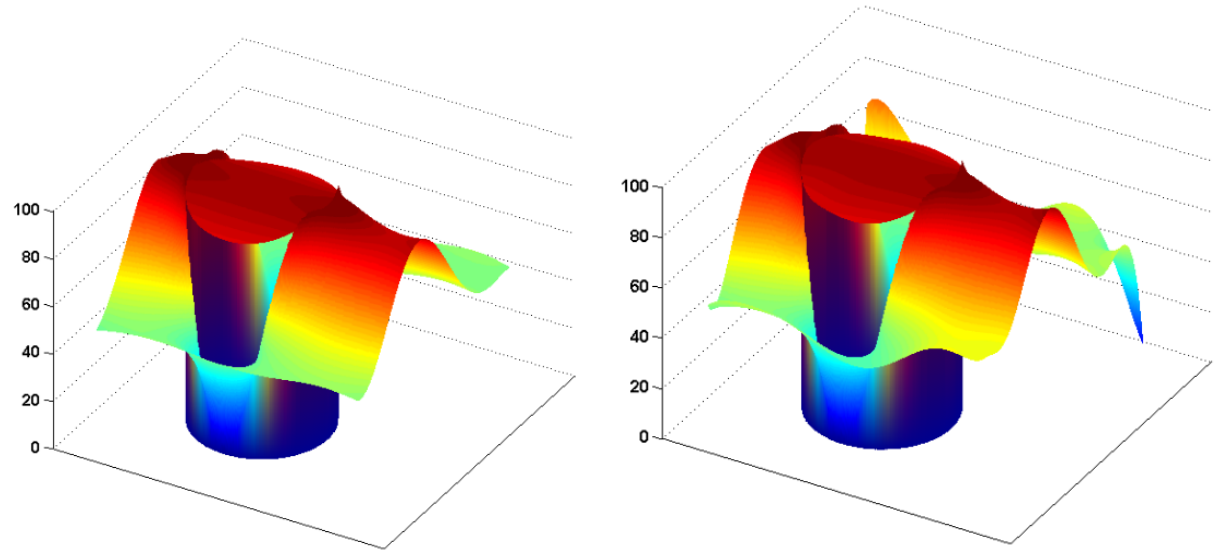

(b) Square array

Balanced variational principle Constrained variational principle

Figure 7.4. Comparison of $\sigma_{22}(y_2, y_3)$ stress fields in unidirectional glass/epoxy containing 0.20 fiber volume fraction for loading by $\bar{\varepsilon}_{22} = 0.01$ generated using 9 harmonics by balanced and constrained variational approaches.

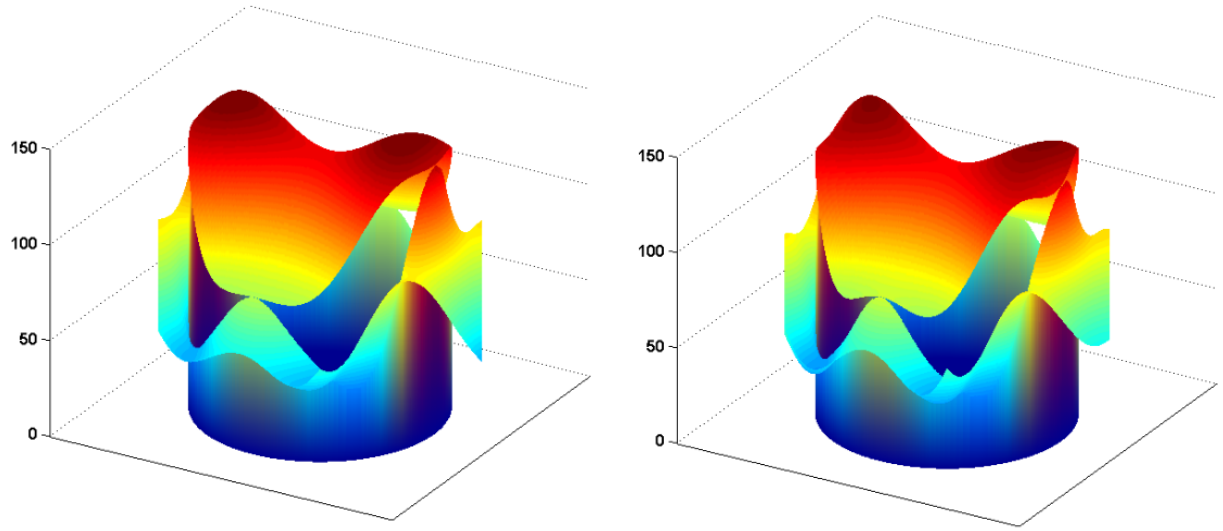

(a) Hexagonal array

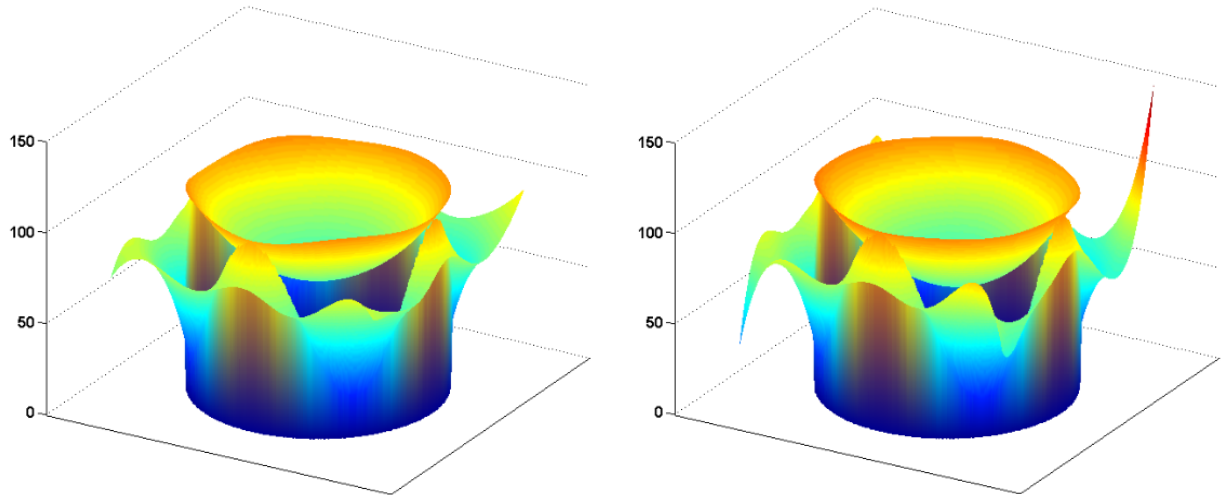

(b) Square array

Balanced variational principle Constrained variational principle

Figure 7.5 Comparison of $\sigma_{23}(y_2, y_3)$ stress fields in unidirectional glass/epoxy containing 0.60 fiber volume fraction for loading by $\bar{\varepsilon}_{23} = 0.01$ generated using 9 harmonics by balanced and constrained variational approaches.

Similar observations hold for uniaxial loading along other directions. This is illustrated in Fig. 7.4 for uniaxial loading by the non-zero homogenized stress $\bar{\sigma}_{22}$ at $\bar{\varepsilon}_{22} = 0.01$, with the remaining normal strains adjusted so as to produce $\bar{\sigma}_{11} = \bar{\sigma}_{33} = 0$. Nine harmonics were used to generate these stress distributions for both hexagonal and square arrays. Large departures of the distributions produced by the constrained variational principle from those based on the balanced principle are observed in the figure, especially around the unit cell boundaries. Examination of the stress field convergence at 2, 8 and 12 harmonics highlights the erratic convergence behavior of the constrained variational principle illustrated in Fig. 7.4 in a snapshot.

Increasing the volume fraction of the glass fibers increases the fluctuations observed in the convergence behavior of the homogenized moduli at low harmonic numbers. The number of harmonics required for converged homogenized moduli depends on the array type and particular modulus for both variational principles. For instance, in the case of the balanced variational principle, 8 harmonics are required for convergence of the transverse Young's modulus E_{22}^{*} for the hexagonal array, with just 4 for the remaining two moduli, whereas all homogenized moduli for the square array converge at 9 harmonics. The constrained variational principle generally requires greater number of harmonics for homogenized moduli convergence, which sometimes exhibits erratic behavior for some moduli. For instance, 15 harmonics are required for converged transverse Young's modulus E_{22}^{*} of the square array.

The above observations carry over to the local stress field convergence. Figure 7.5 compares the local stress fields $\sigma_{23}(y_2, y_3)$ at the applied transverse shear strain $\bar{\varepsilon}_{23} = 0.01$ in hexagonal and square unit cells of the glass/epoxy composite containing 0.60 fiber volume fraction that were generated using 9 harmonics. Unit cells with centered fibers were used in the simulations because of the high fiber volume fraction. At this harmonic, stress field convergence for both hexagonal and square arrays is not achieved using the constrained variational principle, with the difference relative to the balanced variational principle greater for the square array.

7.3.2 Aluminum/Porosity Composite

Figure 7.6 illustrates the comparison of the homogenized moduli convergence behavior of aluminum containing 0.20 volume fraction of cylindrical porosities generated using the two variational principles for the three homogenized moduli E_{22}^{*}, G_{23}^{*} and G_{12}^{*}. For this extreme

inclusion/matrix modulus contrast, the fluctuations observed in the convergence behavior of the homogenized moduli at low harmonic numbers are substantially greater relative to the glass/epoxy composite of the preceding section. The balanced variational principle also produces faster convergence in this case for both hexagonal and square arrays relative to the constrained principle. The erratic convergence behavior generated by the constrained variational principle is observed for both arrays, and is particularly pronounced for the hexagonal array for which 14 harmonics were required to achieve converged homogenized modulus G_{23}^{*}.

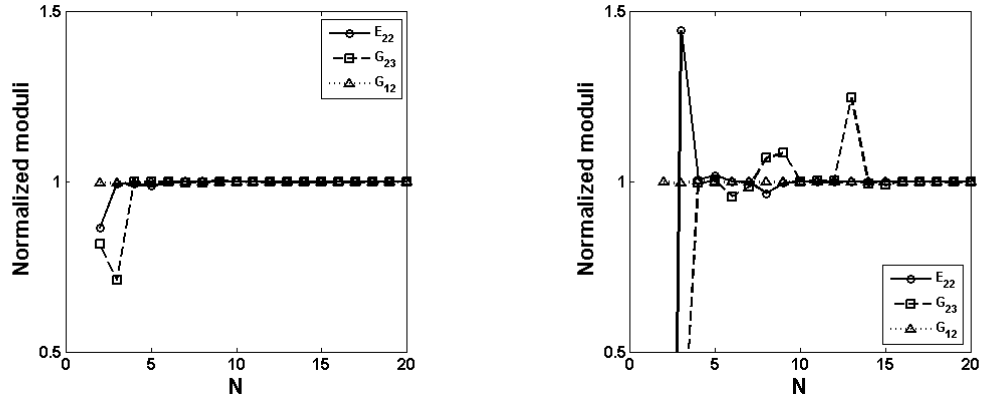

(a) Hexagonal array

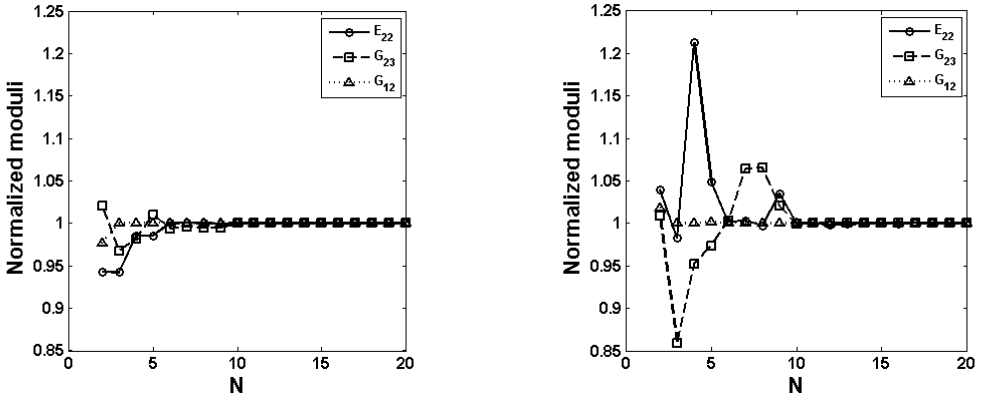

(b) Square array

Balanced variational principle Constrained variational principle

Figure 7.6 Convergence of homogenized moduli $E_{22}^{*}, G_{23}^{*}, G_{12}^{*}$ for aluminum/porosity, containing 0.20 porosity volume fraction, with the number of harmonics used in the displacement field representation.

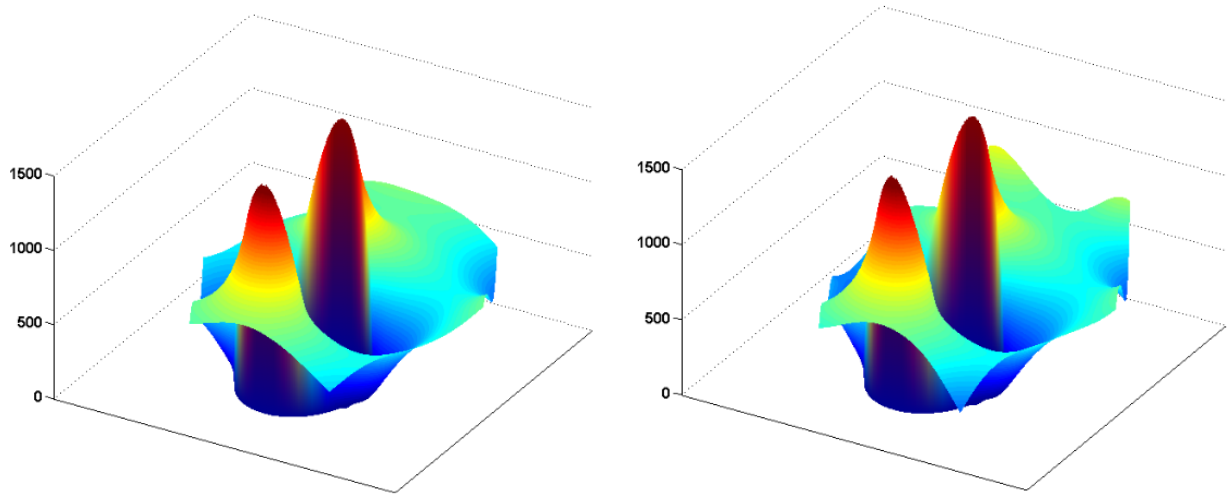

(a) Hexagonal array

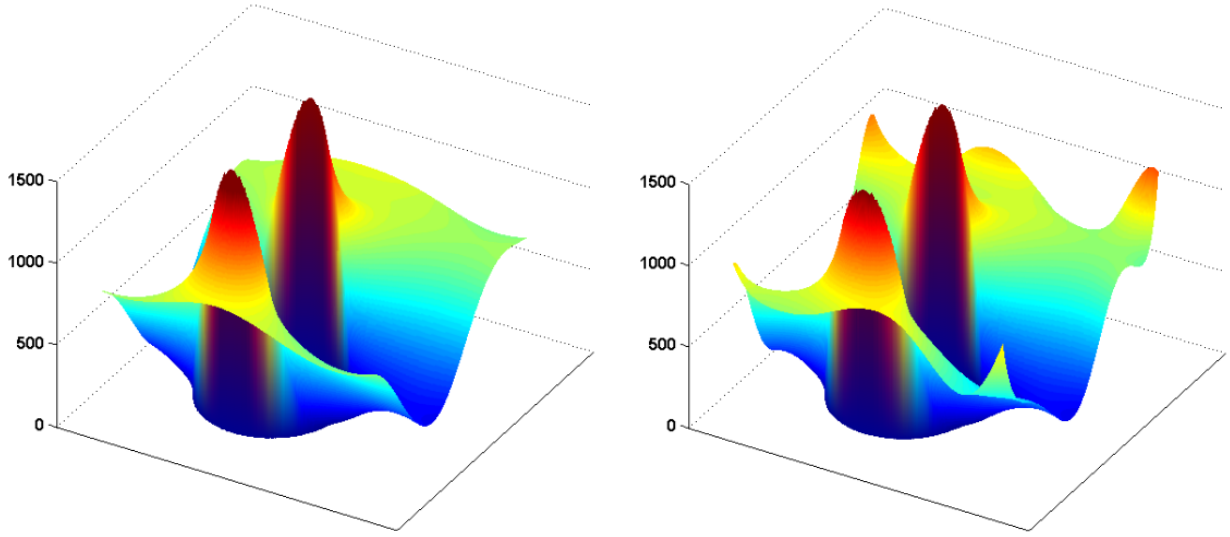

(b) Square array

Balanced variational principle Constrained variational principle

Figure 7.7 Comparison of $\sigma_{22}(y_2, y_3)$ stress fields in aluminum with cylindrical holes containing 0.20 porosity volume fraction for loading by $\bar{\varepsilon}_{22} = 0.01$ generated using 9 harmonics by balanced and constrained variational approaches.

The local stress distributions $\sigma_{22}(y_2, y_3)$ due to uniaxial loading by $\bar{\sigma}_{22}$ at the applied homogenized strain $\bar{\varepsilon}_{22} = 0.01$ that were generated using 9 harmonics are compared in Fig. 7.7 for both arrays. Small differences between the predictions of the balanced and constrained variational principles, limited to the immediately boundary of the unit cell, are observed for the hexagonal array as may be inferred from the convergence behavior observed in Fig. 7.6 at this harmonic number. The balanced variational principle produces converged homogenized modulus E_{22}^* at this harmonic, whereas this modulus obtained from the constrained variational principle has not fully converged. The differences in the stress distributions $\sigma_{22}(y_2, y_3)$ increase for the square array, which is consistent with the convergence behavior of E_{22}^* observed in Fig. 7.6. The balanced variational principle produces fully converged E_{22}^* at the ninth harmonic in contrast with the constrained principle.

7.3.3 Graphite/Epoxy Composite with Coated Fibers

Interphases either arise naturally at the fiber/matrix interface during the consolidation process or are introduced deliberately in the form of coatings to improve fiber adhesion, mitigate residual stresses or control composite toughness. Hence they have been the subject of extensive investigations, and will continue to be studied as new material systems are developed since they control the stress transfer from the matrix phase into the typically stiffer fiber. In light of the interphases' or coatings' importance, their impact on the convergence of homogenized moduli and local stress fields is investigated in this section for a graphite/epoxy composite with 0.5 fiber volume fraction and several coating thicknesses. The fiber/matrix transverse Young's modulus contrast for this material system is smaller than that of the glass/epoxy composite. The coating stiffness is 1.5 of the matrix stiffness. Table 7.1 lists the elastic moduli of the constituent phases for this composite.

The convergence of all the homogenized elastic moduli of hexagonal and square arrays was investigated as a function of the number of harmonics, and the greatest differences between the balanced and constrained variational principles were observed for the transverse Young's modulus E_{22}^*. Fig. 7.8 illustrates the comparison of this convergence behavior for both arrays with three coating thicknesses, ranging from 0.01 to 0.10 of the fiber radius. As observed in all cases, the homogenized transverse modulus converges to larger values with increasing coating

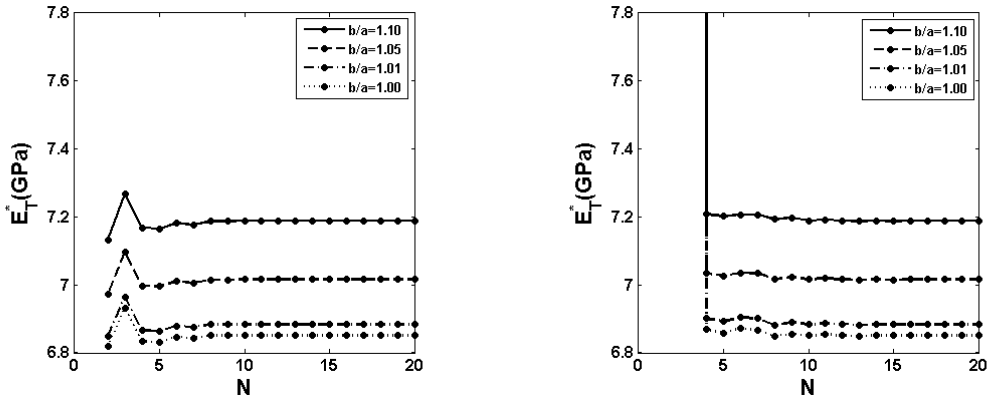

(a) Hexagonal array

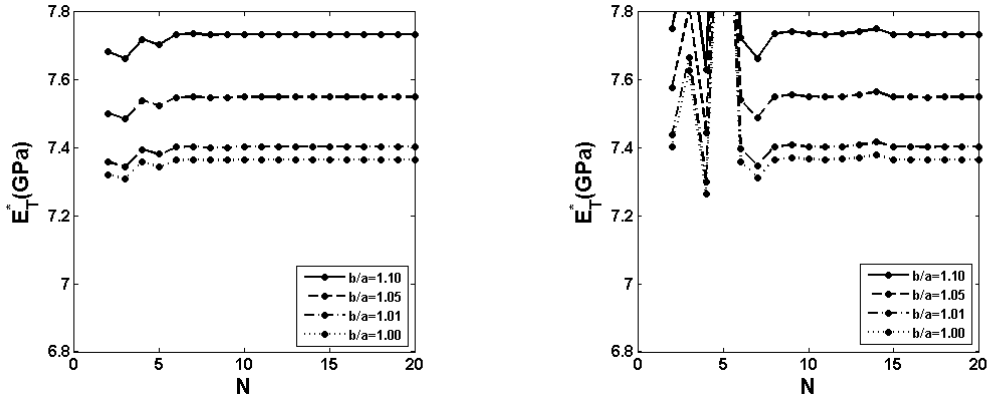

(b) Square array

Balanced variational principle Constrained variational principle

Figure 7.8 Convergence of the homogenized transverse Young's modulus E_{22}^{*} for unidirectional graphite/epoxy with coated fibers, containing 0.50 fiber volume fraction, with the number of harmonics used in the displacement field representation.

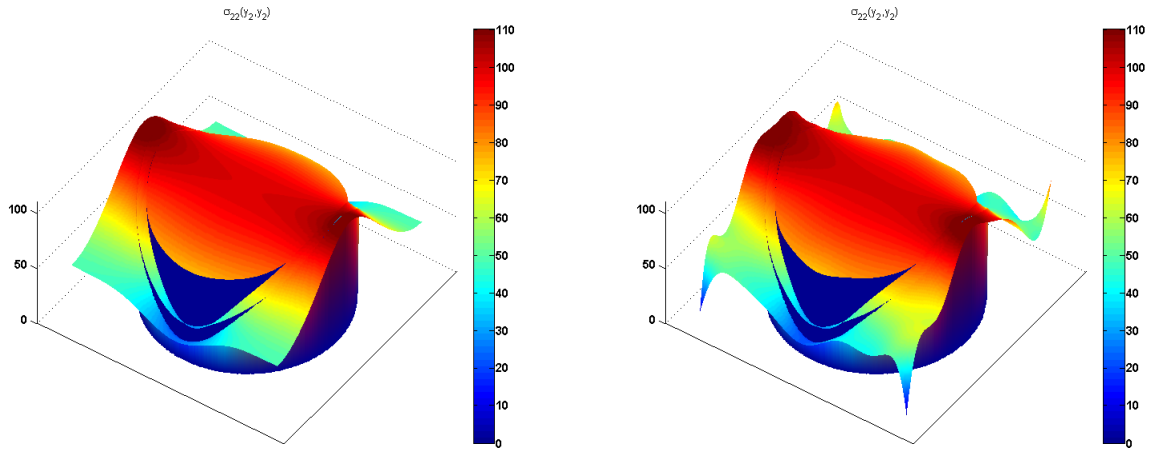

(a) $\sigma_{22}(y_2, y_3)$

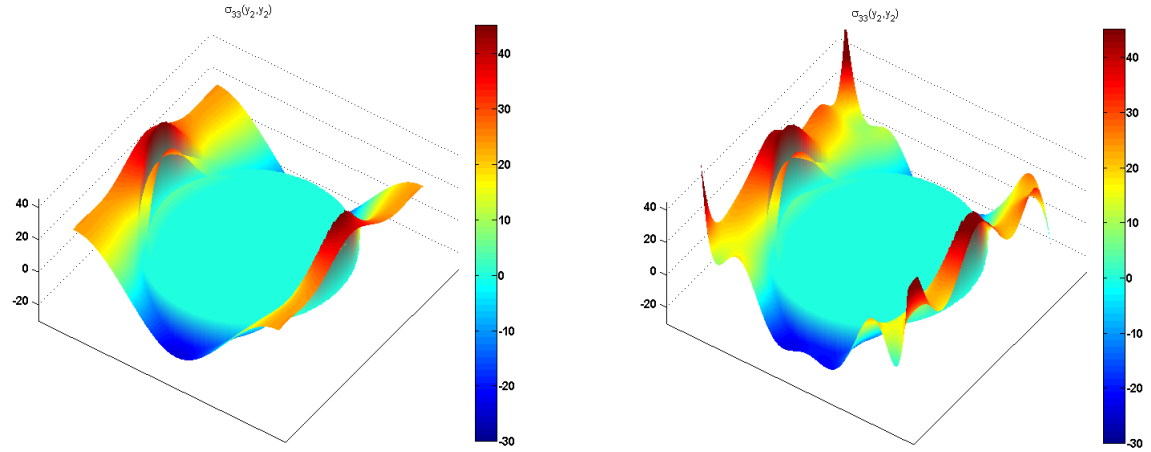

(b) $\sigma_{33}(y_2, y_3)$

Balanced variational principle Constrained variational principle

Figure 7.9 Comparison of $\sigma_{22}(y_2, y_3)$ and $\sigma_{33}(y_2, y_3)$ stress fields in the square unit cell representative of unidirectional graphite/epoxy with coated fibers containing 0.50 fiber volume fraction for loading by $\bar{\varepsilon}_{22} = 0.01$ generated using 14 harmonics by balanced and constrained variational approaches.

thickness since the coating stiffness is larger than that of the matrix phase. The convergence is rapid for the balanced variational principle, and is independent of the coatings thickness both in the number of harmonics required for convergence and the character of the convergence behavior with harmonic number. For the hexagonal and square arrays, 9 and 8 harmonics, respectively, are required for full convergence although acceptable results are obtained with fewer harmonics because of the well-behaved convergence behavior. In contrast, the constrained variational principle produces convergence behavior characterized by large departures from the asymptotic homogenized transverse moduli for small harmonics, and requires greater number of harmonics for convergence. The hexagonal array yields quicker convergence relative to the square array. For instance, 12 and 16 harmonics are required for the hexagonal and square array, respectively, both of which are greater relative to the balanced variational principle.

To demonstrate the quality of the stress fields produced by the balanced variational principle, we compare the stress distributions $\sigma_{22}(y_2, y_3)$ and $\sigma_{33}(y_2, y_3)$ due to uniaxial loading by $\bar{\sigma}_{22}$ at the applied homogenized strain $\bar{\varepsilon}_{22} = 0.01$ that were generated using 14 harmonics in Fig. 7.9 for the square array. At this harmonic number the homogenized transverse modulus E_{22}^{*} generated using the balanced variational principle has converged, whereas the constrained principle requires 16 harmonics. As observed, both stress fields obtained from the constrained variational principle do not satisfy periodicity conditions along the square unit cell boundary, in contrast with the balanced principle distributions.

7.4 Summary

The generated results based on the two ways of implementing the periodic boundary conditions for a wide range of material properties and two array types indicate that all of the homogenized moduli will converge given a sufficient number of harmonic terms. The convergence behavior depends on the method of implementing periodic boundary conditions, the fiber volume fraction and modulus contrast. As observed, the balanced variational principle provides quicker and more stable homogenized moduli in the investigated range of fiber volume fractions and material properties. The homogenized moduli predicted by Jirousek's constrained principle display large deviations from the converged values for small numbers of harmonics, which does not occur for the balanced variational principle. Based on the work of Drago (2008) limited to square unit cells with isotropic elastic moduli of the fiber and matrix phases, weighted

least squares method requires almost the same number of harmonics as Jirousek's variational principle for the convergence of homogenized moduli, and collocation requires the largest number of all four methods.

The convergence of homogenized moduli for hexagonal array usually consumes more harmonic terms than square array because one more set of periodic boundary conditions need to be satisfied. In addition, it takes more harmonic terms for composites with greater modulus contrast. For the graphite/epoxy and glass epoxy composites, 8 harmonics were sufficient to achieve convergence, whereas porous aluminum required 10 when the balanced variational principle was employed. In contrast, more harmonic terms are needed to generate converged homogenized moduli when Jirousek's constrained variational approach is employed. This is particularly evident for the Aluminum/Porosity case shown in Fig. 7.6.

Chapter 8

Summary and Conclusions

8.1 Summary of Accomplishments

Following and expanding on the work of Drago and Pindera (2008), the contribution of this dissertation is the construction of stable and quickly converging elasticity-based locally exact homogenization theory which may be used to:

- efficiently investigate the elastic and viscoelastic response of unidirectional composite materials with rectangular, square, hexagonal and tetragonal periodic microstructures comprised of isotropic, transversely isotropic, and (cylindrically or circumferentially) orthotropic phase constituents, and third phases such as coatings or interphases.

The advantage of this homogenization theory, compared to other micromechanics models or homogenization theories, is rooted in the balanced variational principle which plays a key role in the implementation of non-separable periodic boundary conditions, leading to quickly-converging homogenized moduli and stable local stress distributions. This variational principle, originally proposed by Drago and Pindera (2008) for rectangular unit cell architectures, was extended herein to hexagonal and tetragonal unit cell architectures and demonstrated to produce quickly converging homogenized moduli and local stress fields regardless of phase moduli contrast, orthotropy type or viscoelasticity effects.

The framework of the locally-exact homogenization theory was developed in two steps. In the first step, the equilibrium equations expressed in terms of displacements, or Navier's equations, were solved exactly in the fiber, interface and matrix phases using Fourier series representations of the respective displacement fields. The continuity conditions between

fiber/interphase and interphase/matrix phases, respectively, were then applied one harmonic at a time in the cylindrical coordinate system wherein the problem is separable. This problem is called the interior unit cell problem. The exterior problem, which involves the satisfaction of non-separable boundary conditions in the Cartesian coordinate system for the considered array architectures, and which cannot be solved sequentially one harmonic at a time, is efficiently solved via the balanced variational principle implemented for the different array types. Finally, the homogenized constitutive equations are established to generate homogenized moduli of unidirectional composites which depend on the type of microstructures and material combinations.

The constructed theory has been validated upon comparison with known elasticity solutions and micromechanics models. These include the solution to the Eshelby problem which was used as a benchmark to demonstrate the robustness and stability of the developed unit cell solution approach, and the FVDAM theory which produces high-fidelity results comparable to the finite-element method. Comparison with the classical CCA and Mori-Tanaka micromechanics models establishes applicability and limitations of these approaches based on simplified geometric representation of composite material microstructures. Selected numerical results are generated to provide insight into the efficiency and robustness of the theory. To demonstrate its superior advantage, the key component of the theory, namely the balanced variational principle, is compared with recently adopted approaches based on a derivative variational principle proposed originally in the context of locally-exact finite-element solutions. Finally, the elastic problem has been extended to viscoelastic domain via the elastic-viscoelastic correspondence principle and employed to investigate certain undocumented features of time-dependent response of polymeric matrix composites.

The main contributions of this dissertation may be summarized as follows:

- The constructed locally exact homogenization theory is the only elasticity-based theory of this type with the aforementioned capabilities. These capabilities are applicable in a wide range of fiber volume fractions, constituent phase modulus contrasts and three different array types. The ability to investigate elastic and viscoelastic response of unidirectional composites with cylindrically (both radially and circumferentially) orthotropic fibers,

such as graphite or silicon carbide, is a significant achievement given the singular nature of stress fields in this class of fibers. The problem of singular stress fields in cylindrically orthotropic fibers has been discussed but sidestepped using a replacement scheme based on equivalent transversely isotropic moduli. Another approach is the use of small hollow or transversely isotropic cores at the origin. Herein, this problem is tackled directly by employing orthotropic fiber properties in the homogenization and local stress calculation procedures alike within a unified framework, thereby enabling assessment of the proposed replacement schemes. Homogenization problems containing singularities cannot be easily handled using numerical techniques in contrast with the developed elasticity approach which produces exact expressions for the phase average strains and hence homogenized moduli.

- The developed theoretical framework which admits the presence of third phases in the form of interfaces or interphases has also made possible contributions to this important area of composite mechanics which continues to be explored. Interfaces play a key role in stress transfer between fiber and matrix phases and in protecting fibers from fractures. Numerically based analyses of interfaces using the finite-element approach present convergence issues that must be overcome, which become increasingly more difficult with decreasing interface thickness. The demonstration that the convergence of the locally-exact homogenization theory does not deteriorate (that is, does not require more harmonics terms) and remains stable with decreasing interface thickness provides the composite mechanics and materials science communities with a powerful tool to assess the important effect of interfaces on both the homogenized moduli and local stress fields. In this dissertation, the generated homogenized moduli of composites with different interface geometries and properties have been validated against other numerical and analytically based techniques such as the PMH and three-phase models. Moreover, the elasticity framework enabled efficient parametric studies aimed at investigating the effect of interface or coating stiffness and thickness on both the homogenized moduli and stress distributions. Because of the theory's stability, a simple manipulation of parameters enabled the investigation of homogenized moduli of atomic layer-deposited alumina nanotubes with engineered multifunctional properties, revealing new effects.

- The key pillar supporting the success of the locally exact homogenization theory is the manner of implementing periodic boundary conditions based on a balanced variational principle wherein both tractions and displacements play equivalent roles. This is in contrast with the standard variational approaches based on the minimum potential energy theorem currently implemented in several elasticity-based homogenization techniques. The balanced variational principle is a derivative of a minimum potential energy approach proposed by Jirousek some time ago in the context finite-element based exact displacement field representation. This principle has been recently re-discovered and implemented into several elasticity-based homogenization schemes. The final expressions for the boundary conditions are almost exactly the same in the two approaches and differ only in the "±" signs. In this dissertation, homogenization and local stress fields results generated using both approaches are compared within the same framework for three material systems with different elastic moduli contrasts, namely: graphite/epoxy, glass/epoxy, and aluminum porosity. It is demonstrated that the balanced variational principle exhibits superior convergence of both homogenized moduli and local stress fields with increasing number of harmonics, that is better stability and quicker convergence are observed relative to Jirousek's approach.
- The elastic problem has been extended to the viscoelastic domain for unidirectional composites by including the time-dependent response of polymeric matrix phase. The elastic-viscoelastic correspondence principle is employed to transform the unknown variables in the elastic solution of the unit cell problem to the Laplace transform, with the elastic moduli replaced by their Carson transforms. The Zakian inversion method to the time domain is employed, proved to be a superior and more stable inversion technique than the Schapery method, to efficiently calculate the homogenized moduli and local stress fields in the time domain. Two representations are available for modeling the isotropic matrix response, namely the power-law and the multi-parameter models comprised of combinations of Reuss and Voigt spring and dashpot elements. In addition, two popular adopted assumptions are employed to characterize the matrix response namely: constant Poisson's ratio and constant bulk modulus. The theory is successfully compared with alternative homogenization approaches and experimental data, and employed to study the undocumented effects of array type on the creep compliance

functions, demonstrating substantial evolving differences with time for some functions. Lastly, the theory is employed to study the transmission of phase constitutive behavior to the macroscale in support of the construction of viscoelastic functions from experimental data.

- The accuracy and stability of the locally exact theory renders it an excellent standard for comparison with other models, both classical and numerical. Herein, the results generated using two widely-employed classical models, CCA and Mori-Tanaka models, have been compared with the locally exact predictions for both elastic and viscoelastic problems. Under axisymmetric and axial shear loading in the elastic domain, small differences are observed between the baseline results of LEHT and the two classical models. The differences are substantially greater under transverse normal and shear loading. For instance, the transverse shear modulus predicted by LEHT lies between the upper and lower bounds of the CCA models, while the Mori-Tanaka result is much closer to the CCA's lower bound. The stress distributions of generated by LEHT for hexagonal arrays and CCA are very similar for small or medium fiber volume fractions; for larger fiber volume fraction microstructures, however, the CCA model cannot capture the stress fluctuations in the fiber phase because of the absence of adjacent fiber interactions. Similar differences occur in viscoelastic problems for the types of assumptions on the matrix time-dependent response. The main conclusions from this comparison are that the CCA model provides accurate homogenized moduli and acceptably accurate stress distributions despite inability to predict exactly the missing fifth modulus. The Mori-Tanaka predictions of the homogenized moduli may be generated efficiently with comparative accuracy even though the assumption is based on the average stress in the matrix phase.

8.2 Conclusions

To overcome the shortcomings of traditional micromechanics models based on simplified geometries of actual composite microstructures, and numerical homogenization approaches that utilize popular finite-element commercial packages, a new locally exact homogenization theory has been developed to very efficiently and accurately generate both homogenized moduli and local stress fields of a wide class of unidirectional composites in the elastic and viscoelastic

domains. The shortcomings of the traditional micromechanics models include the inability to generate accurately all the necessary homogenized moduli and local stress fields due to the simplified geometric representations and stress field assumptions necessary to obtain closed-form analytical solutions. Conversely, numerical models involve tedious mesh generation, time-consuming specification of periodic boundary conditions and also suffer from convergence issues when regions of very small dimensions (such as fiber/matrix interfaces) are present, requiring very refined meshes. Moreover, unlike the locally exact homogenization theory, both classical and numerical approaches cannot readily accommodate certain types of phase anisotropy such as cylindrical orthotropy exhibited by graphite fibers.

In contrast, the developed locally exact homogenization theory provides both accurate homogenized moduli and stable stress distributions, which have been validated against many other analytical and numerical techniques. A key feature of the theory is its efficiency and stability in generating homogenized moduli and stress fields with very simple input data construction readily accessible to professionals and non-professionals alike. Hence it is expected that this approach will quickly gain popularity and become not only a design and research tool used by diverse communities involved in materials characterization, design and development, but also a comparison standard for bench-mark purposes.

The efficient and robust computational tool developed in this dissertation can be easily implemented for other analytical purposes, which cannot be easily accomplished using other methods. For instance, optimization of material architectures is expected to be much faster, and multi-scale modeling capability easier to implement. It is also expected that the incorporation of multi-physics phenomena of currently intense interest to the materials science community, such as surface energy effects for nanoscale simulations, will be facilitated by the developed analytical framework. These additional features are left to future work that is discussed in the next section.

8.3 Future work

The extensions based on the present work are listed as follows:

- Optimization. The homogenized response of unidirectional composites can be obtained through experimental characterization at the macroscale, but it is still a challenging

problem to predict the interaction between fiber/matrix and fiber/coating/matrix at the microscale due to lack of available data. Understanding this interaction is necessary for progress in the simulation of damage evolution in the form of matrix cracking and interphase debonding, leading to the development of tough composites. In addition, some of the engineering moduli still cannot be measured directly, such as the properties of the coating/interphase region, or transverse normal and shear moduli of fibers such as graphite and Kevlar because of the small interphase or fiber dimensions. Thus, a reliable optimization-based inverse method is necessary to provide insight into these properties, avoiding laborious and time-consuming experimentation. Particle swarm optimization has been shown to be a robust tool under diverse circumstances, which can be employed in conjunction with LEHT to predict the material properties that are difficult to measure directly, given available experimental data at the macroscale.

- From "millimeter" to "nanometer". The surface energy effect is one of the dominant factors for consideration when material dimensions are on the nanometer scale, which is the case in composite nanomaterials. Due to their wide applications in today's high-tech industry, it is important to use efficient tools to study thermos-mechanical behavior of such nanoscale composite materials. One of the applications in this dissertation has illustrated the theory's capability of calculating the homogenized moduli of an epoxy resin reinforced by atomic layer deposited (ALD) alumina nanotubes, which have been successfully fabricated in the laboratory. However, the surface energy was neglected because it was not significant in the chosen example. This effect may be incorporated in the future. Moreover, extension of the theory to include calculation of thermal expansion and conductivity tensors should be considered in future work as certain nanoscale materials (carbon nanotubes) are widely employed in the micro-electronics industry, necessitating inclusion of multi-physics characteristics.
- Multiscale modeling. This topic is an important focus of modern mechanics, and is rapidly gaining popularity because of the current efforts to understand how the underpinning deformation mechanisms at different scales affect homogenized response. For instance, researchers in the area of bone mechanics will benefit from efficient homogenization tools that allow them to gain insight into stress transfer mechanisms through various scales (from the nanometeric scale up to the organ scale). Two of the

applications presented in Chapter #4, which involve unidirectional composite laminates and cylinders, have demonstrated the ease of LEHT implementation into the multiscale modeling process. Moreover, demonstration of multiscale modeling capability involving viscoelastic response will elevate the theory to a new level and encourage widespread use.

References

Aboudi, J., Pindera, M.-J., Arnold, S.M., 2003. Higher-order theory for periodic multiphase materials with inelastic phases. Int. J. Plast. 19, 805–847.

Antman, S.S., Negrón-Marrero, P.V., 1987. The remarkable nature of radially symmetric equilibrium states of aeolotropic nonlinearly elastic bodies. J. Elast. 18, 131–164.

Asp, L.E., Berglund, L.A., Talreja, R., 1996. Effects of fiber and interphase on matrix-initiated transverse failure in polymer composites. Compos. Sci. Technol. 56, 657–665.

Avery, W.B., Herakovich, C. T., 1986. Effect of fiber anisotropy on thermal stresses in fibrous composites. J. Appl. Mech. 53, 751-756.

Bansal, Y., Pindera, M.-J., 2003. Efficient reformulation of the thermoelastic higher-order theory for functionally graded materials. J. Therm. Stress. 26, 1055–1092.

Bansal, Y., Pindera, M.-J., 2005. A second look at the higher-order theory for periodic multiphase materials. J. Appl. Mech. 72, 177–195.

Bensoussan, A., Lions, J.L., Papanicolaou, G., 2011. Asymptotic analysis for periodic structures. American Mathematical Society, Providence, R.I.

Caporale, A., Feo, L., Luciano, R., 2015. Eigenstrain and Fourier series for evaluation of elastic local fields and effective properties of periodic composites. Compos. Part B Eng. 81, 251–258.

Cavalcante, M.A.A., Marques, S.P.C., 2014. Homogenization of periodic materials with viscoelastic phases using the generalized FVDAM theory. Comput. Mater. Sci. 87, 43–53.

Cavalcante, M.A.A, Marques, S.P., Pindera, M.-J., 2006a. Parametric formulation of the finite-volume theory for functionally graded materials—Part I: analysis. J. Appl. Mech. 74, 935–945.

Cavalcante, M.A.A, Marques, S.P., Pindera, M.-J., 2006b. Parametric formulation of the finite-volume theory for functionally graded materials—Part II: Numerical Results. J. Appl. Mech. 74, 946–957.

Cavalcante, M.A.A., Pindera, M.-J., 2013. Generalized FVDAM theory for periodic materials undergoing finite deformations—Part I: Framework. J. Appl. Mech. 81, 021005.

Cavalcante, M.A.A., Pindera, M.-J., Khatam, H., 2012. Finite-volume micromechanics of periodic materials: Past, present and future. Compos. Part B Eng., Homogenization and Micromechanics of Smart and Multifunctional Materials 43, 2521–2543.

Charalambakis, N., 2010. Homogenization techniques and micromechanics. A survey and perspectives. Appl. Mech. Rev. 63, 30803.

Chatzigeorgiou, G., Efendiev, Y., Lagoudas, D.C., 2011. Homogenization of aligned "fuzzy fiber" composites. Int. J. Solids Struct. 48, 2668–2680.

Chatzigeorgiou, G., Seidel, G.D., Lagoudas, D.C., 2012. Effective mechanical properties of "fuzzy fiber" composites. Compos. Part B Eng. 43, 2577–2593.

Chen, C.H., Cheng, S., 1967. Mechanical properties of fiber reinforced composites. J. Compos. Mater. 1, 30–41.

Christensen, R.M., 1971. Theory of Viscoelasticity: An Introduction. Academic Press.

Christensen, R.M., 1994. Properties of carbon fibers. J. Mech. Phys. Solids 42, 681–695.

Christensen, R.M., Lo, K.H., 1979. Solutions for effective shear properties in three phase sphere and cylinder models. J. Mech. Phys. Solids 27, 315–330.

Cowin, S.C., Fraldi, M., 2005. On singularities associated with the curvilinear anisotropic elastic symmetries. Int. J. Non-Linear Mech. 40, 361–371.

Crouch, S.L., Mogilevskaya, S.G., 2006. Loosening of elastic inclusions. Int. J. Solids Struct. 43, 1638–1668.

Drago, A., 2008. Locally-exact homogenization theory for periodic materials with unidirectional reinforcements. Ph.D. dissertation.

Drago, A., Pindera, M.-J., 2007. Micro-macromechanical analysis of heterogeneous materials: Macroscopically homogeneous vs periodic microstructures. Compos. Sci. Technol. 67, 1243–1263.

Drago, A.S., Pindera, M.-J., 2008. A locally exact homogenization theory for periodic microstructures with isotropic phases. J. Appl. Mech. 75, 51010.

Duan, H.L., Wang, J., Huang, Z.P., Luo, Z.Y., 2005. Stress concentration tensors of inhomogeneities with interface effects. Mech. Mater. 37, 723–736.

Duan, H.L., Wang, J., Karihaloo, B.L., Huang, Z.P., 2006. Nanoporous materials can be made stiffer than non-porous counterparts by surface modification. Acta Mater. 54, 2983–2990. Eischen, J.W., Torquato, S., 1993. Determining elastic behavior of composites by the boundary element method. J. Appl. Phys. 74, 159–170.

Eischen, J.W., Torquato, S., 1993. Determining elastic behavior of composites by the boundary element method. J. Appl. Phys. 74, 159-170.

Eshelby, J.D., 1957. The Determination of the Elastic Field of an Ellipsoidal Inclusion, and Related Problems. Proc. R. Soc. Lond. Math. Phys. Eng. Sci. 241, 376–396.

Fil'shtinskii, L.A., 1964. Stresses and displacements in an elastic plane weakened by a doubly periodic system of identical circular holes. Appl Math. Mech. (Moscow) 28, 430–441.

Gattu, M., Khatam, H., Drago, A.S., Pindera, M.-J., 2008. Parametric Finite-Volume Micromechanics of Uniaxial Continuously-Reinforced Periodic Materials With Elastic Phases. J. Eng. Mater. Technol. 130, 031015–031015.

Golovchan, V.T., Nikityuk, N.I., 1981. Solution of the problem of shear of a fibrous composite medium. Sov. Appl. Mech. 17, 125–130.

Gottesman, T., Hashin, Z., 1980. Analysis of viscoelastic behavior of bones on the basis of microstructure. J. Biomech. 13, 89–96.

Grigolyuk, E.I., Fil'shtinskii, L.A., 1966. Elastic equilibrium of an isotropic plane with a doubly periodic system of inclusions. Sov. Appl. Mech. 2, 1–5.

Guinovart-Díaz, R., Bravo-Castillero, J., Rodríguez-Ramos, R., Sabina, F.J., 2001. Closed-form expressions for the effective coefficients of fibre-reinforced composite with transversely

isotropic constituents. I: Elastic and hexagonal symmetry. J. Mech. Phys. Solids 49, 1445–1462.

Guinovart-Díaz, R., Rodríguez-Ramos, R., Bravo-Castillero, J., López-Realpozo, J.C., Sabina, F.J., Sevostianov, I., 2013. Effective elastic properties of a periodic fiber reinforced composite with parallelogram-like arrangement of fibers and imperfect contact between matrix and fibers. Int. J. Solids Struct. 50, 2022–2032.

Guinovart-Díaz, R., Yan, P., Rodríguez-Ramos, R., López-Realpozo, J.C., Jiang, C.P., Bravo-Castillero, J., Sabina, F.J., 2012. Effective properties of piezoelectric composites with parallelogram periodic cells. Int. J. Eng. Sci. 53, 58-66.

Halsted, D.J., Brown, D.E., 1972. Zakian's technique for inverting Laplace transforms. Chem. Eng. J. 3, 312–313.

Hashin, Z., 1962. The elastic moduli of heterogeneous materials. J. Appl. Mech. 29, 143–150.

Hashin, Z., 1965. Viscoelastic behavior of heterogeneous media. J. Appl. Mech. 32, 630–636.

Hashin, Z., 1966. Viscoelastic fiber reinforced materials. AIAA J. 4, 1411–1417.

Hashin, Z., 1979. Analysis of properties of fiber composites with anisotropic constituents. J. Appl. Mech. 46, 543–550.

Hashin, Z., 1990. Thermoelastic properties and conductivity of carbon/carbon fiber composites. Mech. Mater. 8, 293–308.

Hashin, Z., Rosen, B.W., 1964. The elastic moduli of fiber-reinforced materials. J. Appl. Mech. 31, 223–232.

Hassanzadeh, H., Pooladi-Darvish, M., 2007. Comparison of different numerical Laplace inversion methods for engineering applications. Appl. Math. Comput. 189, 1966–1981.

Heaton, M.D., 1968. A calculation of the elastic constants of a unidirectional fiber-reinforced composite. J. Phys. Appl. Phys. 1, 1039.

Helsing, J., 1995. An integral equation method for elastostatics of periodic composites. J. Mech. Phys. Solids 43, 815–828.

Herakovich, C.T., 1989. Carbon Fibers and Composites Effects of morphology on properties of

graphite composites. Carbon 27, 663–678.

Hershey, A.V., 1954. The elasticity of an isotropic aggregate of anisotropic cubic crystals. J. Appl. Mech.-Trans. ASME 21, 236–240.

Hill, R., 1963. Elastic properties of reinforced solids: Some theoretical principles. J. Mech. Phys. Solids 11, 357–372.

Hill, R., 1965. A self-consistent mechanics of composite materials. J. Mech. Phys. Solids 13, 213–222.

Huang X., 2009. Fabrication and properties of carbon fibers. Materials 2, 2369-2403.

Jasiuk, I., Kouider, M.W., 1993. The effect of an inhomogeneous interphase on the elastic constants of transversely isotropic composites. Mech. Mater. 15, 53–63.

Jirousek, J., 1978. Basis for development of large finite elements locally satisfying all field equations, Comput. Meth. Appl. Mech. Engng. 14, 65-92.

Khatam, H., Pindera, M.-J., 2009. Parametric finite-volume micromechanics of periodic materials with elastoplastic phases. Int. J. Plast. 25, 1386–1411.

Kirsch, G., 1898. Die Theorie der Elastizität und die Bedürfnisse der Festigkeitslehre. Z Ver Dtsch Ing 42, 797–807.

Knott, T.W., Herakovich, C.T., 1991. Effect of fiber orthotropy on effective composite properties. J. Compos. Mater. 25, 732–759.

Koiter, W.T., 1960. Stress distribution in an infinite elastic sheet with a doubly-periodic set of equal holes. The University of Wisconsin Press, Madison.

Kröner, E., 1958. Berechnung der elastischen Konstanten des Vielkristalls aus den Konstanten des Einkristalls. Z. Für Phys. 151, 504–518.

Lagache, M., Agbossou, A., Pastor, J., Muller, D., 1994. Role of interphase on the elastic behavior of composite materials: theoretical and experimental analysis. J. Compos. Mater. 28, 1140–1157.

Leissa, A.W., Clausen, W.E., 1968. Application of point matching to problems in micromechanics. Wiley New York.

Leknitskii, S.G., Fern, P., 1963. Theory of elasticity of an anisotropic elastic body. Holden-Day.

Lipton, R.P., 2003. Assessment of the local stress state through macroscopic variables. Philos. Trans. R. Soc. Lond. Math. Phys. Eng. Sci. 361, 921–946.

Luciano, R., Barbero, E.J., 1995. Analytical expressions for the relaxation moduli of linear viscoelastic composites with periodic microstructure. J. Appl. Mech. 62, 786–793.

Lyytinen, J., Berdova, M., Hirvonen, P., Liu, X.W., Franssila, S., Zhou, Q., Koskinen, J., 2014. Interfacial mechanical testing of atomic layer deposited TiO2 and Al2O3 on a silicon substrate by the use of embedded SiO2 microspheres. RSC Adv. 4, 37320–37328.

Maligno, A.R., Warrior, N.A., Long, A.C., 2010. Effects of interphase material properties in unidirectional fibre reinforced composites. Compos. Sci. Technol. 70, 36–44.

Michel, J.C., Moulinec, H., Suquet, P., 1999. Effective properties of composite materials with periodic microstructure: a computational approach. Comput. Methods Appl. Mech. Eng. 172, 109–143.

Mogilevskaya, S.G., Crouch, S.L., Stolarski, H.K., Benusiglio, A., 2010. Equivalent inhomogeneity method for evaluating the effective elastic properties of unidirectional multi-phase composites with surface/interface effects. Int. J. Solids Struct. 47, 407–418.

Mogilevskaya, S.G., Kushch, V.I., Nikolskiy, D., 2014. Evaluation of some approximate estimates for the effective tetragonal elastic moduli of two-phase fiber-reinforced composites. J. Compos. Mater. 48, 2349–2362.

Mogilevskaya, S.G., Stolarski, H.K., Crouch, S.L., 2012. On Maxwell's concept of equivalent inhomogeneity: When do the interactions matter? J. Mech. Phys. Solids 60, 391–417.

Mori, T., Tanaka, K., 1973. Average stress in matrix and average elastic energy of materials with misfitting inclusions. Acta Metall. 21, 571–574.

Nemat-Nasser, S., Iwakuma, T., Hejazi, M., 1982. On composites with periodic structure. Mech. Mater. 1, 239–267.

Paley, M., Aboudi, J., 1992. Micromechanical analysis of composites by the generalized cells model. Mech. Mater. 14, 127–139.

Papanicolau, G., Bensoussan, A., Lions, J.-L., 1978. Asymptotic Analysis for Periodic Structures. Elsevier.

Pickett, G., 1968. Elastic Moduli of Fiber Reinforced Plastic Composites, in (SCHWARTZ and SCHWARTZ eds.): Fundamental Aspects of Fiber Reinforced Plastic Composites. Intersci. Publ. N. Y. (pp. 13-27).

Pindera, M.-J., Bednarcyk, B.A., 1997. An efficient implementation of the GMC micromechanics model for multi-phased materials with complex microstructures. Technical Report NASA-CR 202350.

Pindera, M.-J., Freed, A.D., 1994. The Effect of Matrix Microstructure on Thermally Induced Residual Stresses in SiC/Titanium Aluminide Composites. J. Eng. Mater. Technol. 116, 215–221.

Pindera, M.-J., Freed, A.D., Arnold, S.M., 1993a. Effects of fiber and interfacial layer morphologies on the thermoplastic response of metal matrix composites. Int. J. Solids Struct. 30, 1213–1238.

Pindera, M.-J., Khatam, H., Drago, A.S., Bansal, Y., 2009. Micromechanics of spatially uniform heterogeneous media: A critical review and emerging approaches. Compos. Part B Eng. 40, 349–378.

Pindera, M.-J., Salzar, R.S., Williams, T.O., 1993b. An evaluation of a new approach for the thermoplastic response of metal-matrix composites. Compos. Eng. 3, 1185–1201.

Reuss, A., 1929. Berechnung der fließgrenze von mischkristallen auf grund der plastizitätsbedingung für einkristalle. ZAMM - J. Appl. Math. Mech. Z. Für Angew. Math. Mech. 9, 49–58.

Rodríguez-Ramos, R., Berger, H., Guinovart-Díaz, R., López-Realpozo, J.C., Würkner, M., Gabbert, U., Bravo-Castillero, J., 2012. Two approaches for the evaluation of the effective properties of elastic composite with parallelogram periodic cells. Int. J. Eng. Sci., Recent advances in Micromechanics 58, 2–10.

Rodríguez-Ramos, R., Yan, P. López-Realpozo, J.C., Guinovart-Díaz, R., Bravo-Castillero, J., Sabina, F.J., Jiang, C.P., 2013. Two analytical models for the study of periodic fibrous elastic composite with different unit cells. Compos. Struct. 93, 709-714.

Sevostianov, I., Rodriguez-Ramos, R., Guinovart-Diaz, R., Bravo-Castillero, J., Sabina, F.J., 2012. Connections between different models describing imperfect interfaces in periodic fiber-reinforced composites. Int. J. Solids Struct. 49, 1518–1525.

Shen, L., Li, J., 2003. Effective elastic moduli of composites reinforced by particle or fiber with an inhomogeneous interphase. Int. J. Solids Struct. 40, 1393–1409.

Sideridis, E., Theotokoglou, E.E., Giannopoulos, I., 2015. Analytical and computational study of the moduli of fiber-reinforced composites and comparison with experiments. Compos. Interfaces 22, 563–578.

Suquet, P.M., 1985. Elements of homogenization for inelastic solid mechanics. In: Snachez-Palencia, E. Zaoui, A. (Eds.), homogenization techniques for composite media. Vol. 272 of lecture notes in physics. Springer Verlag.

Tarn, J.-Q., 2002. Stress singularity in an elastic cylinder of cylindrically anisotropic materials. J. Elast. 69, 1–13.

Tu, W., Pindera, M.-J., 2014. Cohesive zone-based damage evolution in periodic materials via finite-volume homogenization. J. Appl. Mech. 81, 101005–1-16.

Veazie, D.R., Qu, J., 1995. Effects of interphases on the transverse stress-strain behavior in unidirectional fiber reinforced metal matrix composites. Compos. Eng. 5, 597–610.

Versteeg, H.K., Malalasekera, W., 2007. An introduction to computational fluid dynamics: the finite volume method. Pearson Education.

Voigt, W., 1889. Uber die beziehung zwischen den beiden elastizitatskonstanten isotroper korper. Wied. Ann. 38, 573-587.

Wang, G., Pindera, M.-J., 2015. Locally-exact homogenization theory for transversely isotropic unidirectional composites. Mech. Res. Commun. doi:10.1016/j.mechrescom.2015.09.011

Wang, G., Pindera, M.-J., 2016. Locally-exact homogenization of unidirectional composites with coated or hollow reinforcement. Mater. Des. 93, 514–528.

Wang, G., Pindera, M.-J., 2016. Locally-exact homogenization of unidirectional composites with cylindrically orthotropic fibers. J. Appl. Mech. 83, 071010.

Wang, J., Mogilevskaya, S.G., Crouch, S.L., 2005. An embedding method for modeling micromechanical behavior and macroscopic properties of composite materials. Int. J. Solids Struct. 42, 4588–4612.

Wang, X., Zhang, J., Wang, Z., Zhou, S., Sun, X., 2011. Effects of interphase properties in unidirectional fiber reinforced composite materials. Mater. Des. 32, 3486–3492.

Wilson Jr, H.B., Hill, J.L., 1965. Plane Elastostatic Analysis of an Infinite Plate with a Doubly Periodic Array of Holes or Rigid Inclusions. Rohm & Haas Company. Report No. S-50.

Yan, P., Jiang, C.P., 2010. An eigenfunction expansion-variational method based on a unit cell in analysis of a generally doubly-periodic array of cracks. Acta Mech., 210, 117-134.

Yan, P., Jiang, C.P., Song, F., Xu, X.H., 2010. Estimation of transverse thermal conductivity of doubly-periodic fiber reinforced composites. Chinese J. Aeronaut., 23, 54-60.

Yan, P., Jiang, C.P., Song, F., 2011. An eigenfunction expansion-variational method for the anti-plane electroelastic behavior of three-phase fiber composites. Mech. Mater., 43, 586-597.

Yan, P., Jiang, C.P., Song, F., 2013. Unified series solution for the anti-plane effective magnetoelectroelastic moduli of three-phase fiber composites. Int. J. Solids Struct., 50, 176-185.

Yancey, R.N., Pindera, M.-J., 1990. Micromechanical analysis of the creep response of unidirectional composites. J. Eng. Mater. Technol. 112, 157–163.

Yang, S.Y., Jeon, G., Kim, J.K., 2012. A high density array of free standing alumina nanotubes aligned vertically on solid substrates in a large area. J. Mater. Chem. 22, 23017–23021.

Zakian, V., 1969. Numerical inversion of Laplace transform. Electron. Lett. 5, 120–121.

Zakian, V., 1970. Optimisation of numerical inversion of Laplace transforms. Electron. Lett. 6, 677–679.

Appendix

A. Expressions of Stresses in the Matrix Phase in Cartesian Coordinate

Through the transformation between polar coordinate and Cartesian coordinate, the inplane stress distributions for the matrix phase are expressed for the convenience of applying periodic boundary conditions:

$$\begin{aligned}\sigma_{22} &= 2k_T\nu_A\bar{\varepsilon}_{11} + (k_T+\mu_T)\bar{\varepsilon}_{22} + (k_T-\mu_T)\bar{\varepsilon}_{33} + 2k_T F_{01} - 2\mu_T F_{02}\xi^{-2}\cos 2\theta \\ &+ \sum_{n=1}^{\infty}\sum_{j=1}^{4} F_{nj}\xi^{p_{nj}-1}[P_{nj}\cos n\theta\cos^2\theta + S_{nj}\cos n\theta\sin^2\theta - R_{nj}\sin n\theta\sin 2\theta] \\ &+ \sum_{n=1}^{\infty}\sum_{j=1}^{4} G_{nj}\xi^{p_{nj}-1}[P_{nj}\sin n\theta\cos^2\theta + S_{nj}\sin n\theta\sin^2\theta + R_{nj}\cos n\theta\sin 2\theta]\end{aligned} \tag{A.1}$$

$$\begin{aligned}\sigma_{33} &= 2k_T\nu_A\bar{\varepsilon}_{11} + (k_T-\mu_T)\bar{\varepsilon}_{22} + (k_T+\mu_T)\bar{\varepsilon}_{33} + 2k_T F_{01} + 2\mu_T F_{02}\xi^{-2}\cos 2\theta \\ &+ \sum_{n=1}^{\infty}\sum_{j=1}^{4} F_{nj}\xi^{p_{nj}-1}[P_{nj}\cos n\theta\sin^2\theta + S_{nj}\cos n\theta\cos^2\theta + R_{nj}\sin n\theta\sin 2\theta] \\ &+ \sum_{n=1}^{\infty}\sum_{j=1}^{4} G_{nj}\xi^{p_{nj}-1}[P_{nj}\sin n\theta\sin^2\theta + S_{nj}\sin n\theta\cos^2\theta - R_{nj}\cos n\theta\sin 2\theta]\end{aligned} \tag{A.2}$$

$$\begin{aligned}\sigma_{23} &= 2\mu_T\cdot\bar{\varepsilon}_{23} - 2\mu_T F_{02}\xi^{-2}\sin 2\theta \\ &+ \sum_{n=1}^{\infty}\sum_{j=1}^{4} F_{nj}\xi^{p_{nj}-1}[P_{nj}\cos n\theta\sin\theta\cos\theta - S_{nj}\cos n\theta\sin\theta\cos\theta + R_{nj}\sin n\theta\cos 2\theta] \\ &+ \sum_{n=1}^{\infty}\sum_{j=1}^{4} G_{nj}\xi^{p_{nj}-1}[P_{nj}\sin n\theta\sin\theta\cos\theta - S_{nj}\sin n\theta\sin\theta\cos\theta - R_{nj}\cos n\theta\cos 2\theta]\end{aligned} \tag{A.3}$$

$$\begin{aligned}\sigma_{11} &= (E_A + 4k_T\nu_A^2)\cdot\bar{\varepsilon}_{11} + 2k_T\nu_A\cdot\bar{\varepsilon}_{22} + 2k_T\nu_A\cdot\bar{\varepsilon}_{33} + 4k_T\nu_A F_{01} \\ &+ \sum_{n=2}^{\infty}\sum_{j=1}^{4} 2k_T\nu_A[p_{nj} + (1+n\beta_{nj})]\xi^{p_{nj}-1}[F_{nj}\cos n\theta + G_{nj}\sin n\theta]\end{aligned} \tag{A.4}$$

where p_{nj} are the eigenvalues that expressed in Chapter 2, $P_{nj} = (k_T+\mu_T)p_{nj} + (k_T-\mu_T)(1+n\beta_{nj})$,

$S_{nj} = (k_T - \mu_T)p_{nj} + (k_T + \mu_T)(1 + n\beta_{nj})$ and $R_{nj} = \mu_T\left[(p_{nj} - 1)\beta_{nj} - n\right]$.

The out-of-plane stress expressions for the matrix phase are

$$\begin{aligned}\sigma_{12} &= 2\mu_A\bar{\varepsilon}_{12} \\ &+ \mu_A\{\sum_{n=1}^{\infty} nH_{n1}\xi^{n-1}(\cos n\theta\cos\theta + \sin n\theta\sin\theta) + \sum_{n=1}^{\infty} nH_{n2}\xi^{n-1}(\sin n\theta\cos\theta - \cos n\theta\sin\theta) \\ &- \sum_{n=1}^{\infty} nH_{n3}\xi^{-n-1}(\cos n\theta\cos\theta - \sin n\theta\sin\theta) - \sum_{n=1}^{\infty} nH_{n4}\xi^{-n-1}(\sin n\theta\cos\theta + \cos n\theta\sin\theta)\}\end{aligned} \tag{A.5}$$

$$\begin{aligned}\sigma_{13} &= 2\mu_A\bar{\varepsilon}_{13} \\ &+ \mu_A\{\sum_{n=1}^{\infty} nH_{n1}\xi^{n-1}(\cos n\theta\sin\theta - \sin n\theta\cos\theta) + \sum_{n=1}^{\infty} nH_{n2}\xi^{n-1}(\sin n\theta\sin\theta + \cos n\theta\cos\theta) \\ &- \sum_{n=1}^{\infty} nH_{n3}\xi^{-n-1}(\cos n\theta\sin\theta + \sin n\theta\cos\theta) - \sum_{n=1}^{\infty} nH_{n4}\xi^{-n-1}(\sin n\theta\sin\theta - \cos n\theta\cos\theta)\}\end{aligned} \tag{A.6}$$

B. Boundary Condition Implementation – Balanced Variational Principle

The periodic boundary conditions are solved by first assuming

$$H_{D-P} = \frac{1}{2}\int_V \sigma_{ij}\varepsilon_{ij}dV - \int_{S_u} \mathbf{t}_i\mathbf{u}_i^0 dS - \int_{S_t} \mathbf{t}_i^0\mathbf{u}_i dS = 0 \tag{B.1}$$

where $\mathbf{t}=\mathbf{t}^0$ and $\mathbf{u}=\mathbf{u}^0$ are periodic traction and displacement constraints imposed on S_t and S_u, respectively. Taking the first variation of H_{D-P}, and using the fact that the interior elasticity solution satisfies the stress equilibrium equations *a priori*, so that

$$\frac{1}{2}\int_V \sigma_{ij}\varepsilon_{ij}dV = \frac{1}{2}\int_S t_i u_i dS \tag{B.2}$$

The variational principle is obtained in the final form as

$$\int_{S_t} \delta\mathbf{u}_i(\mathbf{t}_i - \mathbf{t}_i^0)dS + \int_{S_u} \delta\mathbf{t}_i(\mathbf{u}_i - \mathbf{u}_i^0)dS = 0 \tag{B.3}$$

The reduced periodicity conditions can be expressed for arrays with different geometries:

Hexagonal array

$$\begin{aligned} u_i'(S_1) = u_i'(S_4),\ \ u_i'(S_2) = u_i'(S_5),\ \ u_i'(S_3) = u_i'(S_6) \\ t_i(S_1) = -t_i(S_4),\ t_i(S_2) = -t_i(S_5),\ \ t_i(S_3) = -t_i(S_6)\end{aligned} \tag{B.4}$$

and, rectangular or parallelogram array

$$u_i'(S_1) = u_i'(S_3), \quad u_i'(S_2) = u_i'(S_4)$$
$$t_i(S_1) = -t_i(S_3), \quad t_i(S_2) = -t_i(S_4) \tag{B.5}$$

where $i = 1, 2, 3$. By implementing the reduced periodicity conditions Eqs. (B.4-5) for the inplane problem in the first variation of the functional, we obtain

Hexagonal array

$$\sum_{i=1}^{3} \int_{S_i} \{\delta t_2(S_i)[u_2'(S_i) - u_2'(S_{i+3})] + \delta t_3(S_i)[u_3'(S_i) - u_3'(S_{i+3})]\} dS$$
$$+ \sum_{i=4}^{6} \int_{S_i} \{\delta u_2'(S_i)[t_2(S_i) + t_2(S_{i-3})] + \delta u_3'(S_i)[t_3(S_i) + t_3(S_{i-3})]\} dS = 0 \tag{B.6}$$

Rectangular or parallelogram array

$$\sum_{i=1}^{2} \int_{S_i} \{\delta t_2(S_i)[u_2'(S_i) - u_2'(S_{i+2})] + \delta t_3(S_i)[u_3'(S_i) - u_3'(S_{i+2})]\} dS$$
$$+ \sum_{i=3}^{4} \int_{S_i} \{\delta u_2'(S_i)[t_2(S_i) + t_2(S_{i-2})] + \delta u_3'(S_i)[t_3(S_i) + t_3(S_{i-2})]\} dS = 0 \tag{B.7}$$

The respective expressions for the out-of-plane problem are

Hexagonal array

$$\sum_{i=1}^{3} \int_{S_i} \{\delta t_1(S_i)[u_1'(S_i) - u_1'(S_{i+3})] dS + \sum_{i=4}^{6} \delta u_1'(S_i)[t_1(S_i) + t_1(S_{i-3})]\} dS = 0 \tag{B.8}$$

Rectangular or parallelogram array

$$\sum_{i=1}^{2} \int_{S_i} \{\delta t_1(S_i)[u_1'(S_i) - u_1'(S_{i+2})] dS + \sum_{i=3}^{4} \delta u_1'(S_i)[t_1(S_i) + t_1(S_{i-2})]\} dS = 0 \tag{B.9}$$

where $t_i = \sigma_{ij} n_j$, and n_j are the unit normals for every side of the microstructures, each type of array has different unit normals due to different geometry.

Hexagonal array

$$S_1 : n_2 = \sqrt{3}/2, n_3 = 1/2; \quad S_2 : n_2 = 0, n_3 = 1$$
$$S_3 : n_2 = -\sqrt{3}/2, n_3 = 1/2; \; S_4 : n_2 = -\sqrt{3}/2, n_3 = -1/2 \tag{B.10}$$
$$S_5 : n_2 = 0, n_3 = -1; \qquad S_6 : n_2 = \sqrt{3}/2, n_3 = -1/2$$

Rectangular array

$$S_1 : n_2 = 1, n_3 = 0; \quad S_2 : n_2 = 0, n_3 = 1$$
$$S_3 : n_2 = -1, n_3 = 0; \; S_4 : n_2 = 0, n_3 = -1 \tag{B.11}$$

Parallelogram array

$$
\begin{aligned}
&S_1 : n_2 = \sin\varphi, n_3 = -\cos\varphi; \qquad S_2 : n_2 = 0, n_3 = 1 \\
&S_3 : n_2 = -\sin\varphi, n_3 = \cos\varphi; \qquad S_4 : n_2 = 0, n_3 = -1
\end{aligned}
\tag{B.12}
$$

Reorganizing the integrals with the Cauchy's stress tensor relationship yields explicit expressions for the boundary conditions with stresses and displacement fields, the integrals in the equations can be evaluated numerically by using Gaussian quadrature rule.

Hexagonal array (Inplane)

$$
\begin{aligned}
&\int_{S_1} [\sqrt{3}\delta\sigma_{22}(S_1) + \delta\sigma_{23}(S_1)][u_2'(S_1) - u_2'(S_4)]dx \\
&+\int_{S_1} [\sqrt{3}\delta\sigma_{23}(S_1) + \delta\sigma_{33}(S_1)][u_3'(S_1) - u_3'(S_4)]dx \\
&+\int_{S_2} \delta\sigma_{23}(S_2)[u_2'(S_2) - u_2'(S_5)]dx + \int_{S_2} \delta\sigma_{33}(S_2)[u_3'(S_2) - u_3'(S_5)]dx \\
&+\int_{S_3} [-\sqrt{3}\delta\sigma_{22}(S_3) + \delta\sigma_{23}(S_3)][u_2'(S_3) - u_2'(S_6)]dx \\
&+\int_{S_3} [-\sqrt{3}\delta\sigma_{23}(S_3) + \delta\sigma_{33}(S_3)][u_3'(S_3) - u_3'(S_6)]dx \\
&+\int_{S_4} \delta u_2'(S_4)[-\sqrt{3}\sigma_{22}(S_4) - \sigma_{23}(S_4) + \sqrt{3}\sigma_{22}(S_1) + \sigma_{23}(S_1)]dx \\
&+\int_{S_4} \delta u_3'(S_4)[-\sqrt{3}\sigma_{23}(S_4) - \sigma_{33}(S_4) + \sqrt{3}\sigma_{23}(S_1) + \sigma_{33}(S_1)]dx \\
&+\int_{S_5} \delta u_2'(S_5)[-\sigma_{23}(S_5) + \sigma_{23}(S_2)]dx + \int_{S_5} \delta u_3'(S_5)[-\sigma_{33}(S_5) + \sigma_{33}(S_2)]dx \\
&+\int_{S_6} \delta u_2'(S_6)[\sqrt{3}\sigma_{22}(S_6) - \sigma_{23}(S_6) - \sqrt{3}\sigma_{22}(S_3) + \sigma_{23}(S_3)]dx \\
&+\int_{S_6} \delta u_3'(S_6)[\sqrt{3}\sigma_{23}(S_6) - \sigma_{33}(S_6) - \sqrt{3}\sigma_{23}(S_3) + \sigma_{33}(S_3)]dx = 0
\end{aligned}
\tag{B.13}
$$

Hexagonal array (Out-of-plane):

$$
\begin{aligned}
&\int_{S_1} [\sqrt{3}\delta\sigma_{12}(S_1) + \delta\sigma_{13}(S_1)][u_1'(S_1) - u_1'(S_4)]dx + \int_{S_2} \delta\sigma_{13}(S_2)[u_1'(S_2) - u_1'(S_5)]dx \\
&+\int_{S_3} [-\sqrt{3}\delta\sigma_{12}(S_3) + \delta\sigma_{13}(S_3)][u_1'(S_3) - u_1'(S_6)]dx \\
&+\int_{S_4} \delta u_1'(S_4)[-\sqrt{3}\sigma_{12}(S_4) - \sigma_{13}(S_4) + \sqrt{3}\sigma_{12}(S_1) + \sigma_{13}(S_1)]dx \\
&+\int_{S_5} \delta u_1'(S_5)[-\sigma_{13}(S_5) + \sigma_{13}(S_2)]dx \\
&+\int_{S_6} \delta u_1'(S_6)[\sqrt{3}\sigma_{12}(S_6) - \sigma_{13}(S_6) - \sqrt{3}\sigma_{12}(S_3) + \sigma_{13}(S_3)]dx = 0
\end{aligned}
\tag{B.14}
$$

Rectangular array (Inplane)

$$\begin{aligned}
&\int_{S_1} \delta\sigma_{22}(S_1)[u_2'(S_1)-u_2'(S_3)]dy + \int_{S_1} \delta\sigma_{23}(S_1)[u_3'(S_1)-u_3'(S_3)]dy \\
&+\int_{S_2} \delta\sigma_{23}(S_2)[u_2'(S_2)-u_2'(S_4)]dx + \int_{S_2} \delta\sigma_{23}(S_2)[u_3'(S_2)-u_3'(S_4)]dx \\
&+\int_{S_3} \delta u_2'(S_3)[\sigma_{22}(S_1)-\sigma_{22}(S_3)]dy + \int_{S_3} \delta u_3'(S_3)[\sigma_{23}(S_1)-\sigma_{23}(S_3)]dy \\
&+\int_{S_4} \delta u_2'(S_4)[\sigma_{23}(S_2)-\sigma_{23}(S_4)]dx + \int_{S_4} \delta u_3'(S_4)[\sigma_{33}(S_2)-\sigma_{33}(S_4)]dx = 0
\end{aligned} \tag{B.15}$$

Rectangular array (Out-of-plane)

$$\begin{aligned}
&\int_{S_1} \delta\sigma_{12}(S_1)[u_1'(S_1)-u_1'(S_3)]dy + \int_{S_2} \delta\sigma_{13}(S_2)[u_1'(S_2)-u_1'(S_4)]dx \\
&+\int_{S_3} \delta u_1'(S_3)[\sigma_{12}(S_1)-\sigma_{13}(S_3)]dy + \int_{S_4} \delta u_1'(S_4)[\sigma_{13}(S_2)-\sigma_{13}(S_4)]dx = 0
\end{aligned} \tag{B.16}$$

Parallelogram array (Inplane)

$$\begin{aligned}
&\int_{S_1} [\sin\varphi\delta\sigma_{22}(S_1)-\cos\varphi\delta\sigma_{23}(S_1)][u_2'(S_1)-u_2'(S_3)]\sqrt{1+\tan^2\varphi}dx \\
&+\int_{S_1} [\sin\varphi\delta\sigma_{23}(S_1)-\cos\varphi\delta\sigma_{33}(S_1)][u_3'(S_1)-u_3'(S_3)]\sqrt{1+\tan^2\varphi}dx \\
&+\int_{S_2} \delta\sigma_{23}(S_2)[u_2'(S_2)-u_2'(S_4)]dx + \int_{S_2} \delta\sigma_{33}(S_2)[u_3'(S_2)-u_3'(S_4)]dx \\
&+\int_{S_3} \delta u_2'(S_3)[-\sin\varphi\sigma_{22}(S_3)+\cos\varphi\sigma_{23}(S_3)+\sin\varphi\sigma_{22}(S_1)-\cos\varphi\sigma_{23}(S_1)]\sqrt{1+\tan^2\varphi}dx \\
&+\int_{S_3} \delta u_3'(S_3)[-\sin\varphi\sigma_{23}(S_3)+\cos\varphi\sigma_{33}(S_3)+\sin\varphi\sigma_{23}(S_1)-\cos\varphi\sigma_{33}(S_1)]\sqrt{1+\tan^2\varphi}dx \\
&+\int_{S_4} \delta u_2'(S_4)[-\sigma_{23}(S_4)+\sigma_{23}(S_2)]dx + \int_{S_4} \delta u_3'(S_4)[-\sigma_{33}(S_4)+\sigma_{33}(S_2)]dx = 0
\end{aligned} \tag{B.17}$$

Parallelogram array (Out-of-plane)

$$\begin{aligned}
&\int_{S_1} [\sin\varphi\delta\sigma_{12}(S_1)-\cos\varphi\delta\sigma_{13}(S_1)][u_1'(S_1)-u_1'(S_3)]\sqrt{1+\tan^2\varphi}dx \\
&+\int_{S_2} \delta\sigma_{13}(S_2)[u_1'(S_2)-u_1'(S_4)]dx \\
&+\int_{S_3} \delta u_1'(S_3)[-\sin\varphi\sigma_{12}(S_3)+\cos\varphi\sigma_{13}(S_3)+\sin\varphi\sigma_{12}(S_1)-\cos\varphi\sigma_{13}(S_1)]\sqrt{1+\tan^2\varphi}dx \\
&+\int_{S_4} \delta u_1'(S_4)[-\sigma_{13}(S_4)+\sigma_{13}(S_2)]dx = 0
\end{aligned} \tag{B.18}$$